Sub-Femtosecond Processes in Molecules Studied by Coincidence Spectroscopy

Im Fachbereich Physik
der Freien Universität Berlin
eingereichte

Dissertation

zur Erlangung des Grades eines
Doktors der Naturwissenschaften

vorgelegt von

Felix Schell

Berlin 2020

Diese Arbeit wurde am Max-Born-Institut für Nichtlineare Optik und Kurzzeitspektroskopie im Forschungsverbund Berlin e.V. angefertigt.

Erstgutachter:
Prof. Dr. Marc Vrakking

Zweitgutachter:
Priv.-Doz. Dr. Robert Moshammer

Tag der Disputation:
17.09.2020

ABSTRACT

Studying dynamics in molecules occurring on the few-femtosecond to sub-femtosecond timescale is a formidable challenge, due to the wealth of phenomena exhibited by molecular systems. Complex manifolds of electronic states featuring electron-nuclear and electron-electron correlations complicate the interpretation of experimental data. In order to improve the situation, it is desirable to perform experiments where as much information as possible is obtained about the processes under scrutiny. When ionization is involved, this amounts to the detection of the full momentum vectors of all charged particles created in a single event, i.e. electrons and ions, the latter of which may dissociate into smaller fragments. This can be accomplished in coincidence experiments using a reaction-microscope detector. In this thesis, a reaction microscope is employed with the aim of studying attosecond dynamics taking place in molecules.

First, the polyatomic molecule 1,3-butadiene is investigated using intense femtosecond laser pulses. According to the well-known three-step model, an electron is released from the molecule via strong-field ionization and may subsequently return to and rescatter from its parent ion, all of which happens within a single laser cycle. A common phenomenon in the response of molecules to strong fields is ionization to multiple final electronic states of the cation. Here, the coincidence capabilities of the reaction microscope are exploited to demonstrate directly for the first time that the resulting multiple electron continua display differences in their rescattering behaviour. Using aligned molecules, it is furthermore shown that the probability for the electron to return to the core is dependent on the orientation of the molecule with respect to the laser polarization direction, since the returning electron wave packet retains structural information on the shape of its initial bound state.

The other goal of the thesis is to take the step from experiments relying on the sub-cycle dynamics occurring in a femtosecond laser pulse to attosecond pump-probe coincidence spectroscopy. To this end, a beamline combining a reaction microscope with a two-colour, attosecond-stable interferometric setup based on high-harmonic generation is presented. The setup is designed to operate at a repetition rate of 100 kHz, which is an order of magnitude larger than other setups currently combining attosecond spectroscopy with coincidence detection and which affords shorter acquisition times for coincidence experiments. First test results, in particular the first full characterization of attosecond pulse trains driven by sub-8 fs pulses at a repetition rate of 100 kHz, permit an optimistic perspective that, in the near future, the beamline will be capable of providing attosecond and few-cycle femtosecond pulses for pump-probe experiments on molecular targets, promising to uncover novel insights into the complex attosecond dynamics of polyatomic molecules.

KURZZUSAMMENFASSUNG

Die direkte Beobachtung ultraschneller dynamischer Prozesse in Molekülen, welche auf einer Zeitskala von weniger als einer Femtosekunde ablaufen können, stellt aufgrund der großen Komplexität solcher molekularen Systeme eine große Herausforderung dar. Daher ist es wünschenswert, experimentell möglichst viele Informationen über die zu untersuchenden Prozesse zugänglich zu machen. Durch Koinzidenzmessungen mit einem Reaktionsmikroskop ist es möglich, in Ionisationsexperimenten die vollständigen Impulsvektoren aller geladenen Teilchen (Elektronen und positiv geladene Ionen), die in einem einzelnen Ionisationsereignis entstehen, zu bestimmen. In der vorliegenden Arbeit wird ein solches Reaktionsmikroskop mit dem Ziel, Attosekunden-Prozesse in Molekülen zu untersuchen, eingesetzt.

Zunächst wird der Einfluss intensiver Femtosekunden-Laserpulse auf das mehratomige Molekül 1,3-Butadien betrachtet. Die Vorgänge, welche in Atomen und Molekülen im starken elektrischen Feld solcher Pulse ablaufen, können durch ein gängiges Dreischrittmodell beschrieben werden, wobei die drei Schritte innerhalb einer einzigen Oszillationsperiode des elektrischen Feldes stattfinden: Ein Elektron wird durch Starkfeldionisation freigesetzt und dann kurze Zeit später durch das Laserfeld zu seinem Mutterion zurückbeschleunigt, an welchem es schließlich rückstreuen kann. Es ist weiterhin bekannt, dass in Molekülen mehrere elektronische Zustände des Ions durch Starkfeldionisation besetzt werden können. Mit Hilfe von Koinzidenzmessungen wird in der vorliegenden Arbeit nun erstmals direkt gezeigt, dass die mehreren daraus resultierenden Elektronenkontinua ein unterschiedliches Rückstreuverhalten aufweisen. Des Weiteren wird mit Hilfe ausgerichteter Moleküle demonstriert, dass in 1,3-Butadien die Rückkehrwahrscheinlichkeit des Elektrons von der Molekülorientierung abhängt, da das zurückkommende Elektronenwellenpaket die Struktur des ursprünglichen gebundenen Zustands des Elektrons teilweise beibehält.

Ein weiteres Ziel dieser Arbeit ist es, Attosekunden-Pump-Probe- und Koinzidenzspektroskopie miteinander zu verbinden. Daher wird ein neuer experimenteller Aufbau vorgestellt, der ein Reaktionsmikroskop und ein attosekundenstabiles Zweifarben-Interferometer, basierend auf der Erzeugung hoher Harmonischer, kombiniert. Die Repetitionsrate von 100 kHz ist um eine Größenordnung höher als in vergleichbaren Aufbauten, die derzeit in Verwendung sind, was eine kürzere Messdauer für Koinzidenzexperimente ermöglicht. Ergebnisse erster Testmessungen mit dieser Apparatur werden vorgestellt, insbesondere die erste vollständige Charakterisierung von kurzen, durch sub-8 fs-Pulse und bei 100 kHz erzeugten Attosekunden-Pulszügen. Diese Ergebnisse zeichnen ein positives Bild im Hinblick auf die Möglichkeit künftiger Koinzidenzexperimente an Molekülen mit Hilfe des präsentierten Attosekunden-Pump-Probe-Aufbaus, welche tiefe Einblicke in die komplexen Vorgänge solcher Systeme ermöglichen könnten.

Contents

Introduction

Time scales of processes in molecules

The relevant time scales for nuclear motion in molecules (rotations, vibrations, and nuclear rearrangement in chemical reactions) range from picoseconds down to a few femtoseconds [1]. Laser sources producing pulses with femtosecond duration have made it possible to observe and control these nuclear dynamics in real time (launching the field of *femtochemistry* [1]), relying on *pump-probe* schemes, where a pump pulse creates a non-stationary superposition of states and a second pulse, after a variable delay, probes the current state of the system's time evolution [2]. Theoretically, the nuclear motion is often studied in terms of the *Born-Oppenheimer approximation*, which assumes that the electronic degrees of freedom can adapt adiabatically to the instantaneous position of the nuclei [2]. The motion of the latter is in turn governed by potential-energy surfaces, each of which is determined by the charge distribution of a specific, stationary electron state. As long as the potential-energy surfaces associated with different electronic states are well separated, the Born-Oppenheim approximation holds and the nuclear and electronic degrees of freedom remain decoupled. Otherwise, *avoided crossings* or *conical intersections* occur [3], where the dynamics become non-adiabatic but still unfold on a femtosecond time scale [2].

Even faster, attosecond dynamics are possible, when multiple electronic states are coherently populated, e.g. by a broadband pulse in the extreme ultraviolet (XUV) spectral regime or sudden removal of an electron [4, 5]. This leads to the concept of *charge migration* [6, 7], where charges may rapidly move from one molecular site to another, purely due to the sub-femtosecond electron dynamics and without the involvement of nuclear motion, which only sets in afterwards. Still, the attosecond electron motion is relevant for chemistry, because it could facilitate the observation and control of novel reaction pathways that are not limited to specific Born-Oppenheimer potential-energy surfaces but instead directly guided by the time-dependent electron wave packet [2]. The time-resolved experimental and theoretical exploration of such sub-femtosecond motion is the topic of the field of *attosecond science*.

Observing attosecond processes

Today, laser sources operating in the near-infrared (IR) spectral domain and based on the titanium:sapphire technology routinely provide pulses with a duration of a few femtoseconds, i.e. consisting of almost only a single oscillation of the electric field [5]. However, such pulses are still too long to directly observe sub-femtosecond processes in a pump-probe configuration. Nonetheless, attosecond science is based on these sources, exploiting non-linear processes that unfold within one oscillation period of the electric field of a femtosecond pulse in the interaction with matter. In detail, when an intense femtosecond laser pulse is focused into a molecular or atomic target, the dynamics can be described by a three-step model [8]: The strong laser field first releases an electron via *strong-field ionization (SFI)* (i). Subsequently, the electron propagates in the continuum (ii) and may finally be driven back to the ion core (*recollision*, iii), from which it either scatters (*rescattering*) or with which it recombines. Coherent, broadband electromagnetic radiation in the XUV spectral domain is emitted in the latter case, a process which is called *high-harmonic generation (HHG)*.

There are two approaches to exploit this mechanism to obtain sub-femtosecond temporal resolution:

- *Attosecond pump-probe spectroscopy*: The electromagnetic radiation generated upon recombination is emitted in bursts, each with a duration down to tens of attoseconds [9]. Since one burst is emitted each half cycle of the driving IR pulse, a train of pulses is formed (*attosecond pulse train*) [10]. Gating techniques exist to isolate a single burst from the pulse train [11, 12], leading to an *isolated attosecond pulse*.
  These attosecond pulses can then be used to investigate another target, where either charged particles or absorption spectra are detected.[1] In order to study dynamics, a pump-probe scheme needs to be implemented. The most obvious solution would be to use attosecond pulses as both the pump and the probe. However, this approach has so far been limited by the low photon flux of attosecond sources based on HHG, which makes two-photon absorption, as required for pump-probe measurements, unlikely [2]. Instead, the most widely adopted route is to replace either the pump or the probe pulse with a replica of the IR pulse driving HHG, which inherently has a well-defined sub-cycle phase relationship to the attosecond pulses. Both attosecond pulse trains and isolated attosecond pulses can be combined with the driving IR to study sub-femtosecond processes [5].
- *Self-probing schemes:* In addition, also the three-step process itself possesses an inherent sub-cycle temporal resolution: Step one, SFI, may launch electronic and nuclear wave packets in the parent ion [16–

[1] The latter case is called *attosecond transient absorption* [13–15] and is not the focus of the present thesis.

18], which evolve during the continuum propagation of the electron. When recolliding with its parent ion, the continuum electron then interrogates the current state of the dynamics, which is encoded in the amplitude and phase of the emitted high-harmonic radiation (*high-harmonic spectroscopy*) [17] and in the momentum distribution of the rescattered electrons (*laser-induced electron diffraction (LIED)*) [18]. The time in the continuum is different for different final energies of the photons or rescattered electrons and can additionally be varied by tuning the driving-laser wavelength [19]. These techniques may make it possible to image electronic and nuclear dynamics with sub-nanometre spatial as well as sub-femtosecond temporal resolution [20].

Thesis goals and outline

The goal of the present thesis is to make a contribution to each of these two approaches to experiments with attosecond temporal resolution, where in both cases a prominent role is played by a *reaction-microscope* detection system. Reaction microscopes facilitate the measurement of the three-dimensional momentum vector for each charged particle created in a single interaction event (typically one or several electrons and a parent ion or ionic fragments), i.e. to perform *kinematically complete coincidence* measurements [21].

The contribution to the first approach consists in the design and initial implementation of an XUV-IR pump-probe beamline in combination with a reaction microscope, operating at a high laser repetition rate and with high enough stability and XUV photon flux to perform attosecond experiments on molecular targets. The increased informational content provided by the reaction microscope compared to less powerful detection systems more commonly used in attosecond pump-probe experiments is expected to help in the interpretation of such measurements [5]. The design of this beamline and first test results are described in detail in part III of the thesis.

The contribution to the second approach, presented in part II, consists in testing some common assumptions related to the underlying three-step model. To this end, experiments are performed using the polyatomic molecule 1,3-butadiene as the target and utilizing the reaction microscope in combination with intense femtosecond laser pulses. The experiments rely crucially on the simplest multi-electron effect exhibited by most polyatomic molecules as part of their response to a strong laser field: the population of multiple electronic states in the ion upon ionization [22], which is also relevant for the preparation of electron wave packets with attosecond dynamics via SFI [16]. The coincidence capabilities of the reaction microscope are exploited to disentangle the distributions of rescattered electrons correlated with different electronic states of the ion. Comparison of these channel-resolved distributions makes it possible to draw conclusions on the three-step model itself. Conceivable implications for high-harmonic spectroscopy and LIED are also discussed.

Part I contains the necessary fundamentals for a proper understanding of the other two parts.

I

Fundamentals

CHAPTER 1

Strong-field and Attosecond Physics

Strong laser fields and the three-step model

Strong-field physics is concerned with the (non-linear) response of matter to a strong external electric field. An electric field is considered to be strong when its magnitude is no longer negligible compared to the field binding electrons to atoms, molecules, or solids. For a hydrogen atom in the electronic ground state, this field amounts to 5×10^{11} V/m [23]. For molecules, which are the major focus of the present thesis, the valence electrons are bound somewhat more weakly. Such strong electric fields can be produced using femtosecond laser sources. These generate intense (millijoules of energy per pulse) laser pulses, which may only consist of a few electric-field oscillations [24]. When such a beam of short pulses is focused, peak electric field strengths comparable to or exceeding the electric forces binding electrons to the nucleus occur.

For not too short multi-cycle or few-cycle pulses with linear polarization and without a chirp[1], the temporal evolution of the electric field $\mathcal{E}(t)$ can be described by [25]

$$\mathcal{E}(t) = \mathcal{E}_0(t) \cdot \cos(\omega t + \phi_{\mathrm{CEP}}), \tag{1.1}$$

where ω is the carrier frequency[2] and $\mathcal{E}_0(t)$ is the envelope function, which describes the amplitude of the oscillations and which is slowly varying compared to the oscillations with frequency ω. The phase ϕ_{CEP} is called the *carrier-envelope phase (CEP)* and characterizes the offset of the maximum of the

[1] A *chirped* pulse is one with a time-dependent carrier frequency $\omega(t)$.

[2] ω is related to the wavelength λ according to $\omega = 2\pi c/\lambda$, where c is the speed of light.

envelope with respect to the nearest maximum of the carrier oscillations. The CEP becomes important for few-cycle pulses. Note that eq. (1.1) contains no spatial dependence, since spatial variations can usually be neglected for atomic or molecular targets, because the wavelength is much larger than the extent of the target (dipole approximation) [26]. While for resonant processes in atomic or molecular physics typically only the envelope of a pulse is relevant, strong-field processes are sensitive to the sub-cycle oscillations of the electric field. It is this sub-cycle dependence of the strong-field response that links strong-field to attosecond physics.

The sub-cycle processes occurring in the target under the influence of the strong laser field are described by the semi-classical three-step model [8], which has been of paramount importance for the development of attosecond physics and for the interpretation of attosecond experiments. It provides a uniform explanation for a number of phenomena initiated by intense short pulses in gaseous targets. The three steps are: 1) strong-field ionization of an electron, 2) propagation of the released electron in the continuum under the influence of the laser field, where the electron may be driven back to its parent ion (also called the *core* in this thesis), and 3) recollision and interaction with the parent ion. The three steps are described in detail in the following sections.

1.1 IONIZATION

Single- and multi-photon ionization

The first step of the three-step model is strong-field ionization (SFI). During ionization, one or several electrons are removed from the target, leaving the target itself in a positively charged state, while the electron is promoted from a discrete bound state to the continuum of unbound states. The difference in energy between the initial bound state and the electronic state of the cation upon ionization is called the *ionization potential (IP)*. When electromagnetic radiation with frequency ω is used to drive ionization, absorption of a single photon with energy $\hbar w$ is sufficient if $\hbar w > \mathrm{IP}$. In this case, the rate of ionization Γ is given by

$$\Gamma(t) \propto \sigma \cdot \mathcal{E}_0(t)^2, \tag{1.2}$$

where σ is the cross section for single-photon ionization.

For increasing intensities[3], multi-photon ionization becomes significant, the rate of which scales as $\sigma_N \cdot \mathcal{E}_0(t)^{2N}$ with the electric field strength, where N is the photon order and σ_N the corresponding cross section. For N-photon absorption, ionization of targets becomes possible for $\mathrm{IP} < N \cdot \hbar\omega$. These processes can be described by perturbation theory, where the laser field is

[3]The electric field $\mathcal{E}$ is related to the intensity I according to $I = \frac{c\varepsilon_0}{2} \cdot \mathcal{E}^2$, where ε_0 is the vacuum permittivity and c is the speed of light.

regarded as perturbation to the larger forces binding the electron to the target [23].

Strong-field ionization

For increasing intensities – entering the regime of SFI – eventually the laser field becomes so strong that it can no longer be seen as a perturbation. Instead it deforms the potential binding the electrons to the core significantly: Consider an electron bound in a Coulomb-like potential. When the laser field is present, it is superimposed on the electric field from this potential. The resulting barrier has only a finite width, enabling the bound electron to tunnel through the barrier into the continuum. This process is called *tunnelling ionization*. The point in space where the electron leaves the barrier is called the *tunnelling exit*. Two different regimes exist, which can be distinguished via the *Keldysh parameter* $\gamma = \omega \frac{\sqrt{2\mathrm{IP} m_\mathrm{e}}}{e\mathcal{E}_0}$, where e is the elementary charge and m_e the electron mass: For $\gamma \ll 1$, the system can adiabatically adjust to the laser field and the barrier remains essentially unchanged while the electron tunnels through it. For $\gamma \gtrsim 1$, the barrier changes during tunnelling and a 'vertical heating' helps the electron to traverse the barrier [27]. Therefore, the process becomes more similar to perturbative multiphoton ionization, and the regime $\gamma > 1$ is called the *multi-photon* regime of SFI.

In the case of pure tunnelling ionization, the rate of ionization Γ has an exponential dependency on the instantaneous field strength $\mathcal{E}(t)$, described by

$$\Gamma(t) \propto \exp\left(-\frac{2(2\mathrm{IP})^{3/2}}{3\mathcal{E}(t)} \cdot \frac{m_\mathrm{e}^{1/2}}{\hbar e}\right). \tag{1.3}$$

This relation is derived within the so-called *strong-field approximation*, where it is assumed that, for the continuum states, the influence of the Coulomb field of the core can be neglected compared to the strong laser field [27]. The pre-exponential proportionality factor is not captured well within the strong-field approximation, but more refined approaches such as ADK theory exist that improve on this point [28, 29].

In addition to the total ionization rate, one can also derive predictions for the momentum distribution of the released electron in the continuum immediately upon ionization from the strong-field approximation, where the momentum $\widetilde{p}_{z,0}$ parallel to the laser polarization direction has to be distinguished from the momentum components $\widetilde{p}_{x,0}$ and $\widetilde{p}_{y,0}$ in the plane perpendicular to it (called *lateral* momentum). The distribution of the former is often assumed to be zero [30–32] whereas the lateral momentum distribution is given by [27, 33]

$$\Gamma(\widetilde{p}_{x,0}, \widetilde{p}_{y,0}) \propto \exp\left(-\frac{\left(\widetilde{p}_{x,0}^2 + \widetilde{p}_{y,0}^2\right) \cdot \sqrt{2\mathrm{IP}}}{\mathcal{E}(t) \cdot \hbar e m_\mathrm{e}^{1/2}}\right). \tag{1.4}$$

Thus, the lateral momentum distribution after tunnelling has the shape of a Gaussian centred around zero momentum. Equation (1.4) remains valid for γ close to 1 [27]. However, it is to be expected that the momentum distribution of the electron before tunnelling also influences the lateral momentum distribution after tunnelling. This is often included heuristically [34] by inserting an additional pre-factor in eq. (1.4) [35–39]:

$$\Gamma(\widetilde{p}_{x,0},\widetilde{p}_{y,0}) \propto \int \mathrm{d}\widetilde{p}_{z,0} |\hat{\psi}(\widetilde{p}_{x,0},\widetilde{p}_{y,0},\widetilde{p}_{z,0})|^2 \times \exp\left(-\frac{\left(\widetilde{p}_{x,0}^2+\widetilde{p}_{y,0}^2\right)\cdot\sqrt{2\mathrm{IP}}}{\mathcal{E}(t)\cdot\hbar e m_\mathrm{e}^{1/2}}\right), \tag{1.5}$$

where $\hat{\psi}$ is the momentum representation of the electron wave function in the bound state, i.e. the Fourier transform of the electrons initial orbital $\psi(\vec{r})$. According to eq. (1.5), the lateral momentum distribution after tunnelling is determined by the projection of the momentum distribution of the bound electron along the laser polarization direction times an exponential tunnelling filter.

For molecules, eq. (1.5) implies that the lateral momentum distribution of the continuum electron depends on the orientation of the molecule with respect to the laser polarization direction, since different parts of the bound electron's orbital are projected onto the lateral plane for different orientations. Similarly, also the total ionization yield eq. (1.3) is expected to depend on the molecular orientation, which has been confirmed by numerous experiments [40–43]. Several approaches exist to calculate this *angular ionization probability* theoretically [44–46], the most commonly employed of which is the molecular ADK theory [47, 48]. Molecular ADK theory agrees well with experimental findings for small, diatomic molecules [40, 42], but discrepancies have been found for larger, polyatomic molecules [42, 43, 49, 50]. The angular ionization probability is denoted by $S(\theta,\phi)$ in this thesis and depends on both the polar θ and the azimuthal ϕ coordinates of the polarization vector in the molecular frame (see section 5.1).

The effect of nodal planes

One particularly important factor that is known to significantly affect SFI in molecules is the presence of nodal planes in the released electron's initial orbital. Nodal planes are planes along which the electron density is zero in a particular orbital, due to destructive interference. The orbital's amplitude is identical on both sides of the nodal plane, but the phase differs by a factor of π. When the ionizing field's polarization vector lies within a nodal plane, the momentum of the electron upon ionization cannot lie in the same plane [16]. To see this, consider, as a simple example, a diatomic molecule with an anti-bonding orbital $\psi(\vec{r})$:

$$\psi(\vec{r}) \propto \phi(\vec{r}-\vec{R}/2) - \phi(\vec{r}+\vec{R}/2), \tag{1.6}$$

where $\phi(\vec{r})$ is the spherical symmetric s-type atomic wave function making up the anti-bonding orbital and the nuclei are positioned at $\vec{R}/2$ and $-\vec{R}/2$. Clearly, for all $\vec{r}$ with $\vec{r} \perp \vec{R}$, $\psi(\vec{r}) = 0$, and therefore the plane perpendicular to $\vec{R}$ through the origin forms a nodal plane of the orbital $\psi(\vec{r})$. The momentum-space orbital $\hat{\psi}(\vec{p})$, i.e. the Fourier transform of $\psi(\vec{r})$, then fulfils

$$|\hat{\psi}(\vec{p})|^2 \propto |\hat{\phi}(\vec{p})|^2 \sin^2\left(\frac{\vec{p}\cdot\vec{R}}{2\hbar}\right), \tag{1.7}$$

where $\hat{\phi}(\vec{p})$ is the Fourier transform of $\phi(\vec{r})$ [51]. Thus, $\hat{\psi}(\vec{p}) = 0$ when $\vec{p}$ lies within the nodal plane (the plane fulfilling $\vec{p}\cdot\vec{R} = 0$), and, when the driving laser polarization direction lies within the same plane, according to eq. (1.5) the ionization probability is also zero. Therefore, ionization with the polarization vector lying in a nodal plane is only possible if the electron acquires a non-zero lateral momentum component. This is also responsible for the suppression in the overall ionization probability when ionizing along nodal planes often observed in experiments [40–42, 47, 52]. The above remains true for more complex orbitals featuring nodal planes and can be derived within the strong-field approximation (see e.g. Supplementary Material in [53]).

Single-active-electron approximation

Initially, strong-field induced processes have been modelled using the *single-active-electron approximation*, where only one electron – the one with the lowest binding energy – is affected by the strong electric field [54]. For atoms, where the binding energy for more strongly bound electrons is significantly higher, this yields good results, because, according to eq. (1.3), the ionization rate is exponentially suppressed with increasing IP. However, it was discovered that the single-active-electron approximation often is not sufficient to describe strong-field induced processes in molecules [22, 55–57]. Instead, direct[4] ionization to excited electronic states of the cation – in addition to the ground state – needs to be taken into account. The reasons for the breakdown of a single-electron description lies in 1) the generally reduced energy gap between the ground and excited states in molecular ions compared to atomic ions [57] and 2) the pre-exponential factor in eqs. (1.3) and (1.5), which depends on the orbital structure and can lead to a reduction of the ionization yield from the highest occupied molecular orbital (HOMO), enhancing the relative yield from lower-lying orbitals [20]. In this case, the relevant one-particle orbitals representing the wave function of the released electron prior to ionization are the so-called *Dyson orbitals* $\Psi^{\mathrm{D}}(\vec{r})$, defined as the overlap of the N-particle electron wave function of the neutral (usually in the ground state) $\Psi_N(\vec{r}_1,\ldots,\vec{r}_N)$ with

[4] Direct ionization to excited cation states needs to be distinguished from an indirect process, where ionization initially takes place to the electronic ground state of the cation, which is only subsequently excited by the laser field.

the $N-1$-particle wave function of the final electronic state of the cation $\Psi_{N-1}(\vec{r}_1,\ldots,\vec{r}_{N-1})$ [54]:

$$\Psi^{\mathrm{D}}(\vec{r}) = \sqrt{N}\int \mathrm{d}\vec{r}_1 \ldots \int \mathrm{d}\vec{r}_{N-1}\Psi_N^*(\vec{r}_1,\ldots,\vec{r}_{N-1},\vec{r})\Psi_{N-1}(\vec{r}_1,\ldots,\vec{r}_{N-1}). \quad (1.8)$$

The Dyson orbital can also be regarded as the hole left in the ion [20].

Within the Hartree-Fock framework, the multi-particle wave functions Ψ_{N-1} and Ψ_N can be expressed as the antisymmetrized product of $N-1$ or N, respectively, single-particle wave functions – the conventional molecular orbitals which are filled with electrons. Within the Koopmans' approximation – which neglects the orbital relaxation which may occur in the ion due to the different potential felt by all the other electrons when one electron is removed – the one-particle wave functions ψ_i making up Ψ_{N-1} and Ψ_N are additionally the same [20]:

$$\begin{aligned}\Psi_N(\vec{r}) &= \mathcal{A}\psi_1(\vec{r}_1)\ldots\psi_N(\vec{r}_N)\\ \Psi_{N-1}(\vec{r}) &= \mathcal{A}\psi_1(\vec{r}_1)\ldots\psi_{N-1}(\vec{r}_{N-1}),\end{aligned} \quad (1.9)$$

where $\mathcal{A}$ is the antisymmetrization operator. In this case, the Dyson orbital Ψ^{D} is simply the orbital ψ_N from which the electron has been removed.

Then, the following simple picture emerges: Interaction with a strong laser field may involve removing electrons from the HOMO or lower lying orbitals HOMO-1, HOMO-2, ... In the former case, the resulting cation will be in the electronic ground state, whereas the latter cases lead to an ion in the first, second, ... electronically excited state. The shape of the orbital from which the electron has been removed dictates the angular ionization probability and the shape of the continuum wave packet (according to eq. (1.5)). The multiple direct ionization pathways that result in a cation in the ground or various electronically excited sates are called *ionization channels* or, when the emphasis is one the released electron, *continuum channels* in this thesis.

1.2 PROPAGATION IN THE CONTINUUM

The second step in the three-step model is the propagation of the released electron in the continuum under the influence of the laser field. Contrary to the first step, which requires a quantum-mechanical description, this motion is often regarded classically, by solving the Newtonian equations of motion in the laser field (and possibly the Coulomb electric field generated by the parent ion) for an ensemble of electrons created at the tunnel exit with a lateral velocity distribution given by eq. (1.5) [37].

Quantum-mechanically the various classical trajectories launched at different instants in time and the phases acquired along them are described by a single continuum wave packet. The different accelerations experienced by different portions of the wave packet due to the varying driving electric field

imply that the wave packet is chirped. The amplitude of the wave packet is given by the instantaneous ionization rate, eq. (1.3), while the lateral shape evolves from the shape of the initial lateral momentum distribution. Generally, the lateral width of the wave packet will increase during continuum propagation, due to the initial spatial confinement, where the amount of wave-packet spreading depends on the details of the initial shape.[5]

Solving the classical equations of motion

Depending on the instant of birth t_0 within a laser cycle, several different outcomes of continuum propagation are possible. Generalizing eq. (1.1), consider an oscillating field $\vec{\mathcal{E}}(t)$ with a single carrier frequency ω, arbitrary ellipticity[6] ε, and (slowly varying) envelope $\mathcal{E}_0$ in the z-x-plane, perpendicular to the propagation y-direction:

$$\vec{\mathcal{E}}(t) = \frac{\mathcal{E}_0}{\sqrt{1+\varepsilon^2}} \times \begin{pmatrix} \varepsilon \sin\omega t \\ 0 \\ \cos\omega t \end{pmatrix}. \tag{1.10}$$

The vector potential to the field in eq. (1.10) is

$$\vec{A}(t) = -\frac{\mathcal{E}_0}{\omega\sqrt{1+\varepsilon^2}} \times \begin{pmatrix} -\varepsilon \cos\omega t \\ 0 \\ \sin\omega t \end{pmatrix}, \tag{1.11}$$

such that $\vec{\mathcal{E}}(t) = -\frac{\partial \vec{A}}{\partial t}$. Neglecting the influence of the Coulomb potential, the motion of the electron $\vec{r}(t)$ is governed by the equation

$$m_\mathrm{e}\ddot{\vec{r}} = -e\vec{\mathcal{E}}, \tag{1.12}$$

whose solution is (setting $\vec{r}(t_0) = 0$, i.e. assuming that the tunnelling exit is at the origin) [58]

$$\begin{aligned} \vec{r}(t) = &-\frac{e\mathcal{E}_0}{m_\mathrm{e}\omega^2\sqrt{1+\varepsilon^2}} \\ &\times \begin{pmatrix} \varepsilon\left(-\sin\omega t + \sin\omega t_0 + \omega\,(t-t_0)\cos\omega t_0\right) \\ 0 \\ -\cos\omega t + \cos\omega t_0 - \omega(t-t_0)\sin\omega t_0 \end{pmatrix} \\ &+ \frac{(t-t_0)}{m_\mathrm{e}}\vec{p}_0, \end{aligned} \tag{1.13}$$

[5] Within the strong-field approximation, the classical trajectories re-emerge using the saddle-point method, where each trajectory acquires a certain phase, which is important to describe interference effects between multiple trajectories [20].

[6] The ellipticity is defined as the ratio of the minor to the major axis of the ellipse that describes the motion of the polarization vector. Accordingly, in eq. (1.10), the major axis points along the z-axis and the minor axis along the x-axis.

where $\vec{p}_0$ is the initial velocity vector of the continuum electron in the space-fixed coordinate system, which is rotated around the y-axis with respect to the electron's initial momentum vector

$$\widetilde{\vec{p}_0} = \begin{pmatrix} \widetilde{p}_{x,0} \\ \widetilde{p}_{y,0} \\ \widetilde{p}_{z,0} \end{pmatrix}$$

defined with respect to the rotating polarization vector. As before, $\widetilde{p}_{x,0}$ and $\widetilde{p}_{y,0}$ are the components perpendicular to the instantaneous direction of the polarization vector, whose distribution is given by eq. (1.5), whereas $\widetilde{p}_{z,0}$ is the momentum component parallel to the polarization vector. Assuming, as is commonly done, $\widetilde{p}_{z,0}$ to be zero, $\vec{p}_0$ can be calculated as [58]

$$\vec{p}_0 = \begin{pmatrix} \widetilde{p}_{x,0} \cdot \cos\beta \\ \widetilde{p}_{y,0} \\ \widetilde{p}_{x,0} \cdot \sin\beta \end{pmatrix} \text{ with} \qquad \beta = \arctan(\varepsilon \tan \omega t_0). \tag{1.14}$$

Direct electrons

If the electron is born before the maximum of the laser field in a given half cycle, its trajectory eq. (1.13) does not come close to the parent ion again before detection [59]. Such electrons are called *direct*. The instantaneous momentum of the electron, born at time t_0 via SFI, is denoted by $\vec{p}(t)$. After a direct electron's birth into the continuum, the canonical momentum

$$\vec{\pi}(t) = \vec{p}(t) - e\vec{A}(t) \tag{1.15}$$

is conserved, since direct electrons do not interact with the core again [25]. The final momentum of the electron $\vec{p}_\mathrm{f}$ is then given by

$$\vec{p}_\mathrm{f} = \vec{p}(\infty) = \vec{p}_0 - e\vec{A}(t_0) + e\vec{A}(\infty).$$

If the laser field is adiabatically turned off, $\vec{A}(\infty) = 0$ and

$$\vec{p}_\mathrm{f} = \vec{p}_0 - e\vec{A}(t_0),$$

i.e. the final momentum of the direct electrons is completely determined by their initial momentum and the vector potential at the instant of birth into the continuum. The mapping of different times of birth t_0 to different final momenta $\vec{p}_\mathrm{f}$ by the laser field is called *streaking*. For linear polarization, only the electron momentum along the stationary polarization direction is affected by the laser field during propagation, whereas for $\varepsilon > 0$ also the momentum distribution in the plane perpendicular to $\vec{\mathcal{E}}(t_0)$ is deformed.

Calculating the final kinetic energy E_f while neglecting $\vec{p}_0$,

$$E_\mathrm{f} = \frac{|\vec{p}_\mathrm{f}|^2}{2m_\mathrm{e}} = \frac{e^2\mathcal{E}_0^2}{2\omega^2 m_\mathrm{e}(1+\varepsilon^2)} \times (\sin^2\omega t_0 + \varepsilon^2\cos^2\omega t_0), \tag{1.16}$$

it can be seen that the maximum energy achievable will not exceed

$$E_\mathrm{f}^\mathrm{max} = 2 \cdot \frac{U_\mathrm{p}}{1+\varepsilon^2}, \tag{1.17}$$

where

$$U_\mathrm{p} = \frac{e^2\mathcal{E}_0^2}{4m_\mathrm{e}\omega^2} \tag{1.18}$$

is the *ponderomotive potential*, i.e. the cycle-averaged quiver energy of an electron due to its oscillatory motion in the laser field [23], which is independent of ε. For $\varepsilon \neq 1$, eq. (1.16) also establishes a one-to-one mapping of times of birth t_0 to the direct-electron final energy, for each half cycle of the laser pulse. The lowest energies for the direct electrons are attained for times of birth close to the field maximum, whereas only electrons with times of birth close to the minimum of the field can reach the maximum energy. Note that, due to the exponential dependence of the ionization yield on the instantaneous electric field (see eq. (1.3)), the yield of direct electrons with energies approaching $2U_\mathrm{p}/(1+\varepsilon^2)$ will also drop exponentially, at least for not too high ellipticities.

ATI structure

In a multi-cycle pulse, part of the bound population is promoted to the continuum during each half cycle of the pulse, and the (direct) continuum electrons are accelerated in the same direction each cycle. The electron bursts created in each cycle interfere and form a series of peaks separated by the photon energy [60, 61]

$$E_n = n\hbar\omega - U_\mathrm{p} - \mathrm{IP}, \tag{1.19}$$

where E_n denotes the energy for the n-th peak. The series of peaks is called an *above-threshold ionization (ATI)* progression [62]. Within the photon picture, it is also often interpreted as an electron absorbing more photons than necessary for ionization, since the spacing with the laser photon energy and the shift according to the IP suggest this interpretation.[7]

For an infinitely long pulse, the peaks are infinitely narrow, whereas they become broader for increasing bandwidth of the driving pulse. Towards the limit of a single-cycle pulse, the interference diminishes, because only a single cycle produces a significant electron burst, and the peaks become so broad

[7] Note, however, that the ATI peaks as a multi-cycle interference phenomenon of very intense fields do not require the quantization of the electric field and can be understood without reverting to notion of photons.

that they start to form a continuum without the ATI modulation (also see the analogous situation for the spectrum of isolated attosecond pulses in section 3.1). As can be seen from eq. (1.19), the ATI peaks also shift with the ponderomotive energy U_p. Thus, in the focus of a real laser pulse, where averaging over varying intensities and thus ponderomotive potentials (see eq. (1.18)) is inevitable, the peaks will be additionally smeared out.

Recolliding trajectories

For an electron born after the field maximum, the trajectory eq. (1.13) for $\varepsilon = 0$ leads back to the parent ion at the origin. This implies that the electron may undergo *recollision*, which enables the occurrence of one of the interactions of step three of the three-step model (see section 1.3). The time span between the instants of birth t_0 and return to the core t_ret is called *excursion time* $\Delta t_\mathrm{exc} = t_\mathrm{ret} - t_0$. The maximum distance from the electron to the core during this time span is called the *excursion distance* Δr_exc. According to eq. (1.13), it can be estimated as [63]

$$\Delta r_\mathrm{exc} = \frac{e\mathcal{E}_0}{m_\mathrm{e}\omega^2\sqrt{1+\varepsilon^2}}. \tag{1.20}$$

The return time t_ret can be calculated by demanding that

$$\vec{r}(t_\mathrm{ret}) = 0. \tag{1.21}$$

Using the expression eq. (1.13), the relations

$$\widetilde{p}_{x,0} = -\frac{e\mathcal{E}_0\varepsilon}{\omega\cos(\beta)\sqrt{1+\varepsilon^2}} \times \left(\frac{\sin\omega t_\mathrm{ret} - \sin\omega t_0}{\omega(t_\mathrm{ret}-t_0)} - \cos\omega t_0\right) \tag{1.22}$$

(where β is given by eq. (1.14)), $\widetilde{p}_{y,0} = 0$, and

$$\begin{aligned}(\varepsilon^2+1)\omega(t_\mathrm{ret}-t_0)\sin\omega t_0\cos\omega t_0 - \varepsilon^2\sin\omega t_0(\sin\omega t_\mathrm{ret} - \sin\omega t_0)\\ + \cos\omega t_0(\cos\omega t_\mathrm{ret} - \cos\omega t_0) = 0\end{aligned} \tag{1.23}$$

can be derived. Equation (1.23) can be solved numerically to obtain t_ret. Note that for $\varepsilon > 0$ the condition eq. (1.21) can only be fulfilled, if the continuum electron possesses a non-zero initial lateral velocity $\widetilde{p}_{x,0}$ given by eq. (1.22) (also see next subsection). Figure 1.1a) displays t_ret in dependence of the time of birth t_0 for various ellipticities. As can be seen, the earlier the electron is born into the continuum after the field maximum the later it returns to the core: The longest excursion time lasting a full cycle is reached when the electron is born immediately after the field maximum, whereas electrons born close to the minimum of the field revisit the core very quickly. For larger

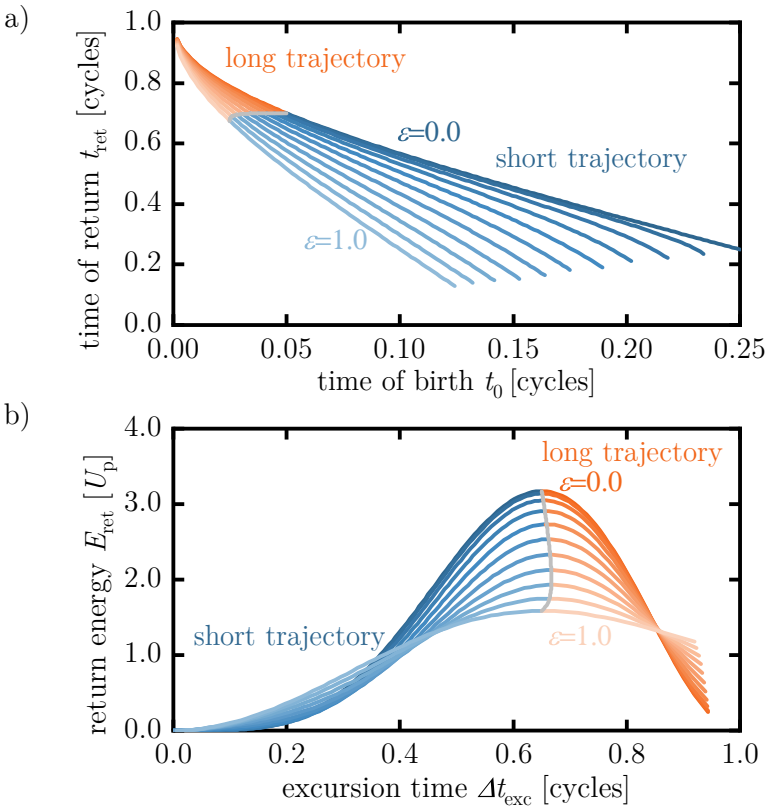

Figure 1.1: a) Return time t_{ret} in dependence of the time of birth t_0 for electrons following the long (orange curves) or short (blue curves) trajectories and for ellipticities ranging from 0.0 to 1.0. b) The energy E_{ret} of an electron when it revisits its parent ion in dependence of the excursion time Δt_{exc} for the same range of ellipticities. All times are given as fractions of a full laser cycle starting at the field maximum. Electrons born in the quarter cycle before the maximum never return to their parent ion. In both cases, the grey curve highlights the points of transition from the long to the short trajectories, for which the maximum return energy is obtained.

ellipticities, electrons born close to the field minimum are no longer able to return to their parent ion.

Before the interaction with the parent ion, the canonical momentum eq. (1.15) is conserved. Thus, the electron momentum at the time of recollision (the *return momentum*), just prior to the interaction, is

$$\vec{p}_{\mathrm{ret}} = \vec{p}(t_{\mathrm{ret}}) = \vec{p}_0 - e\vec{A}(t_0) + e\vec{A}(t_{\mathrm{ret}}). \tag{1.24}$$

The *return energy* $E_{\mathrm{ret}} = \frac{|\vec{p}_{\mathrm{ret}}|^2}{2m_{\mathrm{e}}}$ is plotted for different ellipticities as a function of the excursion time Δt_{exc} in fig. 1.1b). The maximum return energy the electrons can achieve (again neglecting the initial momentum) amounts to

$$E_{\mathrm{ret}}^{\mathrm{max}}(\varepsilon) \approx 3.17 \frac{U_{\mathrm{p}}}{1+\varepsilon^2}. \tag{1.25}$$

Importantly, two classes of recolliding trajectories leading to the same final energy have to be distinguished – the so-called *long* and *short trajectories* (corresponding to the orange and blue curves in fig. 1.1, respectively), referring to the respective excursion time for the trajectories. Electrons following a long trajectory are born closer to the field maximum and take a longer time to return to the core. The earlier they are born, the longer the long trajectory. Electrons following a short trajectory, on the other hand, are born later in the quarter-cycle after the field maximum but return to the core already after a short excursion time. The later they are born, the shorter the short trajectory. The phase of birth where the maximum return energy is obtained and where the long and short trajectories merge is shown as the grey curves in fig. 1.1.

As can be evidenced from fig. 1.1b), there is a (two-to-one) mapping between the electron excursion time and the return energy. In strong-field experiments where in the detected signal (either charged particles or high-harmonic radiation) different return energies can be discriminated, the mapping between Δt_{exc} and E_{ret} effectively gives access to sub-cycle temporal resolution. This is the technique used to "vary" the delay in the second kind of attosecond experiments mentioned in the introduction. The small range of excursion times accessible with this method can be extended by varying the frequency ω of the driving laser, due to the scaling of the excursion time with ω [19].

Note that the electrons following the long trajectories are expected to be much more abundant than those following the short trajectories, due to the birth of the latter at lower field strengths and the exponential suppression eq. (1.3). Also note that trajectories revisiting the parent ion more than once exist. These higher order returns during later laser cycles become, however, increasingly unlikely [19].

In the present thesis, the probability for an electron that has already been released into the continuum to return to the core is denoted by R. It is one of the central goals of the thesis to answer the question if, for molecules, R depends on the direction (θ, ϕ) of the driving-laser polarization vector in the molecular frame, i.e. if $R = R(\theta, \phi)$ (see chapter 10).

Recollision with elliptical polarization

One important point to consider is that, when the ellipticity of the driving field is greater than zero, electrons born with zero lateral velocity never return to the core, because the lateral component of the electric field induces a lateral displacement of the electron during continuum propagation. Then, it is not possible for the electron to interact with the ion core, leading to a suppression of the interaction step. Only electrons with an initial lateral velocity $\widetilde{p}_{x,0}$ given by eq. (1.22) return to and may interact with their parent ion following propagation in an elliptically polarized field.

For atomic targets, the initial lateral velocity distribution is given by eq. (1.4). Using the expression eq. (1.22) for the lateral momentum required for recollision in this equation, the probability of interaction $M^{\mathrm{R}}(\varepsilon)$ in dependence of the ellipticity can be modelled [58]:

$$M^{\mathrm{R}}(\varepsilon) \propto \exp\left(-\frac{\widetilde{p}_{x,0}(\varepsilon)^2 \cdot \sqrt{2\mathrm{IP}}}{|\vec{\mathcal{E}}(t_0)| \cdot \hbar e m_{\mathrm{e}}^{1/2}}\right). \tag{1.26}$$

Note that the only target dependence within this model lies in the IP. The strong suppression of the interaction probability with ellipticity evidenced by eq. (1.26) is frequently used to identify recollision-induced processes [64–69]. For small enough ellipticities and electrons born close to the field maximum (in particular for electrons following a long trajectory), the expression for $\widetilde{p}_{x,0}$ in eq. (1.22) can be approximated by [58]

$$\widetilde{p}_{x,0} = -\frac{e\mathcal{E}_0}{\omega} \cdot f(E_{\mathrm{ret}}) \cdot \varepsilon, \tag{1.27}$$

where the return-energy dependence is exclusively contained within the function[8]

$$f(E_{\mathrm{ret}}) = \frac{\sin\omega t_{\mathrm{ret}} - \sin\omega t_0}{\omega(t_{\mathrm{ret}} - t_0)} - \cos\omega t_0. \tag{1.28}$$

f is a universal function of E_{ret} in units of U_{p}. Equation (1.27) establishes a linear relationship between the initial momentum $\widetilde{p}_{x,0}$ and the ellipticity ε. Using the same approximations, the width[9] $\Delta\varepsilon$ of the curves describing the probability of interaction $M^{\mathrm{R}}(\varepsilon)$ in dependence of the ellipticity according to eq. (1.26) is

$$\Delta\varepsilon = \sqrt{2\log 2} \cdot \sqrt{\frac{\mathcal{E}_0 \hbar m_{\mathrm{e}}^{1/2}}{2e\sqrt{2\mathrm{IP}}}} \cdot \frac{\omega}{\mathcal{E}_0} \cdot \frac{1}{|f(E_{\mathrm{ret}})|}. \tag{1.29}$$

[8] Note again that, for a given (long or short) trajectory, each return energy E_{ret} is uniquely associated with a time of birth t_0 and a time of return t_{ret}.

[9] The $\Delta\varepsilon$ given by eq. (1.29) is the ellipticity value where the yield $M^{\mathrm{R}}(\varepsilon)$ drops to 50 % of the yield at zero ellipticity $M^{\mathrm{R}}(0)$.

1.3 INTERACTION

The final step of the three-step model is the interaction of the returning electron with its parent ion. Two different kinds of interaction are possible:

1) The electron may be recaptured by the ion, returning from the continuum to a bound state. This recombination can be regarded as the inverse process of single-photon ionization [20], and thus a photon is created with an energy of

$$E_{\mathrm{HHG}} = E_{\mathrm{ret}} + \mathrm{IP}. \tag{1.30}$$

E_{HHG} is typically in the XUV energy regime and thus much larger than the driving-wavelength photon energy. The emitted radiation is called *high-harmonic radiation* and the process *high-harmonic generation (HHG)*. It will be treated in more detail in chapter 3.

2) The electron may instead scatter from the potential created by the parent ion, a process which is called *rescattering*. The scattering event may either be inelastic (i.e. energy is transferred) or elastic (only momentum is exchanged). Inelastic scattering occurs when the scattering electron excites or ionizes another bound electron. Rescattering ionization of a second electron is called *non-sequential double ionization*, non-sequential because the two ionization events happen within a single laser cycle of the driving field and the released electrons are correlated [68]. Compared to sequential double ionization, where the two electrons are ionized independently at different instants during the laser pulse, at moderate laser intensities the yield from the non-sequential process is much higher [70].

In the case of elastic rescattering, the state of the parent ion remains unchanged during the scattering interaction, and only the direction of the outgoing electron is affected. Importantly, however, from the momentum distribution of the elastically rescattered electrons, information on the target structure can be extracted, because the returning wave packet diffracts from the target, leading to interference due to scattering from different atomic centres of the target. This process is called *laser-induced electron diffraction (LIED)*. LIED promises the time-resolved imaging of chemical reactions [18]. Imaging of the equilibrium structure of diatomic [19] and polyatomic [71–74] molecules, as well as snapshots of a dissociation reaction [18], a linear-to-bent transition [75], and the deformation of C_{60}-molecules [76] have already been achieved. Elastic rescattering will be the topic of the next chapter.

Factorization of the three-step model

The probability for an electron that has returned to the core to undergo a specific interaction is generally denoted by Q in this thesis. In HHG, Q corresponds to the recombination dipole matrix elements and in non-sequential double ionization and LIED to the cross section for inelastic and elastic scattering, respectively. For molecules, Q depends on the direction (θ, ϕ) of

the driving-laser polarization vector (governing the return direction of the interacting continuum electron) in the molecular frame, $Q = Q(\theta, \phi)$.

Together with the ionization probability S and the return probability R, the interaction probability Q determines the overall probability for a specific outcome according to

$$P = S \times R \times Q. \tag{1.31}$$

Such a factorization into three elements, each of which is associated with one step of the three-step model, can be derived more rigorously from a saddle-point treatment of the strong-field–approximation expressions [20, 77]. The strong-field approximation correctly predicts the exponential dependence of S [27] (see eq. (1.3)), but the interaction cross section Q is only obtained in the first Born approximation (which assumes the scattering states to be plane waves [59]), which is not accurate enough for a quantitative comparison with experimental data [78]. An ad-hoc improvement can be achieved by replacing the strong-field–approximation expression for Q with accurate calculations of the field-free cross section using the correct scattering states [79, 80] (also see page 28). This approach has been criticized, because it was argued that laser-driven recollision is rather different from a stationary scattering problem [81]. Nonetheless, it has been shown to yield quantitative agreement with experiment and time-dependent Schrödinger equation (TDSE) calculations [59, 82, 83]. Within the strong-field approximation, the factor R is governed by the propagation of the electron in the laser field neglecting the influence of the ion core. It includes a wave-packet spreading term proportional to $\Delta t_{\mathrm{exc}}^{-3/2}$ [20]. A saddle-point treatment of the strong-field approximation, however, enforces a target independence of R [79, 84]. There have been efforts to derive the factorization eq. (1.31) analytically without relying on the strong-field approximation [85].

CHAPTER 2

Laser-Induced Rescattering

2.1 Scattering in the presence of the laser field

Final momentum after rescattering

As explained in the previous chapter, in the case of elastic scattering an electron returning with momentum $\vec{p}_{\text{ret}}$ to the core will have momentum $\vec{p}'_{\text{ret}}$ with $|\vec{p}_{\text{ret}}| = |\vec{p}'_{\text{ret}}|$ immediately after rescattering. While before and after this interaction the canonical momentum eq. (1.15) is conserved, it may change during the scattering event (since momentum can be transferred to the parent ion), and, therefore, rescattering off the parent ion is a way for the electron to gain additional energy from the field.

The final energy depends on the instant of birth t_0 and the angle into which the electron is scattered. The electrons return to the core with momentum $\vec{p}_{\text{ret}}(t_0)$ (eq. (1.24)) in the z-x-plane (for linear polarization: along the z-axis). At the same time, the electric field with the associated vector potential $\vec{A}_{\text{ret}} = \vec{A}(t_{\text{ret}})$ given by eq. (1.11) is present. After rescattering, the electron's momentum may point in an arbitrary direction:

$$\vec{p}'_{\text{ret}} = |\vec{p}_{\text{ret}}| \times \begin{pmatrix} \sin(\vartheta)\cos(\varphi) \\ \sin(\vartheta)\sin(\varphi) \\ \cos(\vartheta) \end{pmatrix}, \tag{2.1}$$

where $\vartheta \in [0, \pi]$ and $\varphi \in [0, 2\pi]$. ϑ is the scattering angle, i.e. the angle between $\vec{p}_{\text{ret}}$ and $\vec{p}'_{\text{ret}}$. The probability for the electron to be scattered into a given direction is determined by the elastic scattering cross section (see section 2.2).

From the conservation of canonical momentum after the scattering event, the final momentum detected for the rescattered electrons can be deduced:

$$\vec{p}_{\mathrm{f}} = \vec{p}'_{\mathrm{ret}} - e\vec{A}_{\mathrm{ret}} = |\vec{p}_{\mathrm{ret}}| \times \begin{pmatrix} \sin(\vartheta)\cos(\varphi) \\ \sin(\vartheta)\sin(\varphi) \\ \cos(\vartheta) \end{pmatrix} - e\vec{A}_{\mathrm{ret}}. \tag{2.2}$$

Equation (2.2) describes a spherical shell with radius $|\vec{p}_{\mathrm{ret}}|$ and offset $e\vec{A}_{\mathrm{ret}}$ from the origin, on which all elastically rescattered electrons with a given return momentum $\vec{p}_{\mathrm{ret}}$ lie. This is depicted in fig. 2.1a) for the case of linear polarization and long trajectories. Importantly, for the long trajectories the shells for different $\vec{p}_{\mathrm{ret}}$ do not overlap, such that (neglecting contributions from the short trajectories, which, according to eq. (1.3), are expected to be much smaller) each return energy can be uniquely associated with a specific region in the distribution of rescattered electrons.

The maximum energy for each t_0 is reached when the momentum after rescattering $\vec{p}'_{\mathrm{ret}}$ is parallel to $\vec{A}_{\mathrm{ret}}$ in eq. (2.2), thus

$$E_{\mathrm{f}}^{\mathrm{max}}(t_0) = \frac{1}{2m_{\mathrm{e}}} \cdot \left(|\vec{p}'_{\mathrm{ret}}(t_0)| + |e\vec{A}_{\mathrm{ret}}(t_0)|\right)^2 = \frac{1}{2m_{\mathrm{e}}} \cdot \left(|\vec{p}_{\mathrm{ret}}(t_0)| + |e\vec{A}_{\mathrm{ret}}(t_0)|\right)^2,$$

where $\vec{p}_{\mathrm{ret}}$ and $\vec{A}_{\mathrm{ret}}$ are given by eqs. (1.11), (1.23) and (1.24). For a linearly polarized driving field, this is the case in a back-scattering geometry, i.e. for $\vartheta = 180°$. The maximum final energy is plotted in dependence of the time of birth t_0 in fig. 2.2. Energies of up to

$$E_{\mathrm{f}}^{\mathrm{max}} \approx 10 \cdot \frac{U_{\mathrm{p}}}{1+\varepsilon^2} \tag{2.3}$$

can be obtained. Note that the time of birth where the maximum final energy is reached differs slightly from the time where the maximum return energy is reached, i.e. not the electrons returning with the maximum energy achieve the highest final energy upon rescattering.

General structure of electron momentum distributions including rescattering

Figure 2.1a) also schematically depicts a projection of a typical SFI electron momentum distribution for linear polarization: The direct electrons form a shape elongated along the polarization direction and centred around zero momentum. The two lobes are formed by the superposition of all spherical shells of rescattered electrons from the various return trajectories during a full cycle of the laser field.[1] The distribution has a cylindrical symmetry around the

[1] Note that the above considerations only included the rescattering dynamics occurring during a half cycle of the field, creating only one of the lobes seen in fig. 2.1a). The other lobe is created in the subsequent half cycle, where the same dynamics occur with the field vector pointing in the opposite direction.

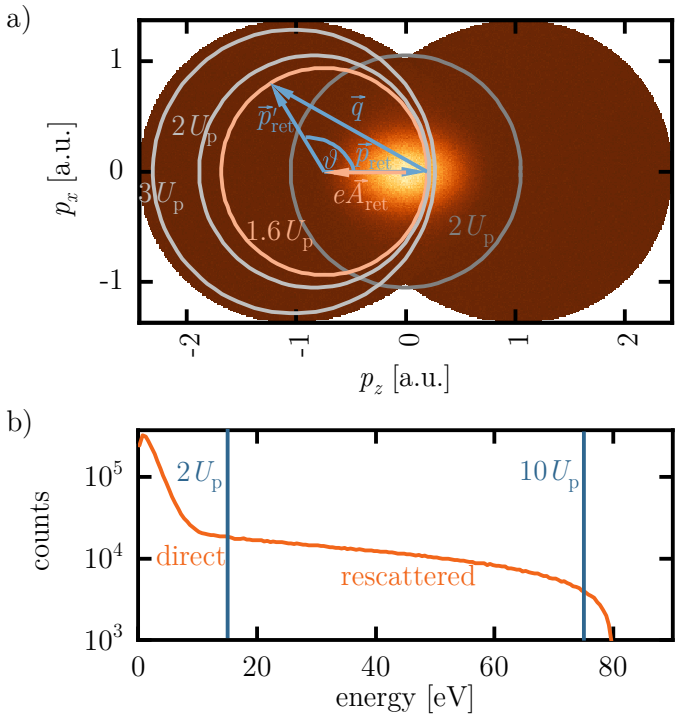

Figure 2.1: a) Schematic depiction of the projection of the electron momentum distribution onto the p_x-p_z-plane for a linear driving-laser polarization. The dark grey circle around the centre delimits the maximum momentum the direct electrons can reach. The orange and light grey circles show the final momenta of rescattered electrons following the long trajectory for different return momenta, corresponding to return energies of $1.6U_\mathrm{p}$, $2U_\mathrm{p}$, and $3U_\mathrm{p}$. For a return energy of $1.6U_\mathrm{p}$ (orange circle), the vector geometry of the relevant vector potential $\vec{A}_\mathrm{ret}$, the return momentum $\vec{p}_\mathrm{ret}$, and the momentum after rescattering $\vec{p}'_\mathrm{ret}$ is also exemplified. ϑ denotes the scattering angle and $\vec{q} = \vec{p}'_\mathrm{ret} - \vec{p}_\mathrm{ret}$ the momentum transfer in the rescattering event. b) Corresponding schematic kinetic-energy distribution. Also shown are the cut-offs for the direct and rescattered electrons.

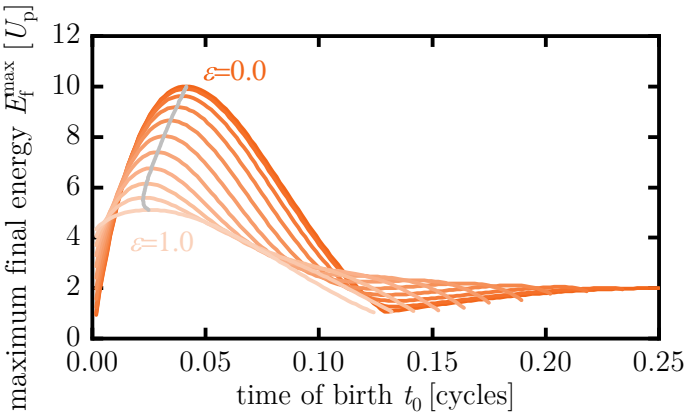

Figure 2.2: Maximum (with respect to the scattering angles ϑ, φ) final energy E_f^{max} in units of the ponderomotive potential U_p as a function of the time of birth t_0 in fractions of a cycle, for ellipticities ranging from 0.0 to 1.0. The grey curve highlights the overall maximum energy for each ellipticity.

polarization axis. Note that the direct electrons, which are centred around zero momentum and reach momenta of up to $\sqrt{2m_e \cdot 2U_p}$ (see eq. (1.17)), partly overlap with the rescattered electrons, preventing a discrimination in the small-momentum region. However, the higher momentum cut-off for the rescattered electrons ensures that there is a significant portion of the distribution which is exclusively populated by the rescattered electrons.

A schematic kinetic-energy distribution is shown in fig. 2.1b). It consists of two clearly discernible regions: The direct electrons, up to $2U_p$, whose yield drops off exponentially with increasing energy, and the rescattered electrons, which form a region of almost constant yield, called the *rescattering plateau* or *rescattering tail*. Beyond $10U_p$, the electron yield drops to zero. Note that interference effects such as ATI are not considered in the schematic depictions in fig. 2.1.

2.2 LASER-INDUCED ELECTRON DIFFRACTION

The differential cross section for elastic scattering

Consider a monochromatic plane wave of electrons with asymptotic momentum $\vec{p}$ impinging on a scattering target with a short-range potential.[2] The outgoing

[2] A Coulomb contribution to the potential adds a slight complication to the problem, which can, however, be resolved [59].

scattered wave $\psi'(\vec{r})$ is asymptotically a spherical wave:

$$\psi'(\vec{r}) \propto f(\vartheta,\varphi,E)\cdot\frac{\exp\left(\frac{i}{\hbar}\sqrt{2m_\mathrm{e}E}\cdot r\right)}{r},$$

where $E=|\vec{p}|^2/2m_\mathrm{e}$, $r=|\vec{r}|$, and $f(\vartheta,\varphi,E)$ is the *scattering amplitude*. The latter is a complex quantity which is related to the *differential elastic scattering cross section (DCS)* $\frac{\partial\sigma}{\partial\Omega}$ according to

$$\frac{\partial\sigma}{\partial\Omega}(\vartheta,\varphi,E)=|f(\vartheta,\varphi,E)|^2,$$

where Ω is the solid angle [86]. The DCS determines the probability for an incoming electron with energy E to be scattered into a certain solid angle Ω, and it can be measured experimentally [87]. It also encodes the information on the target structure. Integration over the solid angle yields the total cross section

$$\sigma(E)=\int\frac{\partial\sigma}{\partial\Omega}\mathrm{d}\Omega=\int_0^{2\pi}\int_0^{\pi}|f(\vartheta,\varphi,E)|^2\sin\vartheta\mathrm{d}\vartheta\mathrm{d}\varphi, \tag{2.4}$$

which determines the overall probability for an elastic scattering interaction for an incoming electron with energy E.

The independent-atom model

To determine molecular structure from electron-scattering experiments accurately – in particular from LIED experiments – one usually compares the measured cross sections (in dependence of ϑ or E or both) with theoretically calculated cross sections for various target geometries, i.e. for various bond-length and -angle configurations. This is efficiently done using the so-called *independent-atom model*, which regards the molecule as being made up of independent, non-interacting atomic scatterers and which is a good approximation for high enough electron energies [82].

The atomic scattering amplitudes can be obtained relatively easily from time-independent potential scattering theory (see ref. [59]) and need to be calculated only once for each atomic species in the molecule. They can then be used to calculate the molecular DCS. For a given molecular structure, each of the N atomic centres of the molecule with scattering amplitude $f_i(\vartheta)$[3] is placed at a certain position $\vec{R}_i$. The molecular DCS is then given by [71]

$$\begin{aligned}\frac{\partial\sigma}{\partial\Omega}(\vartheta,\varphi,E;\vec{R}_1,...,\vec{R}_N)&=\sum_{i,j}f_if_j^*\exp\left(\frac{i}{\hbar}\vec{q}\cdot(\vec{R}_i-\vec{R}_j)\right)\\&=\sum_i|f_i|^2+\sum_{i\neq j}f_if_j^*\exp\left(\frac{i}{\hbar}\vec{q}\cdot(\vec{R}_i-\vec{R}_j)\right),\end{aligned} \tag{2.5}$$

[3] Due to the spherical symmetric scattering potential of atoms, the scattering amplitude only depends on ϑ but not on φ.

where $\vec{q} = \vec{p}'_{\mathrm{ret}} - \vec{p}_{\mathrm{ret}}$ ($\vec{p}_{\mathrm{ret}}$ is given by eq. (1.24) and $\vec{p}'_{\mathrm{ret}}$ by eq. (2.1)) is the momentum transfer, i.e. the difference between the electron's momentum after and before scattering. The molecular DCS in eq. (2.5) consists of the incoherent sum of the atomic DCSs, which is the same for all molecular configurations, and an interference term, which depends on the positions of the atomic centres $\vec{R}_i$. Note that via the product $\vec{q}\cdot(\vec{R}_i - \vec{R}_j)$ the molecular DCS depends on the relative orientation between the molecule and the incoming electron.

Modelling of rescattered-electron distributions using the field-free differential scattering cross section

According to the three-step model, the situation in strong-field–driven rescattering is qualitatively similar to conventional diffraction using prepared beams of electrons. The returning strong-field–driven electron wave packet can be regarded as a polychromatic beam of electrons diffracting from the target, i.e. the parent ion. This view is now commonly known under the name of *quantitative rescattering theory (QRS)* [59, 78, 80], and it has been shown in numerous studies that this description is accurate enough for a quantitative comparison with experimental data and TDSE calculations [59, 82, 88, 89]. Using the QRS, the field-free DCS can be extracted from a measurement done in the presence of the laser field [90, 91]. Thus, information on the structure of the molecular ion at the instant of recollision can be obtained from the distribution of rescattered electrons.

According to the QRS, the yield $D^{\mathrm{resc}}(\vec{p}_{\mathrm{f}})$ of rescattered electrons (following a long trajectory) with final momentum $\vec{p}_{\mathrm{f}}$ on the detector is given by

$$D^{\mathrm{resc}}(\vec{p}_{\mathrm{f}}) = W(|\vec{p}_{\mathrm{ret}}|)\cdot \frac{\partial\sigma}{\partial\Omega}(|\vec{p}_{\mathrm{ret}}|,\vartheta,\varphi), \tag{2.6}$$

where $\vec{p}_{\mathrm{f}}$ can be calculated from $\vec{p}_{\mathrm{ret}}$, ϑ, and φ using eq. (2.2). Equation (2.6) factorizes the distribution of rescattered electrons into an incoming electron density W and the DCS $\frac{\partial\sigma}{\partial\Omega}$ (which is independent of the laser field). Note that the core assumption of the QRS model is that W depends only on $|p_{\mathrm{ret}}|$ and not on the angles ϑ and φ (otherwise the factorization eq. (2.6) would be trivial). In addition, eq. (2.6) assumes a returning electron asymptotically exhibiting a planar wavefront, since otherwise additional return directions different from $\vec{p}_{\mathrm{ret}}/|\vec{p}_{\mathrm{ret}}|$ would need to be taken into account (also see page 132).

Laser-induced electron diffraction in molecules

For molecules, the DCS and the returning wave packet are additionally dependent on the relative orientation of the laser polarization direction and the molecule, parametrized by the angles θ and ϕ (see section 5.1), i.e. eq. (2.6) becomes

$$D^{\mathrm{resc}}(\vec{p}_{\mathrm{f}}) = W(|\vec{p}_{\mathrm{ret}}|,\theta,\phi)\cdot \frac{\partial\sigma}{\partial\Omega}(|\vec{p}_{\mathrm{ret}}|,\vartheta,\varphi,\theta,\phi). \tag{2.7}$$

A further assumption made in LIED experiments is that the dependence of the returning wave-packet amplitude on the molecular orientation is exclusively given by the orientation-dependent ionization probability $S(\theta,\phi)$ in the molecular frame, whereas the remaining part W', which is given by the return probability R (see eq. (1.31)), does not depend on (θ,ϕ) [18, 19, 71] :

$$W(|\vec{p}_{\mathrm{ret}}|,\theta,\phi) = S(\theta,\phi)\cdot W'(|\vec{p}_{\mathrm{ret}}|). \tag{2.8}$$

In anticipation of relations presented in section 5.1, averaging over the whole molecular ensemble using an alignment distribution denoted by $A(\theta',\chi',\phi')$ then results in the total rescattered-electron yield (according to eq. (5.1))

$$\begin{aligned}\frac{D^{\mathrm{resc}}_{\mathrm{avg}}(\vec{p}_{\mathrm{f}})}{W'(|\vec{p}_{\mathrm{ret}}|)} \propto \frac{1}{8\pi^2}\cdot\int_0^{2\pi}\int_0^{\pi}\int_0^{2\pi} & S(\theta(\theta',\chi',\phi'),\phi(\theta',\chi',\phi')) \\ \cdot\frac{\partial\sigma}{\partial\Omega}(|\vec{p}_{\mathrm{ret}}|,\vartheta,\varphi,\theta(\theta',\chi',\phi'),\phi(\theta',\chi',\phi'))\cdot A(\theta',\chi',\phi')&\mathrm{d}\chi'\sin\theta'\mathrm{d}\theta'\mathrm{d}\phi'.\end{aligned} \tag{2.9}$$

For a given return momentum, $D^{\mathrm{resc}}_{\mathrm{avg}}$ is the electron momentum distribution as detected in an experiment, disregarding the direct electrons and electrons moving along the short trajectories, which partially overlap with $D^{\mathrm{resc}}_{\mathrm{avg}}$. Importantly, the factorizations eqs. (2.7) and (2.8) allow moving the returning wave-packet amplitude $W'(|\vec{p}_{\mathrm{ret}}|)$ before the integral.

Thus, using the transformation eq. (2.2), the *orientationally averaged DCS* can be measured experimentally in dependence of the scattering angle ϑ up to a constant normalization factor $W'(|\vec{p}_{\mathrm{ret}}|)$ for each return energy. Specifically, this is achieved by choosing a return energy $|\vec{p}_{\mathrm{ret}}|$, calculating the corresponding $\vec{A}_{\mathrm{ret}}$, and extracting the electron yield within a small volume around the spherical shell given by eq. (2.2) for different angles ϑ. Modulations in the DCS $\frac{\partial\sigma}{\partial\Omega}$ remain observable after averaging even in a completely random ensemble of molecules [82]. At the same time – assuming both the alignment distribution A and the orientation-dependent ionization probability S are known – the quantity eq. (2.9) can also be calculated theoretically, e.g. using the independent-atom model. By comparing the distributions calculated for various geometries $\vec{R}_i$ to the experimental one, the molecular structure of the ion can be deduced [71].

The importance of long driving wavelengths

According to eq. (2.5), the frequency of the modulations in the DCS in LIED depends on the momentum transfer $\vec{q}$ from the target to the electron. Thus, in order to resolve molecular structure by measuring the distribution of scattered electrons, it is crucial to have sufficiently high momentum transfers. Clearly, high values of $|\vec{q}|$ are attainable for large scattering angles ϑ and magnitudes of the return momentum $|\vec{p}_{\mathrm{ret}}|$. As shown in section 1.2, the maximum return energy is proportional to the ponderomotive potential U_{p} (see eq. (1.25)).

According to eq. (1.18), U_p scales linearly with the intensity and quadratically with the wavelength of the driving laser. The driving-laser intensity cannot be increased indefinitely, since too high intensities could already completely ionize the target before the maximum of the electric field, thus supressing the recolliding trajectories. Therefore, most LIED experiments have been performed at longer driving wavelengths ranging from 1600 nm to 3600 nm, i.e. in the mid-IR regime.

An additional benefit of longer driving-laser wavelengths is that the rescattered electrons exclusively occupy a larger region in momentum space: While the cut-offs for both the direct and the rescattered electrons scale proportionally to U_p, this is only relevant for the direction parallel to the polarization vector, whereas the lateral width of the direct-electron momentum distribution is approximately independent of the driving wavelength. Therefore, for longer wavelengths the rescattered electrons can be distinguished from the direct electrons in a larger portion of the momentum distribution, and the DCS can be measured for a larger range of scattering angles [83]. Furthermore, more energetic collisions also better justify the use of the independent-atom model in the modelling of LIED experiments.

The disadvantage of using long-wavelength driving pulses is that the yield of rescattered electrons drops dramatically with wavelength (namely $\propto \lambda^{-4}$), due to a decreasing scattering cross section and the longer excursion time with resulting increased wave-packet diffusion [92]. This means that for longer driving wavelengths, generally longer data acquisition times are required to obtain enough statistics to be able to identify the diffraction pattern in the rescattered electrons.

CHAPTER 3

High-Harmonic Generation

3.1 Single-Emitter Response

As explained in section 1.3, not only electrons are released from atomic or molecular systems as a response to a strong laser field, but also high-harmonic electromagnetic radiation is emitted when an electron released via SFI is driven back to its core and recombines with it. An alternative description of the process is that the returning continuum portion of the electron interferes with the remaining bound portion and thus creates a rapidly oscillating dipole, which leads to the emission of electromagnetic radiation [20, 25, 93]. This also implies that there will be no high-harmonic emission if the target has been fully singly ionized, i.e. if there is no remaining bound portion.

According to eq. (1.30), the energy of the emitted radiation is given by the sum of the return energy of the electron E_{ret} and the IP. From the maximum return energy eq. (1.25), the high-energy cut-off for high-harmonic radiation can be derived:

$$E_{\mathrm{HHG}}^{\mathrm{max}} = 3.17 U_{\mathrm{p}} + \mathrm{IP}. \tag{3.1}$$

Using a driving laser with a wavelength of 800 nm and rare gas targets with IPs ranging from 10 eV to 25 eV, the emitted electromagnetic radiation has energies in the 10 eV to 200 eV range, i.e. in the extreme ultraviolet (XUV) regime. Again, since U_{p} scales with λ^2, the cut-off can be extended to higher energies by using a longer driving-laser wavelength λ. By using mid-IR driving lasers, high harmonics with energies exceeding 1500 eV have been generated [94].

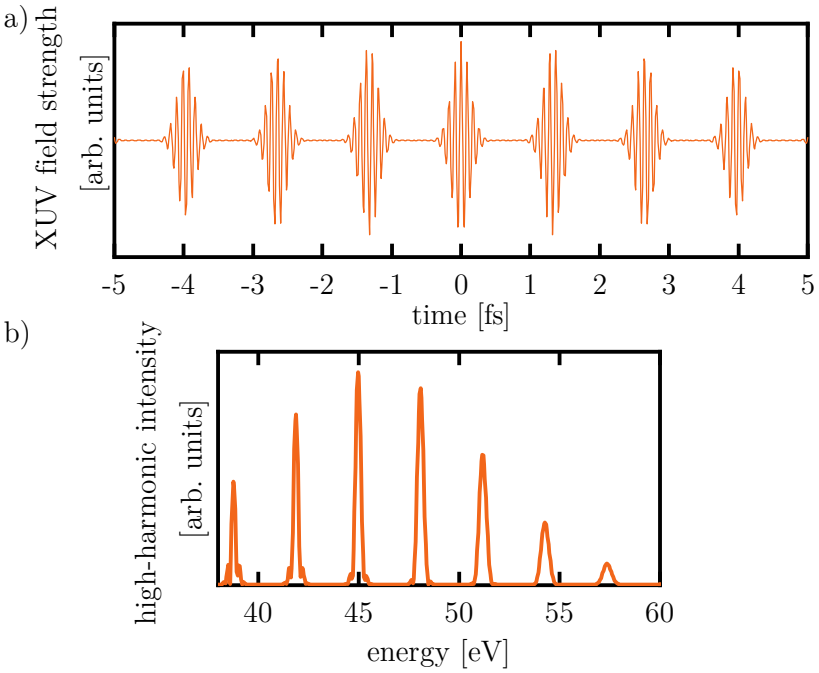

Figure 3.1: a) Schematic temporal structure of an attosecond pulse train generated by a multi-cycle femtosecond driving pulse with a central wavelength of 800 nm. Only contributions from the short trajectory are included. b) High-harmonic spectrum corresponding to the pulse train in a).

Temporal and spectral structure of high-harmonic radiation

The emission of electromagnetic radiation occurring every half cycle of the driving laser pulse is confined to bursts with a duration of a fraction of the driving-laser period. Two bursts with different properties are emitted per half cycle, created by electrons following the long/short trajectory, respectively. Via phase matching (see section 3.2), it can be achieved that only one group of bursts (usually the ones from the short trajectory) contributes macroscopically. The duration of the bursts is determined by the available bandwidth of the spectrum, ranging from IP to IP$+3.17U_p$. Since the trajectories corresponding to different return energies spend a different time in the continuum, the emitted bursts of electromagnetic radiation will be chirped (as the continuum electron wave packet itself). Therefore, if this chirp is not corrected, the bursts will not be transform-limited.[1]

In a multi-cycle driving pulse, the three-step process is repeated in each

[1] A transform-limited (also called bandwidth-limited) pulse has the minimum possible duration at a given spectral bandwidth [95].

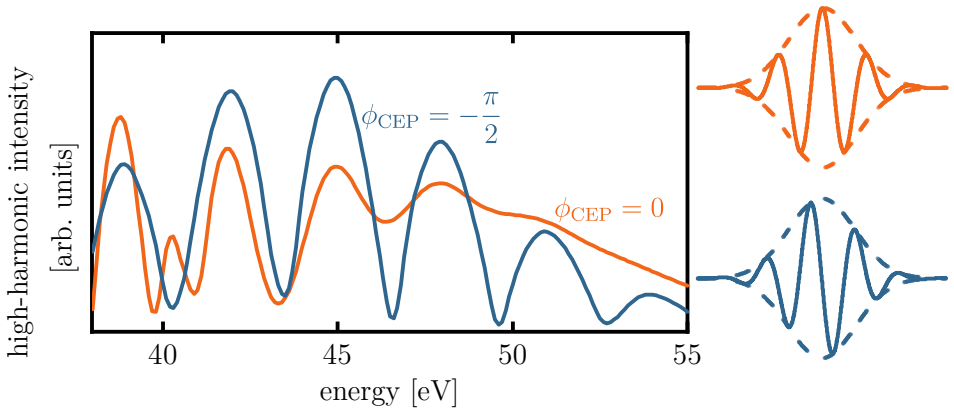

Figure 3.2: Schematic plot of the high-harmonic intensity as a function of energy for $\phi_{\mathrm{CEP}} = 0$ (orange) and $\phi_{\mathrm{CEP}} = -\frac{\pi}{2}$ (blue). The two corresponding driving pulses are shown on the right hand-side.

half cycle, i.e. – under suitable phase-matching conditions – a train of sub-femtosecond pulses (called an *attosecond pulse train*) as shown in fig. 3.1a) is generated. In the spectral domain, similar to ATI, the interference among the bursts generated in the various half cycles leads to discrete peaks occurring at odd multiples of the driving-laser frequency, which explains the name *high-harmonic* radiation. A schematic high-harmonic spectrum is shown in fig. 3.1b). The width of the peaks is determined by the driving-pulse duration: The more cycles interfere, the narrower the peaks are. For shorter and shorter driving pulses, the high-harmonic peaks become broader and broader and eventually start to merge into a continuum, beginning at the highest energies. This is because, for short driving pulses, U_{p} is different for different cycles of the driving pulse, reaching its highest value only for a short time. Thus, the highest energies are obtained for a single half cycle, and there are no multi-cycle interferences in the spectrum for these energies.

Generation of isolated attosecond pulses

For the same reason, for few-cycle driving laser pulses the HHG spectrum also starts to depend on the CEP, which determines how many half cycles interfere at the highest magnitude of the envelope. This is illustrated in fig. 3.2. While at lower energies the spectrum displays discrete peaks for all values of the CEP, at the highest energies, close to the cut-off, the spectrum changes from discrete to continuous for certain CEP values. This is the case when there is only a single oscillation peak at the maximum of the envelope (orange pulse in fig. 3.2) instead of two oscillation peaks of similar magnitude (blue pulse). Thus, controlling the CEP and selecting only the continuum high-energy portion of the spectrum using a suitable filter (thin metal filters and/or multilayer

mirrors [11]) is one way to isolate a single attosecond pulse from the generated train of attosecond bursts, for very short driving pulses. This technique is called *amplitude gating* [11, 96].

There are several more of such gating techniques facilitating the generation of *isolated attosecond pulses* [97]. Well-suited for slightly longer few-cycle pulses is the *polarization-gating* technique [12, 98]. It relies on the fact that (at least for atomic targets) the HHG yield is suppressed for a sufficiently elliptically polarized driving field (see section 1.2). A combination of a quartz plate and a quarter-wave plate is used to create two counter-rotating, circularly polarized pulses delayed by a time Δt determined by the thickness of the quartz plate. The superposition of these two pulses results in a pulse whose polarization is linear only during a time window approximately given by $0.3\tau^2/\Delta t$, where τ is the pulse duration [99]. In order to suppress HHG in all but one half cycle, this gate width must be smaller than the optical cycle, i.e. the pulse needs to be short and/or the delay large. However, using too large delays leads to a shift of the linear portion of the pulse to low field strengths compared to the peak field strength, resulting in a low high-harmonic yield. Thus, the driving pulse still needs to be short (~ 3 cycles) in order to use polarization gating [25]. Further gating schemes include *double optical gating* [100, 101], *ionization gating* [102, 103], and the *attosecond lighthouse effect* [104, 105].

The advantage of using attosecond pulse trains is that their discrete spectrum allows somewhat more control over which states are excited in the target system [106]. On the other hand, in attosecond pulse trains, the process under study is launched several times, leading to interferences, which complicate the interpretation of the experimental observations [5]. Thus, while technically more difficult to implement, isolated attosecond pulses are preferable in some cases.

High-harmonic spectroscopy

As mentioned in the introduction, the XUV radiation from HHG can not only be used to excite or ionize another target, as in time-resolved electron or ion pump-probe spectroscopy or transient absorption spectroscopy, but also the emitted radiation itself can be characterized to gain information on the high-harmonic emitter, a technique named *high-harmonic spectroscopy*. According to eq. (1.31), in addition to the interference effects in a multi-cycle pulse leading to the characteristic peaks in the spectrum, the high-harmonic spectrum will also depend on the interaction cross section Q. In HHG, Q corresponds to the recombination dipole matrix element, which contains information on the state of the ion [20]. In high-harmonic spectroscopy, this information is extracted from the recorded high-harmonic spectra.

Early applications include the measurement of nuclear dynamics in molecules [107–111]. However, the sub-cycle temporal resolution [112] of high-harmonic spectroscopy also allows the measurement of electron dynamics following SFI

on an attosecond timescale [17, 57, 113–115]. Furthermore, high-harmonic spectroscopy has been used to measure, among others, the femtosecond dissociation dynamics in electronically excited molecules [116–118], the modification of electronic structure due to the strong laser field [119], and to reconstruct tomographic images of bound-state wave functions (a technique called *high-harmonic tomography*) [113, 120–122]. Multidimensional approaches using two-colour driving fields have also been implemented [123, 124].

3.2 PHASE MATCHING

Microscopic vs. macroscopic response

So far, only the response of a single target atom or molecule to the driving strong field was considered. However, only when the radiation from many emitters in the focus coherently adds up, an appreciable high-harmonic intensity can be achieved. It is, therefore, necessary that emitters in a significant interaction volume have a proper phase relationship with respect to each other. The adjustment of the parameters of the focus and the medium to achieve this is called *phase matching*.

HHG is driven in a medium with density $\rho(\vec{x})$ by a laser field with local intensity $I(\vec{x})$, such that at each point in space $\vec{x}$ the emitted high-harmonic radiation is equal to $\rho(\vec{x})$ times the response from a single emitter (eq. (1.31)) driven by a field with intensity $I(\vec{x})$. For each $\vec{x}$, the harmonic emission constitutes a source of non-linear polarization in Maxwell's equations, which can then be solved to obtain the macroscopic electric field of the high-harmonic radiation [25]. This macroscopic response can be quite different from the microscopic response of a single emitter.

In particular, as mentioned before, phase matching can be used to filter out a single group of trajectories (long or short). While the microscopic intensity of the emitted radiation is higher for the long trajectory (see eq. (1.3) and fig. 1.1), after phase matching HHG can still be dominated by the short trajectory. Since the divergence of the generated beam is lower for short-trajectory than for long-trajectory harmonics [125, 126], they are better spatially confined, which is why the short-trajectory harmonics are often preferred in the applications of high-harmonic radiation. Phase matching of the short trajectory is optimized, suppressing the long trajectory, when the target is placed slightly behind the focus [127].

Conditions for efficient HHG

The phase of the emitted high-harmonic radiation with respect to the driving laser is influenced by several factors (for details, see e.g. [128, 129]). In particular, the dispersion of the fundamental and high-harmonic beams while propagating through the target medium plays an important role, because

it can be easily adjusted via the density of the target, i.e. by changing the pressure of the target gas. There are two contributions – with opposite sign – to dispersion depending on the pressure: dispersion due to the neutral gas and dispersion due to plasma generated via SFI in the target. The former is also able to cancel out the geometric contribution[2] to the phase mismatch between the fundamental and the high-harmonic radiation, but only if the fraction of ionized target emitters is low (below the so-called *critical ionization fraction* [130]) and the density of the target is high enough.

On the other hand, a high density of the medium also limits the efficiency of the HHG process, due to re-absorption of the high-harmonic radiation in the medium. The optimum interaction length of the medium L_{med} thus has to be chosen with different length scales in mind: the coherence length L_{coh} over which phase matching leads to constructive interference of the driven emitters and the absorption length $L_{\mathrm{abs}} = \frac{1}{\sigma\rho}$ – given by the target density ρ and the (wavelength-dependent) absorption cross section σ – above which absorption becomes significant. Optimum HHG is achieved for $L_{\mathrm{coh}} > 5L_{\mathrm{abs}}$ and $L_{\mathrm{med}} > 3L_{\mathrm{abs}}$ [131], which is called *absorption-limited* HHG.

The conversion efficiency of a well phase-matched, absorption-limited high-harmonic source for attosecond experiments is on the order of 10^{-6} [132] and, thus, much lower than what is typical for perturbative non-linear processes, e.g. second-harmonic generation in a crystal [25]. This also implies that the intensity of the driving laser field remains essentially unchanged by the HHG process. It has been shown that for low energy-per-pulse driving laser sources the conversion efficiency can be just as high as for high energy-per-pulse sources, if tighter focusing conditions are implemented and the target density is increased [128, 129].

3.3 CHARACTERIZATION OF ATTOSECOND PULSES

Spectrometer

The simplest way to characterize the generated radiation with photon energies in the XUV regime is through the determination of the magnitude of its spectral components. This can be achieved with a spectrometer, which includes an XUV grating. In analogy to an optical prism, the grating separates the various spectral components, because only for specific angles constructive interference is possible. These angles are different for different wavelengths λ, according to

$$\beta_m = \arcsin\left(\sin\beta_{\mathrm{i}} - \frac{m\lambda}{d}\right), \tag{3.2}$$

[2] This contribution arises because of the different focus sizes and wavelengths of the fundamental and high-harmonic beams and the accordingly different phase shifts when going through the focus.

where β_m is the angle of order m for which constructive interference occurs, β_i is the angle of incidence on the grating, and d is the spacing of grooves in the grating [25].

While the spectrum of the high-harmonic radiation does provide information on the temporal structure of the generated attosecond pulses (continuous vs. discrete spectrum, see fig. 3.2), the phase structure of the radiation is unknown and, therefore, the pulses cannot be completely characterized using only a spectrometer.

RABITT

RABITT[3] is a technique that can be used to completely characterize attosecond pulse trains generated by multi-cycle driving pulses. It assumes that the width of the harmonics in the spectrum is zero, i.e. each harmonic corresponds to a monochromatic wave with amplitude A_q, frequency $\omega_q = q \cdot \omega$, and emission phase ϕ_q (where q is the harmonic order), such that the resulting temporal intensity profile of the attosecond pulse train is given by

$$I_\mathrm{XUV}(t) \propto \left| \sum_q A_q \exp\left(i\left(\omega_q t + \phi_q\right)\right) \right|^2 . \tag{3.3}$$

The A_q can be determined from the intensity of the individual harmonics in the spectrum. To determine the ϕ_q, the RABITT technique detects the photoelectron energy distribution resulting from the ionization of a rare-gas target by the high-harmonic radiation in the presence of a moderately intense ($10^{11}\,\mathrm{W/cm^2}$ to $10^{13}\,\mathrm{W/cm^2}$) fundamental laser field, as a function of the (sub-cycle–stable) time delay τ between the two pulses [10].

When the high-harmonic radiation alone is made to interact with some target atom, electrons may be released via single-photon absorption from the spectral components of the pulse with energies greater than the atom's IP.[4] The probability for this to happen is given by the single-photon ionization cross section $\sigma(E)$ (see eq. (1.2)). The kinetic energy of the released electron can be calculated according to

$$W = E_\mathrm{HHG} - \mathrm{IP}. \tag{3.4}$$

If the ionization cross section does not change too much over the spectral range of the pulse, the kinetic-energy spectrum of the electron will be very similar to the spectrum of the pulse (shifted by IP), i.e. it will also feature a series of peaks spaced by 2ω [25]. Again, the photoelectron energy spectrum from one-photon ionization alone does not afford access to the phase structure of the pulse.

[3] reconstruction of attosecond beating by interference of two-photon transitions

[4] Note that typically the intensity of the high-harmonic radiation is too weak for two-photon or higher order processes to occur.

However, in the presence of the fundamental driving field, sidebands appear in the photoelectron spectrum between the peaks corresponding to specific harmonics. These are due to one-photon transitions in the continuum induced by the fundamental field. Each sideband has two contributions: The electron may be ionized by harmonic q ($q+1$) and subsequently gain (lose) an energy $\hbar\omega$ via absorption (stimulated emission). These two contributions interfere and lead to a modulation of the sideband intensity I_q with the delay τ, according to [20]

$$I_q(\tau) \propto \left(1 + \cos\left(2\omega\tau + \phi_{q+1} - \phi_{q-1} - \Delta\phi_{\mathrm{at}}\right)\right). \tag{3.5}$$

$\Delta\phi_{\mathrm{at}}$ is an additional contribution to the phase difference characteristic of the target, which, for noble gas atoms, can be accurately calculated and is typically small [20]. Therefore, by scanning the delay and measuring the phase shifts of the oscillating sideband intensities in the electron momentum distribution, the relative phases of the individual harmonics ϕ_q can be measured, and thus the reconstruction of the attosecond pulse train eq. (3.3) is possible. If the phase structure of the attosecond pulse train is known instead, RABBIT can also be used to extract information on the target atom or molecule, i.e. to determine the term $\Delta\phi_{\mathrm{at}}$ in eq. (3.5) [133–137].

FROG-CRAB

In addition to the RABITT technique, developed for the characterization of long attosecond pulse trains, a method called *attosecond streak camera* [11, 138, 139] allows the reconstruction of close-to-isolated attosecond pulses, by streaking the electrons released by the XUV burst, i.e. mapping their time of birth to the final energy in the electron distribution, again using the fundamental field. Both approaches are put on common ground and generalized by the *FROG-CRAB*[5] technique [140].

FROG-CRAB makes it possible to completely reconstruct the temporal structure of the XUV pulses (with the exception of the CEP [141]), again by recording the energy-resolved photoelectron yield in a specific direction resulting from the ionization of a rare-gas target by the XUV pulse in the presence of the fundamental field, for different delays between the XUV and IR pulses. The technique relies on the fact that the concomitant fundamental field (whose vector potential is denoted by $\vec{A}(t)$) effectively acts as a phase gate $\exp(i\Phi(t))$ on the electron wave packet $\chi(\vec{p},t)$ released by the XUV pulse in the interaction with the target, such that the detected electron-momentum distribution in dependence of the delay τ (called a *spectrogram*) is given by [24]

$$S(\vec{p},\tau) = \left| \int_{-\infty}^{\infty} \chi\left(\vec{p},t\right) \exp\left(i\Phi\left(t-\tau\right)\right) \exp\left(\frac{i}{\hbar}\frac{|\vec{p}|^2}{2m_{\mathrm{e}}}t\right) \mathrm{d}t \right|^2 .$$

[5] frequency-resolved optical gating for complete reconstruction of attosecond bursts

$\Phi(t)$ is the phase the electron acquires in the interaction with the fundamental laser field [25]. Several algorithms exist to simultaneously reconstruct both $\exp(i\Phi(t))$ and $\chi(\vec{p},t)$ from the spectrogram measured for a given direction of $\vec{p}$ [142–145]. From these, the complete evolution of the streaking fundamental field and the complex envelope of the high-harmonic field can be determined, respectively.[6]

[6]For the expressions relating $\Phi(t)$ to $\vec{A}(t)$ and $\chi(\vec{p},t)$ to XUV field's envelope, see ref. [24].

CHAPTER 4

Reaction Microscopes

Kinematically complete coincidence experiments

As described in section 1.1, both the interaction of a target with a strong laser field (SFI) and with a beam of energetic photons (single-photon ionization) may lead to the ejection of charged particles (electrons and ions), whose initial momentum vector upon ionization may point in any direction in space. For single ionization of atomic targets, momentum conservation dictates that the momenta of the created electron and ion have the same magnitude but point in opposite directions.[1] Therefore, one can be deduced from the other. In molecular systems, on the other hand, fragmentation of the ion may occur following ionization, where momentum is shared among charged and/or neutral fragments. Simultaneous detection of the momentum vector of all charged particles created in a single interaction event then provides additional information compared to e.g. velocity-map-imaging detection systems (see section 13.2), where only a projection of the overall electron or ion momentum distribution is recorded. This helps to disentangle the complex dynamics occurring in these systems upon excitation with electromagnetic radiation (also see chapter 11).

The coincident detection of the three-dimensional momenta of all charged particles is facilitated by a *reaction microscope* [21, 146]. Coincidence detection refers to the notion that all detected particles can be correlated to a single interaction event of the electromagnetic radiation with a target atom or molecule. This implies that in a single laser pulse at most one target particle should be ionized in most cases. Otherwise, *false coincidences* may occur, when some of the resulting charged particles are missed due to non-perfect

[1] The electromagnetic radiation contributes only negligibly to the total momentum.

detection efficiencies. In such cases, charged particles may be falsely assumed to be correlated, when they are created in the same laser pulse but actually do not originate from ionization of the same target particle. To keep the rate of false coincidences at an acceptable level, the rate of ionization events per laser pulse must be well below one event per pulse.[2]

In this chapter, the working principle of a reaction microscope and the path from the acquisition of raw data to the calculation of physical momenta will be shortly summarized. More details on reaction microscopes in general can be found in ref. [21] and, specifically on the reaction microscope employed for the experiments presented in part II, in the PhD thesis of Sascha Birkner [147].

4.1 DESCRIPTION OF THE REACTION MICROSCOPE

Overview

Figure 4.1 schematically depicts a reaction microscope as used in experiments involving femtosecond lasers or attosecond pulses. The figure also defines the laboratory-frame coordinate system used throughout this thesis. In the centre of the reaction microscope, a beam of electromagnetic radiation incoming along the y-axis is crossed perpendicularly with a supersonic gas beam (*molecular beam*) propagating along the x-axis. The beam of radiation can either be focused into the molecular beam from outside the reaction microscope (as in the attosecond beamline presented in part III) or, when a short focal length is required, with a mirror within the reaction microscope (as in the experiments in part II). The region in space where the two beams overlap and interact is called the *interaction region* in this thesis. Its centre defines the origin of the employed coordinate system.

Perpendicular to both the molecular beam and the beam of radiation, i.e. parallel and anti-parallel to the z-direction, respectively, homogenous electric and magnetic fields are applied, which guide the charged particles created in the radiation-gas interaction to one of the detectors at either end of the *time-of-flight* path along the z-axis. The electric field is generated by a stack of electrodes within the reaction-microscope vacuum chamber, with an appropriate voltage applied to each electrode such that a homogeneous field results. The magnetic field is generated by an electric current through three copper coils from outside the reaction microscope. Wherever possible, materials within and close to the coils have a low magnetic permeability in order to disturb the homogeneity of the magnetic field as little as possible. Four additional large-diameter coils create another, weaker magnetic field to compensate for external disturbances such as Earth's magnetic field.

[2] For a rate of 0.1 to 0.2 ionization events per laser pulse, according to Poissonian statistics, the probability to ionize two or more target particles ranges from 0.5 % to 1.7 %.

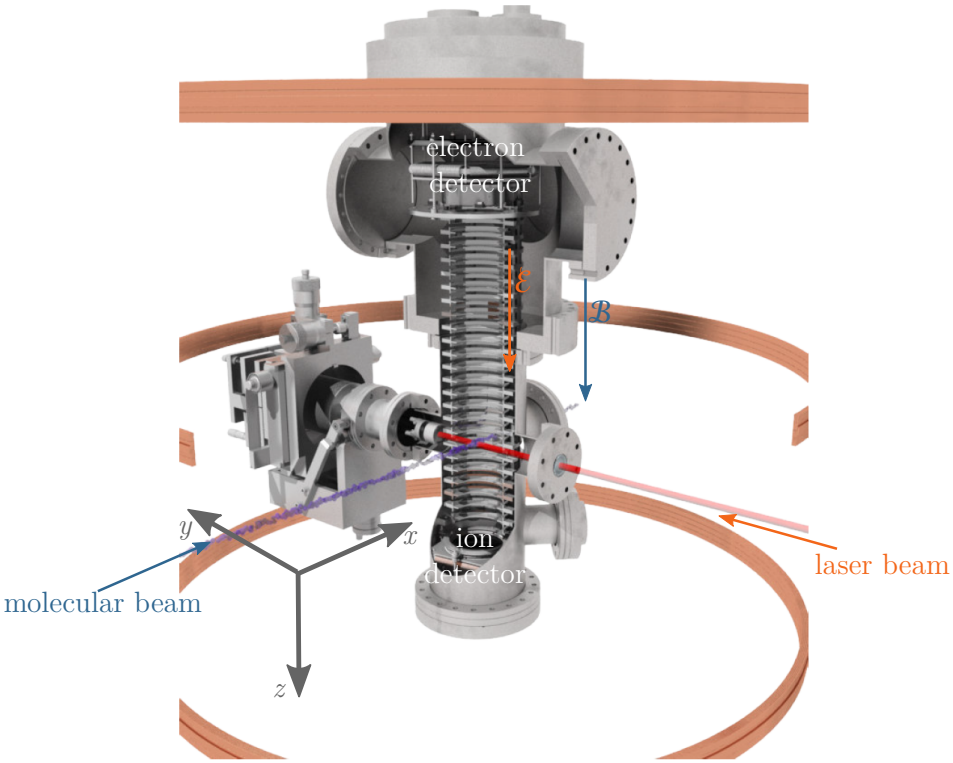

Figure 4.1: Schematic overview of the reaction microscope. Electrons and ions are guided by homogeneous electric and magnetic fields to their respective detector. The coordinate system at the bottom defines the laboratory frame used throughout this thesis. Image modified from ref. [147].

Position-sensitive charged-particle detectors

Due to the polarity of the electric field, negatively charged particles (i.e. electrons) are accelerated in the negative z-direction, where the detector biased for electron detection is placed at a distance of 400 mm from the interaction region. The detector (Roentdek HEX75) with an active area of 75 mm consists of a multi-channel plate (MCP) and a position-sensitive delay-line anode [148]. An MCP features an array of small channels, in which, when a charged particle or energetic electromagnetic radiation hits the front surface of the MCP, a cascade reaction creates a localized cloud of electrons at the same position at the back surface, when a suitably chosen acceleration voltage is applied between front and back [149]. This cloud of electrons subsequently induces pulsed currents in the three lines of the delay-line anode, which are arranged to form a hexagonal grid [147]. On each of the delay lines, depending on where

the electron cloud is located, the induced current signal requires a certain time to reach its two ends. These times are recorded on a computer using two synchronized time-to-digital converter cards (Roentdek TDC8HP), and from the difference between the arrival times on each delay line, the position of the electron cloud and thus of the impact of the initial charged particle can be inferred. While a square grid of delay lines is sufficient to determine the impact position on the detector, the hexagonal arrangement improves the image quality and the multi-hit capabilities, i.e. it performs better when more than one particle hit the detector in quick succession such that the signals on the delay lines from the two hits are not clearly separated in time. In addition to the signals induced on the delay-line anodes, the amplified signal directly from the MCP is also recorded, timed with respect to a trigger signal from the laser, from which the instant of interaction can be deduced. In this way, the detector is capable of recording both the time of flight from the interaction point to the detector and the impact position on the detector.

Cations are accelerated along the positive z-direction towards the second detector 160 mm away from the interaction region and opposite to the electron detector. The ion detector is a Roentdek DLD75 (active area: 75 mm), which also consists of an MCP and a delay-line arrangement, in this case, however, with just two delay lines forming a square grid. In front of the ion detector, a gold mesh is installed, which shields the high negative voltage bias at the front of the MCP from the lower potential in the time-of-flight region, thus reducing lensing effects on the ion trajectories at the cost of lowering the transmission of ions to the detector slightly (transmission: 90 %).

All timing signals from the detectors are amplified and discriminated using constant-fraction discriminators (Roentdek FAMP8 and CFD8c (electron detector) and ATR19 (ion detector)). A discriminator turns the signals from the detector, which display irregularities such as varying pulse heights, into a standard signal that can be fed to the time-to-digital converter. Constant-fraction discriminators reduce the timing jitter due to variations in the input pulse height compared to discriminators relying on a simple threshold [147]. The recorded times from the time-to-digital converter can be monitored in real time using the software CoboldPC from Roentdek.

4.2 POST-EXPERIMENTAL DATA PROCESSING

After the end of the data acquisition, a more detailed analysis of the data takes place that cannot be performed in real time. First, a proprietary algorithm from Roentdek performs an improved position reconstruction from the timing information on the delay-line anodes. This algorithm is, in particular, able to infer the position even if one or several of the delay-line signals are missing in an event. Note that, for all data presented in this thesis, only events where the signals from all delay lines were present and consistent were used for the

further analysis steps.

Reconstruction of particle momenta

From the recorded impact position on and time of flight to the detector, one can then reconstruct the full momentum vector for each particle, if the electric and magnetic field strengths (denoted by $\mathscr{E}$ and $\mathscr{B}$, respectively) are known. These can be inferred from the supplied voltage and current, respectively. For the underlying calibration, see ref. [147]. The momentum reconstruction is performed by relying on the Newtonian equations of motion to determine the trajectories of the particles from the interaction region to the detector. The homogeneous magnetic and electric fields inside the reaction microscope force the particles with charge q and mass m created in the interaction region onto trajectories determined by the equations

$$m\ddot{\vec{x}} = q\left(\mathscr{E}\vec{e}_z + \mathscr{B}\dot{\vec{x}} \times \vec{e}_z\right). \tag{4.1}$$

Using the initial conditions

$$\vec{x}(0) = \vec{x}_0 = \begin{pmatrix} x_0 \\ y_0 \\ z_0 \end{pmatrix} \text{ and } \dot{\vec{x}}(0) = \frac{\vec{p}}{m} = \frac{1}{m}\begin{pmatrix} p_x \\ p_y \\ p_z \end{pmatrix},$$

the solution to this equation is

$$\vec{x}(t) = \begin{pmatrix} x(t) \\ y(t) \\ z(t) \end{pmatrix} = \begin{pmatrix} \frac{1}{m\omega_\mathrm{c}}(p_x \sin\omega_\mathrm{c}t - p_y\cos\omega_\mathrm{c}t + p_y) + x_0 \\ \frac{1}{m\omega_\mathrm{c}}(p_x\cos\omega_\mathrm{c}t + p_y\sin\omega_\mathrm{c}t - p_x) + y_0 \\ \frac{q\mathscr{E}}{2m}t^2 + \frac{p_z}{m}t + z_0 \end{pmatrix}, \tag{4.2}$$

where

$$\omega_\mathrm{c} = \frac{q\mathscr{B}}{m}. \tag{4.3}$$

$\vec{p}$ is the initial momentum vector that we seek to reconstruct. Equation (4.2) describes a helical trajectory starting from $\vec{x}_0$, with a period given by the *cyclotron frequency* ω_c. This can be seen explicitly by rewriting the transverse part of eq. (4.2) using trigonometric identities:

$$\begin{pmatrix} x(t) - x_0 \\ y(t) - y_0 \end{pmatrix} = \frac{1}{m\omega_\mathrm{c}}|\vec{p}_{tr}| \cdot \begin{pmatrix} \sin(\omega_\mathrm{c}t - \beta) \\ \cos(\omega_\mathrm{c}t - \beta) \end{pmatrix} + \frac{1}{m\omega_\mathrm{c}}\begin{pmatrix} p_y \\ -p_x \end{pmatrix} \tag{4.4}$$

$$= \frac{2}{m\omega_\mathrm{c}}|\vec{p}_{tr}|\sin\frac{\omega_\mathrm{c}t}{2} \cdot \begin{pmatrix} \cos\left(\beta - \frac{\omega_\mathrm{c}t}{2}\right) \\ \sin\left(\beta - \frac{\omega_\mathrm{c}t}{2}\right) \end{pmatrix}, \tag{4.5}$$

where $\tan\beta = \frac{p_y}{p_x}$ and $|\vec{p}_\mathrm{tr}| = \sqrt{p_x^2 + p_y^2}$. Equation (4.4) shows that the projection of the particle trajectory onto the x-y-plane is a circle with radius $|\vec{p}_{tr}|/m\omega_\mathrm{c}$ centred around $1/m\omega_\mathrm{c}\left(p_y, -p_x\right)$.

Considering the motion along the z-axis, the trajectory ends where the charged particle hits the detector a distance of d away from $\vec{x}_0$ at a time t_f:

$$d \stackrel{!}{=} z(t_\mathrm{f}) - z_0.$$

This can be solved for t_f,

$$t_\mathrm{f} = -\frac{p_z}{q\mathscr{E}} + t_{\mathrm{f},0}\sqrt{1 + \frac{p_z^2}{2mq\mathscr{E}d}},$$

where

$$t_{\mathrm{f},0} = \sqrt{\frac{2md}{q\mathscr{E}}},$$

to obtain the time of flight to the detector and for p_z to obtain the initial momentum in the z-direction (the *longitudinal momentum*) from the time of flight,

$$p_z(t_\mathrm{f}) = \frac{q\mathscr{E}}{2}\frac{t_{\mathrm{f},0}^2 - t_\mathrm{f}^2}{t_\mathrm{f}} = q\mathscr{E}(t_{\mathrm{f},0} - t_\mathrm{f}) + \mathscr{O}\left(\left(t_{\mathrm{f},0} - t_\mathrm{f}\right)^2\right). \tag{4.6}$$

Here, $t_{\mathrm{f},0}$ denotes the time of flight of a particle with $p_z = 0$. It relates the mass-to-charge ratio m/q of different ion species to the time of flight. The approximation to first order in $(t_{\mathrm{f},0} - t_\mathrm{f})$ in eq. (4.6) is valid for heavy enough particles, or more precisely for $p_z^2/2m \ll dq\mathscr{E}$ [147]. In the present thesis, the approximate expression is used for the determination of p_z for ions, whereas for electrons the exact expression is applied.

To reconstruct the momentum components (p_x, p_y) (*transverse momentum*)[3] from the time of flight t_f and impact position on the detector

$$\begin{pmatrix} x_\mathrm{f} \\ y_\mathrm{f} \end{pmatrix} = \begin{pmatrix} x(t_\mathrm{f}) \\ y(t_\mathrm{f}) \end{pmatrix},$$

the transverse part in eq. (4.2) needs to be solved for (p_x, p_y):

$$\begin{pmatrix} p_x \\ p_y \end{pmatrix}(x_\mathrm{f}, y_\mathrm{f}, t_\mathrm{f}) = \frac{m\omega_\mathrm{c}}{2\sin\frac{\omega_\mathrm{c}t_\mathrm{f}}{2}} \cdot \begin{pmatrix} \cos\frac{\omega_\mathrm{c}t_\mathrm{f}}{2} & -\sin\frac{\omega_\mathrm{c}t_\mathrm{f}}{2} \\ -\sin\frac{\omega_\mathrm{c}t_\mathrm{f}}{2} & -\cos\frac{\omega_\mathrm{c}t_\mathrm{f}}{2} \end{pmatrix} \cdot \begin{pmatrix} x_\mathrm{f} - x_0 \\ y_\mathrm{f} - y_0 \end{pmatrix} \tag{4.7}$$

For small ω_c, i.e. for heavy particles, a Taylor expansion to first order in $\omega_\mathrm{c}t$ in eq. (4.2) yields the simpler relation

$$\begin{pmatrix} p_x \\ p_y \end{pmatrix}(x_\mathrm{f}, y_\mathrm{f}, t_\mathrm{f}) = \frac{m}{t_\mathrm{f}} \begin{pmatrix} x_\mathrm{f} - x_0 \\ y_\mathrm{f} - y_0 \end{pmatrix} \tag{4.8}$$

[3] To distinguish the momentum perpendicular to the driving-laser polarization direction from the momentum perpendicular to the time-of-flight direction in the reaction microscope, the former is called lateral whereas the term transverse is reserved for the latter in this thesis.

between the impact position and the initial momenta. Again, this approximation is only used for ions in the present thesis.

From eq. (4.5), it can be seen that for times of flight $t_{\mathrm{f},n}$ fulfilling $\omega_{\mathrm{c}} t_{\mathrm{f},n} = n \cdot 2\pi$, where n is an integer, the impact position is the same regardless of the initial transverse momentum. Accordingly, eq. (4.7) diverges and the transverse momentum components cannot be retrieved for these $t_{\mathrm{f},n}$, which correspond, according to eq. (4.6), to specific values of the longitudinal momentum $p_z(t_{\mathrm{f},n})$. In the reconstructed momentum distribution, the planes given by $p_z = p_z(t_{\mathrm{f},n})$ are called *nodes* [21]. Already close to the nodes, the quality of the reconstruction of the transverse momentum degrades, due to the small extent of the particle distribution on the detector and the limited spatial resolution of the detector (also see eq. (4.11)). The relative position of the nodes with respect to the momentum distribution changes when varying the extraction fields, and, in principle, for an appropriate choice of the magnitudes of the electric and magnetic fields, the electron distribution can be made free from nodes, which is the case when the occurring p_z momenta all correspond to times of flight between two adjacent nodes. The times of flight $t_{\mathrm{f},n}$ also allow the determination of the strength of the applied magnetic field $\mathscr{B}$. In addition, by comparing the $t_{\mathrm{f},n}$ for several values of $\mathscr{B}$, the instant of interaction with respect to the laser trigger can be accurately deduced. For ions, the cyclotron motion is negligible and the nodes play no role.

In order to use eqs. (4.6) to (4.8) to reconstruct the full momentum vector of a particle, the parameters x_0, y_0, and $t_{\mathrm{f},0}$ need to be determined. In practice, this is achieved iteratively by centring the resulting distributions of projections along p_x, p_y, and p_z for each particle species around zero.

Maximum detectable momentum

Equation (4.4) determines the radius of the helical electron motion, which depends on the transverse momentum $|\vec{p}_{\mathrm{tr}}|$. The radius of the detector r_{MCP} must be twice as large as the radius corresponding to the maximum transverse momentum $|\vec{p}_{\mathrm{tr}}|^{\mathrm{max}}$in order for all electrons to reach the detector:

$$|\vec{p}_{\mathrm{tr}}|^{\mathrm{max}} = \frac{r_{\mathrm{MCP}}}{2} q\mathscr{B}. \tag{4.9}$$

For ions, the maximum detectable transverse momentum can be deduced from eq. (4.8), where one also has to take into account the shift of the ions away from the detector centre due to the velocity of the molecular beam (see section 4.3).

The maximum longitudinal momentum component, on the other hand, is limited by the excursion distance towards the respective opposite detector for those particles with $p_z > 0$ (electrons)/$p_z < 0$ (ions), since the charged particle will be reflected by the potential step present at the opposite detector and thus the corresponding trajectory will be disrupted. For particles with initial momentum towards their own detector, the only limit for the maximum

detectable longitudinal momentum is posed by the temporal resolution of the time-to-digital converter.

Momentum resolution

The temporal resolution also determines the achievable longitudinal momentum resolution of the detector, whereas the momentum resolution in the transverse plane is additionally determined by the spatial resolution of the detector, in both cases disregarding uncertainties due to target preparation in the molecular beam (see next section) and the focus size of the laser. The following expressions can be derived [150]:

$$\Delta p_z = \left| \frac{q\mathscr{E}}{2d^2} + \frac{md}{t^2} \right| \cdot \delta t \tag{4.10}$$

$$\Delta p_{\mathrm{tr}} = \frac{m\omega_{\mathrm{c}}}{2\left|\sin\frac{\omega_{\mathrm{c}}t}{2}\right|} \sqrt{\delta r^2 + \left(\frac{\sqrt{x_{\mathrm{f}}^2 + y_{\mathrm{f}}^2}\,\omega_{\mathrm{c}}}{2\tan\frac{\omega_{\mathrm{c}}t}{2}} \right)^2 \delta t^2}, \tag{4.11}$$

where δt and δr are the uncertainties in the determination of the time of flight and the impact position on the detector, respectively. Note that the transverse momentum resolution depends on both the impact position and the time of flight. Close to the nodes, the transverse momentum resolution diverges, as expected. Also note that, while the maximum detectable momenta may be increased by using larger extraction fields, this will deteriorate the momentum resolution. In the experiments in part II, rather large extraction fields are used to detect high-momentum particles. However, momentum resolution is not critical, since only quantities integrated over relatively large regions in momentum space are considered.

4.3 MOLECULAR BEAMS

Supersonic cooling

The molecular beam is a jet of gas created by the adiabatic expansion of the gas through a small nozzle (in the present case with a diameter of 10 μm) into vacuum. When using a high enough stagnation pressure, the velocity v of the jet becomes larger than the local speed of sound, leading to a *supersonic expansion*. In such an expansion, thermal energy stored in the random motion of the atoms or molecules and compression energy are transformed into the kinetic energy of a directional motion of the jet. From energy conservation, the relations

$$\frac{T_{\parallel}(v)}{T_0} = \left(\frac{\rho(v)}{\rho_0} \right)^{\frac{2}{f}} = 1 - \left(\frac{v}{v_\infty} \right)^2 \tag{4.12}$$

can be derived for an ideal gas [151], where

$$v_\infty = \sqrt{\frac{k_\mathrm{B} T_0}{m_\mathrm{gas}} (f+2)}, \tag{4.13}$$

T_0 and ρ_0 are the initial gas temperature and density before the expansion, respectively, and $T_\parallel(v)$ and $\rho(v)$ are the temperature and density along the jet, which vary with the jet velocity v. k_B is the Boltzmann constant, f is the number of degrees of freedom of the gas and m_gas is the mass of the particles making up the beam. The distribution of v along the jet, also determining the spatial profile of $T_\parallel$ and ρ, depends on the geometry of the nozzle and cannot be easily calculated. From eq. (4.12), it is clear that both $T_\parallel$ and ρ decrease as v increases. The expansion thus leads to a cooling of the jet, from the temperature T_0 down to a few Kelvin. v_∞ is the maximum velocity the jet could reach if cooling to a temperature of 0 K were possible, the so-called *isentropic limit*. For helium and $T_0 = 300\,\mathrm{K}$, $v_\infty = 1766\,\mathrm{m/s}$.

In reality, cooling always stops before reaching 0 K, because, as the density of the jet decreases, at some point no collisions take place any more among the constituents of the beam, and therefore the exchange of energy stops [152]. To obtain a high particle density and thus better cooling, a high stagnation pressure is desirable. On the other hand, the stagnation pressure is limited by the formation of clusters [152], in particular in molecules due to van-der-Waal forces. The released binding energy of the clusters increases the jet temperature, thus limiting the achievable cooling. The clustering of molecules can be decreased significantly by supersonically expanding only a small fraction of the molecules in a rare-gas carrier such as helium (so-called *seeded beams*). Cluster formation in helium occurs only at very low temperatures [152], thus cold targets can be prepared. Using helium in molecular SFI experiments, instead of other rare-gas carriers, has the additional benefit of ionization in helium being negligible at the laser intensities necessary for the SFI of molecules, due to its high IP.

The temperature $T_\parallel$ only characterizes the distribution of velocities along the jet propagation direction, whose FWHM width Δv is given by [153]

$$\Delta v = 2\sqrt{\log 2}\sqrt{2k_\mathrm{B} T_\parallel / m_\mathrm{gas}}.$$

For ions, this velocity distribution affects the achievable momentum resolution in the jet direction (the x-direction according to the coordinate system in fig. 4.1).[4] Similarly, a temperature $T_\perp$ can be defined, characterizing the velocity spread in the direction perpendicular to the molecular beam. $T_\perp$ is determined by the geometry of the apertures confining the jet in the directions perpendicular to the propagation direction and is typically much smaller than $T_\parallel$ [147, 150].

[4] For electrons, the velocity from the molecular beam does not contribute significantly to the momentum due to the small electron mass.

The molecular-beam setup in the reaction microscope

If no further measures are taken, then the directional motion of the beam only reaches a distance $x_M = d \cdot 0.67 \sqrt{\frac{p_0}{p_1}}$ (where d is the nozzle diameter and p_0 and p_1 the pressure before and behind the nozzle, respectively) behind the nozzle (the so-called *zone of silence*), before the molecular beam would collapse [151]. This is prevented by placing a skimmer (in the present case with a diameter of 300 μm) into the zone of silence, which results in a drop of pressure in the region behind the skimmer due to *differential pumping*[5], thus allowing the molecular beam to continue propagation.

In the employed setup, the distance from nozzle to skimmer is 5 mm. After the skimmer, the beam propagates for another 55 cm, before it enters the reaction-microscope main chamber through another orifice with a diameter of 1 mm. This orifice is 81 mm away from the interaction region. After traversing the interaction region, the molecular beam is caught by a pumped catcher to limit the rise of background pressure in the main chamber due to the introduced gas. Typical pressures in different parts of the reaction microscope as employed in the experiments in part II are summarized in table 4.1.

	background pressure	with molecular beam
reaction-microscope main chamber	1.5×10^{-10} mbar	2×10^{-9} mbar
molecular-beam source chamber	6×10^{-9} mbar	4×10^{-4} mbar
differential-pumping stage	7×10^{-10} mbar	4×10^{-7} mbar
beam dump	$<1 \times 10^{-9}$ mbar	8×10^{-8} mbar

Table 4.1: Typical pressures in different parts of the reaction-microscope setup. The molecular beam is operated with 20 bar of 0.03 % of butadiene seeded in helium. The differential-pumping stage is located between the skimmer and the entrance orifice to the reaction microscope.

[5] This is due to the low vacuum conductance of a small orifice, limiting the gas flow and thus allowing a large steady-state pressure differential to exist between the two parts connected by the orifice [154].

CHAPTER 5

Molecular Alignment

5.1 Theory of non-adiabatic alignment

Laboratory-frame vs. molecular-frame measurements

When a molecular target is prepared in a molecular beam, the resulting ensemble is usually randomly aligned, i.e. any orientation of the molecules with respect to the laser polarization axis is equally likely. The response of a molecule to an electromagnetic field will, however, generally depend on the relative orientation of the molecule and the field's polarization vector.

In general, an ensemble of molecules is characterized by an alignment distribution $A(\chi', \theta', \phi')$, where χ', θ', and ϕ' are the Euler angles describing the transition from a space-fixed frame to the molecular frame.[1] The molecular frame, whose axes are denoted by $\hat{x}$, $\hat{y}$, and $\hat{z}$ in the present thesis, is the frame that is attached to and thus rotates with the molecule. $A(\theta', \chi', \phi')$ gives the probability of finding a molecule rotated by the angles χ', θ' and ϕ' with respect to the space-fixed frame.

Within the molecular frame, the direction of the electromagnetic field's polarization vector can be described in spherical coordinates by the angles θ and ϕ. Generally, in an ensemble with alignment distribution A, when measuring a quantity $N(\theta, \phi)$, which is produced by the interaction with an electromagnetic field (called the driving or SFI field within this thesis) and

[1] The transition from one frame to another can always be achieved by means of three rotations: by an angle ϕ' around the z-axis, then by an angle θ' around the new y-axis, and finally by an angle χ' around the new z-axis. This is equivalent to a series of rotations around the axes of the original space-fixed coordinate system: first by an angle χ' around the z-axis, then by an angle θ' around the y-axis, and finally by an angle ϕ' around the z-axis.

which depends on the direction of the (linear) polarization vector of this field in the molecular frame, only the incoherent sum of all contributing orientations

$$N_{\mathrm{avg}} = \frac{1}{8\pi^2} \cdot \int_0^{2\pi} \int_0^{\pi} \int_0^{2\pi} N(\theta(\theta',\chi',\phi'),\phi(\theta',\chi',\phi')) \cdot A(\theta',\chi',\phi') \mathrm{d}\chi' \sin\theta' \mathrm{d}\theta' \mathrm{d}\phi' \tag{5.1}$$

can be determined, i.e. the measurable response to the electromagnetic field is given by the convolution of A with the molecular-frame quantity N [42, 155]. The functions $\theta(\theta',\chi',\phi')$ and $\phi(\theta',\chi',\phi')$ govern the transformation from the space-fixed to the molecular frame.

Thus, when using a randomly oriented ensemble of molecules, the dependence of N on the direction of the polarization vector is lost. When one is interested in the response of the molecule for a certain relative orientation of molecule and laser polarization, one has to prepare the molecular ensemble with an alignment distribution that is peaked along a specific direction, such that the molecular response for this direction has more weight in the average eq. (5.1).

Interaction of a laser field with a rigid rotor

One way to achieve this is to align the molecules using a moderately strong ($10^{11}\,\mathrm{W^2/cm}$ to $10^{12}\,\mathrm{W^2/cm}$) non-resonant laser pulse prior to the interaction producing the quantity N. The alignment laser field interacts with the dipole moment of the molecule. The effect of a permanent dipole moment, which only couples to a DC electric field, averages to zero in an oscillating electric field [156]. The induced dipole moment dynamically created by the displacement of the electrons in the molecule driven by the oscillating, linearly polarized alignment laser field, couples to the laser field, whose envelope has the components $\mathcal{E}_{0i}$, as described by the interaction [157]

$$\hat{V}(t) = -\frac{1}{4} \sum_{i,j} \mathcal{E}_{0,i}(t) \alpha_{ij} \mathcal{E}^*_{0,j}(t). \tag{5.2}$$

α_{ij} is the polarizability tensor, which quantifies the strength of the induced dipole moment along different directions in the molecule [158]. The rotational part of the field-free Hamiltonian is given, within the rigid-rotor model, by [156]

$$\hat{H}^{\mathrm{ff}}_{\mathrm{rot}} = \frac{\hat{J}^2_{\hat{x}}}{2I_{\hat{x}\hat{x}}} + \frac{\hat{J}^2_{\hat{y}}}{2I_{\hat{y}\hat{y}}} + \frac{\hat{J}^2_{\hat{z}}}{2I_{\hat{z}\hat{z}}}, \tag{5.3}$$

such that the total rotational Hamiltonian is

$$\hat{H}_{\mathrm{rot}}(t) = \hat{H}^{\mathrm{ff}}_{\mathrm{rot}} + \hat{V}(t). \tag{5.4}$$

$\hat{J}_{\hat{x}}$, $\hat{J}_{\hat{y}}$, and $\hat{J}_{\hat{z}}$ are the components of the angular-momentum operator in the molecular frame. $I_{\hat{x}\hat{x}}$, $I_{\hat{y}\hat{y}}$, and $I_{\hat{z}\hat{z}}$ are the principal moments of inertia,

which also define the molecular frame [156]. Different molecules are classified according to the relative magnitude of the principal moments of inertia [159]: Molecules with no special relation among the principal moments are called *asymmetric-top* molecules. In *symmetric-top molecules*, two of the principal moments are identical, where the third one can be either larger (*oblate* symmetric top) or smaller (*prolate* symmetric top) than the other two. In the case of a prolate symmetric-top molecule, the axis with the smaller principal moment of inertia will be called the *long axis* in this thesis. A special case of a prolate symmetric top is a *linear* molecule, where the third principal moment of inertia is much smaller than the other two. In general, the major axes of the polarizability and inertia tensors need not be identical, but for symmetric-top molecules the two coordinate systems are the same and two of the principal values of the polarizability tensor are also identical [156, 160].

Specializing on the case of prolate symmetric-top molecules from now on, the interaction potential eq. (5.2) can be written as

$$\hat{V}(t) = -\frac{\mathcal{E}_0(t)^2}{4}\left(\left(\alpha_\parallel - \alpha_\perp\right)\cos^2\theta' + \alpha_\perp\right), \tag{5.5}$$

where $\mathcal{E}_0$ is the magnitude of the instantaneous alignment-field envelope, θ' is the angle between the long axis of the molecule and the alignment-field polarization direction (called the *alignment axis*), $\alpha_\perp$ is the common principal value of the polarizability tensor for two of its major axes, and $\alpha_\parallel$ is the larger principal value for the third major axis [156]. From eq. (5.5), it can be seen that the energy is minimized when the angle θ' is 0 or π, i.e. when the long axis of the molecule is aligned (anti-)parallel to the alignment axis.

The field-free Hamiltonian eq. (5.3) in the case of a prolate symmetric-top molecule reads

$$\hat{H}_{\text{rot}}^{\text{ff}} = \frac{\hat{J}^2}{2I_\perp} + \hat{J}_\parallel^2\left(\frac{1}{2I_\parallel} - \frac{1}{2I_\perp}\right),$$

where $\hat{J}^2 = \hat{J}_{\hat{x}}^2 + \hat{J}_{\hat{y}}^2 + \hat{J}_{\hat{z}}^2$ is the squared total angular-momentum operator, $\hat{J}_\parallel^2 = \hat{J}_{\hat{z}}^2$ is the square of the component of the angular-momentum operator along the long axis of the molecule, and $I_\perp$ and $I_\parallel$ are the moments of inertia defined in analogy to $\alpha_\perp$ and $\alpha_\parallel$, i.e. $I_\parallel$ is the moment of inertia for rotations around the longer molecular axis and $I_\perp$ the one for rotations around axes perpendicular to it. The eigenvalues $E_{j,k}$ of $\hat{H}_{\text{rot}}^{\text{ff}}$ can be shown to be [158, 161]

$$\frac{E_{j,k}}{\hbar^2} = \frac{j(j+1)}{2I_\perp} + k^2\left(\frac{1}{2I_\parallel} - \frac{1}{2I_\perp}\right), \tag{5.6}$$

where j and k are integer numbers with $j \geq 0$ and $|k| \leq j$.

Prompt alignment

In *non-adiabatic alignment* (also called *impulsive alignment*), the laser pulse aligning the molecules is short with respect to the time scale set by the

rotational constants $B_\perp = \hbar/4\pi I_\perp$ and $B_\parallel = \hbar/4\pi I_\parallel$ [157, 162, 163]. In the transition from the field-free to the field-dressed and back to the field-free case, the system cannot adapt fast enough to be in the momentary eigenstate of the full time-dependent Hamiltonian, but instead a coherent superposition of field-free eigenstates $|jkm\rangle$[2] has been populated by the end of the pulse [156]. More precisely, while the laser field of the pulse is present, the molecule will undergo a series of Raman transitions[3], which populate states with different j but with the same k and m. After the alignment pulse is over, the field-free temporal evolution of the wave packet is described by

$$|\Psi\rangle(\tau) = \sum_j c_j |jkm\rangle \exp\left(\frac{i}{\hbar} E_{j,k}\tau\right), \tag{5.7}$$

where c_j denotes the population of the eigenstate $|jkm\rangle$ immediately after the alignment pulse and τ is the delay with respect to this instant. The coherent population of the j-states leads to an aligned ensemble shortly after the pulse (*prompt alignment*). This can be explained both classically and quantum-mechanically by regarding the alignment pulse as a very short kick (a δ-kick) acting on the molecules, which results in an angular velocity that is approximately proportional to the angular deviation from the alignment axis. All molecules in an ensemble thus align approximately along the alignment axis a short delay after the kick [165]. In addition, when analytically continuing the time evolution to negative delays, shortly before the prompt alignment there would be an instant of high *anti-alignment* [166], which means that the molecules are delocalized in a plane perpendicular to the alignment axis. The more j-states are involved, the sharper peaked the (anti-)alignment distribution is.

Revival structure

From eqs. (5.6) and (5.7), it can also be seen that the temporal evolution of the rotational wave packet is $\Delta\tau_{\text{rev}}$-periodic, where

$$\Delta\tau_{\text{rev}} = \frac{1}{2B_\perp}. \tag{5.8}$$

In particular, this implies that – while the different phases $\exp\left(\frac{i}{\hbar}E_{j,k}\tau\right)$ for the components making up the rotational wave packet in eq. (5.7) quickly lead to a reduction of the degree of alignment following the prompt alignment – a time $\Delta\tau_{\text{rev}}$ after the prompt alignment the phase difference between adjacent

[2] The quantum number m is the eigenvalue with respect to the z'-component of the angular-momentum operator in the space-fixed coordinate system [164]. States with the same j and k but different m are degenerate.

[3] A Raman transition occurs within a molecule when a photon scatters inelastically from it, to compensate for the energy transferred to the photon [158].

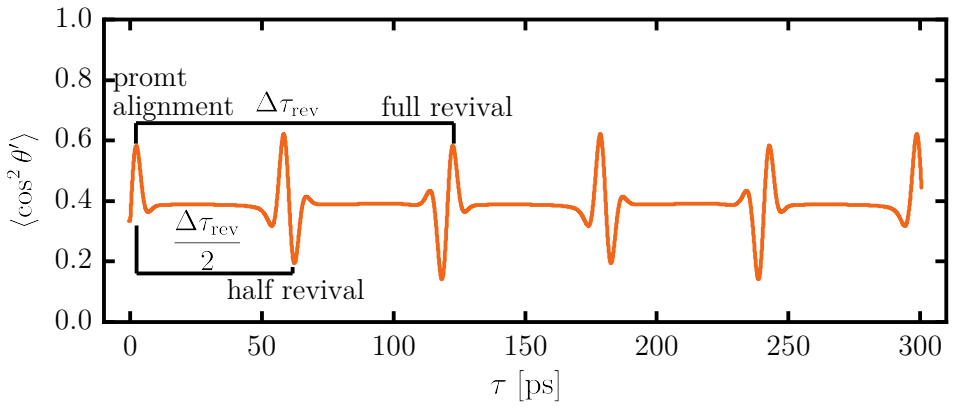

Figure 5.1: Simulated $\langle\cos^2\theta'\rangle$ for 1,3-butadiene in the symmetric-top approximation as a function of the delay τ after the alignment pulse with a duration of 150 fs and a peak intensity of 3.2×10^{12} W/cm^2. The rotational temperature of the ensemble was 3 K. For the relevant constants in butadiene, see table 9.1.

j-states is a multiple of 2π, so all components are in phase again, and a high degree of alignment is restored. This is called a *full revival* of the wave packet. The anti-alignment that can be deduced from the δ-kick model for negative time delays can actually be observed at the full revival shortly before the instant of alignment.

The degree of alignment can be quantified by means of the $\langle\cos^2\theta'\rangle$ value, which can be expressed as [156]

$$\begin{aligned}\langle\cos^2\theta'\rangle(\tau) &= \sum_{j,j'} c_j^* c_{j'} \exp\left(-\frac{i}{\hbar}\left(E_{j',k}-E_{j,k}\right)\tau\right)\langle jkm|\cos^2\theta'|j'km\rangle \\ &= \sum_j |c_j|^2\cdot\langle jkm|\cos\theta'|jkm\rangle \\ &+ \sum_j 2|c_j||c_{j-1}|\cdot\langle j-1km|\cos^2\theta'|jkm\rangle\cdot\cos\left(\frac{E_{j,k}-E_{j-1,k}}{\hbar}\tau-\text{const}\right) \\ &+ \sum_j 2|c_j||c_{j-2}|\cdot\langle j-2km|\cos^2\theta'|jkm\rangle\cdot\cos\left(\frac{E_{j,k}-E_{j-2,k}}{\hbar}\tau-\text{const}\right).\end{aligned} \tag{5.9}$$

Figure 5.1 shows the temporal evolution of $\langle\cos^2\theta'\rangle$ for 1,3-butadiene (see chapter 6 and section 9.1) in the symmetric-top approximation. The values of $\langle\cos^2\theta'\rangle$ range from 0 to 1. A $\langle\cos^2\theta'\rangle$-value of 1/3 signifies a random ensemble of molecules, whereas higher values imply alignment of the long molecular axis along the alignment axis and lower values anti-alignment in the plane perpendicular to it [167].

Equation (5.9) displays three contributions: The first term does not depend on τ and, thus, it results in a *permanent-alignment* component for the alignment distribution. This can be seen in fig. 5.1, where the base value of $\langle\cos^2\theta'\rangle$ is larger than $1/3$ even away from the revivals. The second and third terms, on the other hand, are due to the beating of states with $\Delta j = \pm 1$ and $\Delta j = \pm 2$, respectively.[4] The $\Delta\tau_{\mathrm{rev}}$-periodicity is also evident in eq. (5.9). Accordingly, in fig. 5.1 the high degree of alignment from the prompt alignment is restored in intervals of $\Delta\tau_{\mathrm{rev}} = 119\,\mathrm{ps}$ (see eq. (5.8) and table 9.1). In addition, for the last part of the last term in eq. (5.9) the relation

$$\cos\left(\frac{E_{j,k} - E_{j-2,k}}{\hbar}\left(\tau + \frac{\Delta\tau_{\mathrm{rev}}}{2}\right) - \mathrm{const}\right) = -\cos\left(\frac{E_{j,k} - E_{j-2,k}}{\hbar}\tau - \mathrm{const}\right) \tag{5.10}$$

holds. For linear molecules (and for symmetric-top molecules initially in a state $|jkm\rangle$ with $k = 0$ or $m = 0$), the selection rule $\Delta j = \pm 2$ for Raman transitions [168] implies that the second term in eq. (5.9) does not contribute to $\langle\cos^2\theta'\rangle(\tau)$. In this case, it can be concluded from eq. (5.10) that at a delay of approximately $\Delta\tau_{\mathrm{rev}}/2$ a so-called *half revival* occurs, where alignment and anti-alignment are also restored, however – due to the minus sign in eq. (5.10) – in inverse order compared to the full revivals. For symmetric-top molecules, in general also $\Delta j = \pm 1$ Raman transitions are possible [168], but the overall behaviour is expected to be similar to linear molecules, since the last term dominates the second term in eq. (5.9) [156]. This is evidenced by the clear half revival in fig. 5.1.

Eventually, the degree of alignment at the revivals decreases in real systems, because the rigid-rotor model, underlying the evenly spaced energy levels, ignores the effect of centrifugal elongation of a rotating molecule, which changes the moment of inertia for higher j-states [169].

For asymmetric-top molecules, the energy level structure becomes much more complex, leading to so-called C-type revivals in addition to the J-type revivals of symmetric tops, which become the more pronounced the further the deviations from a symmetric-top description are (for more details see refs. [156, 167, 170]). Furthermore, it should be mentioned that, using elliptically polarized alignment pulses, asymmetric-top molecules can be fixed in space in all three dimensions [156].

Returning to the case of symmetric-top molecules, the following field-free alignment scheme can be devised: By initiating the process which one would like to study – producing the molecular-frame quantity N – at a delay τ corresponding to alignment at one of the (half) revivals, an aligned ensemble can be achieved without the (potentially disturbing) alignment laser field being present during the process itself. Since alignment takes place along the polarization direction of the alignment pulse, different directions of the

[4] Higher-order beatings cannot be observed in the $\langle\cos^2\theta'\rangle$ time evolution [156].

long molecular axis can be probed by varying the polarization direction of the alignment laser pulse with respect to the driving-laser polarization.

Finite temperature of the molecular ensemble

So far, it was assumed that all relevant $|jkm\rangle$-states are populated coherently by the alignment laser. For this, it is necessary that before the interaction with the alignment laser pulse only a single rotational state is populated. In general, however, in a thermal ensemble of molecules, several states are incoherently populated even before the interaction. The population of each state with energy $E_{j,k}$ (given by eq. (5.6)) is governed by the Boltzmann factor

$$\exp\left(-\frac{E_{j,k}}{k_{\mathrm{B}}T_{\mathrm{rot}}}\right), \tag{5.11}$$

where T_{rot} is the rotational temperature [156]. This decreases the coherence of the rotational wave packet launched by the alignment pulse and, thus, the achievable degree of alignment. In order to limit this, the rotational temperature of the prepared molecular ensemble should be low [171]. The rotational temperature depends on the translational temperature of the molecular beam, considered in section 4.3, and on the efficiency of the energy exchange between the translational and rotational degrees of freedom due to collisions among the constituents of the molecular beam. Since – as the density of the molecular beam decreases and collisions become rare – there is an intermediate regime where translational cooling still takes place but where the internal degrees of freedom (rotations and vibrations) are no longer in thermal equilibrium with the translational degrees of freedom [152], the translational temperature generally imposes a lower limit for T_{rot}.

5.2 EXPERIMENTAL DETERMINATION OF THE ALIGNMENT DISTRIBUTION

After pre-aligning (symmetric-top) molecules using non-adiabatic alignment, as described in the previous section, the molecules have an axis distribution $A(\theta')$[5], which is peaked along the alignment-laser polarization direction. Knowing the alignment distribution that is present when probing the quantity N with the SFI pulse is useful to compare experimental data with theoretical calculations, which can then include averaging over A. In addition, it is also possible – by experimentally determining the quantity N_{avg} eq. (5.1) for several angles α' between the polarizations of the alignment and the probe laser fields[6] – to

[5] In the case of a linearly polarized alignment pulse and symmetric-top molecules, the alignment distribution $A(\chi',\theta',\phi')$ does not depend on ϕ' and χ' [172].

[6] The polarization direction of the alignment laser defines the z'-axis of the 'space-fixed' coordinate system (x',y',z'), whereas the y'-axis is defined by the common propagation

deconvolve the alignment distribution from the measured $N_{\mathrm{avg}}(\alpha')$ and thus obtain the original molecular-frame dependence $N(\theta)$ (see next section).

While it is possible to measure the alignment distribution directly by rapidly dissociating the molecules with a short intense laser pulse [173], such measurements rely on the *axial-recoil approximation*, which assumes the produced fragments to have their momentum along the molecular axis. This is well fulfilled for diatomic molecules but may fail for larger molecules [174]. Therefore, one often turns to numerical simulations of the alignment distribution, for which, however, the alignment pulse parameters (intensity, duration, focal averaging) and the rotational temperature of the molecular ensemble in the molecular beam need to be known. In particular the alignment intensity and the rotational temperature are very difficult to measure accurately. Mikosch et al. [49, 160] introduced a method to determine the most likely alignment distribution prepared via non-adiabatic alignment without precisely knowing some of these input parameters. The method relies on two experimental scans of the quantity N_{avg}, as a function of the delay τ for a fixed angle α' and as a function of the angle α' for a suitable fixed value of τ. These scans are then compared to a series of symmetric-top alignment simulations for a range of input alignment intensities and rotational temperatures, choosing the alignment distribution which describes this experimental data best. Since the procedure plays an important role in part II of the thesis, it will be briefly described here. For more details see ref. [160].

Parametrizing molecular-frame quantities

The molecular-frame quantity $N(\theta,\phi)$ can be expanded in terms of spherical harmonics Y_{lm} as

$$N(\theta,\phi) = \sum_{l=0}^{\infty} \sum_{m=-l}^{l} a_{lm} Y_{lm}(\theta,\phi)$$

For symmetric-top molecules N does not depend on ϕ, and the expansion can be simplified to

$$N(\theta) = \sum_{l=0}^{\infty} a_l \mathcal{P}_l(\cos\theta), \tag{5.12}$$

where $\mathcal{P}_l$ are the Legendre polynomials. Furthermore, if the molecule has inversion symmetry, only even l contribute to the sum in eq. (5.12). In practice, often only the first few terms are relevant to adequately describe the θ-dependence of an actual quantity. Therefore, the expansion can be truncated

direction of the alignment and driving laser pulses. Since the polarization vector of the driving laser is always pointing along the z-direction of the laboratory frame (see fig. 4.1), the 'space-fixed' coordinate system is rotated around the y-axis with respect to the laboratory frame by the angle α'.

and only terms up to $l_{\max}$ are considered:

$$N(\theta) \approx \sum_{l=0}^{l_{\max}} a_{2l} \mathcal{P}_{2l}(\cos\theta). \tag{5.13}$$

Equation (5.13) facilitates the parametrization of the θ-dependent quantity N using only a few parameters. The quantity parametrized in this way then needs to be convolved with simulated alignment distributions of the molecular ensemble to compare with experimental data.

Symmetric-top alignment simulations

In the simulations, which were performed using a code from Bisgaard [156], the angular-momentum states of the molecular ensemble are initially incoherently populated, weighted by the Boltzmann factor eq. (5.11) using the input rotational temperature. The interaction with the alignment pulse, whose intensity and duration are given as input parameters, is simulated by solving the time-dependent Schrödinger equation, using the Hamiltonian eq. (5.4), to obtain the complex c_j in eq. (5.7), which then govern the field-free evolution after the alignment laser pulse. Intensity averaging over the focal volume of the alignment laser beam is taken into account, using the focal spot sizes of the pump and probe beams and averaging over different slices making up the interaction volume.

The result of a simulation is a time-dependent simulated alignment distribution $A^i(\theta', \tau)$, where the index i labels the set of variable input parameters $\{T_{\mathrm{rot}}, I\}_i$.

Determination of the most likely alignment distribution

Rewriting eq. (5.1) for the case of symmetric-top molecules and for a probe-laser polarization direction at an angle α' with respect to the alignment axis and including a time dependence τ for the alignment distribution, one obtains [42]

$$N_{\mathrm{avg}}(\alpha', \tau) = \frac{1}{8\pi^2} \cdot \int_0^{2\pi} \int_0^{\pi} N(\theta(\theta', \phi', \alpha')) \cdot A(\theta', \tau) \sin\theta' \mathrm{d}\theta' \mathrm{d}\phi', \tag{5.14}$$

where in this case the function $\theta(\theta', \phi', \alpha')$ is given by

$$\cos\theta = \cos\alpha' \cos\theta' - \sin\alpha' \sin\theta' \sin\phi'.$$

Inserting the expansion eq. (5.13) for N and the simulated A^i into eq. (5.14), one obtains expressions that can be fitted to the experimental data.

For each of the alignment simulations i, the expression

$$\frac{1}{8\pi^2} \cdot \int_0^{2\pi} \int_0^{\pi} \sum_{l=0}^{l_{\max}} a_{2l} \mathcal{P}_{2l}(\cos\theta(\theta', \phi', \alpha')) \cdot A^i(\theta', \tau = \tau_{\mathrm{a}}) \sin\theta' \mathrm{d}\theta' \mathrm{d}\phi', \tag{5.15}$$

is fitted to a corresponding experimental angular scan performed at a pump-probe delay $\tau = \tau_\mathrm{a}$ where the ensemble is aligned. The a_{2l} are the free fitting parameters, and their respective best-fit values when using the alignment simulation with index i are denoted by a^i_{2l}. Accordingly, the N and N_avg obtained for each i from eq. (5.13) and eq. (5.14), respectively, are denoted by N^i and N^i_avg. l_max is chosen globally in such a way that good fits result for all alignment simulations. In practice, this is always possible using not very high l_max, implying that any simulated alignment distribution can be made consistent with the experimental angular scan by assuming an appropriate angular dependence of N^i in the molecular frame.

In order to find out which simulated alignment distribution A^i is the closest to the actual experimental alignment distribution, the predictions from eq. (5.14) for the temporal evolution of $N^i_\mathrm{avg}(\alpha' = \alpha'_0, \tau)$ are compared with an experimental delay scan recorded for a fixed $\alpha' = \alpha'_0$. To this end, each N^i_avg is fitted to the experimental scan using the expression

$$C^i_1 \cdot N^i_\mathrm{avg}(\alpha' = \alpha'_0, \tau - C^i_2) \tag{5.16}$$

with fitting parameters C^i_1 and C^i_2, allowing for an overall scaling of the distribution and a slight miscalibration of the experimental time zero, respectively. The quality of the fit is then quantified for each i by calculating the reduced χ^2-value $\left(\chi^2_\mathrm{red}\right)^i$. The most likely alignment distribution, which is labelled with the index i_min, is the one that leads to the smallest reduced χ^2, $\chi^2_\mathrm{red,min} = \left(\chi^2_\mathrm{red}\right)^{i_\mathrm{min}}$. Furthermore, all simulations with $\left(\chi^2_\mathrm{red}\right)^j < \chi^2_\mathrm{red,min} + 1$ form a 1σ-confidence interval for A^{i_min}, by calculating the maximum and minimum envelope functions

$$A^\mathrm{max}(\theta', \tau = \tau_\mathrm{a}) = \max_j \left\{ A^j(\theta', \tau = \tau_\mathrm{a}) \middle| \left(\chi^2_\mathrm{red}\right)^j < \chi^2_\mathrm{red,min} + 1 \right\}$$

and

$$A^\mathrm{min}(\theta', \tau = \tau_\mathrm{a}) = \min_j \left\{ A^j(\theta', \tau = \tau_\mathrm{a}) \middle| \left(\chi^2_\mathrm{red}\right)^j < \chi^2_\mathrm{red,min} + 1 \right\}.$$

Confidence intervals for N^{i_min} and $C^{i_\mathrm{min}}_1 \cdot N^{i_\mathrm{min}}_\mathrm{avg}(\alpha' = \alpha'_0, \tau - C^{i_\mathrm{min}}_2)$ can be obtained analogously.

5.3 DECONVOLUTION OF MOLECULAR-FRAME QUANTITIES

Having obtained the alignment distribution in this way, it can be used to remove its influence on other experimental observables $M_\mathrm{avg}(\alpha')$ that have been measured in dependence of the angle α' between the alignment- and driving-laser polarizations in an experiment with aligned molecules. This will result in a corresponding quantity $M(\theta)$ depending on the angle θ between the

molecular axis and the driving-laser polarization. The transformation from M to M_{avg} is given analogously to eq. (5.14), and the aim of this section is to revert this transformation. This *deconvolution* will be used in chapter 10 to obtain the molecular-frame angular ionization and rescattering probabilities.

Deconvolution procedure

The sought-after quantity $M(\theta)$ may again be written as a series of Legendre polynomials in analogy to eq. (5.13), with expansion coefficients b_{2k}. The coefficients b_0, b_2, …, $b_{\mathrm{k_{max}}}$ are determined by fitting the expression

$$\frac{1}{8\pi^2}\cdot\int_0^{2\pi}\int_0^{\pi}\sum_{k=0}^{k_{\mathrm{max}}} b_{2k}\mathcal{P}_{2k}(\cos\theta(\theta',\phi',\alpha'))\cdot A^{i_{\mathrm{min}}}(\theta',\tau=\tau_{\mathrm{a}})\sin\theta'\mathrm{d}\theta'\mathrm{d}\phi' \quad (5.17)$$

to the experimentally measured $M_{\mathrm{avg}}(\alpha')$. $A^{i_{\mathrm{min}}}$ is the most likely alignment distribution determined in the previous section. This fit thus determines the most likely dependence for the molecular-frame quantity $M(\theta)$ from which the $M_{\mathrm{avg}}(\alpha')$ originates.

Determination of the error of the deconvolved quantity

Let $\Delta M_{\mathrm{avg}}(\alpha')$ denote the experimental error associated with the quantity $M_{\mathrm{avg}}(\alpha')$ and j the indices of the simulated alignment distributions forming the 1σ-confidence interval, as determined in the previous section. To calculate the error $\Delta M(\theta)$ of $M(\theta)$, two contributions have to be considered:

- The uncertainty in the alignment distribution described by the $A^j(\theta)$ also translates into an uncertainty in the deconvolved $M(\theta)$. Performing the fit eq. (5.17) using each of the $A^j(\theta)$ instead of $A^{i_{\mathrm{min}}}(\theta)$ yields a set of distributions $M^j(\theta)$, whose minimum and maximum envelopes form the first contribution to $\Delta M(\theta)$, called the *alignment uncertainty*.
- To also consider the error $\Delta M_{\mathrm{avg}}(\alpha')$ of $M_{\mathrm{avg}}(\alpha')$ itself, a Monte-Carlo approach is applied: From $M_{\mathrm{avg}}(\alpha')$ and $\Delta M_{\mathrm{avg}}(\alpha')$, n_{MC}[7] alternative $M^{i'}_{\mathrm{avg}}(\alpha')$ distributions consistent with the original data are created by sampling from Gaussian distributions with mean $M_{\mathrm{avg}}(\alpha')$ and standard deviation $\Delta M_{\mathrm{avg}}(\alpha')$ for each α'. The similarity of each $M^{i'}_{\mathrm{avg}}(\alpha')$ to the measured data $(M_{\mathrm{avg}}(\alpha'),\Delta M_{\mathrm{avg}}(\alpha'))$ is evaluated by calculating the weighted Euclidian distance (which is called the *Mahalanobis distance* in statistics [175])

$$d^{i'} = \sum_{\alpha'}\frac{M^{i'}_{\mathrm{avg}}(\alpha') - M_{\mathrm{avg}}(\alpha')}{\Delta M_{\mathrm{avg}}(\alpha')}. \quad (5.18)$$

[7] In chapter 10, $n_{\mathrm{MC}} = 10000$.

The 68 % of the $M_{\text{avg}}^{i'}(\alpha')$ with the smallest $d^{i'}$ are consistent with $(M_{\text{avg}}(\alpha'), \Delta M_{\text{avg}}(\alpha'))$ to the 1σ-confidence level, and each of these $M_{\text{avg}}^{i'}(\alpha')$ is subsequently fitted using eq. (5.17) and the most likely alignment distribution $A^{i_{\min}}(\theta)$. This results in $0.68 n_{\text{MC}}$ deconvolved $M^{i'}(\theta)$, whose maximum and minimum envelopes form the second contribution to $\Delta M(\theta)$, called the *statistical uncertainty*.

II

Channel-Resolved Rescattering in 1,3-Butadiene

CHAPTER 6

Motivation

Common assumptions related to the three-step model

Due to its clarity and simplicity, the three-step model forms the basis of strong-field and attosecond physics, allowing the rationalization of countless experiments in an intuitive way [24]. However, over time, it became clear that many of the initial assumptions made in the formulation of the three-step model had to be modified to explain experimental observations even on a qualitative level, especially when applying the model to increasingly more complex targets, such as polyatomic molecules. Among those assumptions are [176] the neglect of the ionic potential during continuum propagation [177], the use of field-free scattering states, additionally exhibiting an asymptotically planar wavefront [20, 81, 84] (also see section 10.4), the adiabaticity of the electron dynamics [178–180], and the single-active electron approximation (see page 11). The breakdown of the latter has been established in a series of experiments [22, 55–57] and manifests itself, in its most basic form, in the participation of more than one molecular orbital in the strong-field response.

Experimental evidence for the breakdown of the single-active electron approximation

First indications for this phenomenon were found in HHG in molecular systems. McFarland et al. [56] presented the first clear evidence for the participation of several continuum channels in HHG in an experiment using aligned N_2 molecules, which displayed enhancements of the high-harmonic yield in the cut-off region (where contributions from the lower-lying orbitals are expected to be strongest due to the higher IP (see eq. (1.30))) for alignment angles

where, according to the structure of the Dyson orbitals, ionization from the HOMO – but not from the HOMO-1 – is suppressed. Further milestones were the simultaneous tomographic reconstruction of the HOMO and HOMO-1 via high-harmonic tomography in N_2 [113], as well as the reconstruction of dynamics induced by the superposition of the multiple electronic states in the ion populated by the strong field [57].

First evidence for the generation of multiple continua arising from photoelectrons was presented by Akagi et al. [55], who compared photoelectron distributions from direct ionization to detailed theoretical calculations. Relying much less on computations, these results were confirmed in ref. [22] directly from experimental observations, using a technique called channel-resolved ATI (CRATI): The authors exploited that the ATI peak structure formed by photoelectrons created via SFI shifts with the IP of the state from which they originate (see eq. (1.19)). This means that the ATI combs formed by direct ionization from the HOMO and the HOMO-1 are displaced with respect to each other by their difference in IP. Participation of multiple orbitals in SFI should thus result in multiple overlapping ATI combs in the total photoelectron energy spectrum, whose relative amplitude is given by the ionization yield of the respective channel. Since the yield from the lower-lying orbitals may be small and the overlapping combs therefore difficult to discern, the authors made use of a property of the employed molecule, 1,3-butadiene, namely that the electronic state of the ion upon ionization can be determined in some cases from specific ionic fragments detected in correlation with the photoelectron. It is this property that makes 1,3-butadiene especially well-suited for performing ionization channel–resolved measurements, which is also the reason why it has been chosen as the target for the experiments presented in this part.

Electronic structure of 1,3-Butadiene

To explain the relation between ion species and electronic state of the cation in 1,3-butadiene, fig. 6.1a) schematically depicts the relevant states in neutral and singly charged butadiene and the resulting fragments. 1,3-butadiene, C_4H_6, is a flat molecule consisting of four C-atoms connected by conjugated double bonds, i.e. alternating double and single bonds. It belongs to the C_{2h} symmetry group, which means that, in its equilibrium configuration, the molecule is invariant with respect to a reflection about the molecular plane as well as to a rotation by an angle of 180° around an axis perpendicular to this plane through the centre of mass. This also implies invariance with respect to spatial inversion. The eigenfunctions of the electronic Hamiltonian then also must remain unchanged modulo a phase factor of π with respect to these symmetry operations. Accordingly, electronic states in 1,3-butadiene (and its cation) can be labelled by whether the electron wave function remains identical or changes sign when applying the rotation (labels a and b (for single-electron states) or A and B (for the total electron wave function), respectively) or

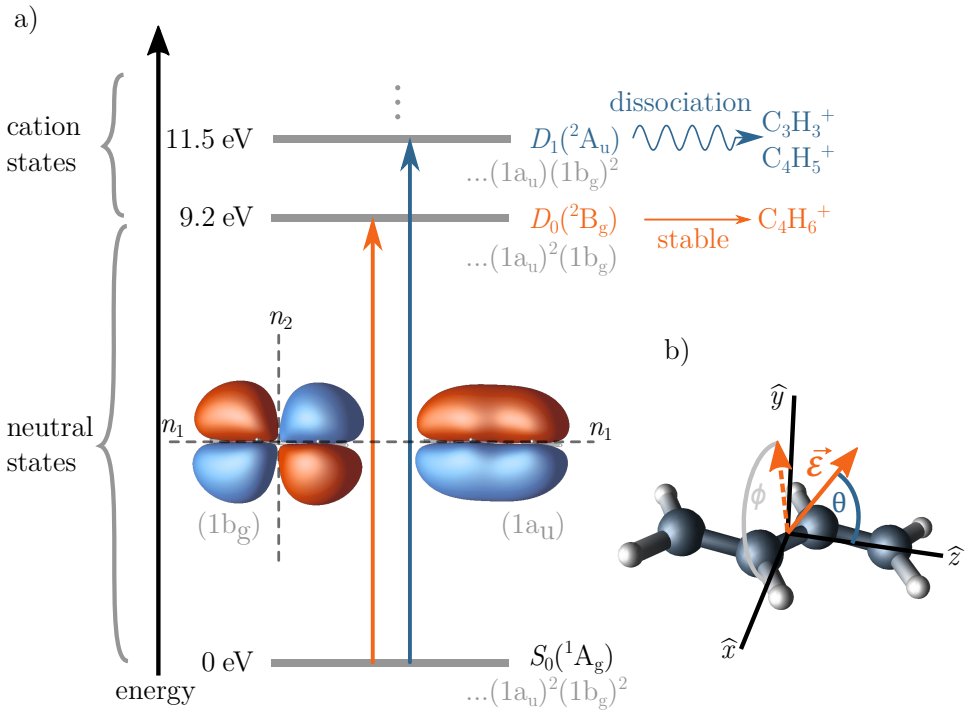

Figure 6.1: a) Schematic illustration of states in 1,3-butadiene relevant for CRATI and the discussions in this thesis. The Dyson orbitals (see section 1.1) for ionization from the S_0 neutral ground state to the D_0 cation ground state and to the D_1 cation first excited state, respectively, are also displayed, along with their nodal planes n_1 and n_2. The labels in light grey below the state labels indicate the symmetry of the highest occupied molecular orbitals. Ionization to the D_1 state can be distinguished from ionization to the D_0 state by the subsequent formation of different ion species. b) Employed molecular-frame coordinate system. The polar angle θ denotes the angle between the principal axis of the inertia tensor with the lowest magnitude ($\hat{z}$-axis) and the polarization vector $\vec{\mathcal{E}}$ of the laser driving SFI (solid orange arrow). The azimuthal angle ϕ is the angle between the projection of $\vec{\mathcal{E}}$ onto the $\hat{x}$-$\hat{y}$-plane (shown as dashed orange arrow) and the $\hat{x}$-axis. For $\phi = 0°$, the polarization vector lies within the molecular plane.

inversion (subscript labels g and u, gerade or ungerade parity, respectively) symmetry operations. The electronic ground state of the neutral is a singlet state S_0 (all electrons are paired and the total electron spin is 0), whereas the two lowest states of the singly charged ion are doublet states (i.e. one of the orbitals contains an unpaired electron, leading to a total spin of $1/2$), where, in this thesis, the shorthand notation D_0 and D_1 will be used for these states [181].

The two highest occupied molecular orbitals in the S_0 ground state of the neutral, i.e. the $1b_g$ HOMO and the $1a_u$ HOMO-1 states, which are also shown in fig. 6.1a), are of particular relevance for the channel-resolved experiments. Ionization of an electron in the HOMO (requiring an energy of 9.2 eV to overcome the IP) results, within the Hartree-Fock-Koopmans' picture, in an ion in the ground D_0 state. Ionization of an electron from the HOMO-1 requires an energy of 11.5 eV and yields an ion in the first excited D_1 state. The two relevant direct ionization pathways are called the D_0 and D_1 channels in this thesis, respectively, according to the final state of the ion.

Correlating ionization channels with photofragments in 1,3-butadiene

In butadiene, as in many polyatomic molecules, only the electronic ground state of the singly charged ion is stable, whereas all electronically excited states undergo unimolecular fragmentation. This can be deduced from the appearance energies of singly charged fragments in single-photon studies using a tunable wavelength [182]. There, the $C_3H_3^+$ and $C_4H_5^+$ fragments start to appear only at energies beyond 11.5 eV. This is indicative of the involvement of the D_1 state in the dissociation reactions leading to these fragments [183]. Other fragments all have appearance energies larger than the D_2 state [181, 183].

The dissociation of $C_4H_6^+$ into $C_3H_3^+$ and CH_3 requires an isomerization to occur, since the structure of the 1,3-butadiene cation does not include a CH_3 group. The decay mechanism for this fragmentation pathway is the following [181, 184]: The butadiene cation in the D_1 state first relaxes to the D_0 ground state, where, however, the excess energy is converted to excite vibrations in the molecule. This vibrational energy enables the molecular ion to overcome a barrier of 2.0 eV necessary for the isomerization to a 3-methylcyclopropene cation (which possesses a CH_3 group) as well as the barrier to separate the CH_3 group. The reaction $C_4H_6^+ \rightarrow C_4H_5^+ + H$ is less well studied, but it is known that the H-atom is more likely to be removed from one of the inner C-atoms [185].

In ref. [22], it was additionally observed that in each of the photoelectron energy distributions correlated with the $C_4H_6^+$, $C_3H_3^+$, and $C_4H_5^+$ ions a single ATI progression was present. The combs correlated with the $C_3H_3^+$ and $C_4H_5^+$ fragments were not shifted with respect to each other, but they were displaced with respect to the parent ion by the difference in IP between the D_0 and

D_1 states (when correcting for the field-induced Stark shifts). Therefore, in addition to the experimental demonstration of multiple ionization continua participating in SFI, these results also show that the $C_3H_3^+$ and $C_4H_5^+$ fragments are created, in significant quantities, only from the relaxation of the D_1 state, since otherwise multiple combs would overlap in the photoelectron energy distributions correlated with these species. Thus, a very clear scenario emerges, in which ionization to the electronic ground state of the ion D_0 results in the detection of a stable $C_4H_6^+$ parent ion along with the photoelectron, whereas the detection of a $C_3H_3^+$ or a $C_4H_5^+$ fragment indicates direct ionization to the first excited D_1 state of the ion. In particular, field-induced transitions between D_1 and D_0 in the remaining pulse after ionization (post-ionization excitation) play a negligible role, at least for the conditions of the experiment in ref. [22].

Channel-resolved experiments with aligned butadiene

Following the original CRATI experiment, channel-resolved measurements have been extended to a determination of the molecular-frame angular ionization rates in butadiene [49, 160], by laser-aligning butadiene molecules prior to ionization and measuring the $C_4H_6^+$ parent-ion and the $C_3H_3^+$ and $C_4H_5^+$ fragment-ion yields in dependence of the angle between the polarization direction of the SFI laser and the long molecular axis. To describe the relative orientation of butadiene molecules and the polarization direction of the laser field driving SFI, the angles θ and ϕ defined with respect to the molecular-frame coordinate system are used in this thesis, as shown in fig. 6.1b). The angle between the polarization vector and the long axis of the molecule is characterized by θ (polar angle). The angle ϕ denotes the azimuthal angle of the polarization vector in the molecular-frame coordinate system, where $\phi = 0°$ means that the polarization vector lies within the molecular plane.

In ref. [49], it was found that the D_0 and D_1 channels show significant differences in the orientation dependence of the ionization probability. The reason for this lies in the different Dyson orbitals (displayed in fig. 6.1a)), characterizing the initial bound electron states for the two channels. The D_0 and D_1 Dyson orbitals feature distinct nodal structures, which makes them well-suited for the investigation of the influence of nodal planes under otherwise identical conditions: The D_0 channel has two nodal planes, one in the $\hat{z}$-$\hat{x}$-plane (denoted as n_1) and the other in the $\hat{x}$-$\hat{y}$-plane (denoted as n_2). In the D_1 channel, on the other hand, only the nodal plane n_1 is present .

When the polarization vector of the SFI laser field lies within a nodal plane, the SFI rate is usually expected to be suppressed (see section 1.1). However, in ref. [49], the correspondence between ionization in the direction of a nodal plane and suppression of the ionization amplitude was found to be not as clear in the polyatomic molecule butadiene as for simpler molecules: Ionization for $\theta = 90°$ was suppressed in the D_1 channel, despite the absence of the nodal

plane n_2 in the corresponding Dyson orbital. In contrast, no pronounced influence of the nodal plane n_1 could be observed in the ionization amplitude for both channels. Again, this shows that assumptions well-established for smaller molecules may have to modified when studying more complex targets.

Goal: Channel-resolved measurement of rescattered electrons

The experiments described in the previous subsections have established that multiple ionization continua have to be considered in SFI and HHG when using molecular targets. However, as described in section 1.3, apart from direct ionization and high-harmonic emission, there is a third possible outcome for strong-field–driven systems, namely elastic or inelastic rescattering. For rescattering, the role multiple continua play has not been assessed so far. Due to the similarity with HHG, it seems clear that the multiple continua populated via SFI will also take part in rescattering. In ref. [68], the participation of multiple continuum channels has been suggested as a potential explanation for observed deviations in the alignment-angle and ellipticity dependence of non-sequential double ionization in CO_2 from the expectations for the HOMO. LIED experiments (see section 2.2) have so far ignored a possible influence of multiple channels onto the rescattered-electron distribution. However, as LIED is applied to more complex molecules, the role of multiple continua should be expected to increase.

To demonstrate that multiple channels are also relevant in rescattering, in the framework of the present thesis, a series of further channel-resolved measurements was performed in the 1,3-butadiene molecule. In contrast to the experiments presented in refs. [22, 49, 160], which were exclusively concerned with direct electrons or the total ion yield, here, the focus is on the rescattered electrons, measured in coincidence with various ion species.

Outline

The outline of part II of the thesis is as follows: After describing the employed experimental setup and the procedure for the analysis of the experimental data, the results from first preparatory measurements are presented, verifying the proper functioning of the experimental setup (chapter 7). In chapter 8, a detailed discussion of a channel-resolved experiment studying the rescattering behaviour of the photoelectrons for varying driving-pulse ellipticity is presented. The results of this experiment constitute clear evidence for the participation of multiple ionization continua in rescattering, since the two channels display a distinct behaviour in their dependence on the ellipticity. The differences are traced back to the structure of the D_0 and D_1 Dyson orbitals and the evolution of the created wave packet in the continuum.

This explanation relying on different shapes of the returning wave packets for different channels then leads the discussion to another assumption often

made in high-harmonic spectroscopy and LIED, namely that the returning wave packet retains no information on the structure of the state from which the electron was born. This implies, among other things, that the composition of the returning wave packet is independent of the relative orientation between the molecule and the laser polarization axis [54]. In the notation introduced in eq. (1.31), this means that, while the angular dependence of the ionization probability $S(\theta)$ is often taken into account in the theoretical modelling of experimental results, the return probability $R(\theta)$ is most often assumed to be independent of θ. This is, for example, the case in LIED experiments [18, 19, 71–75] (which rely heavily on theoretical modelling of the orientationally averaged DCS, see section 2.2) and many high-harmonic–spectroscopy studies [17, 113, 120, 122, 186–188].

A combined experimental and theoretical study performed to test this assumption of a θ-independent return probability is presented in chapter 10. There, it is exploited that the channel-resolved measurement of both direct and rescattered electrons in 1,3-butadiene allows the separation of all three steps of the three-step model. Using laser-aligned butadiene molecules along with a linearly polarized SFI laser field, the channel-resolved yields of direct and rescattered electrons were measured in dependence of the angle θ. Supported by numerical calculations, it is observed that the structure of the electron's initial Dyson orbital is not completely lost during continuum propagation but leads to differences in the return probability depending on the channel and the orientation of the molecule, thus influencing the rescattering (or recombination) process. The experiment requires the non-adiabatic alignment of butadiene molecules as well as the knowledge of the alignment distribution in order to transform the measured laboratory-frame to molecular-frame distributions (see section 5.3). Evaluation of the degree of alignment is presented in chapter 9.

Note that the experiments presented here rely crucially on the coincidence capabilities of the reaction microscope. Counting the yields of different ion species as was done in ref. [49] is not sufficient, since the kinetic-energy release for the fragments makes a distinction between the direct and rescattered regime impossible. Furthermore, using a reaction microscope makes it easier to discern the small signals of rescattered electrons from background, since additional filtering operations can be implemented, and acquiring three-dimensional momentum distributions allows for more sophisticated data evaluation protocols, such as an analysis of the return-energy dependence.

CHAPTER 7

Experimental Setup and First Results

7.1 Experimental Setup

The laser system

All experiments presented in this part of the thesis were performed using a laser system operating at 10 kHz (Aurora, Amplitude Technologies). The ∼7 fs-pulses created in a titanium:sapphire oscillator (Rainbow, Femtolasers) at a repetition rate of 76.6 MHz were – after being stretched to a duration of a few hundreds of picoseconds – amplified in a chain consisting of a regenerative and two multipass amplifiers. These amplifiers were pumped by a Nd:YAG laser (Etna, Thales). Before amplification, an acousto-optic pulse shaper (Dazzler, Fastlite) was used to adjust the spectral phase of the pulses to yield short output pulses. The same device also reduced the repetition rate to 10 kHz. After compression in a grating-based compressor, the system output pulses at a central wavelength of 800 nm with a pulse duration of ∼30 fs and ∼1.2 mJ of energy per pulse.

In order to perform the experiments presented in this part of the thesis, in particular those in chapters 9 and 10, a Mach-Zehnder interferometer was set up to implement the pump-probe scheme necessary for non-adiabatic alignment.

Beam path to the reaction microscope: 1290 nm-beam

As schematically depicted in fig. 7.1, the output from the laser system was split up using a 90 : 10 beam splitter, where the larger fraction was sent to

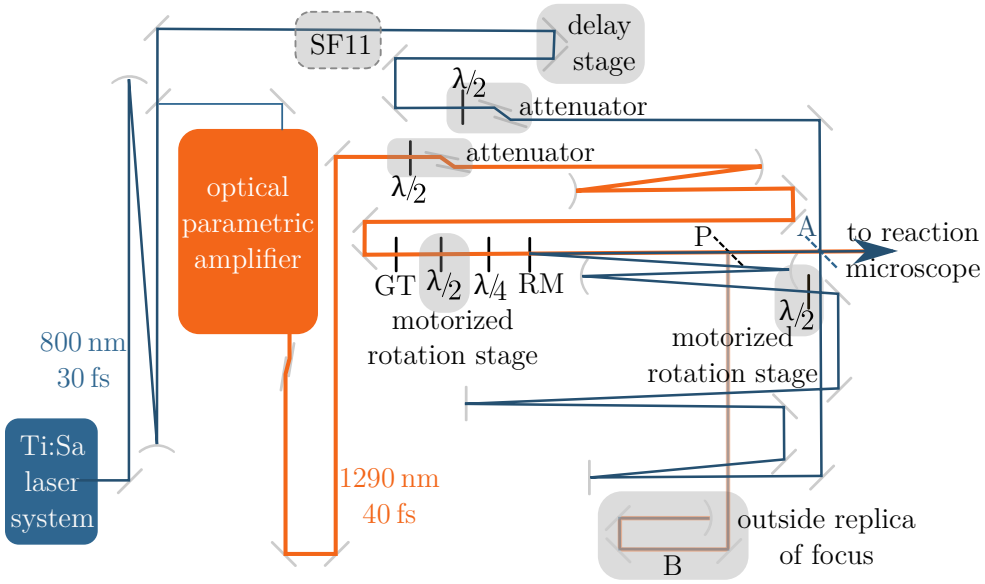

Figure 7.1: Experimental setup as used for the experiments in this part of the thesis (in particular in chapters 9 and 10). Abbreviations: RM - recombination mirror, GT - Glan-Taylor polarizer, $\lambda/2$ - half-wave plate, $\lambda/4$ - quarter-wave plate. The recombined beams could be sent to a replica of the focusing mirror in the reaction microscope on the outside by inserting a mirror at position P. When using the 800 nm-beam not for alignment but to drive SFI (in particular in chapter 8), the beam was sent directly to the reaction microscope by inserting a mirror at position A. In that case, the SF11 glass to stretch the 800 nm-pulses was removed.

a commercial optical parametric amplifier[1] (HE-TOPAS, Light Conversion). There, the fundamental input beam was converted in two stages utilizing β-Barium borate crystals into a signal beam with a wavelength of 1290 nm and an idler beam with a wavelength of 2190 nm. The signal beam was used to drive SFI in most of the experiments presented here. A conversion efficiency of ∼20 % was typically obtained, i.e. ∼2.5 W of energy were transformed into the signal and idler, with the majority of the energy going to the signal. The output power of the optical parametric amplifier was optimized by adjusting the second and third order dispersion of the fundamental using the pulse shaper. This is also expected to lead to close to transform-limited signal pulses. From the spectral width of the pulse, the pulse duration of the signal is estimated to be ∼40 fs.

[1] Also see page 144.

A dichroic mirror was used to separate the signal from the idler beam, and the signal beam was subsequently sent to an attenuator, which could be used to adjust the signal beam's energy per pulse. The attenuator consisted of the combination of a half-wave plate and Germanium plates serving as a reflective polarizer at the signal beam's wavelength.

The attenuated beam was then sent through a $3:1$-telescope to decrease the beam diameter. A smaller beam diameter before focusing leads to a larger focused beam in the interaction region with a longer Rayleigh range. This reduces intensity averaging, since the intensity varies less over the extent of the interaction volume with the molecular beam for a longer Rayleigh range. At the same time, the focusing also needed to be tight enough to reach the necessary peak intensities and to ensure that the focal volume of the 1290 nm-beam was contained in the fundamental beam used for alignment (see below).

Behind the telescope, the beam passed through a Glan-Taylor polarizer (GT in fig. 7.1) in order to clean up the polarization of the beam, making it very well polarized perpendicular to the table surface (s-polarization). The Glan-Taylor polarizer had an attenuation ratio of $1:10^6$, i.e. after passage through the polarizer the ellipticity ε was less than 10^{-3}.[2] Note that the polarizer, which consisted of 13.5 mm of calcite, did not significantly stretch the signal pulses, due to the low dispersion of the material at a wavelength of 1290 nm.

The beam then passed through a combination of a motorized half-wave plate and a fixed-in-space quarter-wave plate. This allowed the precise adjustment of the ellipticity of the beam while keeping the major axis of the polarization ellipse perpendicular to the table surface. Using just a quarter-wave plate would instead have additionally rotated the major axis of the ellipse away from the time-of-flight (z-)axis of the reaction microscope when varying the ellipticity.

Afterwards, the beam was recombined with the fundamental beam (see below) by passing through the backside of the fused-silica substrate of a mirror with a dielectric coating which reflected the fundamental (recombination mirror, RM in fig. 7.1). Note again that the 6 mm of fused-silica glass did not have any significant effect on the signal beam, due to the almost zero dispersion of fused silica at this wavelength. Also note that after the ellipticity of the beam had been cleaned and adjusted, no reflections at non-normal incidence occurred, which might have distorted the polarization of the beam. For the same reason, great care had been taken to place the quarter- and half-wave plates precisely perpendicular to the beam.

[2] This is because the attenuation ratio is defined in terms of the intensity, whereas the ellipticity is defined in terms of the electric field.

Beam path to the reaction microscope: 800 nm-beam

Following the beam path of the fundamental beam (when it was used as the alignment beam (chapters 9 and 10)) behind the beam splitter, the beam first passed through 35 mm of SF11 glass, before being sent to the delay stage. The glass stretched the fundamental pulses to a duration of 550 fs, which is suitable for alignment (also see page 108).

The delay stage was used to adjust the delay between the fundamental and the signal beam from the optical parametric amplifier. A retroreflector on top of the stage made sure that the incoming and outgoing beams were parallel, such that the beam pointing and thus the position of the focus did not change when moving the stage, which moved along a direction parallel to the beams.

Afterwards, the fundamental could be attenuated using a combination of a half-wave plate and a polarizer, and several additional mirror reflections were introduced to match the length of the beam paths in both arms of the interferometer. Using a 1 : 4-telescope, the beam diameter was subsequently decreased to make the focal spot size and the Rayleigh range larger than those of the 1290 nm-beam. This was done in order for the 1290 nm-beam to be completely contained in the 800 nm-beam over the extent of the interaction region, causing all interaction events to originate from aligned molecules.

The fundamental beam then passed through a motorized half-wave plate to rotate the polarization direction (and therefore the orientation of the alignment axis). Subsequently, the beam was reflected off the recombination mirror at a small angle of incidence, and the two beams (fundamental and 1290 nm) propagated colinearly towards the focusing mirror within the reaction microscope. Alternatively, a pick-off mirror (P in fig. 7.1) could be inserted behind the recombination mirror to replicate the focusing conditions present within the reaction microscope on the outside. This could be used to measure the beam profiles of the two beams in the focus using a beam-profiling camera and to find the temporal and spatial overlap of the beams (see section 9.1).

Some of the measurements in this chapter and in chapter 8 did not utilize the fundamental beam for alignment but as the SFI laser in a non–pump-probe configuration. In that case, the glass stretching the pulses was removed and the beam was picked off at position A in fig. 7.1 and sent directly to the reaction microscope, passing on its way through a combination of a half- and a quarter-wave plate to adjust the ellipticity.

7.2 PREPARATORY MEASUREMENTS

Choosing suitable extraction fields

The experiments presented in this part of the thesis required the detection of rescattered electrons generated using a driving wavelength of 1290 nm. This demands that the reaction microscope needed to be able to collect all

electrons with energies up to ∼90 eV, irrespective of the direction of their initial momentum vector. To this end, relatively high (electric and magnetic) extraction fields were needed. A high magnetic field strength facilitates the detection of electrons with large initial transverse momentum $|\vec{p}_{\mathrm{tr}}| = \sqrt{p_x^2 + p_y^2}$ (see section 4.2). To collect electrons with ∼90 eV that initially have only transverse and no longitudinal momentum p_z, according to eq. (4.9) and using the electron detector diameter of 75 mm, a magnetic field of 17 Gauss is required.[3] The electric field strength, on the other hand, needed to be high since the high magnetic field implies that the difference between the times of flight of the slowest (highest positive longitudinal momentum) and the fastest (highest negative longitudinal momentum) electrons is larger than the cyclotron period eq. (4.3) for a weak electric extraction field. This means that at several values of longitudinal momentum, nodes (see section 4.2) in the momentum distribution would make it impossible to determine the transverse momentum. Since the experiments performed here required accurate counting of electrons, integrating over large momentum regions, it was desirable not to have nodes in the distribution. This can be achieved by increasing the electric field strength, thereby 'shrinking' the distribution along the longitudinal direction in order for it to fit between two nodes – at the cost of reducing the longitudinal momentum resolution (see eq. (4.10)). Since the maximum applicable field was limited to ∼3.5 kV/m by the design of the electrical vacuum feedthroughs of the reaction microscope, a compromise was found by removing all nodes in one hemisphere of the electron distribution (the electrons with $p_z < 0$, i.e. the faster ones), while having a node cut through the distribution of electrons with $p_z > 0$ (at $p_z \approx 1$ a.u.). This made the second hemisphere unusable for the data analysis. However, for long enough pulses (where CEP effects are negligible), by symmetry all information is already contained in one of the hemispheres [189].

Detection of high-energy electrons

The purpose of the measurements reported in the following is to demonstrate the capabilities of the employed reaction microscope to detect the rescattered electrons. Figure 7.2 shows the electron kinetic-energy distribution of argon ionized by linearly and elliptically polarized driving pulses with a wavelength of 800 nm. The major axis of the polarization ellipse was parallel to the time-of-flight axis of the reaction microscope. The electric and magnetic extraction fields were 3.0 kV/m and 17 Gauss, respectively, and, as described above, only the momentum hemisphere with $p_z < 0$ was used for the energy distributions shown in fig. 7.2. Displayed are electrons in coincidence with the singly charged

[3] Note that the maximum energies attainable by rescattered electrons are, however, reached for close-to-backscattering geometries (see section 2.1), i.e. the highest-energy electrons will have a significant longitudinal component, since the driving-laser polarization vector points in the longitudinal direction.

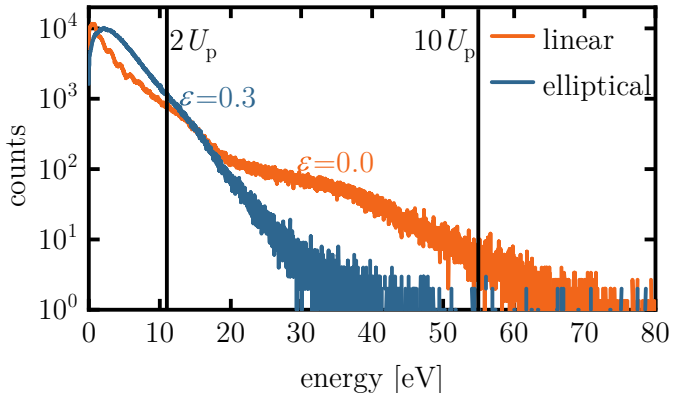

Figure 7.2: Photoelectron kinetic-energy spectra in argon ionized by 800 nm driving pulses with linear (orange) and elliptical (blue, ellipticity $\varepsilon = 0.3$) polarization. The introduction of a lateral component leads to a clear suppression of the signal of electrons with energies in the rescattering regime.

parent ion Ar^+, with the additional coincidence condition that the sum of the Ar^+ and electron momenta in the z-direction is smaller than 0.05 a.u..

For linear polarization, two distinct regions in the spectrum can be observed: At low energies, up to ∼11 eV, the direct electrons dominate the kinetic-energy distributions. The yield drops off rapidly with energy until, at ∼20 eV, the rate of decrease becomes more moderate, due to the onset of the plateau of rescattered electrons. At around 40 eV, the yield starts to drop off more quickly again. From the positions of the cut-offs for direct and rescattered electrons located at $2U_p$ and $10U_p$, respectively, U_p can be estimated to be ∼5.5 eV, leading, according to eq. (1.18), to an intensity of 9×10^{13} W/cm^2. Also note indications of ATI modulations visible at low energies, which are, however, not very pronounced due to intensity averaging in the focus and due to the degradation of the reaction microscope's momentum resolution owing to the high extraction fields.

For atomic targets, using elliptically polarized driving fields – and thus introducing a field component perpendicular to the initial direction of SFI during continuum propagation – is known to suppress rescattering due to the electron missing the core (see section 1.2). This is exactly what is observed for $\varepsilon = 0.3$ in fig. 7.2: The plateau seen for $\varepsilon = 0$ is gone for $\varepsilon = 0.3$, confirming that the plateau is indeed formed by the rescattered electrons – not by some background in the reaction microscope – and that the employed reaction microscope is able to reliably detect these higher-energy electrons.

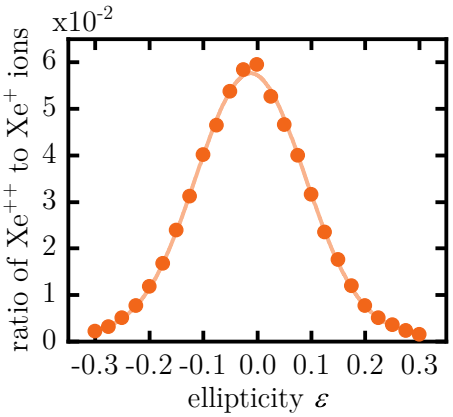

Figure 7.3: Ratio of single to (non-sequential) double ionization in xenon using a driving wavelength of 1290 nm. The data is described well by the shown Gaussian fit. Error bars arising from counting statistics are smaller than the utilized symbols.

Ellipticity calibration in xenon

The experiments presented in chapter 8 require fine adjustment of the driving laser's ellipticity. As a test of whether the experimental setup is able to control the ellipticity accurately, a measurement of the double to single ionization ratio of xenon was performed in dependence of the ellipticity, using a wavelength of 1290 nm. For the employed intensity ($<10^{14}$ W/cm^2), double ionization is expected to be predominantly non-sequential [190], i.e. highly sensitive to the ellipticity. The result is shown in fig. 7.3.

As can be seen, the detected ratio closely follows a Gaussian distribution, demonstrating that the combination of the Glan-Taylor polarizer, the half-, and the quarter-wave plate is capable of controlling the ellipticity very precisely, thus paving the way for the ellipticity-dependent measurements in chapter 8.

7.3 General results for the strong-field ionization of randomly-aligned 1,3-butadiene

Ion time-of-flight spectrum

We now proceed to analyse the time-of-flight spectrum for 1,3-butadiene, shown in fig. 7.4, which was recorded using a driving wavelength of 1290 nm, linear polarization, an intensity of 5×10^{13} W/cm^2, and a stagnation pressure of 20 bar of 0.03 % of butadiene seeded in helium.

In general, the time-of-flight spectra recorded with a reaction microscope provide information on the mass-to-charge ratio of the detected ions and additionally on the longitudinal momentum distribution. Sharp features point

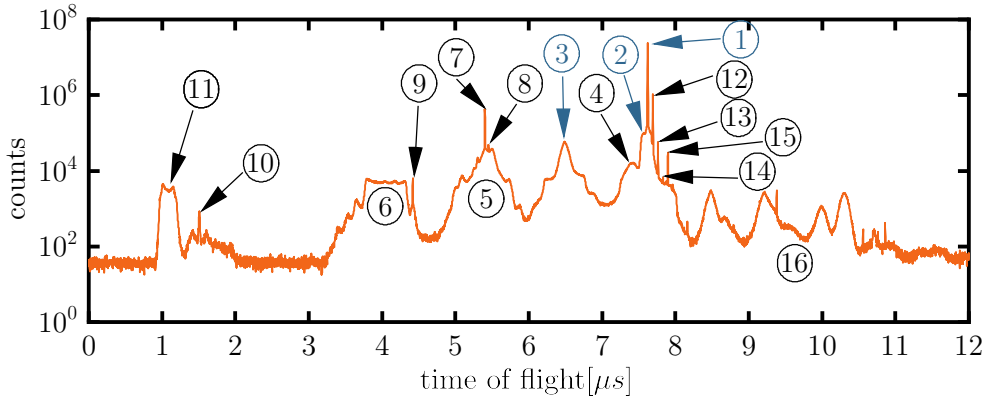

Figure 7.4: Ion time-of-flight spectrum for the SFI of butadiene using a driving wavelength of 1290 nm and an intensity of 5×10^{13} W/cm^2. All major features are labelled in the figure. The assignment of the labels can be found in table 7.1. Of particular importance for the present work are the $C_4H_6^+$ (1), $C_3H_3^+$ (3), and $C_4H_5^+$ (2) peaks, in coincidence with which photoelectron momentum distributions were studied.

1	$C_4H_6^+$	9	H_2O
2	$C_4H_5^+$	10	H_2^+
3	$C_3H_3^+$	11	H^+
4	$C_4H_3^+$	12	$^{13}CC_3H_6^+$
5	$C_2H_x^+$	13	$^{13}C_2C_2H_6^+$
6	CH_x^+	14	$^{13}C_3CH_6^+$
7	$C_4H_6^{++}$	15	$C_4H_6^+$He
8	$^{13}CC_3H_6^{++}$	16	cluster fragments

Table 7.1: Assignment of ion species to the labels given in fig. 7.4.

towards ions originating from the cool supersonic molecular beam which have not undergone dissociation. The width of these sharp peaks predominantly stems from SFI and subsequent acceleration in the laser electric field. Broad peaks indicate that the corresponding ion species was produced from background gas, which has a thermal velocity distribution corresponding to room temperature (see section 4.3), or that the detected ion species is a fragment from a dissociation process with kinetic-energy release.

The most important features for the experiments presented in this work are the $C_4H_6^+$, $C_4H_5^+$, and $C_3H_3^+$ peaks at times of flight of 7622 ns, 7563 ns and 6487 ns (labels 1-3 in fig. 7.4), respectively. As expected, the $C_4H_6^+$ parent-ion peak (label 1) is very sharp, since it cannot be broadened by kinetic-energy release from dissociation and indicating that most of the detected parent ions

originate from the molecular beam. Below the sharp $C_4H_6^+$ peak, there is a broader base, formed by the background butadiene gas in the chamber, which is two orders of magnitude less intense than the signal from the molecular beam.

Next to the main parent-ion peak towards longer times of flight (labels 12-15), there is a series of smaller peaks, which stem from the ionization of butadiene molecules with one, two, three, or all four C-12 atoms replaced by the heavier C-13 isotope, respectively.[4] Clearly, the peak with label 15 is too intense to be solely explained by the very rare $^{13}C_4H_6^+$ ion species. This is likely due to a second species populating the same time-of-flight interval, supposedly singly charged clusters consisting of one butadiene molecule and one helium atom, formed in the expansion when using high stagnation pressures. The complex peak structure observed between 8000 ns and 12 000 ns (label 16) likely stems from ionization and fragmentation of butadiene clusters, e.g. dimers.

Adjacent to the sequence of parent-ion peaks towards smaller times of flight, the $C_4H_5^+$ fragment peak is situated (label 2). It features a broader distribution due to the kinetic-energy release in the dissociation and is much less abundant than the parent ion. It is dominated by the dissociation of $C_4H_6^+$ ions in the first excited electronic state (see page 68). The time of flight of the broad peak with the label 4 corresponds to the $C_4H_3^+$ fragment and is the only other clearly identifiable fragment with four C-atoms.

The $C_3H_3^+$ peak has two contributions: a broad peak superimposed by an even broader plateau. As has been shown in ref. [147], the features originate from very different processes: The central peak is due to unimolecular dissociation of singly charged butadiene in the first excited state (again see page 68), as for the $C_4H_5^+$ fragment. These are the $C_3H_3^+$ fragments relevant in the experiments presented in the following chapters, and, thus, they have to be separated from the plateau contribution, originating from the Coulomb explosion[5] of doubly charged butadiene $C_4H_6^{++}$, which is achieved by relying on the kinetic-energy distribution of the fragments (see below).

The peak progression between 5000 ns and 6500 ns (label 5) is due to $C_2H_x^+$ fragments with $0 < x < 4$. Superimposed on this structured continuum are two sharp peaks (labels 7 and 8), corresponding to double ionization (without dissociation) of C_4H_6 and the most abundant isotope $^{13}CC_3H_6$, respectively. This can be deduced from the small width of the features, because the peak corresponding to the $C_2H_3^+$ fragment, which has the same mass-to-charge ratio as $C_4H_6^{++}$ and thus the same time of flight, would be broader. The sharp peak

[4] There are two stable carbon isotopes, ^{12}C and ^{13}C, whose abundance in nature is 98.9 % and 1.1 %, respectively [191].

[5] Coulomb explosion of a molecule occurs when electrons are removed from several centres in the molecule at once. These charged centres repel each other due to the Coulomb force, leading to a rapid dissociation of the molecule [192].

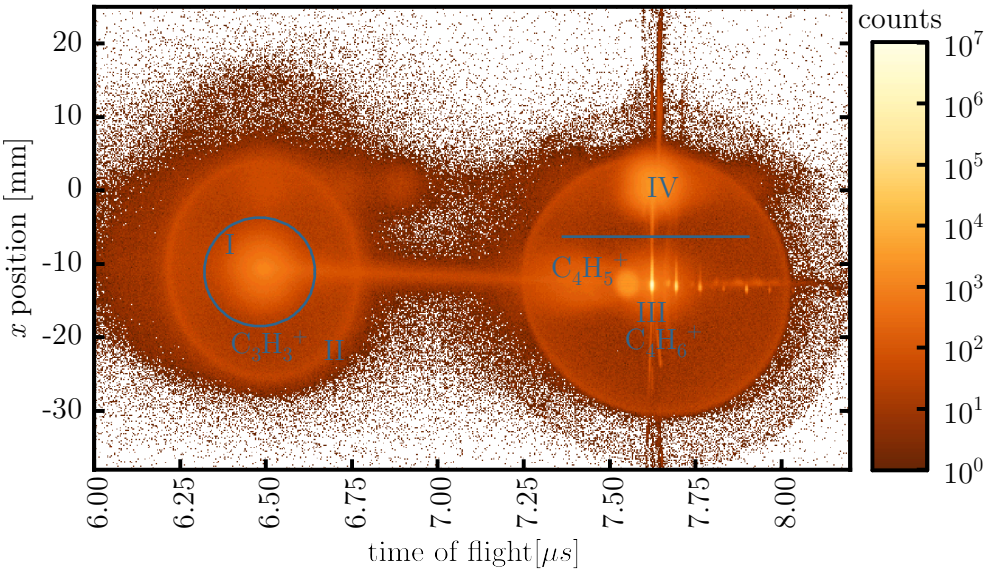

Figure 7.5: Ion yield as a function of the time of flight and the impact position on the detector along the direction of the molecular beam (x). Four regions are indicated: The region labelled with I stems from unimolecular dissociation of singly charged 1,3-butadiene molecules in the D_1 electronically excited state, whereas the ring denoted by II results from the Coulomb explosion of doubly charged parent ions. Contribution III results from parent ions from the molecular beam and contribution IV from parent ions from the background gas. The horizontal line between III and IV delimits the region used to spatially filter out background in the data analysis.

with label 9 and the broader feature below stem from water present in the molecular beam and as background in the reaction microscope, respectively.

The broad feature between 3600 ns and 4400 ns (label 6) can be attributed to the CH_x fragments with $0 < x < 4$. Peak 10 corresponds to H_2^+, which – according to the sharpness of the peak – appears to have been present in the molecular beam. The feature labelled with 11 is a double peak corresponding to H^+, which could stem from both the dissociation of molecular H_2 and fragmentation channels of butadiene. Note that no sharp peak corresponding to helium is observed – despite its high abundance in the molecular beam – due to its high IP of ∼25 eV.

Ion time-of-flight vs. impact position

In addition to pure time-of-flight spectra, the data from a reaction microscope allows one to separate the various contributions from different ion species and

their origin even better by additionally utilizing the impact position of the ions on the detector in the direction along the molecular beam (x-direction). Such a plot, displaying the yield in dependence of the ion time of flight and impact position, is shown – for the region relevant for the presented experiments – in fig. 7.5. As can be seen, in particular the contributions originating from background gas in the reaction-microscope chamber (region IV for the parent ion) and those stemming from the molecular beam (region III) can be well separated, compared to a time-of-flight-only spectrum, where they overlap. This is due to the fact that ions from the molecular beam initially have a velocity of $\sim$1750 m/s (see eq. (4.13)[6]) along the x-direction, which offsets the impact position on the detector. The offset depends linearly on the time of flight, according to eq. (4.8). Particles ionized from background gas, on the other hand, have no high initial directed velocity, and, thus, they hit the detector close to the centre.

For $C_3H_3^+$, it can be seen that the overlapping plateau and peak in fig. 7.4 (feature 3) form well-separated regions in fig. 7.5: The broad peak in fig. 7.4 corresponds to the accumulation close to the expected impact position for $C_3H_3^+$ ions due to the molecular-beam velocity (region I). In contrast, the plateau in fig. 7.4 translates into a ring around the same centre (region II) in fig. 7.5, whose large radius is due to the high kinetic-energy release in the Coulomb explosion. The line going from region I to the $C_4H_6^+$ peak is likely due to a small amount of vibrationally hot parent ions that dissociate into $C_3H_3^+$ fragments only during the travel time to the detector [181], whereas those that form the region I have already dissociated faster, such that they are influenced as $C_3H_3^+$ ions by the electric extraction field during the whole time of flight. The second large circle, on the right hand side of fig. 7.5, must also originate from a Coulomb explosion (due to the large kinetic-energy release), supposedly from parent-ion dimers.

Data selection

In the experiments presented in the following chapters, in addition to limiting the detected ionization rate to $\lesssim 0.2$ events per laser pulse, a range of filters has been applied to the data to reduce the contribution from background and false coincidences:

1. Only ions with a time of flight corresponding to $C_4H_6^+$, $C_4H_5^+$, or $C_3H_3^+$ have been considered for further data evaluation.
2. Of all remaining events, only those containing exactly one electron and one ion are selected (weak coincidence condition).
3. For events containing an ion with a time of flight corresponding to $C_4H_6^+$ and $C_4H_5^+$, only those with an ion impact position smaller than

[6]Note that the mass of helium atoms can be used as m_{gas} in eq. (4.13), due to the small fraction of butadiene molecules in the molecular beam.

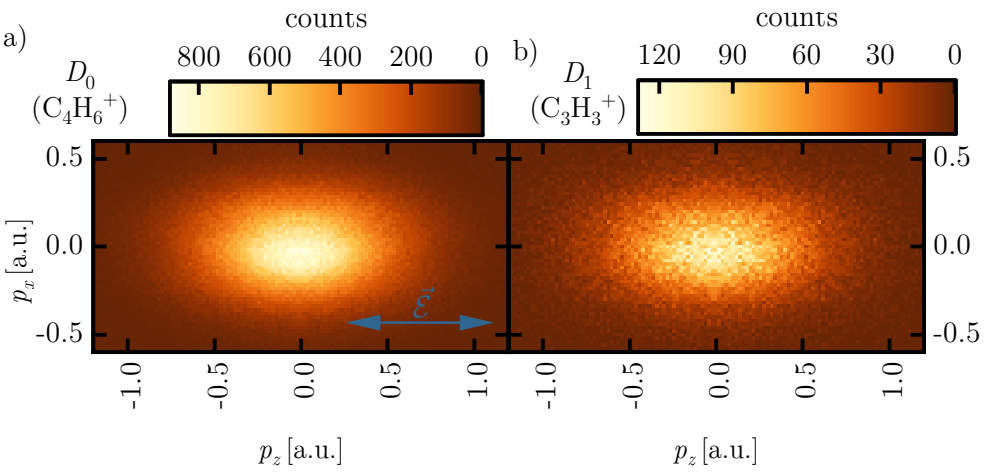

Figure 7.6: Projection of the electron momentum distribution onto the p_x-p_z-plane in coincidence with a) the $C_4H_6^+$ parent ion and b) the $C_3H_3^+$ fragment. Note the differing colour scales between a) and b). Apart from the overall yield, the distributions look qualitatively very similar.

−8 mm (i.e. only events originating from the molecular beam and not from the background) were processed further.

4. For events containing an ion with a time of flight corresponding to $C_3H_3^+$, the kinetic energy of the ion was calculated using all three momentum components. Only events with a resulting kinetic energy below 0.5 eV, i.e. only those originating from unimolecular dissociation of singly charged butadiene, were chosen.
5. Only events with $p_z < 0$, where p_z is the electron momentum component in the time-of-flight direction, were selected (see section 7.2).

Channel-resolved photoelectron momentum distributions

Figure 7.6 displays projections of photoelectron momentum distributions onto the p_x-p_z-plane, in coincidence with the $C_4H_6^+$ parent ion (a)) and the $C_3H_3^+$ fragment (b)) using linearly polarized driving pulses with a wavelength of 1290 nm and an intensity of 7×10^{13} W/cm^2. The polarization direction is along the z-axis. To display a full distribution, even though only data with $p_z < 0$ has been selected, a mirror image of the data with $p_z < 0$ is shown for $p_z > 0$. As described in the previous chapter, it has been established that electrons detected in coincidence with these ion species left the ion in the electronic ground state (D_0) and the first excited state (D_1), respectively. According to eq. (1.5), the electronic structure of the initial bound state should affect the shape of the continuum electron momentum distributions. However, in this

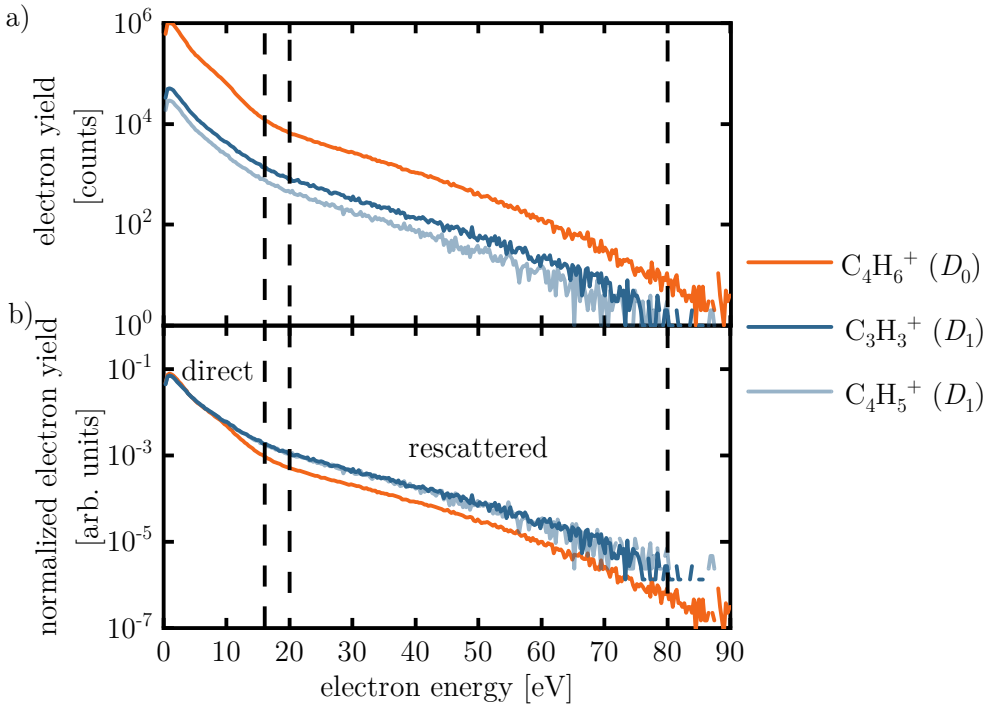

Figure 7.7: Photoelectron kinetic-energy distributions in coincidence with the $C_4H_6^+$ (orange), $C_3H_3^+$ (dark blue), and $C_4H_5^+$ (light blue) ion species, resulting from the ionization of 1,3-butadiene with a linearly polarized 1290 nm driving pulse, a) as measured and b) with each distribution normalized to the same total yield. The dashed lines delimit the regions of direct and rescattered electrons, ranging from 0 to $2U_p$ and from $2.5U_p$ to $10U_p$, respectively. The normalized distributions in coincidence with the $C_3H_3^+$ and $C_4H_5^+$ fragments agree very well with each other but are significantly different from the distribution in coincidence with the $C_4H_6^+$ parent ion.

side-by-side comparison, apart from the overall yield, which is much higher in a) than in b), no differences can be discerned. Both distributions are elongated along the laser polarization axis. The projections onto the p_y-p_z-plane (not shown) look identical to the distributions shown in fig. 7.6, which is expected due to the cylindrical symmetry around the laser polarization axis.

Channel-resolved photoelectron kinetic-energy distributions

From the three-dimensional momentum distribution, the kinetic-energy distribution can be calculated. This is shown for the $C_4H_6^+$, $C_3H_3^+$, and $C_4H_5^+$ ion species in fig. 7.7, using a wavelength of 1290 nm, linearly polarized driving

pulses, and an intensity of $5 \times 10^{13}\,\mathrm{W/cm^2}$. Figure 7.7a) displays the data as measured, where the abundance of the various ion species is reflected in the relative yield of the respective coincident electron distribution.

Qualitatively, the three kinetic-energy distributions display a very similar behaviour: The recollision plateau is less distinct than for the atomic target (fig. 7.2), rather forming a tail which drops off slowly with increasing energy. This is likely a consequence of the structured orbitals of butadiene, leading to a wider and more complex lateral momentum distribution of the electron, whereas the classical cut-off laws were derived for electrons with zero lateral momentum. This leads to smoother transitions between the different regimes of the electron distributions. This behaviour is typical for molecular targets [71, 193, 194]. Consequences of the orbital structure for the momentum and kinetic-energy distributions will be discussed in great detail in the following chapters. The lack of ATI structure in the distributions in fig. 7.7 can be attributed to tighter employed focusing conditions compared to fig. 7.2, leading to more intensity averaging within the focal volume and thus to smearing of the ATI peaks.

For better comparison of the electron energy distributions measured in coincidence with different ion species, in fig. 7.7b) they are normalized to the same number of total counts, thus removing the influence of the differences in the overall probability for the occurrence of a certain ion species. It can be seen that the normalized distributions in coincidence with the $C_3H_3^+$ and $C_4H_5^+$ fragments are identical, which confirms the observations from previous CRATI experiments that they both tag the same channel (D_1) for the present experimental conditions. Furthermore, they differ significantly from the distribution coincident with the parent ion (which tags the D_0 channel). Therefore, the differences in the electron's initial state for the two channels result in observable differences in the final kinetic-energy distribution of the electron: The normalization renders the D_0 and D_1 distributions very similar in the low-energy regime of the direct electrons, but in the regime of rescattered electrons the yield is then significantly higher for the distributions corresponding to the D_1 channel than for the one corresponding to the D_0 channel. This means that a larger fraction of the released electrons is rescattered into the high-energy portion of the spectrum in the D_1 than in the D_0 channel. This observation will be further expanded on in chapters 8 and 10.

Due to the fact that the electron distributions in coincidence with the $C_3H_3^+$ and $C_4H_5^+$ fragments show identical behaviour, when the integrated yield of direct/rescattered electrons for the D_1 channel is presented in the following chapters, it is the sum of electrons counted in coincidence with $C_3H_3^+$ and $C_4H_5^+$.

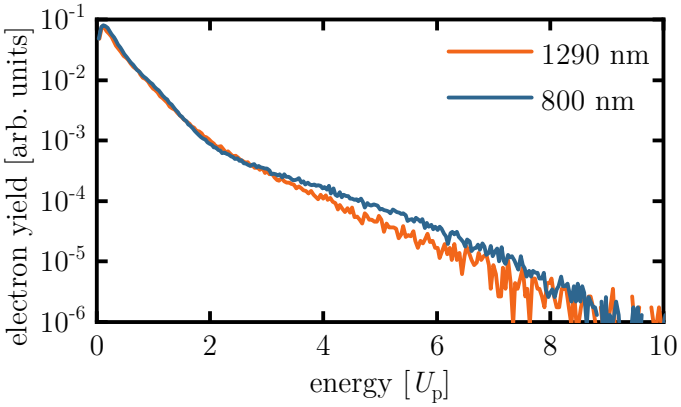

Figure 7.8: Comparison of photoelectron kinetic-energy spectra for driving wavelengths of 800 nm (blue) and 1290 nm (orange). The energy axis is given in units of U_p in order to better compare the two wavelengths. The yield has been scaled such that the direct electrons overlap as well as possible. The electron signal in the rescattering regime is then clearly reduced for a wavelength of 1290 nm compared to 800 nm, as expected.

Comparison of rescattering at 800 nm and 1290 nm

In fig. 7.8, a comparison of electron energy distributions (recorded in coincidence with the parent ion and with linear polarization) for wavelengths of 800 nm and 1290 nm is shown. The energy is given in units of the respective U_p. The corresponding intensities were 1.2×10^{14} W/cm^2 (800 nm) and 7×10^{13} W/cm^2 (1290 nm). While the general shape is very similar for the two spectra, the electron yield in the rescattering regime is significantly reduced for a wavelength of 1290 nm compared to 800 nm. This is expected due to the increased electron continuum excursion time and thus increased wave-packet spreading for the longer wavelength (see page 30).

Despite the decreased yield, the majority of the experiments presented in the following chapters were performed at a wavelength 1290 nm, for the following reasons: 1) For 800 nm and the intensity given above, the excursion distance of the electron given by eq. (1.20) is ∼9 Å, which is on the order of the size of the molecule (∼6 Å), i.e. the electron never really propagates far away from the molecules before rescattering. This could potentially complicate the interpretation of observations, since the three-step model may be invalid in this regime. In comparison, for a wavelength of 1290 nm and the intensity given above, the excursion distance is 18 Å. 2) A longer driving wavelength decreases the Keldysh parameter ($\gamma = 0.8$ for 800 nm compared to $\gamma = 0.6$ for 1290 nm (using the above intensities)), meaning that experiments performed at 1290 nm are deeper in the tunnelling regime. 3) The longer excursion time for

the longer wavelength is expected to enhance the sought-after effects due to an increased time span for wave-packet spreading. 4) The longer wavelength is closer to what is typically used in LIED experiments [18, 19, 71, 72], increasing the similarity of the experiments presented here to – and thus their relevance for – LIED studies.

CHAPTER 8

Channel-Resolved Rescattering

8.1 Introduction

After the verification that the presented setup can be used to detect both direct and rescattered electrons while at the same time distinguishing two continuum channels in 1,3-butadiene, we now proceed with measurements of the dependence of the channel-resolved yield of rescattered electrons on the driving laser's ellipticity. The goal of this study is to demonstrate that multiple continua can be distinguished in rescattering by their different dependence on the ellipticity. The explanation for the observed differences will rely on the different shapes of the initial molecular orbitals for the two channels, a topic which will then be further studied in the experiment presented in chapter 10 using aligned molecules.

Ellipticity dependence of recollision-induced processes in molecules

The ellipticity dependence of strong-field processes has been subject of many studies in the past decades: Early, it has been recognized that, in atomic systems, increasing the driving laser field's ellipticity leads to a suppression of HHG and rescattering [8, 60, 66, 195]. The origin of the suppression lies in the lateral component of the driving field for $\varepsilon \neq 0$, which shifts the electron away from its parent ion and thus prevents the interaction step in the three-step model (see section 1.2).

For molecules, however, the situation is less clear. First differences in the ellipticity dependence of the high-harmonic yield between atoms and molecules

were observed in refs. [196, 197]. Around the same time, Bhardwaj et al. studied the ellipticity dependence of the non-sequential double ionization yield in unaligned benzene molecules [67]. Using a driving-laser wavelength of 1.4 μm, it was observed that the non-sequential double ionization yield did not peak at zero ellipticity but at a value of $\varepsilon \approx 0.1$, leading to a local minimum at $\varepsilon = 0$, in contrast to atomic targets where the maximum yield is obtained for $\varepsilon = 0$. The fact that the HOMO of benzene possesses nodal planes was used to explain this observation. As described in section 1.1, when the polarization vector of the driving field lies within a nodal plane of the molecular orbital from which the electron is released, ionization from the lobes on either side of the plane leads to destructive interference of the continuum wave packet within the nodal plane. This means that, when ionizing along a nodal plane, there will be a minimum in the continuum wave packet, which is assumed to persist during continuum propagation, leading to a low returning wave-packet density for a linearly polarized field. Only by pushing the minimum away from the centre with a lateral component of the laser field, i.e. using an elliptically polarized driving field, a significant portion of the electron wave packet can return to the core to rescatter inelastically [51]. This effect was assumed to survive averaging over the random molecular orientations in ref. [67]. This study constitutes the first example where persistence of structural information from the initial orbital of the released electron was proposed to explain experimental findings.

A similar local minimum in the ellipticity dependence was observed by Kanai et al. for HHG in aligned N_2 molecules [198]. They also found that the high-harmonic yield decreased more rapidly with increasing ellipticity for CO_2 and O_2 molecules aligned parallel with respect to the laser polarization than for perpendicular alignment. Both observations were, however, attributed to destructive interference [199] and the size of the valence orbital, respectively, in the recombination step rather than to the first two steps of the three-step model.

A very extensive study of the ellipticity dependence of the high-harmonic yield for different molecular alignment angles in N_2 and CO_2 was performed by Mairesse et al. [45]. Their findings are similar to those of Kanai et al., however, they rationalize their results in terms of different widths of the continuum wave packet in momentum space for different alignment configurations due to the structure of the HOMO. In addition, they also uncover subtle shifts of the centre of the Gaussian-shaped ellipticity-dependence distributions due to the different return direction of the electron for elliptically polarized driving fields compared to the linear case, which effectively slightly changes the angle between the returning electron and the molecule for different ellipticities.

Recently, Alharbi et al. presented a study of the ellipticity dependence of HHG in a series of larger ring-type molecules [200]. Despite all of the employed molecules possessing nodal planes, deviations from the behaviour expected for atomic targets only occurred in those molecules where the angular ionization probability, according to numerical calculations, is not strongly suppressed

when ionizing along a nodal plane. The differences were, again, explained with the structure of the continuum wave packet. Their results indicate that, at least for randomly aligned samples of molecules, the influence of nodal planes in the electron's initial orbital on the ellipticity dependence of recollision-induced processes may depend on the molecular species in a non-straightforward way. Further studies where the ellipticity dependence of a recollision-induced process in molecular targets played a role include refs. [64, 68, 115, 201, 202].

Chapter outline

In this chapter, the channel-resolved ellipticity dependence of the rescattering yield in randomly-aligned butadiene is studied. The yield of elastically rescattered electrons is determined directly by counting the number of electrons in the rescattering tail, in contrast to other related studies, which focus either on the high-harmonic or the non-sequential double ionization yields. A comparison of the ellipticity dependence of two different continuum channels in butadiene reveals clear differences in their rescattering behaviour. This directly establishes, for the first time, the participation of multiple strong-field continua in elastic rescattering. From the ellipticity dependence of the rescattered-electron yield for different return energies, which can be derived from the full three-dimensional momentum distribution acquired with the reaction microscope, further evidence for this proposition arises. These observations also lead to a rationalization – similar to some of the experiments mentioned above [45, 67, 200] – in terms of the nodal structure of the HOMO and HOMO-1 persisting into the continuum and influencing the returning wave packet.

8.2 RESULTS

Experimental parameters

The setup used for the experiments presented in this chapter is described in detail in section 7.1. However, only either the signal beam from the optical parametric amplifier, centred at a wavelength of 1290 nm, or the fundamental beam (wavelength 800 nm) was used for a given measurement, i.e. all presented measurements were single-beam experiments. Note that, in the fundamental beam path, the mirror at point A in fig. 7.1 was inserted and the glass was removed, resulting in a pulse duration of ∼30 fs. The pulses in the 1290 nm-beam had a duration of ∼40 fs. Each of the beam paths featured a combination of a motorized half-wave plate and a fixed quarter-wave plate in order to adjust the ellipticity without altering the major axis of the polarization ellipse, which was always aligned along the time-of-flight direction of the reaction microscope.

Butadiene was supplied with a stagnation pressure of 20 bar (800 nm) or 6 bar (1290 nm), seeded with a fraction of 0.03 % in the helium carrier gas. Using low fractions of butadiene prevents clustering of the molecules during the

expansion and keeps the ionization rate low (which is necessary for coincidence detection, see chapter 4) by limiting the number of molecules within the laser focus in spite of the high pressures. The detected ionization rate was $\lesssim 0.2$ events per laser pulse. The electric and magnetic extraction fields in the reaction microscope were $3.0\,\mathrm{kV/m}$ and 17 Gauss, respectively.

From the position of the transition from the direct electrons to the rescattering tail in the electron energy distribution (not shown but very similar to fig. 7.7), U_p is estimated to be 7 eV (800 nm) and 11.5 eV (1290 nm). According to eq. (1.18), this corresponds to peak intensities of $1.2 \times 10^{14}\,\mathrm{W/cm^2}$ and $7 \times 10^{13}\,\mathrm{W/cm^2}$, respectively, for $\varepsilon = 0$. Note that adjusting the ellipticity in the way described above keeps U_p constant for different ε, whereas the peak intensity I decreases as $I(\varepsilon) \propto (1+\varepsilon^2)^{-1}$.

For the data presented in this chapter, the coincident photoelectron momentum and photoion momentum and time-of-flight information was acquired as described in section 7.3, for different values of the ellipticity. In total, for the 800 nm data, 62 h of acquisition took place, yielding 3.2×10^8 laser pulses for each of the seven ellipticity values. The data for 1290 nm consists of 4.0×10^8 laser pulses for each of the ten data points, obtained during a total of 110 measurement hours. To minimize systematic effects due to variations of the laser parameters over time, the ellipticity was changed to a different value drawn in random order from the pool of chosen ellipticity values every two minutes, and data was acquired for each of the ellipticity values over many such short measurement intervals.

Ellipticity dependence of the rescattering yield

The distributions obtained for each wavelength, channel, and ellipticity value were first normalized to the same number of total counts, as exemplified in fig. 7.7b). Subsequently, for each of the normalized distributions the yields of the direct electrons M^D in the interval $[0,2]\cdot U_\mathrm{p}$ and of the rescattered electrons M^R in the interval $[2.5,10]\cdot U_\mathrm{p}$ were counted, in each case using the U_p corresponding to the employed wavelength and intensity. Integrating over the yield of rescattered electrons in the normalized spectra amounts to obtaining a probability for an electron to be rescattered into the $[2.5,10]\cdot U_\mathrm{p}$ energy range given that it has already been released into the continuum, i.e. it factors out the ellipticity-dependent ionization probability (which is expected to vary with ellipticity due to the different peak intensities present for different ellipticities). In this chapter, this normalized rescattering yield will be denoted as *rescattering probability*, even though it does not include rescattered electrons overlapping with the direct electrons, i.e. mostly those scattered in forward direction. The rescattering probability obtained in this way constitutes, in fact, a lower bond for the actual rescattering probability including all rescattered electrons.

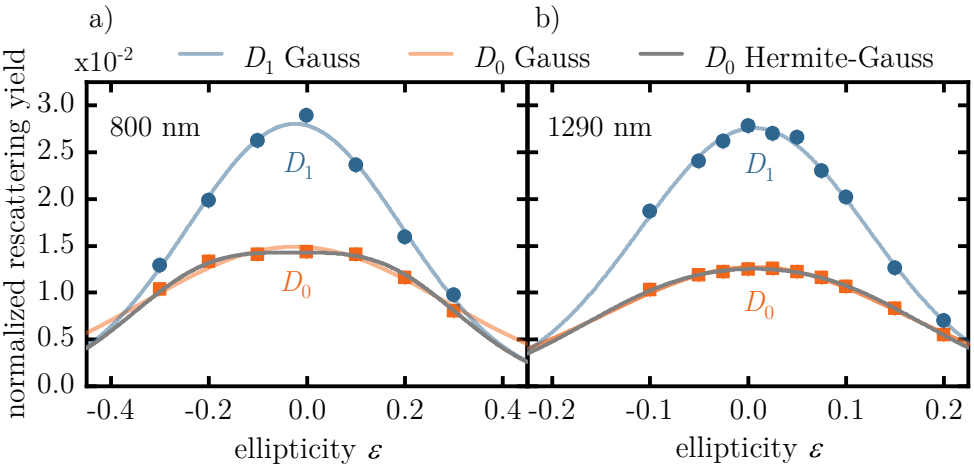

Figure 8.1: Channel-resolved normalized rescattering yield as a function of the driving field's ellipticity ε for a) 800 nm and b) 1290 nm, as obtained by integration over the rescattering tail from 2.5 to $10U_\mathrm{p}$ in normalized spectra (see fig. 7.7b)) for the various ellipticities. The orange rectangles and blue circles indicate the experimental data points for the D_0 and D_1 channels, respectively. Error bars, given by the counting statistics, are smaller than the used symbols. Also shown are Gaussian fits to the data in the D_1 channel (blue curve) and Gaussian and Hermite-Gaussian (see eq. (8.2)) fits to the data in the D_0 channel (orange and grey curve, respectively). Note the different scales on the ε-axis between a) and b).

The ellipticity dependence for this rescattering probability is shown in fig. 8.1 for the two channels and both wavelengths. In all cases, the dependence seems to follow a Gaussian function reasonably well. However, for the D_0 channel and a wavelength of 800 nm, the region around zero ellipticity appears to be slightly too flat to be precisely described by a Gaussian distribution, reminiscent of a local minimum as observed in refs. [45, 67]. This will be quantified using fits below.

Generally, for linear polarization, the rescattering probability is clearly higher in the D_1 compared to the D_0 channel. However, in the D_1 channel, the rescattering probability also drops off significantly faster with ellipticity than in the D_0 channel. This is true for both employed laser wavelengths. Comparing the two wavelengths, the decrease in the rescattering probability with ellipticity is much faster for 1290 nm than for 800 nm. The difference between the two wavelengths is larger than the difference between the two channels.

Gaussian fits

To quantify the widths of the shown distributions further and since they all seem to display a close-to-Gaussian behaviour, fig. 8.1 also shows a fit to the data using a Gaussian function

$$f_1(\varepsilon) = A \cdot \exp\left(-\log 2 \cdot \left(\frac{\varepsilon - \varepsilon_0}{\Delta\varepsilon}\right)^2\right), \tag{8.1}$$

where $\Delta\varepsilon$ is given by the ellipticity value at which the rescattering probability is reduced to 50 % of the value at $\varepsilon = \varepsilon_0$. A is a scaling factor, and ε_0 allows for a slight miscalibration of the zero ellipticity.[1] A, ε_0, and $\Delta\varepsilon$ are free parameters for the fit to the respective D_1 channel, and A and $\Delta\varepsilon$ are free parameters for the fit to the respective D_0 channel with ε_0 taken from the fit to the D_1 channel for the same wavelength. The reason for this is that the data in the D_1 channel displays a dependence closer to Gaussian than the D_0 channel, which is slightly flattened out around $\varepsilon = 0$. Thus a Gaussian fit to the D_1 data should result in a more accurate determination of the zero ellipticity, which is the same for both channels.

A comparison of the obtained best-fit values is shown in table 8.1. The difference in $\Delta\varepsilon$ between D_0 and D_1 is significant for both wavelengths, yielding higher values for the width $\Delta\varepsilon$ in the D_0 channel.

	800 nm		1290 nm	
	D_0	D_1	D_0	D_1
$\varepsilon_0[\times 10^{-3}]$	-	-2.4 ± 0.4	-	6 ± 2
$\Delta\varepsilon$	0.36 ± 0.02	0.258 ± 0.005	0.179 ± 0.003	0.138 ± 0.002
$A[\times 10^{-2}]$	1.49 ± 0.04	2.80 ± 0.04	1.27 ± 0.01	2.76 ± 0.02

Table 8.1: Resulting fitting parameters for the Gaussian fits shown in fig. 8.1, according to eq. (8.1). For the fits to the D_0 channel, ε_0 was not a free parameter (see text), hence no value is given. The width $\Delta\varepsilon$ is significantly larger in the D_0 than in the D_1 channel for both wavelengths.

Hermite-Gaussian fits

In addition to the Gaussian fit eq. (8.1), another fit to the data using the function

$$f_2(\varepsilon) = \left(A + B \cdot \left(-\log 2 \cdot \left(\frac{\varepsilon - \varepsilon_0}{\Delta\varepsilon'}\right)^2\right)\right) \cdot \exp\left(-\log 2 \cdot \left(\frac{\varepsilon - \varepsilon_0}{\Delta\varepsilon'}\right)^2\right) \tag{8.2}$$

[1] Note that the distribution is expected to be symmetrical about zero ellipticity, since unaligned molecules are used.

is shown in fig. 8.1 to account for deviations from Gaussian behaviour. Functionally, increasing the value of $|B|$ with $B < 0$ while keeping both A and $\Delta\varepsilon'$ constant, increases the width of the curve and leads to a flattening around and eventually to a local minimum at ε_0. $\Delta\varepsilon'$ thus generally no longer corresponds to the ellipticity value where the rescattering probability drops to 50 % compared to zero ellipticity but rather to the width the curve would have for $B = 0$. The actual 50 %-width $\Delta\varepsilon$ can be calculated numerically from A, B, and $\Delta\varepsilon'$.

To perform the Hermite-Gaussian fits, the fitting parameters A and $\Delta\varepsilon'$ were first initialized using the values for A and $\Delta\varepsilon$ from table 8.1 with $B = 0$, i.e. those obtained from the purely Gaussian fit. This provides reasonable starting values and thus a better convergence for the case where B is an additional free fit parameter. ε_0 was kept fixed at the previously determined values for all fits. The fits according to eq. (8.2) to the data in the D_0 channel then resulted in the best-fit values shown in table 8.2. For both wavelengths, for the D_1 channel $B \sim 0$ is obtained, i.e. the functional dependency of the data is described well by a Gaussian.[2] The calculated 50 %-width is also shown in table 8.2.

For the D_0 channel, the resulting values for B are appreciable compared to A, especially in the case of 800 nm, with $|B/A| \approx 1$ and 0.6 for a wavelength of 800 nm and 1290 nm, respectively. This confirms that the D_0 channel deviates from a Gaussian dependency and is better described by the modified function. In the case of 1290 nm, this function is still very similar to Gaussian and only slightly flattened around zero ellipticity, whereas for 800 nm the Hermite-Gaussian fit function displays a shallow local minimum at $\varepsilon = \varepsilon_0$. In both cases, the 50 %-width $\Delta\varepsilon$ obtained from the Hermite-Gaussian fit for the D_0 channel is still significantly larger than the $\Delta\varepsilon$-values obtained for the D_1 channel (see table 8.1).

	800 nm	1290 nm
$\Delta\varepsilon'$	0.225 ± 0.009	0.133 ± 0.002
$A[\times 10^{-2}]$	1.43 ± 0.02	1.255 ± 0.004
$B[\times 10^{-2}]$	-1.4 ± 0.1	-0.76 ± 0.03
$\Delta\varepsilon$	0.35 ± 0.01	0.179 ± 0.003

Table 8.2: Resulting fitting parameters $\Delta\varepsilon'$, A, and B for the Hermite-Gaussian fits to the D_0 channel shown in fig. 8.1, according to eq. (8.2), and the calculated 50 %-width $\Delta\varepsilon$.

[2] However, it should be noted that in the case of the underlying data being approximately Gaussian, the errors for both B and $\Delta\varepsilon'$ become substantial, since for not too large B the broadening of the function eq. (8.2) is much more marked than the flattening around zero, which is why B and $\Delta\varepsilon'$ can compensate each other over a range of values.

Return-energy dependence of the width of the ellipticity curves

Using the full three-dimensional photoelectron momentum information available from the reaction microscope – instead of the energy distribution as in the previous subsections – makes it possible to extract the channel-resolved rescattering probability additionally in dependence of the electron's return energy (see section 2.1).

In detail, the following protocol was used for the extraction of the return energy–dependent data: For a chosen return momentum $|\vec{p}_{\mathrm{ret}}|$, all electrons within a $\pm 5\,\%$ interval $[|\vec{p}^{\,\mathrm{min}}_{\mathrm{ret}}|, |\vec{p}^{\,\mathrm{max}}_{\mathrm{ret}}|]$ ($|\vec{p}^{\,\mathrm{min}}_{\mathrm{ret}}| = 0.95 \cdot |\vec{p}_{\mathrm{ret}}|$, $|\vec{p}^{\,\mathrm{max}}_{\mathrm{ret}}| = 1.05 \cdot |\vec{p}_{\mathrm{ret}}|$) were counted for this return momentum. Then, the vector potentials $\vec{A}^{\,\mathrm{min}}_{\mathrm{ret}}(\varepsilon)$ and $\vec{A}^{\,\mathrm{max}}_{\mathrm{ret}}(\varepsilon)$ at the instant of rescattering were calculated for $|\vec{p}^{\,\mathrm{min}}_{\mathrm{ret}}|$ and $|\vec{p}^{\,\mathrm{max}}_{\mathrm{ret}}|$, respectively, according to eqs. (1.11), (1.23) and (1.24), for each of the employed ε. Note that the direction of the vector potential is along the z-axis only for $\varepsilon = 0$, whereas for $\varepsilon \neq 0$ it also has a component in the x-direction. For each electron acquired with the ellipticity set to ε, it is then decided if its (final) momentum value lies within the volume in momentum space whose boundaries are formed by the spherical shells centred around $\vec{A}^{\,\mathrm{min}}_{\mathrm{ret}}(\varepsilon)$/ $\vec{A}^{\,\mathrm{max}}_{\mathrm{ret}}(\varepsilon)$ and with radius $|\vec{p}^{\,\mathrm{min}}_{\mathrm{ret}}|$/$|\vec{p}^{\,\mathrm{max}}_{\mathrm{ret}}|$, respectively. If this is the case and the measured final momentum vector additionally lies outside a sphere centred around zero momentum and with radius $\sqrt{2m_{\mathrm{e}} \cdot 2U_{\mathrm{p}}}$ (where the signal from the direct electrons overlaps the rescattered electrons), the electron is counted as rescattering yield for the corresponding return energy $E_{\mathrm{ret}} = |\vec{p}_{\mathrm{ret}}|^2/2m_{\mathrm{e}}$.

In fig. 8.2, the yield of rescattered electrons in dependence of the ellipticity is plotted for two different return energies ($E_{\mathrm{ret}} = 1.0U_{\mathrm{p}}$ and $2.2U_{\mathrm{p}}$) and for the two wavelengths. Also shown are the Gaussian (eq. (8.1)) and, in the case of D_0, Hermite-Gaussian (eq. (8.2)) fits to the data. The fits were performed as for the integrated data (fig. 8.1) using the fixed values given in table 8.1 for ε_0. As for the integrated data, for the D_1 channel, employing a Hermite-Gaussian fit function resulted in $B \sim 0$ in all cases, i.e. the D_1 data is best described by a Gaussian distribution. This is also true for the D_0 channel in the case of a wavelength of 1290 nm and a return energy of $1.0U_{\mathrm{p}}$. From fig. 8.2c), it can be seen that the ellipticity-dependent rescattering yields at a return energy of $1.0U_{\mathrm{p}}$ and for a wavelength of 1290 nm qualitatively display a similar behaviour as the corresponding integrated data for both channels (fig. 8.1b)). For a return energy of $2.2U_{\mathrm{p}}$ (fig. 8.2d)), the deviations from Gaussian behaviour are more pronounced. This is also true for the case of a wavelength of 800 nm (fig. 8.2b)), where, however, the non-Gaussian shape is already evident from the data at a return energy of $1.0U_{\mathrm{p}}$ (fig. 8.2a)). There, and even more so at the higher return energy, a clear local minimum can be seen around zero ellipticity, which is well described by the Hermite-Gaussian fit function. Note that this is the first time such a dip, which is analogous to the one found in ref. [67] in non-sequential double ionization, has been observed directly in the yield of elastically rescattered electrons.

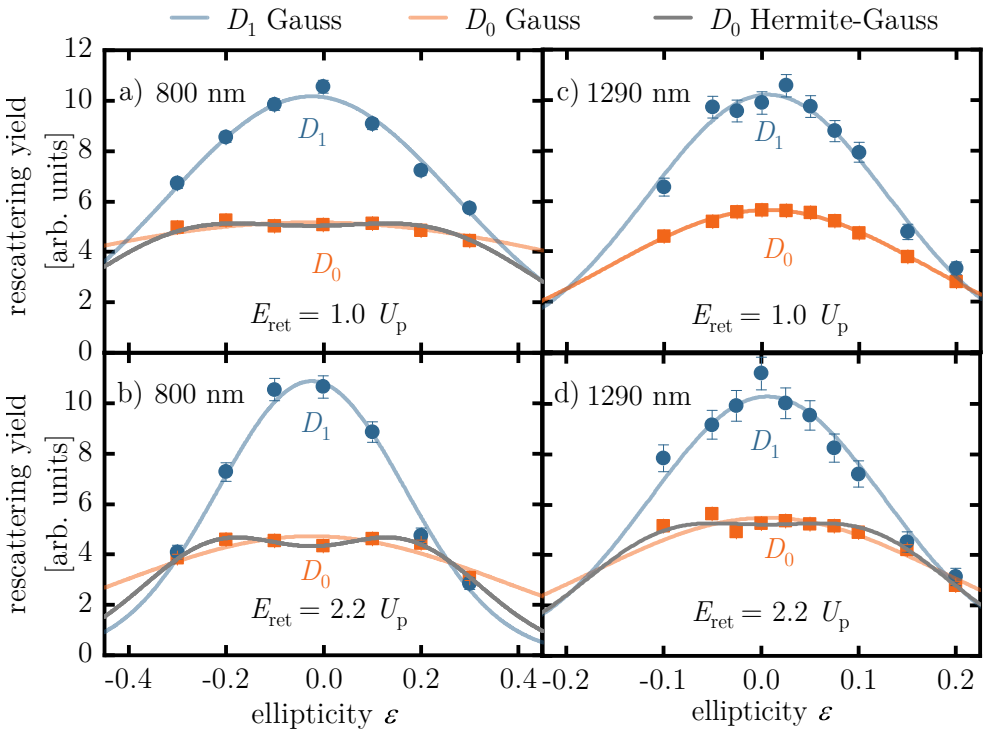

Figure 8.2: Channel-resolved, arbitrarily scaled rescattering yield as a function of the driving field's ellipticity ε for a),b) 800 nm and c),d) 1290 nm, for return energies of $E_{ret} = 1.0U_p$ (a) and c)) and $E_{ret} = 2.2U_p$ (b) and d)), respectively. The orange rectangles and blue circles indicate the experimental data points for the D_0 and D_1 channels, respectively. Error bars are given by counting statistics. Also shown are Gaussian fits to the data in the D_0 and the D_1 channels (orange and blue curves, respectively) and, for a), b), and d), Hermite-Gaussian (see eq. (8.2)) fits to the data in the D_0 channel (grey curves). Note the different scales in the ε-axis between a),b) and c),d).

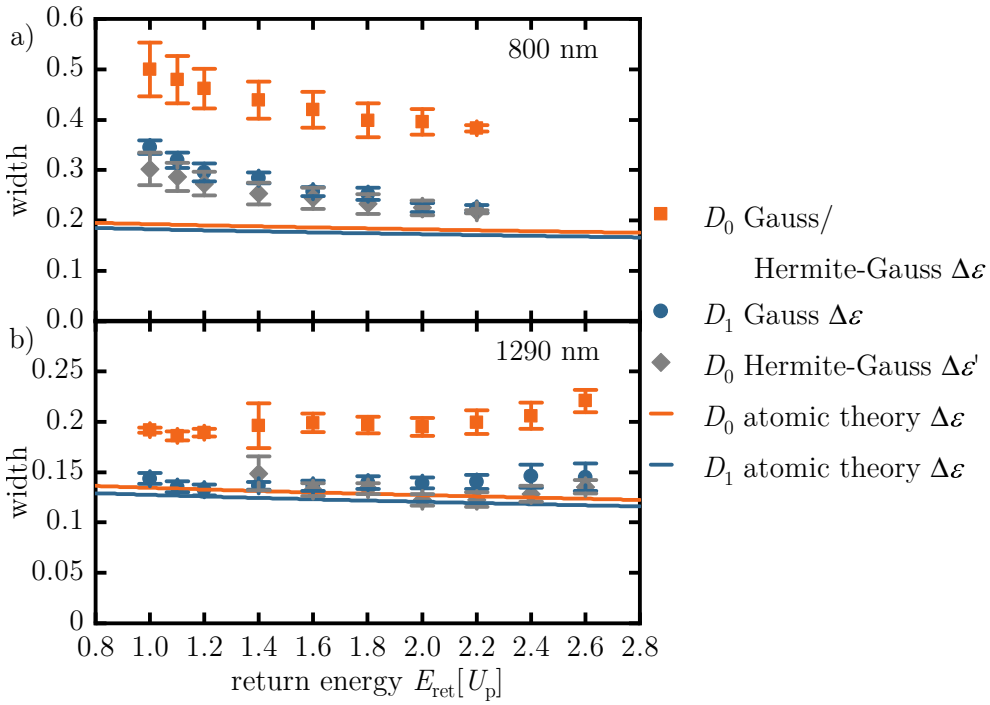

Figure 8.3: Dependence of the width of the ellipticity curves (as shown exemplarily in fig. 8.2) on the return energy E_{ret} for a wavelength of a) 800 nm and b) 1290 nm. The 50 %-width $\Delta\varepsilon$ (orange squares (D_0) and blue circles (D_1)) was determined using a pure Gaussian for the D_1 channel and using a Hermite-Gaussian fit for the D_0 channel (except for the lowest three E_{ret}-values in the case of 1290 nm, where $B \sim 0$ was obtained from the Hermite-Gaussian fit and thus purely Gaussian fits were used). Additionally, the width $\Delta\varepsilon'$ from the Hermite-Gaussian fit is shown where applicable (grey diamonds). The shown error is given by the uncertainty resulting from the fits. Also shown are the expectations for atoms with IPs corresponding to the D_0 (orange curves) and D_1 (blue curves) channels as obtained from the simple model eq. (1.29). Note that the scale on the vertical axis is different between a) and b).

In fig. 8.3, the width as obtained from a Gaussian fit eq. (8.1) or from a Hermite-Gaussian fit eq. (8.2) is shown in dependence of the return energy E_{ret}. The fits were performed as before.[3] The shown confidence intervals are determined by the errors from the fit. Also included in the figure is the expected dependence for atomic targets as obtained from eq. (1.29).

As can be seen, the model predicts an almost constant and only very slightly decreasing dependence of the width on the return energy, with the width for the D_0 channel being slightly larger than for the D_1 channel due to the lower IP. Also for the experimentally determined widths the $\Delta\varepsilon$-values obtained for D_0 are generally significantly larger than those for the D_1 channel. However, the difference in width is much larger than what would be expected from theory for atoms based solely on the difference in IP. This is due to the experimental $\Delta\varepsilon$-values for the D_0 channel being significantly larger than the theory predictions, whereas for the D_1 channel the atomic-model predictions agree better with the experimental observations, in particular for a wavelength of 1290 nm. The ratio of the widths obtained experimentally for D_0 and D_1 is larger for a wavelength of 800 nm than for 1290 nm, such that the D_0 channel at a wavelength of 800 nm deviates the most from the atomic theory. Thus, for the D_0 channel, the increase in width with decreasing wavelength is larger in the experiment than what would be expected for atomic targets.

Regarding the dependence on the return energy, both channels display the same trend, which is however different for the two different wavelengths: For 1290 nm, the return-energy dependence is almost constant, conforming to the predictions from the atomic theory, with possibly a slight increase at the highest return energies. For 800 nm, on the other hand, there appears to be a decrease of the width with increasing return energy. The qualitatively different behaviour of the return-energy dependence between the two wavelengths is in conflict with the simple atomic model, which predicts the dependence on the return energy to be the same for all wavelengths and IPs, differing only in an overall scaling factor (see eq. (1.28)).

Interestingly, the width $\Delta\varepsilon'$ (i.e. the width one would obtain if the distributions were not flattened around zero but purely Gaussian instead ($B = 0$)) from the Hermite-Gaussian fit to the data in the D_0 channel agrees, within the error bars, with the width $\Delta\varepsilon$ obtained for the D_1 channel and is also closer to the model predictions for atoms. This indicates that the deviations from Gaussian behaviour and the increased width are related phenomena.

[3] Note that fewer points are shown in the 800 nm case than for a wavelength of 1290 nm, since the measurement at the shorter wavelength included higher ellipticity values for which the highest return energies cannot be attained (see fig. 1.1b) and eq. (1.25)).

8.3 DISCUSSION

Effect of the molecular-orbital structure on rescattering

To explain the observed differences between the channels, the interpretation pioneered in ref. [67] is applied, namely that rescattering is influenced by the shape of the continuum wave packet launched by SFI. Directly following ionization, the continuum wave packet is determined by the shape of the Fourier transform of the Dyson orbital of the respective channel (see eq. (1.5)). In particular, the initial width of the continuum wave packet in momentum space derives from the width of the projection of the Fourier transform of the Dyson orbital perpendicular to the driving-laser polarization at the instant of ionization. The larger the initial width is in momentum space, the more rapidly the wave packet will laterally diffuse during the subsequent continuum propagation. The presence of a nodal plane in the Dyson orbital close to the laser polarization direction additionally increases the lateral spread of the continuum wave packet, since a nodal plane forces an electron to have lateral momentum, as zero lateral momentum is forbidden by symmetry (see page 10). In addition, the node itself also persists into the continuum, leading to a minimum of the initial electron wave-packet density at the nodal plane.

The initial lateral momentum structure of the wave packet is then expected to influence the rescattering process, because it dictates the density of the returning wave packet interacting with the ion core. The more the wave packet spreads during continuum propagation, the more diffuse it will be upon return to its parent ion, and thus the lower the probability for an interaction will be. At the same time, a greater amount of diffusion will also lead to a larger overall size of the returning wave packet and, therefore, to a higher ellipticity required to drive the wave packet completely away from the target in order to suppress rescattering. Additionally, a minimum in the electron density due to a nodal plane may also survive continuum propagation, since all electrons have momentum pointing away from the nodal plane, leading to deviations from a Gaussian-like returning wave packet.

This reasoning shows how different shapes of the Dyson orbitals – in particular the presence of nodal planes – may lead to differences in the dependence of the rescattering probability on the ellipticity. The results from this chapter will be rationalized in terms of these considerations in the following.

Differences between D_0 and D_1

As just explained, nodal planes lead to an increased width of the returning wave packet and possibly to deviations from a Gaussian shape, due to the acquired initial lateral momentum. The Dyson orbital in the D_0 channel possesses one more nodal plane compared to the D_1 channel (see fig. 6.1b)). Apparently, when averaging over the random ensemble of molecules, this leads to a slower decrease of the rescattering yield with increasing ellipticity and to

larger deviations from Gaussian behaviour for the D_0 than for the D_1 channel. In particular, this also manifests itself in the local minimum at $\varepsilon = 0$ observed for the D_0 channel in the return energy–dependent data (fig. 8.2), especially for high return energies. For the D_1 channel, on the other hand, the shape can be described well by a Gaussian in all instances. For a perpendicular configuration of nodal planes, as in the D_0 channel in butadiene, there are many more relative orientations of the molecule with respect to the laboratory system where a nodal plane affects the relevant $\widetilde{p}_x$-momentum component, compared to an orbital with a single nodal plane. This explains why the influence of the nodal planes is stronger in the D_0 than in the D_1 channel.

To confirm the effect of orientational averaging on the resulting initial lateral momentum distributions, which, as explained above, are expected to govern the returning wave packets, a simple model calculation has been performed, which is very similar to the approach presented in ref. [45]: For a given molecular orientation of butadiene with respect to the laser polarization direction, the initial lateral momentum distributions have been calculated using eq. (1.5). The orbitals used in this equation were the Fourier transforms of the HOMO (D_0) and HOMO-1 (D_1) of butadiene, calculated for simplicity using the Hückel method [203]. The employed field strength was the same as in the experiment at a wavelength of 1290 nm.[4] Orientational averaging has been performed using a Lebedev grid of 9th order [204] to average over the Euler angles θ' and ϕ' (see page 51), whereas averaging over χ' has been done by uniform sampling in steps of $\pi/6$.

The resulting orientationally averaged distributions for the two channels are shown in fig. 8.4a). The lack of complete rotational symmetry can be attributed to an insufficient number of averaged orientations. Nonetheless, a qualitative comparison to the experimental data is possible. Figure 8.4b) shows cuts through the distributions as indicated in a). According to eq. (1.27), the ellipticity dependencies are related to these distributions by linear rescaling. As in the experiment, the effect of the nodal planes is much more pronounced for the D_0 than for the D_1 channel: A clear minimum can be observed at $p_x = 0$ for the D_0 channel, whereas the D_1 channel is close to Gaussian and only slightly flattened around $p_x = 0$. The simple model calculation thus confirms the experimental observation that, when taking into account averaging over all molecular orientations, the ellipticity dependence of the D_1 channel is close to Gaussian despite the presence of the nodal plane n_1. The fact that in the simulations the effect of the nodal planes is slightly more visible than in the experiment for both channels can be attributed to the simplicity of the model, which neglects, for example, intensity averaging within the focal volume.

[4] Using the field strength of the experiment at 800 nm yields qualitatively the same results.

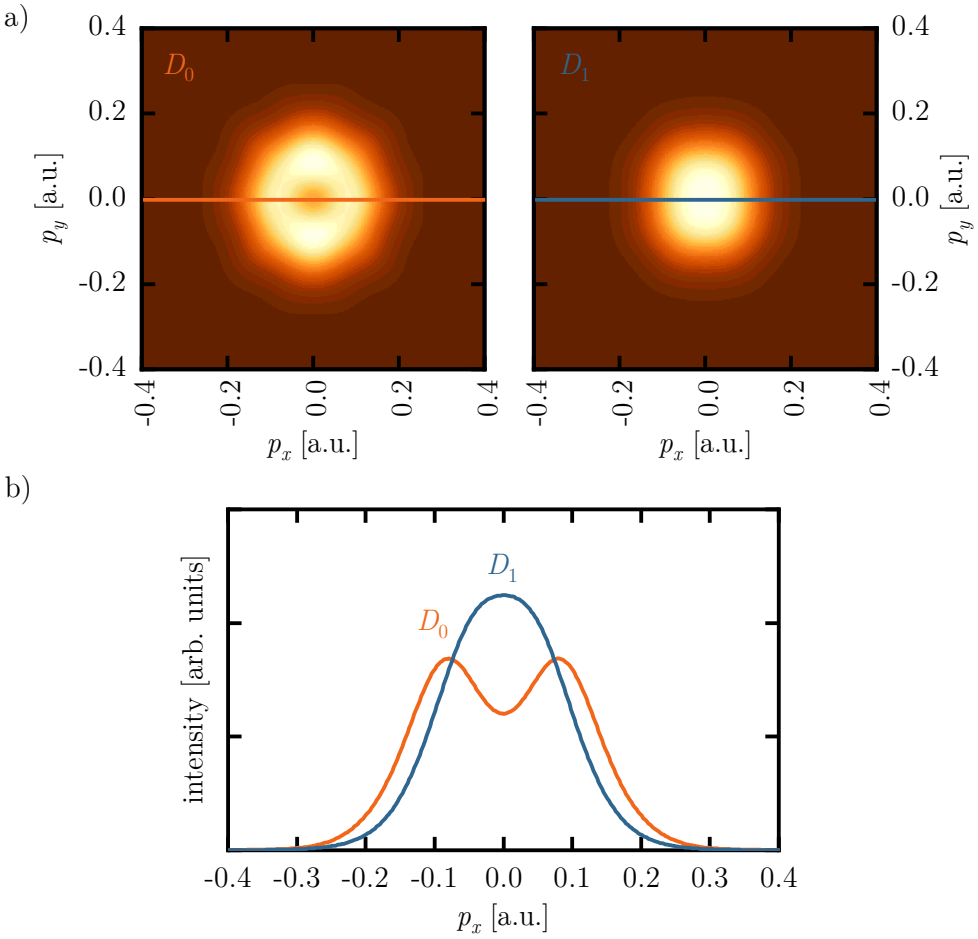

Figure 8.4: a) Simulated initial momentum distribution according to eq. (1.5), including averaging over all molecular orientations, for the D_0 channel (left hand side) and the D_1 channel (right hand side). b) Cuts through the distributions shown in a) along the p_x-axis, as indicated by the horizontal lines. The distributions have been normalized to the same number of total counts.

Deviations from atomic predictions and return-energy dependence

Both the D_0 and the D_1 channel feature nodal planes, which are expected to lead to an increase of the width of the returning continuum wave packet compared to atomic targets with the same IP when the polarization vector lies within or close to one of the nodal planes n_1/n_2. Evidently, for the D_0 channel, this leads to an overall higher width when averaging over the randomly aligned ensemble compared to the predictions for atomic targets. This is the same observation that has been made previously for the ellipticity dependence of HHG in molecules whose HOMO features nodal planes [45, 198, 200]. The D_1 orbital of butadiene has only one nodal plane and also features directions where the electron is delocalized over an extended region in space, leading to a small lateral spread of the continuum wave packet. This explains why, when averaging over all orientations, the D_1 channel agrees better with the atomic model and does not display a pronounced increase in width, as the D_0 channel does. These observations demonstrate that, in a randomly aligned ensemble, molecular orbitals featuring a nodal plane may still conform closely to atomic behaviour. However, for molecules with several nodal planes, deviations from atomic predictions, as well as from Gaussian behaviour, are expected to become important.

Concerning the data shown in fig. 8.3, for a wavelength of 800 nm the width of the curves describing the ellipticity-dependent rescattering probability decreases with the return energy, contrary to the expectations for atoms, where, for the long trajectory, an almost constant dependence is expected.[5] In general, the return-energy dependence arises from the different excursion time for different return energies (see fig. 1.1), which alters the time span available for the electron wave packet to evolve laterally on the one hand and for the lateral component of the electric field to deflect the electron on the other [205]. While the overall differences in the width of the ellipticity curves can be explained by nodal planes, it is unclear how nodal planes would influence the dependence on the return energy, which is expected to be universally given by eq. (1.28). Consistently, the two channels display the same dependence on the return energy for each of the two wavelengths. However, when comparing the two wavelengths, the behaviour is qualitatively different. Since the dependence on the return energy is closer to the expected behaviour at 1290 nm, a possible explanation for the differing behaviour at 800 nm may be an invalidation of the three-step model itself due to the insufficient excursion length (see page 87). However, note that also in ref. [200], using a wavelength of 1800 nm, qualitative differences were observed for the return-energy dependence of the width of the ellipticity-dependent high-harmonic yield from atomic expectations. The origin of such deviations may be an interesting subject of future investigations.

[5] Note that for the short trajectory, dominating HHG but of minor importance for rescattering, a decrease with return energy is predicted [205].

Another observation is that the deviations from Gaussian behaviour in the D_0 channel become more pronounced for the shorter wavelength and, for both wavelengths, with increasing return energies. Both, decreasing the wavelength and increasing the return energy, lead to shorter excursion times. This shows that longer propagation times in the continuum lead to a closer-to-Gaussian behaviour, which is in agreement with the common expectation that non-planar wavefronts are washed out during continuum propagation.

Conclusion

The main observation taken from the data presented in this chapter is that the two separated channels differ significantly in their rescattering behaviour. More specifically, the rate of decrease in the rescattering probability with ellipticity is lower for the D_0 than for the D_1 channel for both wavelengths and in both the integrated and the return energy–resolved data. In addition, the functional dependency on the ellipticity is described well by a Gaussian function for the D_1 channel, whereas the data in the D_0 channel can be better described by a flattened Gaussian in most cases. In particular, this is the case for the return energy–dependent data. These differences observed for the rescattered electrons between the D_0 and the D_1 channel constitute a direct demonstration that the multiple ionization continua released via SFI are relevant for rescattering. The observed channel dependence in rescattering may have implications for future LIED experiments, when applying the technique to more complex polyatomic molecules than presently is the case, since contributions from other orbitals than the HOMO are non-negligible for many larger molecules and the different rescattering behaviour of different channels may complicate the interpretation of such experiments.

The arguments used for the explanations of the observations in this chapter – similarly to refs. [45, 67, 200] – suggest that, contrary to what is often assumed, information from the electron's initial bound state is retained during the second step of continuum propagation. The influence of the structure of the electron's initial orbital may invalidate further assumptions made in the analysis of LIED experiments (see section 2.2), in particular the assumption of a uniform angular return probability (i.e. the density of the returning electron wave packet being proportional to the ionization probability for all molecular orientations) and the assumption of the returning electron's wavefront being asymptotically planar over the extent of the parent-ion target. Indication of a non-planar returning wavefront have already been observed in the present chapter in the form of deviations from Gaussian behaviour for the ellipticity-dependent rescattering probability, in particular the local minimum around zero ellipticity. However, the fact that the deviations from Gaussian behaviour in the D_0 channel are larger for a wavelength of 800 nm than for a wavelength of 1290 nm also seems to indicate that the effects may not be as severe for the long driving wavelengths typically used in LIED experiments. In chapter 10,

a channel-resolved experiment – using aligned molecules and thus reducing the influence of angular averaging – will be presented, which demonstrates the orbital imprint in laser-induced rescattering in a different way and which explicitly falsifies the assumption of a uniform angular return probability.

CHAPTER 9

Strong-Field Ionization of Aligned Butadiene

9.1 Non-adiabatic alignment of butadiene

Polarizability and inertia tensors

The elongated shape of 1,3-butadiene suggests that the molecule possesses a significant anisotropy in the polarizability. Therefore, it is eligible for laser-induced molecular alignment. Indeed, a degree of alignment characterized by $\langle \cos^2 \theta' \rangle = 0.69$ has been achieved for butadiene in ref. [160] using non-adiabatic alignment.

The principal axis of the inertia tensor with the lowest eigenvalue (i.e. the long axis) lies within the molecular plane and is rotated with respect to the axis through the first and fourth C-atom by about 4°. The remaining two principal components are similar in magnitude, and, thus, butadiene can be approximated as a prolate symmetric-top molecule (see section 5.1). This approximation works well for low alignment laser intensities and becomes more inaccurate as the alignment laser intensity increases [49]. Within the symmetric-top approximation, the coordinate systems spanned by the principal axes of the polarizability and inertia tensors are identical [156, 160]. Therefore, the long axis of the butadiene molecules aligns along the alignment-laser polarization direction. Treating butadiene in the symmetric-top approximation renders the simulations used for the determination of the experimental alignment distribution (see section 5.2) more manageable (although codes for asymmetric-top molecules do exist [206]). The relevant principal values for the inertia and

polarizability tensors within the symmetric-top approximation are given in table 9.1.

	perpendicular	parallel
rotational constant in GHz	4.2	41.1
polarizability in $Å^3$	6.2	12.2

Table 9.1: Rotational constants and polarizabilities parallel and perpendicular to the long axis for butadiene in the symmetric-top approximation. Values taken from ref. [160].

Experimental conditions

For the experiments presented in this and the following chapter, the goal was to non-adiabatically align butadiene molecules prior to the initiation of the strong-field processes driven by 1290 nm-pulses from an optical parametric amplifier (see section 7.1). To this end, as explained in chapter 5, two requirements need to be fulfilled: 1) The pulse driving SFI has to be preceded by another pulse launching a rotational wave packet in the butadiene molecules and 2) the rotational temperature of the molecules must be small.

The intensity of the alignment pulse has to be low enough not to lead to ionization and to stay within the symmetric-top approximation [49], thus in the 10^{11} W/cm^2 to 10^{13} W/cm^2 range (compared to $>10^{13}$ W/cm^2 to drive SFI and rescattering). The pulse duration must be short enough to remain in the non-adiabatic regime (much smaller than the rotational periods corresponding to the values given in table 9.1) but long enough to transfer a significant amount of angular momentum in the kick from the alignment pulse [156]. Since the excitation of the rotational wave packet occurs non-resonantly, the wavelength of the alignment pulse is not important. Therefore, here the fundamental pulses with a wavelength of 800 nm stretched to a duration of 550 fs are used (see section 7.1).

To reach low rotational temperatures, a high stagnation pressure was applied before the supersonic expansion through the nozzle into vacuum. To be able to apply such high pressures – despite the vapour pressure of butadiene being only 2.4 bar at room temperature – butadiene was seeded using a low fraction of 0.03 % in helium, as before.

Optimization of the temporal and spatial overlap

The spatial overlap between the alignment and the SFI laser beams was first achieved roughly by making sure that the beams overlapped at the recombination mirror and in the replicated focus outside the reaction microscope (part B in fig. 7.1). The interval for the temporal overlap was first narrowed down using a fast photodiode and an oscilloscope and then more precisely via

sum-frequency generation in a β-Barium borate crystal: When scanning the delay, within a small interval (given by the pulse duration of the fundamental) a turquoise sum-frequency signal was visible by eye behind the crystal in addition to the blue/orange second-harmonic signals from the fundamental beam and the beam from the optical parametric amplifier. The time zero τ_0 was then taken to be the centre of this interval. This method was accurate enough to see an enhancement of the ionization rate (for the polarizations of the pump and probe beams being parallel) compared to the SFI laser beam alone, when delaying the SFI laser by $\tau_a = 58\,\text{ps}$ with respect to τ_0 (i.e. moving to the point of maximum alignment in the first half revival). This enhancement is due to the higher ionization probability in the parallel configuration compared to randomly aligned molecules (see fig. 10.2). The enhancement of the signal has been monitored in real time by using a shutter wheel in the alignment beam path and comparing the number of ion counts with and without the alignment beam, evening out fluctuations of the count rate due to fluctuations in the power or duration of the 1290 nm-pulse. The spatial and temporal overlap was then optimized by maximizing the measured enhancement of the ionization rate.

9.2 CHARACTERIZATION OF THE ALIGNMENT DISTRIBUTION

Experimental scans

As detailed in section 5.2, the alignment distribution of the molecular ensemble prepared in the interaction region can be estimated by comparing an experimental angular and an experimental delay scan to numerical simulations of the non-adiabatic alignment process for different input parameters. In the present case, the quantity N_{avg} is the yield of singly charged parent ions, denoted by S_{avg}. The scans used for the procedure are shown in fig. 9.1. They were performed under the same conditions as and directly after the long measurement in which the channel-resolved data presented in this and the following chapter was acquired. They can, therefore, serve to quantify the alignment present during the long measurement.

Figure 9.1a) shows an experimental delay scan around the half revival, where the parent-ion yield was measured as a function of the delay between the alignment and SFI laser beams with $\alpha' = \alpha'_0 = 0°$, where α' denotes the angle between the polarizations of the alignment and SFI laser beams. The displayed yield is the sum of five consecutive scans ranging from 44.9 ps to 71.3 ps in steps of 330 fs. In total, each delay step contains 2.5×10^5 laser pulses. The shown error bars of the data points are given by counting statistics.

As can be seen fig. 9.1a), the parent-ion yield starts to increase at a delay of around 55 ps, before it reaches a maximum at $\sim 58\,\text{ps}$. This corresponds to the point of maximum alignment τ_a, where the enhancement in the ionization rate

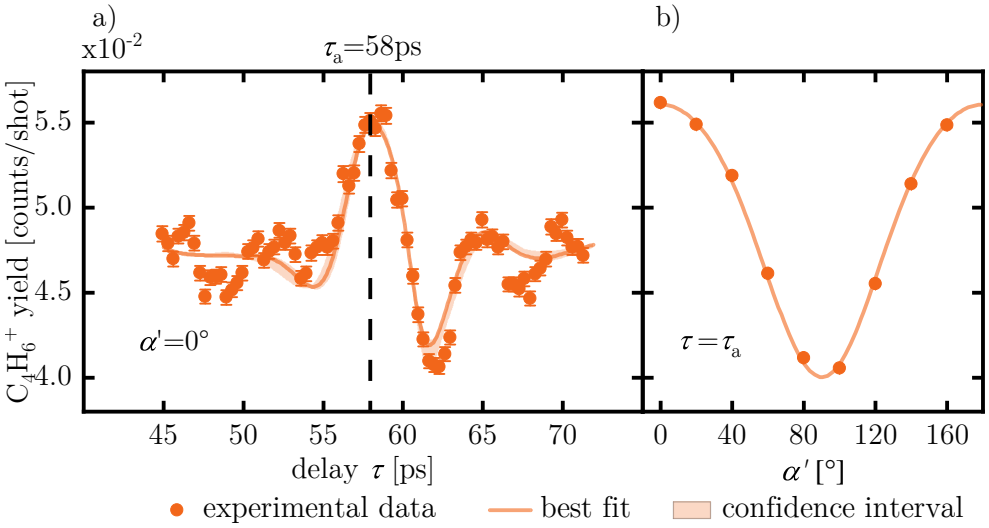

Figure 9.1: Experimental scans for the determination of the alignment distribution. The orange circles indicate the experimental data points. Error bars are given by counting statistics and are smaller than the symbols in b). a) shows a scan of the parent-ion yield in dependence of the delay between the alignment and the SFI pulses around the time of the first half revival for parallel polarization of the two beams ($\alpha' = 0°$). The instant of maximum alignment τ_a is indicated in the figure. Also shown is the best fit according to eq. (5.16) to the scan and its confidence interval. b) displays a scan of the parent-ion yield in dependence of the angle α' between the alignment- and SFI-laser polarizations at a delay corresponding to maximum alignment τ_a. A fit according to eq. (5.15) is also shown. Both scans were performed immediately following the acquisition of the experimental data in this chapter and in chapter 10, without altering the experimental conditions.

for molecules aligned along the SFI-laser polarization direction (see fig. 10.2) becomes the most pronounced. The value is close to the expected position for the half revival at 58.5 ps obtained from the smaller rotational constant in table 9.1 using eq. (5.8). For longer delays, the ion yield decreases and drops below the average, reaching a minimum at ∼62 ps, which corresponds to the instant of maximum anti-alignment. Afterwards, the yield increases again to the average value.

The simulated alignment trace describing the measured data best (see next subsection) also shown in the figure, agrees well with the experimental data around the positions of maximum alignment and anti-alignment. However, at delays $\tau < 55$ ps and $\tau > 66$ ps the experimental data oscillates around the simulated alignment trace. This was also observed in refs. [49, 160] and was

explained by the influence of asymmetric-top effects.

Figure 9.1b) shows a scan of α' performed at a fixed delay of $\tau = \tau_a = 58\,\text{ps}$, i.e. at the instant of maximum alignment at the half revival. For the scan, α' was varied in steps of 20° from 0° to 160° in 66 consecutive scans, resulting in 3.3×10^6 laser pulses for each angle. Error bars are again given by counting statistics. The α'-dependent yield observed in fig. 9.1b) is explained by the angular dependence of the ionization rate, displayed in fig. 10.2.

Determination of the most likely simulated alignment distribution

To fit the experimental data, a series of 184 simulations was performed for a range of input rotational temperatures T_{rot} and alignment laser intensities I. The measured alignment pulse duration (550 fs), the measured spot sizes of the alignment (63 μm) and SFI (28 μm) laser beams in the focus, and the rotational constants and polarizabilities given in table 9.1 were used as fixed input parameters for all simulations. Each simulation resulted in an alignment distribution $A^i(\theta', \tau)$ depending on the polar angle θ' and on the delay τ. i labels the various simulations $\{T_{\text{rot}}, I\}_i$. These simulations were then ranked by how well they describe the experimental data in fig. 9.1 as detailed in section 5.2. The employed l_{max} in eq. (5.15) was 3.

The resulting $\left(\chi^2_{\text{red}}\right)^i$ for the various employed T_{rot} and I are shown in fig. 9.2a). The alignment distribution which is most consistent with the experimental scans and is thus most likely the one present in the experiment is obtained for $T_{\text{rot}} = 1.6\,\text{K}$ and $I = 1.5 \times 10^{12}\,\text{W/cm}^2$, achieving a $\chi^2_{\text{red,min}}$ of 8.9. Its θ'-dependence for the delay τ_a used in the experiment $A^{i_{\text{min}}}(\theta', \tau = \tau_a)$ is shown in fig. 9.2b). This distribution is characterized by a $\langle \cos^2 \theta' \rangle$ (see eq. (5.9)) of $0.70^{+0.04}_{-0.07}$, similar to the value obtained in ref. [160].

The curves shown with solid lines in fig. 9.1 are the quantities $C_1^{i_{\text{min}}} \cdot S^{i_{\text{min}}}_{\text{avg}}(\alpha' = \alpha'_0, \tau - C_2^{i_{\text{min}}})$ (a)) and $S^{i_{\text{min}}}_{\text{avg}}(\alpha', \tau = \tau_a)$ (b)), i.e. the best fits to the respective experimental data. Eight further simulations are used for the construction of the confidence intervals, as explained in section 5.2.

9.3 ALIGNED MOMENTUM DISTRIBUTIONS

Experimental details

The SFI of aligned 1,3-butadiene was studied using 1290 nm-pulses to drive SFI and stretched 800 nm-pulses for non-adiabatic alignment (quantified by the alignment distribution shown in fig. 9.2b)). The employed experimental setup is described in section 7.1. The three-dimensional electron and ion momentum distributions were measured in coincidence using the reaction microscope (extraction fields: 3.0 kV/m and 17 Gauss, as before) for different angles α' between the polarizations of the alignment and SFI pulses in a single

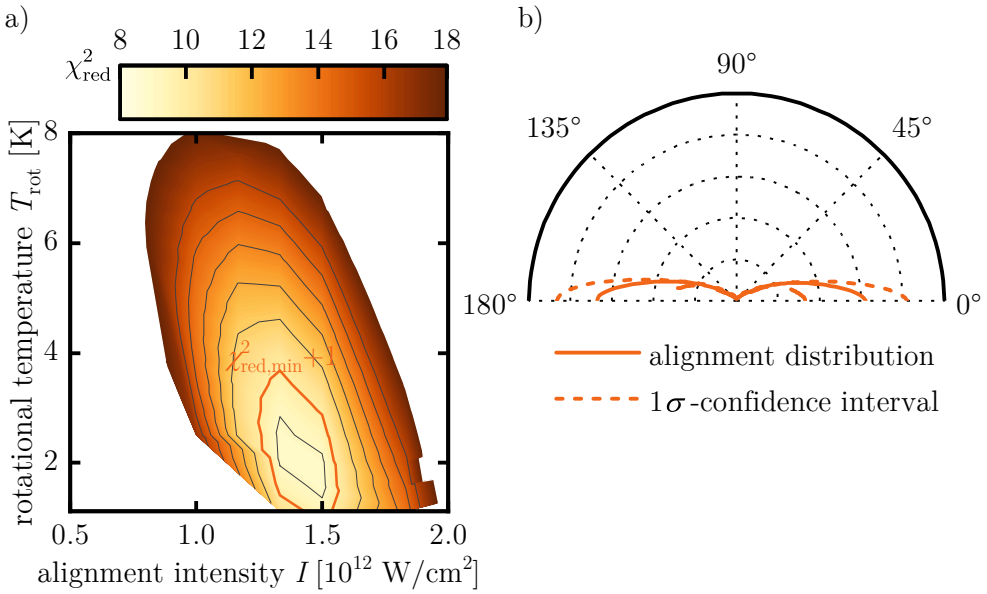

Figure 9.2: a) The value of the reduced χ^2 as obtained from the fit to the delay scan (see fig. 9.1a)) using eq. (5.16) for the simulations with varying input rotational temperatures T_{rot} and intensities I of the alignment pulse. The orange line delimits the region of parameters which yield a reduced χ^2 no more than 1 higher than the minimum value $\chi^2_{\mathrm{red,min}} = 8.9$, i.e. those simulations that fall within the 1σ-confidence interval. b) Polar plot of the most likely alignment distribution $A^{i_{\mathrm{min}}}(\theta', \tau = 58\,\mathrm{ps})$ (solid line), resulting in the minimum value $\chi^2_{\mathrm{red,min}}$, and its 1σ-confidence interval (dashed lines).

63 h long data acquisition run. As in previous chapters, determining the ion species measured in coincidence with each detected electron makes it possible to deduce the ionization channel (D_0 or D_1) of the electron. The parameters for the alignment pulse can be found in section 9.2. The intensity of the SFI laser field in the focus was $(5 \pm 3) \times 10^{13}$ W/cm^2, determined as before from the point of transition from direct to rescattered electrons in the photoelectron spectrum. Butadiene was supplied seeded in helium with a fraction of 0.03 %, using a stagnation pressure of 20 bar. The ionization rate in the reaction microscope was again limited to $\lesssim 0.2$ events per laser pulse.

The direction of the linear alignment-laser polarization was varied using the motorized half-wave plate in the fundamental beam path in fig. 7.1, while the linear polarization of the SFI laser beam was always pointing along the z-axis. The angle of the polarization vector of the alignment beam was set to a different value (from the pool of chosen values) every two minutes in random order to reduce the influence of potential systematic changes in the experimental

conditions. To acquire enough statistics in the very small signal of rescattered electrons in the fragments (analysed in detail in the next chapter), only 5 different angles α' for the alignment-laser polarization direction were used, each containing in total 3.8×10^8 laser pulses, corresponding to 10.5 h of data acquisition. In addition to the aligned data recorded at a delay of $\tau = 58$ ps, also 10.5 h of data using unaligned molecules was acquired by changing the delay to a value of $\tau = -30$ ps (i.e. the alignment pulse arrived long after the SFI pulse) for short time intervals in between the acquisition of the aligned data.

Channel-resolved direct-electron momentum distributions for aligned butadiene

Before proceeding with the analysis of the rescattered electrons in the next chapter, here the momentum distributions of the direct electrons will be examined. Since it is difficult to discern any differences between the distributions for different α' and channels, normalized-difference distributions $D_{\mathrm{nd}}^{\alpha'}(\vec{p})$ are calculated, using the momentum distributions obtained for unaligned molecules (acquired in the same measurement run) as a reference:

$$D_{\mathrm{nd}}^{\alpha'}(\vec{p}) = \frac{D^{\alpha'}(\vec{p}) - D^{\mathrm{rnd}}(\vec{p})}{D^{\alpha'}(\vec{p}) + D^{\mathrm{rnd}}(\vec{p})}. \tag{9.1}$$

$D^{\alpha'}(\vec{p})$ and $D^{\mathrm{rnd}}(\vec{p})$ denote the momentum distributions measured for molecules aligned with an angle α' and unaligned molecules, respectively. Each of the $D^{\alpha'}$ and D^{rnd} have been normalized to the same number of counts prior to the application of eq. (9.1) to remove the influence of variations in the overall yield. Using eq. (9.1), small differences between the distributions can be identified.

The resulting distributions $D_{\mathrm{nd}}^{\alpha'}(\vec{p})$ (as projections onto the p_x-p_y-, p_x-p_z-, and p_y-p_z-planes) are shown in fig. 9.3 for the D_0 channel and in fig. 9.4 for the D_1 channel, for $\alpha' = 0°$ and $\alpha' = 90°$. Focusing on the direct electrons delimited by circles in the figure, distinct structures can be seen. In particular for the D_0 channel, the distributions for the two angles look very different. For $\alpha' = 0°$, the p_x-p_y-projection of the distribution (i.e. the distribution perpendicular to the SFI-laser polarization direction (lateral momentum distribution)) forms a ring-like structure, whereas for $\alpha' = 90°$ there is a node visible along the p_y-axis where the electron density is lower compared to the distribution for randomly-oriented molecules. The density is higher in the direction perpendicular to this node. The node vanishes for higher momenta. The p_x-p_z- and p_y-p_z-distributions are identical for $\alpha' = 0°$, whereas they differ for $\alpha' = 90°$.

Comparing the D_1 to the D_0 distributions for $\alpha' = 0°$, it can be observed that they look very similar: Despite the high noise level due to a lower number of counts in the fragments, the features seen for the D_0 channel are also visible for the D_1 channel. For $\alpha' = 90°$, the high level of noise makes a comparison

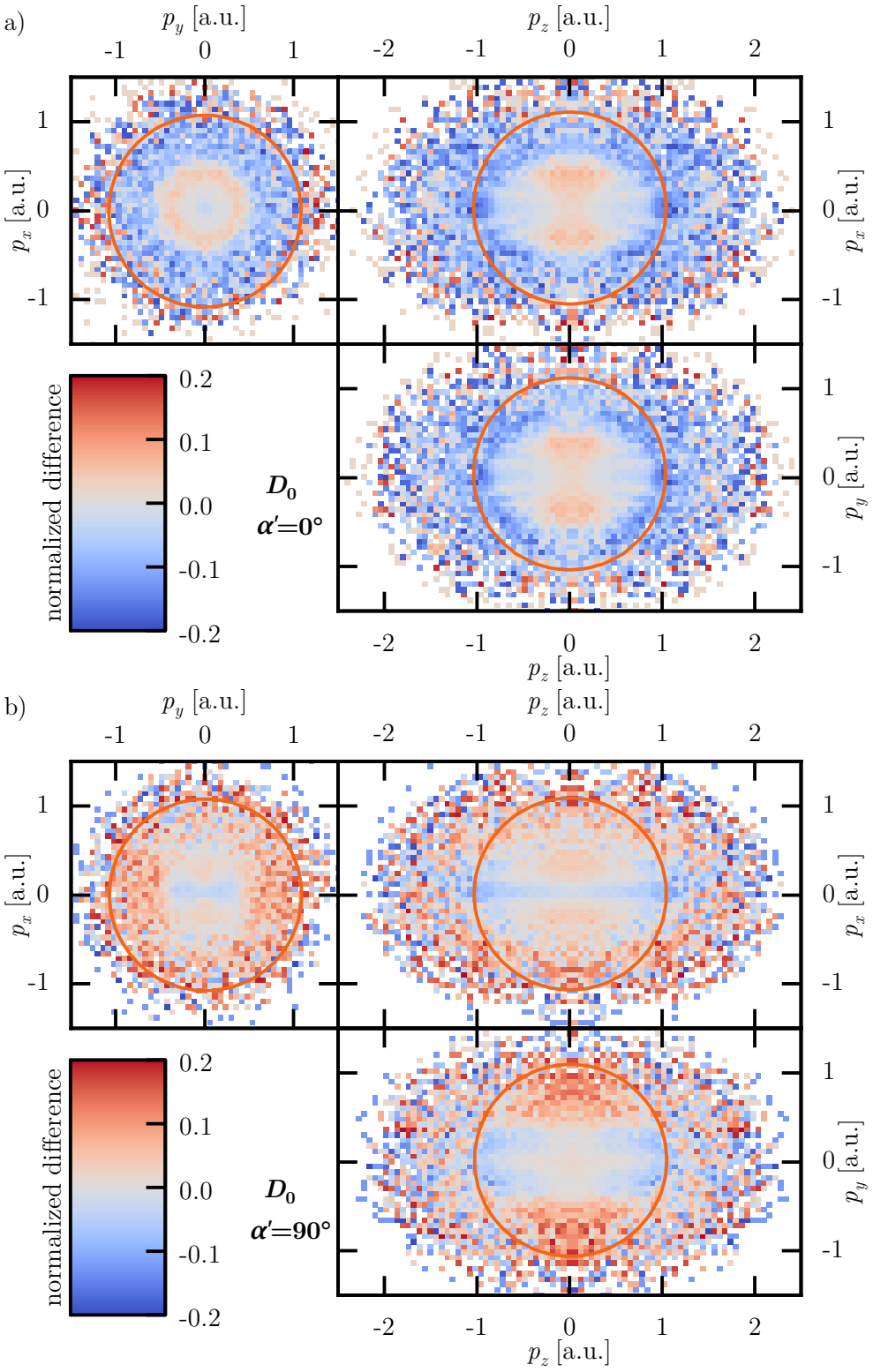

Figure 9.3: Projections of the normalized difference of three-dimensional aligned electron momentum distributions in the D_0 channel onto the p_x-p_y-, p_x-p_z-, and p_y-p_z-planes for a) $\alpha' = 0°$ and b) $\alpha' = 90°$. The normalized difference is calculated according to eq. (9.1) with respect to the momentum distribution of randomly-aligned molecules. The orange circles indicate the $2U_\mathrm{p}$-cut-off for the direct electrons.

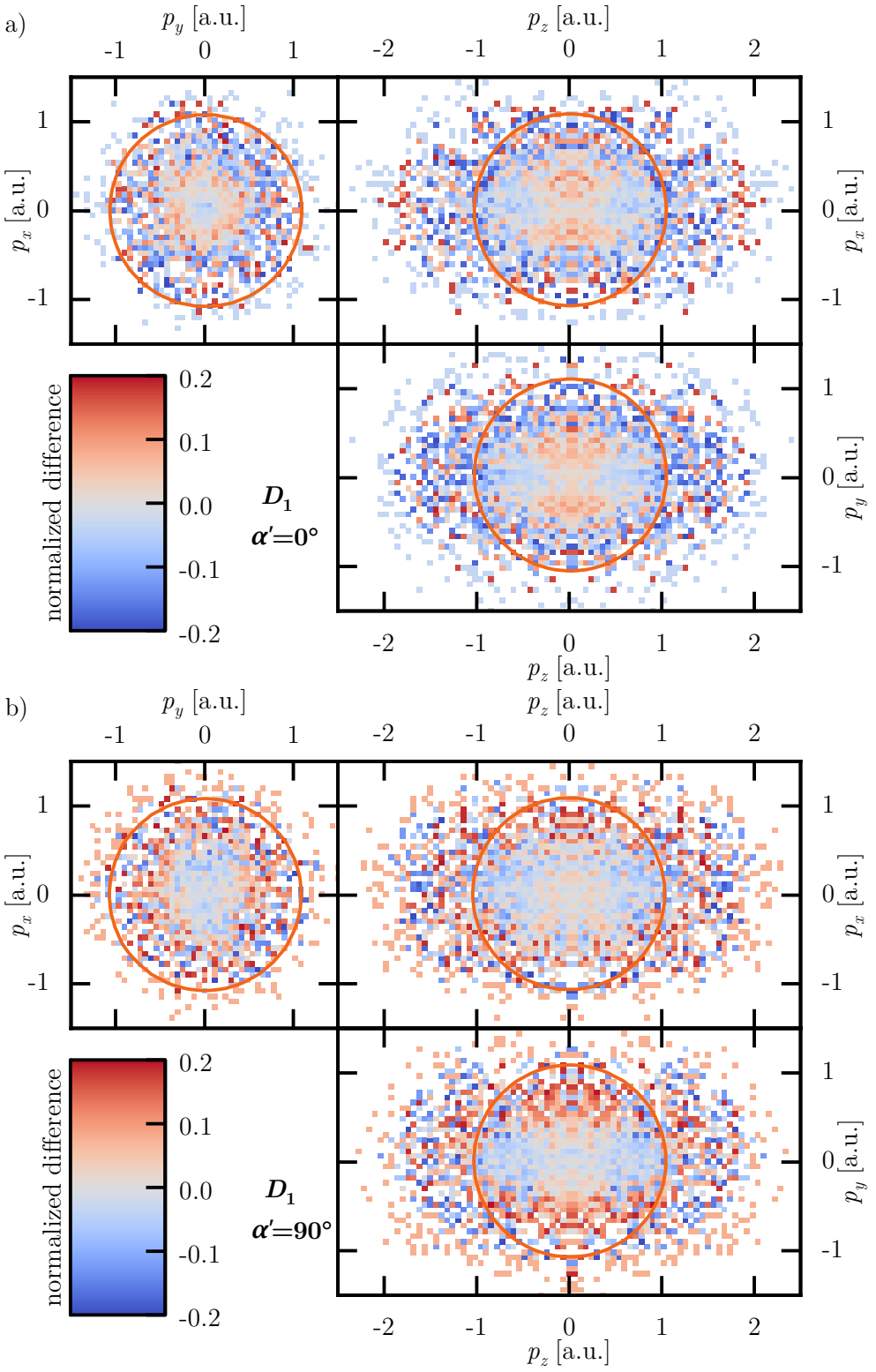

Figure 9.4: The same as fig. 9.3, but for the D_1 channel.

very difficult, but the structures observed for the D_0 channel do not seem to be present for the D_1 channel.

Interpretation

For a qualitative interpretation of the data, it is useful to recall that, according to eq. (1.5), the lateral momentum-space electron density immediately after tunnelling is proportional to the projection of the square of the Fourier transform of the electron's Dyson orbital onto a plane perpendicular to the laser polarization direction, filtered by a Gaussian tunnelling exponential. By assuming that the long axis of the molecules is aligned perfectly along the alignment-laser polarization direction (i.e. $\theta' = 0°$ and therefore $\alpha' = \theta$)[1] and that they are completely free to rotate around that axis (i.e. the angle χ' can take any value), the experimental projections onto the p_x-p_y-plane can be compared to the averaged lateral momentum distributions predicted by eq. (1.5). For the functional dependency along the p_z-axis, the temporal evolution of the wave packet in the field for different instants of birth is relevant and, therefore, the p_x-p_z- and p_y-p_z-projections are more difficult to explain qualitatively. For parallel orientation of the molecule with respect to the laser polarization direction, $\alpha' = 0°$, the molecule and the electric field vector are both perpendicular to the p_x-p_y-plane. For one particular angle χ' of rotation of the molecule around its own axis (e.g. $\chi' = 0°$ as shown on the left hand side of fig. 9.5a)), the relevant projections of the Dyson orbitals (see fig. 6.1b)), which are similar for both channels, consist of two lobes symmetric about the nodal plane n_1 (which corresponds to a line in the p_x-p_y-plane). When averaging over all angles χ', the nodal line and the lobes vary in direction, leading to a concentric ring of higher electron density around zero lateral momentum (see right hand side of fig. 9.5a)), which is what is observed experimentally in both the D_0 and the D_1 channel (see fig. 9.3a) and fig. 9.4a)). Since the molecules are free to rotate around the z-axis for $\alpha' = 0°$, the p_x-p_z- and p_y-p_z-distributions are expected to be the same, which is indeed the case for both D_0 and D_1.

For $\alpha' = 90°$, the long axis of the molecule points along the x-axis. In the D_0 channel, for all angles χ', the polarization vector lies within the nodal plane n_2 in the centre of the molecule along the y-axis. The nodal plane n_1, on the other hand, is only relevant for values of χ' close to 0°/180°. Accordingly, in the averaged lateral momentum distribution, the electron density is only reduced for the nodal plane n_2 (see upper part of the right hand side of fig. 9.5b)), which is also what is observed experimentally (fig. 9.3b)). The experimental distribution consistently also qualitatively agrees with the corresponding normalized-difference distribution for O_2 in ref. [35] for the same configuration of molecule and laser polarization, since the HOMO of O_2 looks

[1] See chapter 5 for the definition of these angles.

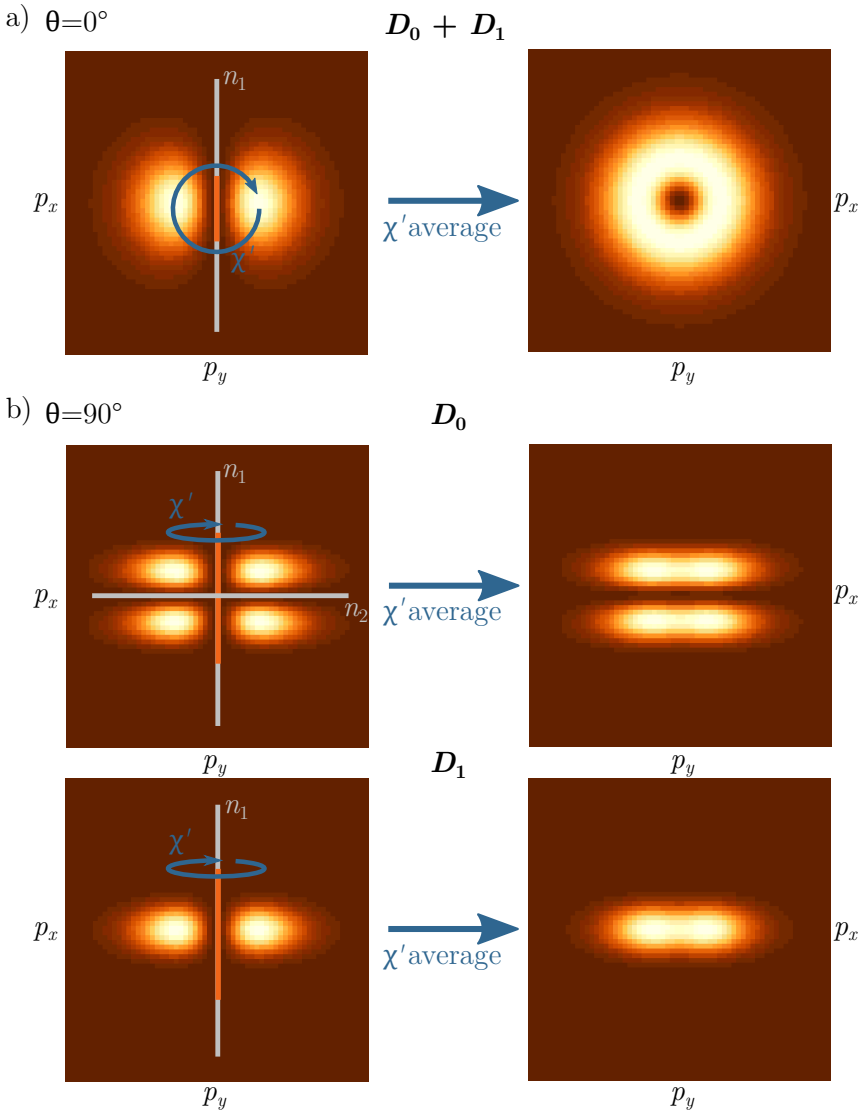

Figure 9.5: Depiction of the initial lateral momentum distributions expected according to eq. (1.5) for $\chi' = 0°$ (left hand side) and averaged over the angle χ' (right hand side) and for $\theta = 0°$ (a)) and $\theta = 90°$ (b)). For molecules which are perfectly aligned, $\theta = \alpha'$. The orange line depicts the butadiene molecule. The blue arrow indicates how the molecule rotates in the laboratory frame as the angle χ' is varied. The nodal planes are shown as grey lines.

similar to the D_0 Dyson orbital in 1,3-butadiene.[2]

For the D_1 channel and $\alpha' = 90°$, from the averaged Dyson orbitals one would not expect to see any clear nodes in the lateral momentum distribution, since the nodal plane n_2 that caused the suppression for $p_x = 0$ in the D_0 channel is not present in the D_1 channel (see fig. 9.5b)). This is consistent with the experimental data, where no clear structures are visible (fig. 9.4)b). Note that, while the experimental data is very noisy, the structures observed for the D_1 channel for $\alpha' = 0°$ lead to the expectation that features as seen for the D_0 channel and $\alpha' = 90°$ could also be observed for the same α' in the D_1 channel, if they were present.

Conclusion

The observation of the lateral momentum distributions allows one to draw conclusions on the structure of the electron's initial orbital, as demonstrated in refs. [35, 37, 207] and here, if aligned molecules are used and normalized differences are studied. In particular, differences induced by the different shapes of the D_0 and D_1 Dyson orbitals can be observed (even though the suboptimal signal-to-noise ratio – in spite of the long data acquisition times – make definite statements about the D_1 channel difficult). Observation of such differences in the electron distributions in coincidence with different fragments is an alternative way to directly show the participation of multiple continua in SFI, similar to the original CRATI experiment (see chapter 6), and also helps to establish the correspondence between continuum channels and the observed ion species for the present case. Electron momentum distributions for aligned acetylene molecules in coincidence with different fragments – similar to the data shown in this chapter – were also presented in ref. [208].

Having studied the channel-resolved direct-electron momentum distributions for aligned molecules and various alignment angles α', in the next chapter it will be investigated how the structure of the Dyson orbitals affects the angular dependence of electron rescattering.

[2]Note, however, that in ref. [35] the distribution for anti-aligned molecules was employed in eq. (9.1), instead of the distribution of unaligned molecules.

CHAPTER 10

Channel-Resolved Rescattering in the Molecular Frame

10.1 Introduction

In the previous chapter, it was shown that, using non-adiabatic alignment, butadiene molecules could be aligned to a substantial degree and that the alignment distribution could be extracted. A channel-resolved measurement performed with aligned butadiene molecules for different angles α' was also presented, focusing on the momentum distributions of the direct electrons. The goal of the present chapter is to analyse the acquired α'-dependent data with regard to the rescattered electrons, thus improving the understanding of the structure of the returning wave packet and studying the implications for techniques relying on recollision, such as LIED and high-harmonic spectroscopy. Using the known alignment distribution, the deconvolution procedure presented in section 5.3 grants access to information in the molecular frame, i.e. in dependence of the angle θ between the molecular axis and the SFI-laser polarization direction (see fig. 6.1b)), thus at least partially removing the smearing due to averaging over the alignment distribution.

By measuring the α'-dependent rescattering yield, the central portion (whose size is given by the size of the ion-core target) of the electron density of the returning wave packets can be probed for different angles between the molecule and the polarization direction, whereas varying the ellipticity ε probes the lateral distribution of the returning wave packet for a fixed or random

alignment but without the possibility to remove the influence of the alignment distribution. Naturally, varying both α' and ε, thus probing the lateral shape of the returning wave packet for different molecular orientations, would result in the highest amount of information on the structure of the returning wave packet. This is, however, out of reach using the 10 kHz laser system that was available for the experiments, due to the prohibitive acquisition times for a sufficient signal-to-noise ratio in the rescattering tail.[1]

Some previous studies have featured α'-dependent measurements of recollision-induced processes [45, 68, 209]. However, directly counting the yield of electrons in the rescattering tail in dependence of α' is a novel approach that has not been exploited before, even more so in combination with a channel-resolved measurement and while using the known alignment distribution for a transformation from laboratory-frame to molecular-frame observables.

Varying the angle α' between the alignment- and SFI-laser polarization directions while measuring the channel-resolved yields of direct and rescattered electrons makes it possible to extract both the molecular-frame angular ionization $S(\theta)$ and rescattering $(R \times Q)(\theta)$ probabilities (see eq. (1.31)), independently for both continuum channels. The simultaneous measurement of $(R \times Q)(\theta)$ for the two channels then allows the comparison of the channel-resolved return probabilities $R(\theta)$, which are found to be different and thus cannot be independent of θ for at least one channel. Furthermore, the $(R \times Q)(\theta)$-distributions for both channels also directly reflect the shape of the corresponding Dyson orbitals, whose nodal planes are evident in the distributions.

The interpretation of the experiment relies heavily on the ability to separate two continuum channels in butadiene and on the fact that $Q(\theta)$ is identical for the two channels (which is explicitly confirmed by a calculation), thus making it possible to study the molecular-frame dependence of all three steps of the three-step model in isolation. The experimental findings agree well with state-of-the-art TDSE calculations. Finally, implications for current experiments relying on recollision – and thus on the shape of the returning wave packet – are discussed. The results and discussion presented here, in parts closely follows the reasoning in ref. [53], where the results from this chapter have been published.

10.2 EXPERIMENTAL DATA

Experimental details

For the measurements presented in this chapter, the pump-probe setup as shown in fig. 7.1 was employed. The experimental conditions are described

[1] Varying the ellipticity when using aligned molecules may also involve additional complications in the interpretation, since a non-zero ellipticity also changes the angle of incidence between the impinging electron and the target [45].

in section 9.3 of the previous chapter. The analysis of the acquired channel- and α'-dependent momentum distributions is performed analogously to the ellipticity-dependent data in chapter 8: From the coincident detection of the electron momentum distribution and the ion time of flight, for each angle α' between the alignment- and SFI-laser polarization vectors, one can obtain the kinetic-energy distributions for electrons belonging to the D_0 or the D_1 channel. The filter operations explained in section 7.3 were applied. The yields of the direct ($M^{\mathrm{D}}(\alpha')$; 0 eV to 16 eV) and rescattered ($M^{\mathrm{R}}(\alpha')$; 25 eV to 55 eV) electrons were determined for each angle α' and channel D_0/D_1 separately. Contrary to chapter 8, however, the unnormalized yields were used, because normalization is applied after the deconvolution by division by $S(\theta)$.

α' dependence

The α'-dependent, channel-resolved yields of the direct and rescattered electrons are shown in fig. 10.1, where the error bars are given by Poissonian statistics. As can be seen, there is an order-of-magnitude difference between the different kinds of electron yields. The yields of direct electrons decrease monotonically from $\alpha' = 0°$ to $\alpha' = 90°$, whereas the yields of the rescattered electrons display a different behaviour: For the D_0 channel, the rescattered-electron yield first slightly increases at small α', before decreasing to a minimum value at $\alpha' = 90°$. For the, D_1 channel, on the other hand, an increase from small to large α' is observed.

Before proceeding with the interpretation, each of the data plots is transformed from the laboratory frame to the molecular frame using the known alignment distribution (see fig. 9.2b)) as described in section 5.3. The employed $k_{\max}$ was 2 in order to prevent overparametrization of the fits to the limited number of experimental data points. The fits from this procedure are also shown in fig. 10.1. The deconvolution of $M^{\mathrm{D}}(\alpha')$ results in the molecular-frame quantity $S(\theta)$, the θ-dependent ionization probability, whereas the deconvolution of $M^{\mathrm{R}}(\alpha')$ yields the product $(S \times R \times Q)(\theta)$ of the θ-dependent ionization, return, and high-angle scattering probabilities.[2]

Channel-resolved angular ionization amplitude

The channel-resolved $S(\theta)$ are plotted in fig. 10.2a) and agree qualitatively with the ones reported in ref. [49]. Quantitative differences can be explained by the fact that a SFI wavelength of 800 nm was used in ref. [49], compared to the 1290 nm used here. The confidence intervals in fig. 10.2a) are obtained as explained in section 5.3 and are dominated by the uncertainty in the alignment

[2]Note again that the rescattering yield M^{R} considered here only includes electrons with final energies in the regime exclusively populated by rescattered electrons, which implies that electrons with small scattering angles are excluded.

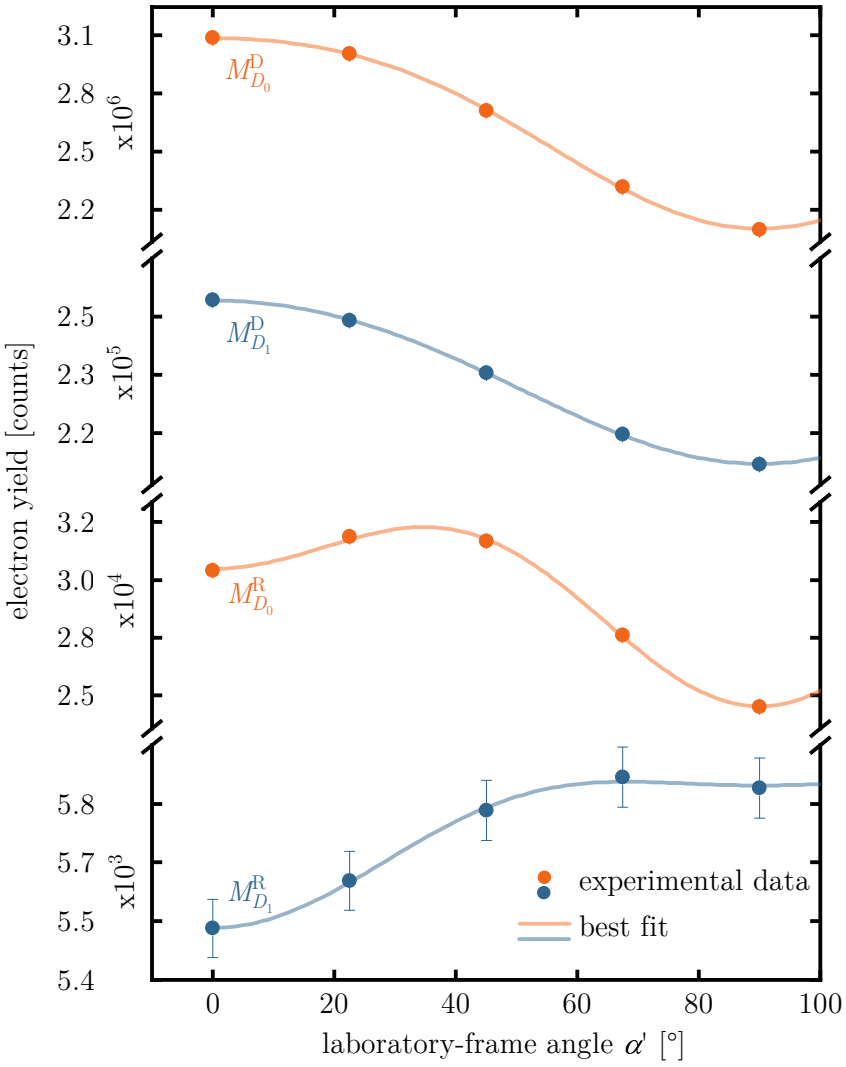

Figure 10.1: Channel-resolved yields (orange and blue circles) of direct ($M^{D}_{D_0}$,$M^{D}_{D_1}$) and rescattered ($M^{R}_{D_0}$,$M^{R}_{D_1}$) electrons as a function of the angle α' between the polarizations of the alignment and SFI laser fields. The solid lines denote best fits from the deconvolution of the molecular-frame ionization and rescattering probabilities using the known alignment distribution (see eq. (5.17)). Error bars, given by counting statistics, are smaller than the utilized symbols for $M^{D}_{D_0}$, $M^{D}_{D_1}$, and $M^{R}_{D_0}$. Note the breaks on the yield axis and the orders-of-magnitude differences among the various relevant signals.

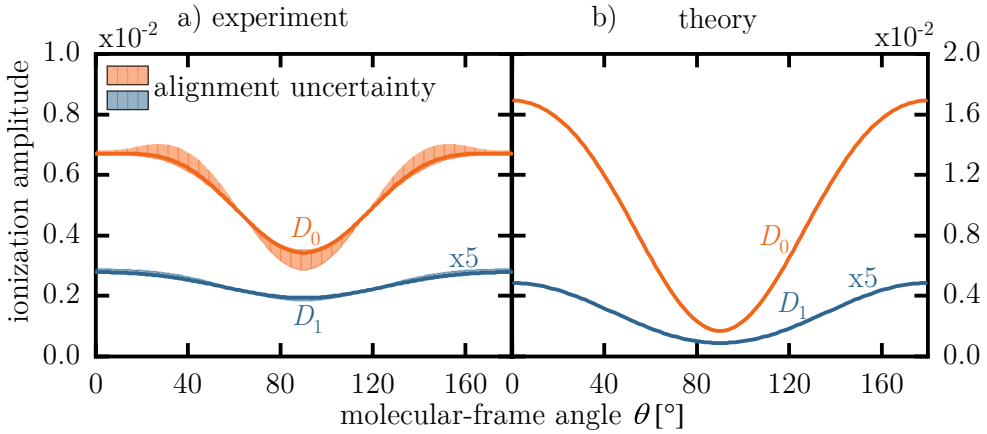

Figure 10.2: a) Channel-resolved ionization amplitude $S(\theta)$, obtained from the deconvolution of $M^{\mathrm{D}}_{D_0}$ and $M^{\mathrm{D}}_{D_1}$ in fig. 10.1, as a function of the polar angle θ in the molecular frame (see coordinate system fig. 6.1b)). The shaded areas denote the confidence intervals due to the uncertainty in the alignment distribution. The absolute scale for the ionization amplitude is arbitrary, but the relative scale between the D_0 and D_1 channels reflects their respective contribution to ionization. b) The same observables as in a) but obtained from TDRIS simulations.

distribution. Figure 10.2b) shows the results of a theory calculation and will be discussed in section 10.3.

In fig. 10.2a), both channels display a minimum for $\theta = 90°$, i.e. for a perpendicular orientation of the laser polarization to the molecular axis, but the minimum is more pronounced for the D_0 than for the D_1 channel. The clearer minimum for D_0 can be explained by the nodal plane n_2 that is present for the D_0 channel, since ionization along nodal planes is commonly expected to lead to a suppression of the ionization amplitude. Still, despite the absence of the nodal plane n_2 in the D_1 channel, a minimum is observed. Also note that the ionization amplitude reaches its maximum value at $\theta = 0°/180°$ for both the D_0 and the D_1 channels, despite the polarization vector of the SFI electric field lying within the nodal plane n_1 in this direction for both channels, leading to the expectation of a suppressed ionization amplitude. This shows that, despite the nodal planes being visible in the direct-electron momentum distributions in section 9.3, this does not necessarily lead to a reduction in the integrated yield. The breakdown of the simple relation between nodal planes and suppression of the ionization amplitude for polyatomic molecules has been noted earlier in refs. [43, 49, 200].

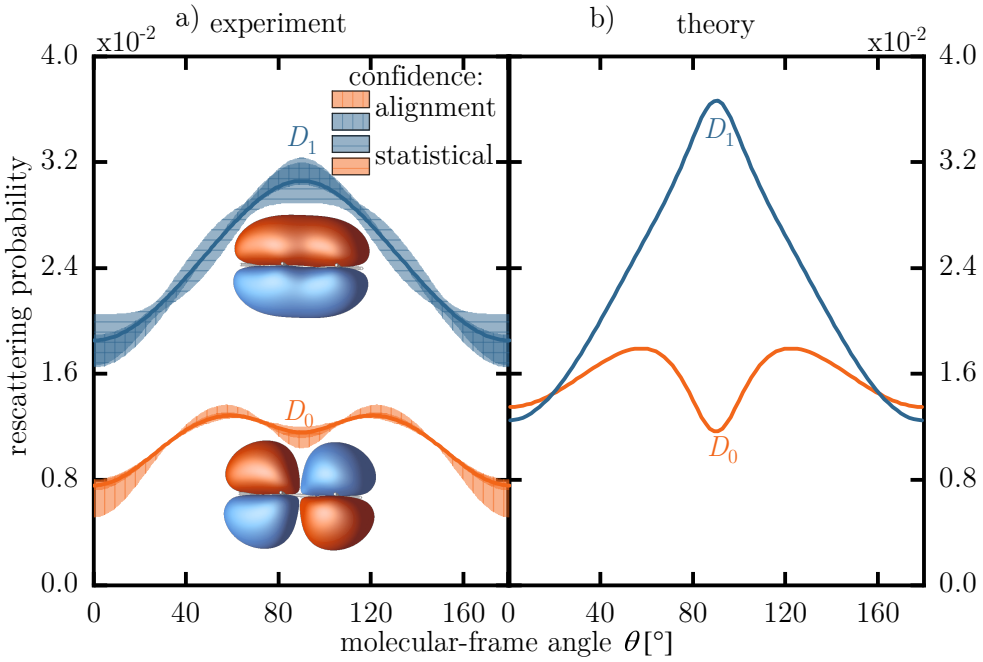

Figure 10.3: a) Channel-resolved rescattering probability $(R \times Q)(\theta)$ obtained from the deconvolution of $M^{\mathrm{R}}_{D_0}$ and $M^{\mathrm{R}}_{D_1}$ in fig. 10.1, as a function of the polar angle θ in the molecular frame. The vertically shaded areas denote the confidence intervals due to the uncertainty in the alignment distribution, whereas the horizontally shaded areas reflect the uncertainty in the quantities $M^{\mathrm{R}}_{D_0}$ and $M^{\mathrm{R}}_{D_1}$ (error bars in fig. 10.1). Also shown are the corresponding Dyson orbitals, whose nodal structure is very well reflected in the $(R \times Q)(\theta)$-distributions. b) The same observables as in a) but obtained from TDRIS simulations.

Channel-resolved rescattering probability

Dividing $(S \times R \times Q)(\theta)$ by $S(\theta)$ results in the channel-resolved rescattering probability $(R \times Q)(\theta)$, which is plotted in fig. 10.3a) along with the confidence intervals. Again, the theory results shown in fig. 10.3b) will be discussed in section 10.3. In contrast to the angular ionization probability $S(\theta)$, the channel-resolved product $(R \times Q)(\theta)$ of the return probability R and the high-angle scattering probability Q reflects the nodal planes of the Dyson orbitals (also shown in the figure) much better. In particular, pronounced differences – both in shape and in amplitude – can be observed in the $(R \times Q)(\theta)$-distributions between the D_0 and the D_1 channels. It should be noted that the distributions shown in fig. 10.3a) have not been rescaled and give the actual probability for an electron, given that it has been released into the continuum (from the HOMO or HOMO-1), to return to the core and to be scattered into the energy

interval over which integration is performed.

As was already observed in chapters 7 and 8, the overall rescattering probability is larger for the D_1 (1.85 % to 3.05 %) than for the D_0 (0.75 % to 1.3 %) channel. Concerning the shape, both channels have a global minimum at $\theta = 0°/180°$, i.e. when the laser polarization direction lies within the nodal plane n_1 irrespective of the rotation of the molecule around its own long axis. At $\theta = 90°$, on the other hand, only the D_0 channel has a (local) minimum, whereas the D_1 channel maximizes the $(R \times Q)(\theta)$-distribution along this direction. Again, this relates to the Dyson orbitals, since for the D_0 channel the polarization vector lies within the nodal plane n_2 for arbitrary rotations around the long axis, whereas there is no nodal plane along this direction for the D_1 channel (except for $\phi = 0°/180°$, where the polarization vector lies again in n_1). For the D_0 channel, $(R \times Q)(\theta)$ is maximized at around $\theta = 60°/120°$, where the D_0 Dyson orbital has no nodal planes.

The correspondence between nodal structure of the Dyson orbitals and the $(R \times Q)(\theta)$-distributions must arise from $R(\theta)$, since $Q(\theta)$ is expected to be the same for the two channels (see discussion in section 10.3). Thus, while channel-resolved $R(\theta)$-distributions cannot be obtained from the data, the different $(R \times Q)(\theta)$-distributions for the two channels are direct experimental proof for the propositions that 1) $R(\theta)$ is not the same for the two channels, and, thus, 2) at least one of the of the two channels has a return probability $R(\theta)$ that does depend on θ.

The fact that the channel-resolved $(R \times Q)(\theta)$-distributions reflect the nodal planes of the corresponding Dyson orbitals so well furthermore strongly suggests that the dependence of R on θ results from the ionization direction–dependent differences in the continuum wave-packet structure immediately upon ionization, which is determined by the Dyson orbitals. It is thus experimental evidence for the assertion that information on the initial orbital is preserved during continuum propagation, supporting the correctness of the interpretation for the observed dependence of the rescattering yield on ellipticity in chapter 8 and for similar experiments.

Changing the angle between the molecule and the laser polarization direction changes the projection of the relevant Dyson orbital that determines the continuum wave packet according to eq. (1.5). Thus, the initial continuum wave packet looks different for the two channels and for different angles θ. Different widths and nodal planes in the Dyson-orbital projections affect the momentum composition of the wave packet upon ionization. This was also observed experimentally for the direct-electron momentum distributions in section 9.3. This different momentum composition leads to a varying amount of spread of the wave packet during continuum propagation, which, by the time the wave packet returns to the core, leads to a different size of the returning wave packet and thus to a different electron density interacting with the core. In particular, nodal planes lead to a large spread of the wave continuum wave packet: The smaller the separation of the lobes around the nodal plane is in

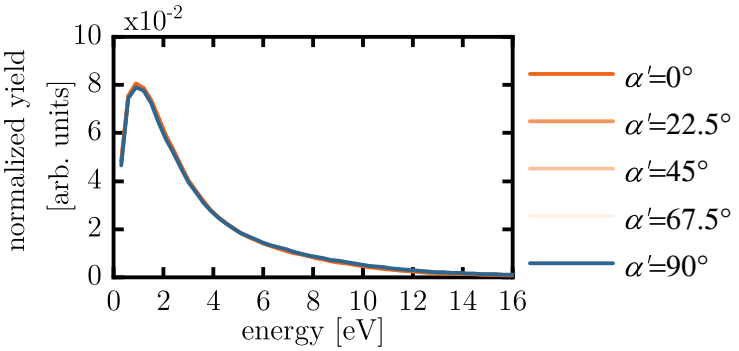

Figure 10.4: Kinetic-energy distributions for the direct electrons in the D_0 channel for various angles α'. All distributions are almost identical, showing that the angular ionization probability $S(\theta)$ is independent of the instant of birth in the laser cycle.

the position-space Dyson orbitals, the larger the spreading during continuum propagation will be. In addition, as was also observed in chapter 8, the minimum itself may survive the continuum propagation and further minimize the returning wave-packet density for linear polarization. These remarks explain why the return probability R may depend on the angle θ and on the initial bound state from which the electron originated: For the D_0 channel, the spacing of the lobes is larger for $\theta = 90°$ than for $\theta = 0°/180°$, leading to less wave-packet spreading and, thus, to a higher returning density, consistent with the observations. In contrast, for the D_1 channel the polarization vector does not generally lie within a nodal plane for $\theta = 90°$ and, thus, a maximum is observed, since the wide Dyson orbital leads to a small momentum spread.

Independence of $S(\theta)$ from the instant of birth

A potential objection against the division by the experimentally determined $S(\theta)$ in the previous subsection is that the distribution $S(\theta)$ determined for the direct electrons may not be the same as the $S(\theta)$ for the electrons undergoing rescattering, i.e. that the distribution $S(\theta)$ depends on the instant of birth during the laser cycle. The recorded experimental data makes it possible to falsify this assertion by comparing the angular dependence of the direct-electron yield for different kinetic energies. This has been done for N_2 in the past [210] and is shown fig. 10.4 for the present case of butadiene. For better comparison, the presented direct-electron energy distributions are normalized to the same number of events (otherwise their different overall intensity would reflect the angular distribution $S(\theta)$ shown in fig. 10.2).

As can be seen, the distributions agree well at all energies, meaning that there is no strong dependence of $S(\theta)$ on the final energy of the direct electrons,

which can be mapped one-to-one to the time of birth (see eq. (1.16)). The differences between different energies are smaller than the error interval of $S(\theta)$. The direct electrons are all born before the maximum of the electric field, whereas the rescattered electrons along the dominant long trajectory are born directly after the field maximum. Since there is no dependence of $S(\theta)$ on the instant of ionization before the field maximum – as fig. 10.4 evidences – one should not expect any after it, and thus it is valid to use $S(\theta)$ from the direct electrons also for the rescattered electrons.

10.3 THEORY CALCULATIONS

Simulation method

In this section, ab-initio (i.e. without incorporating any experimental data) TDSE calculations are presented to compare with the experimental results and to assist in their interpretation. The calculations were performed by Timm Bredtmann employing the *time-dependent resolution-in-ionic-states (TDRIS)* method [46]. Even though the experiments whose results are presented in this chapter were performed at a wavelength of 1290 nm, the calculations had to be done at a shorter wavelength of 800 nm. This is due to longer wavelengths leading to larger excursion distances of the electron away from the parent ion (see eq. (1.20)), which demands performing the calculations on a larger numerical grid. Doing computations on a grid large enough for a wavelength of 1290 nm would not have been feasible for the many required orientations between laser polarization and the molecular axis. Still, even the calculations done at a wavelength of 800 nm agree qualitatively with the experimental results.

Three different kinds of simulations were performed:

1. Channel-resolved kinetic-energy distributions of the direct electrons were simulated using a half-cycle laser pulse with an intensity of $3 \times 10^{13}\,\mathrm{W/cm^2}$. These simulations were used for the determination of the angular ionization probabilities $S(\theta)$.
2. Channel-resolved kinetic-energy distributions for the rescattered electrons were simulated using a 1.65-cycle pulse with an intensity of $3 \times 10^{13}\,\mathrm{W/cm^2}$. Using a pulse consisting of more than half a cycle allows the electrons to be driven back to and rescatter from their parent ion at the cost of a higher computational effort. The pulse features a soft turn-on and -off to suppress artefacts that would result from a sudden presence of the electric field. The simulations with this pulse were used in the calculation of the theoretical $(R \times Q)(\theta)$-distributions.
3. A simulation using the same pulse as in 2) but with the actual continuum wave packet replaced by a Gaussian wave packet at the turning point of the $10U_\mathrm{p}$-trajectory. The initial width at the turning point was 6.3 a.u. for all molecular orientations. This is similar to the approach

in ref. [176] and ensures that a chirped wave packet with a planar wavefront returns to the core.

For details on the computations, see ref. [53].

Results for $S(\theta)$ and $(R \times Q)(\theta)$

The experimental results for the channel-resolved molecular-frame ionization probability and the channel-resolved molecular-frame rescattering probability can be compared to the same quantities obtained from the numerical calculations. The theoretical $S(\theta)$ and $(R \times Q)(\theta)$ are shown in fig. 10.2b) and in fig. 10.3b), respectively, next to their experimental counterparts. As the experiment, the simulations include averaging over rotations around the long axis of the molecule. $S(\theta)$ was obtained using simulation method 1), whereas for $(R \times Q)(\theta)$ method 2) was used.

Qualitatively, the agreement between theory and experiment is good in all cases. Quantitative agreement is not to be expected, due to the different wavelength and pulse duration used in the calculations and due to intensity averaging within the focal volume present in the experiment but not considered in the simulations. However, all key features from the experimental distributions are also present in the calculated distributions. In the $S(\theta)$-distributions, the general shape of the curves is reproduced very well, even though the minima at $\theta = 90°$ are more pronounced in the calculations for both the D_0 and the D_1 channels. Similarly, in the $(R \times Q)(\theta)$-distributions, the features are sharper in the calculations. In addition, for the D_0 channel, the theory curve is offset to an overall higher rescattering probability compared to the experiment. This leads to a situation where, at angles close to $\theta = 0°/180°$, the D_0 and the D_1 rescattering probabilities have approximately the same magnitude in the calculation, whereas in the experiment the rescattering probability is higher everywhere for the D_1 channel than for the D_0 channel. Thus, the simulation conforms more closely to the qualitative expectations presented in section 10.2, since for $\theta = 0°/180°$ the projections of the D_0 and D_1 Dyson orbitals look very similar and are therefore expected to lead to a similar magnitude for the rescattering probability. The positions of the global maxima are the same as in the experiment.

Channel independence of $Q(\theta)$

One crucial feature that is exploited in the interpretation of the channel-resolved measurements in this chapter is the assumption that the (high-angle) scattering cross section[3] $Q(\theta)$ is the same for the two channels. This is based

[3] In principle, Q is the total elastic scattering cross section given by eq. (2.4), additionally integrated over all return energies. However, as before, the Q investigated here only includes electrons whose final energy lies within the rescattering tail, i.e. the integration excludes small scattering angles.

on a plausible physical picture: The potential seen by the returning electron during rescattering is formed by all 29 electrons of the molecular ion (and by the nuclei), which are all in the same state for the two channels, except for the least bound electron. Therefore, the scattering potentials for the two channels are expected to be very similar. To confirm this assertion, a simulation (using method 3) was performed where the shape of the returning wave packet is known to be plane and the same for all orientations, i.e. $R(\theta)$ is constant by design.

One example of this Gaussian–wave-packet scattering is shown in fig. 10.5a) at two instants in time ($t = 1.2\,\text{fs}$ (i.e. when the initial Gaussian wave packet is launched) and $t = 1.9\,\text{fs}$). The colour scale indicates the phase of the wave packet, and, therefore, the parallel stripes at $t = 1.9\,\text{fs}$ show that the wave packet is planar.

The simulation was repeated for several orientations of the molecules, and the yield of rescattered electrons in dependence of the polar angle θ, again including averaging over rotations of the molecule around its long axis, is plotted in fig. 10.5b) for the two channels. For both channels, modulations in the rescattering probability can be observed.[4] More importantly, however, the distributions obtained for the two channels are almost identical. This shows that the assumption of a channel-independent scattering cross section $Q(\theta)$ is well justified already at a wavelength of 800 nm. For the longer wavelength employed in the experiment, the returning electrons have more kinetic energy, and, therefore, the state of the valence electrons is expected to play an even less important role, since more energetic collisions imply that the electron penetrates the target more deeply. It is thus concluded that, under the conditions of the experiment, the scattering target for the two channels can be regarded as identical.

10.4 DISCUSSION

Summary of the results and implications for strong-field spectroscopy studies

The key result of the present chapter is fig. 10.3, which constitutes a direct demonstration that the fraction R of the continuum electron wave packet revisiting the core depends on the angle θ between the molecular axis and the polarization direction of the SFI laser field. From fig. 10.3, it is clear that in particular the nodal planes of the initial orbitals are still evident in the rescattering probabilities. Thus, an imprint of the initial orbital structure survives continuum propagation and influences the recollision event. Contrary to previous studies relying on the molecular orbital imprint on recollision for

[4] This is in contrast to what was observed in ref. [176], where it was argued that the structure of N_2 could not be resolved with the 800 nm SFI laser, and, thus, no modulations were observed. However, the butadiene molecule being larger than N_2 explains why modulations are observed in the present case despite employing the same wavelength.

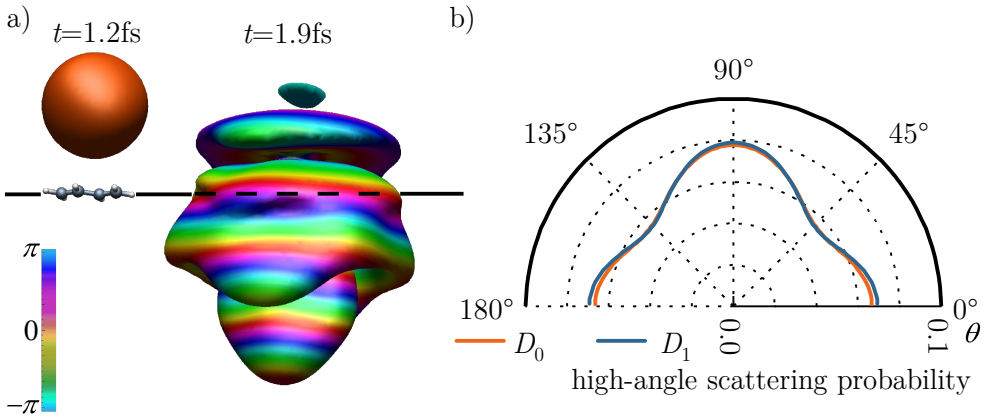

Figure 10.5: Simulated field-driven scattering of a three-dimensional Gaussian continuum wave packet (replacing the actual channel-dependent wave packet launched by SFI) off the parent ion in the D_0 or in the D_1 state. a) Snapshots of the electron density isosurfaces (of value $2.5 \times 10^{-5} a_0^{-3}$, where a_0 is the Bohr radius) at two instants in time for $\theta = 90°$ and $\phi = 90°$ (see coordinate system fig. 6.1b)) and the ion in the D_0 ground state. $t = 0$ corresponds to the maximum of the oscillating electric field. Shown are the initial Gaussian wave packet at the classical turning point $t = 1.2$ fs of the $10U_p$-trajectory and the scattering wave packet at $t = 1.9$ fs. A full laser cycle lasts 2.7 fs. The colour scale describes the phase of the electron wave function. b) Comparison of the computationally obtained rescattering probability $(R \times Q)(\theta)$ (averaged over rotations around the long molecular axis) for a Gaussian wave packet scattering off the $C_4H_6^+$ ion in the D_0 (orange) and the D_1 (blue) state. Each data point in b) corresponds to a simulation as exemplified in a), for different orientations of the molecule with respect to the returning wave packet. Because the return probability $R(\theta)$ is channel- and angle-independent by design in this calculation, the calculation shows that the high-angle scattering probability $Q(\theta)$ does not depend on the electronic state of the cation. The simulations were performed by Timm Bredtmann.

their interpretation [45, 67, 200], the present approach makes it possible to clearly separate the influence of all three steps of the three-step model, uniquely tracing the observed effect of nodal structure back to the composition of the returning continuum wave packet.

The dependence of R on θ is expected to be a universal feature for many molecular targets. The reason why butadiene was chosen in this work, in preference to other molecules, is because it allows the separation of different continuum channels necessary to draw conclusions on $R(\theta)$ from the measured $(R \times Q)(\theta)$. However, for any target where ionization takes place from orbitals with non-spherical symmetry and in particular in the presence of nodal planes, R should be expected to exhibit a dependence on θ. Also note that the modulations in the $R(\theta)$-distribution are not expected to be diminished when employing longer SFI-laser wavelengths.

While it has been acknowledged experimentally and theoretically [35, 45, 67, 200, 207] that the continuum wave packet is influenced by the shape of the electron's initial orbital and the direction along which ionization takes place, the resulting differences in the subsequent continuum propagation and the return probability have been mostly not considered. In particular, when extracting structural information on molecules from LIED experiments (see section 2.2), it is necessary to weight the DCS calculated for different orientations according to the density of the returning wave packet when averaging over the alignment distribution (see eq. (2.9)). So far, the weight has been taken to be exclusively determined by $S(\theta)$ (see eq. (2.8)), while R has been assumed to be constant, $\partial R/\partial\theta = 0$ [18, 19, 71–75]. Similarly, high-harmonic–spectroscopy experiments often assume R to be independent of θ [17, 113, 120, 122, 186–188]. The results presented in this chapter caution that the strong modulations of R with θ observed for butadiene may be a non-negligible effect in LIED and high-harmonic–spectroscopy experiments with molecular targets.

Assumption of a planar wavefront

The strong dependence of R on θ observed in this chapter, as well as the observations of non-Gaussian behaviour in the ellipticity dependency in chapter 8, naturally lead to the discussion of another assumption of LIED and high-harmonic–spectroscopy experiments, namely that the returning wave packet exhibits a planar wavefront, at least over the extent of the target. It is evident from eq. (1.5) that, when ionizing directly along a nodal plane, the wavefront of the continuum wave packet will be heavily curved. What is commonly assumed to happen, however, is that, as the wave packet diffuses during continuum propagation, by the time it returns to the ion core, the wavefront has flattened out and can be approximated as asymptotically planar over the extent of the target [54, 79, 84]. The longer excursion times for longer wavelengths are expected to be conducive to this effect. To some extent, this was also confirmed by the wavelength dependence in chapter 8.

From theory, it is expected that, when ionizing precisely along a nodal plane, symmetry dictates that the destructive interference is preserved all the way in the continuum [51], resulting in a curved wavefront when recolliding (also see Supplementary Material in [53]). However, as soon as the SFI-laser polarization direction deviates only slightly from the nodal plane, the symmetry is broken and the returning wave packet may be approximately planar again, such that, from general theory considerations alone, it is not possible to evaluate the significance of the nodal planes for the curvature of the returning wave packet in experiments, where a certain degree of orientational averaging is inevitable and thus deviations from perfect symmetry considerations are to be expected.

The assumption of a planar wavefront implies that the returning wave packet is composed of states whose momentum only varies in magnitude, whereas the direction of return is along the laser polarization for all states. In contrast, when the wavefront of the returning wave packet is curved, several return-momentum directions must be included and only their mean direction must be (anti-)parallel to the laser polarization [20]. In other words, if the incoming wave packet $\Psi(\vec{r})$ does not asymptotically exhibit a planar wavefront, the general expression

$$\Psi(\vec{r}) = \int \hat{\Psi}(\vec{p}) \exp\left(-\frac{i}{\hbar}\vec{p}\cdot\vec{r}\right) d^3\vec{p} \tag{10.1}$$

must be used to asymptotically describe the returning wave packet, where the integration is performed over all return-momentum directions $\vec{p}$. Therefore, for example in LIED, the DCS calculated for states with an asymptotically flat wavefront might still be useful even in the case of a returning wave packet with a curved wavefront, if the composition $\hat{\Psi}(\vec{p})$ of the returning wave packet is known, by treating electron scattering for each return direction individually and, in the end, integrating the scattered-electron distribution over all relevant return directions weighted by $\hat{\Psi}(\vec{p})$. If this is not done despite the returning wave packet having a curved wavefront, a fit of the free parameters of a one-component DCS to the experimental data (see section 2.2) may lead to the retrieval of incorrect molecular structure [84].

Note that the discussion here is only loosely related to the so-called plane-wave approximation, which assumes the scattering states used for the calculation of the recombination dipole matrix elements in HHG or the DCS in elastic rescattering to be given by plane waves. This approximation has been discussed in the past mostly in the context of high-harmonic tomography [54, 79, 186, 211–213], where, in the case of plane-wave scattering states, the orbital to be reconstructed is given by the Fourier transform of the recombination dipole matrix elements [20, 120]. However, the asymptotic planarity of the wavefront has not been challenged in that context.

Testing the planarity of the wavefront experimentally

Unfortunately, while the experimental data presented in this chapter and in chapter 8 makes it evident that some information on the initial orbital is preserved until the instant of recollision, the presented data does not make it possible to draw direct conclusions regarding the planarity of the wavefront. Figure 10.3 suggestively shows that the Dyson-orbital structure is reflected in the return probability $R(\theta)$. However, it has to be kept in mind that the distributions shown in the figure do not represent the angular component of an actual continuum wave packet. Figure 10.3 only represents the central portion of the returning electron density for different angles between molecular axis and SFI-laser polarization: For each angle θ, a *different* wave packet is launched into the continuum, from which elastic rescattering probes the central portion interacting with the core. The deviations from Gaussian behaviour in the ellipticity dependence presented in chapter 8, in particular the occurrence of a local minimum at zero ellipticity, do indicate that the returning wave packet has a globally non-planar wavefront. Yet, it is unclear if the curvature over the extent of the target is large enough to affect the interpretation of LIED and high-harmonic–spectroscopy experiments.

Therefore, the shape of the continuum wave packet and the local curvature of the wavefront are not directly accessible with the currently available data. However, an extension of the technique presented in this chapter could be used to investigate the planarity of the wavefront and assess its potential influence for LIED and high-harmonic spectroscopy, namely performing an actual channel-resolved LIED experiment in 1,3-butadiene. A first step towards this goal, using unaligned butadiene molecules and a SFI laser wavelength of 1290 nm is shown in fig. 10.6. Clearly, the extracted experimental orientationally averaged DCS (which was obtained using the procedure outlined in section 2.2) for the D_0 channel is different from the one for the D_1 channel. This is to be expected, since the shown experimental quantity features averaging over different orientations, weighted by both $S(\theta)$ and $R(\theta)$, which are (see figs. 10.2 and 10.3) not the same for the two channels.

In order to test the assumption of a planar wavefront, a theoretical modelling of the DCS is required. This may imply performing the experiment at a longer wavelength to get into the range of validity of the independent-atom model (i.e. to achieve return energies >100 eV), or, otherwise, more sophisticated theoretical modelling of the DCS is needed [73, 214]. Then the averaged DCS for the equilibrium configuration of butadiene can be calculated, weighting the orientations with the respective channel-dependent $S(\theta)$ and $R(\theta)$, which can be determined experimentally as shown in this chapter. For the determination of $R(\theta)$ from $(R \times Q)(\theta)$, $Q(\theta)$ needs to be known, which however can be calculated from the modelled DCS as described by eq. (2.4). Appropriate alignment of the molecules prior to the LIED interaction should enhance the effect of nodal planes.

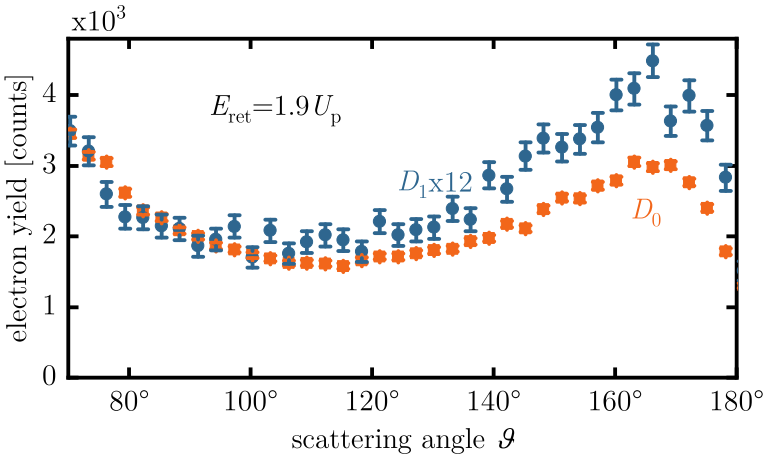

Figure 10.6: Experimentally extracted orientationally averaged DCS as obtained from a channel-resolved measurement (consisting of 2.1×10^9 laser pulses or 59 h of data acquisition) using randomly-aligned 1,3-butadiene molecules. Other than that, the experimental parameters were the same as for the previous measurement in this chapter. The return energy used for the determination of the DCS eq. (2.9) according to eq. (2.2) was $E_{\text{ret}} = 1.9U_{\text{p}}$ ($U_{\text{p}} = 8\,\text{eV}$). The width of the shell used for integration was $\pm 14\,\%$ of that value. Note that the yield in the D_1 channel (blue) has been scaled by a factor of 12 compared to the D_0 channel (orange). Error bars are given by counting statistics.

If the calculated averaged DCSs for the two channels agree with the ones determined from experiment, the potential non-planarity of the returning wave packet does not play a significant role and can be ignored. If, however, one or both of the theory predictions deviate significantly from the measurement (deviations are expected to be larger for D_0, since it possesses more nodal planes), then this would be a strong indication of the breakdown of the approximation of a planar wavefront. An additional benefit of the experiment is that it not only assesses the potential non-planarity of the returning wave packet but also directly probes the significance of the $R(\theta)$-dependence for LIED experiments.

Conclusion

In conclusion, in this chapter it was shown that in the SFI of 1,3-butadiene the probability for an electron to return to its core depends both on the ionization channel and the orientation of the molecule with respect to the polarization

direction of the ionizing laser pulse. This result was achieved by combining a channel-resolved measurement, afforded by the coincident detection of ions and electrons, with laser alignment. The latter makes it possible to transform into the molecular frame using the known alignment distribution, whereas the former allows one to factor out the influence of the elastic scattering cross section $Q(\theta)$, which is identical for both channels, and thus to compare directly the angular dependence of the return probability $R(\theta)$ of the two channels. Both the channel dependence and the dependence of the return probability on θ may complicate the interpretation of LIED and high-harmonic–spectroscopy experiments, when these are applied to polyatomic molecular targets.

III

Towards Attosecond Pump-Probe Spectroscopy at High Repetition Rates

CHAPTER 11

Motivation

Attosecond pump-probe experiments

As explained in the general introduction, while attosecond temporal resolution can be obtained using single femtosecond laser pulses, another approach to the investigation of ultrafast electron dynamics is based on two-pulse pump-probe measurements using sub-femtosecond pulses. Such pulses are available from tabletop sources relying on HHG (see chapter 3), which provide either isolated or trains of bursts with a duration of a few tens to a few hundreds of attoseconds. The spectrum of the pulses is in the XUV, and their short duration makes it possible to precisely initiate and probe electron dynamics. While attosecond XUV-XUV pump-probe experiments have already been performed [215–217], a currently more widely adopted approach is to exploit the sub-cycle timing of the IR pulses driving HHG with respect to the generated attosecond bursts, i.e. to do two-colour XUV-IR pump-probe measurements. Using this technique, numerous experiments have been performed with atomic [134, 218–221] and molecular [222–227] targets.

However, especially in the case of molecules, the broadband nature of the attosecond XUV pulses makes the interpretation of experimental data very challenging, since generally a range of (electronic, vibrational) states is populated, already in diatomics, initiating overlapping and often coupled nuclear and electronic dynamics in the complex energy landscapes of molecular systems [5]. Thus, experiments with molecular targets have mostly relied heavily on numerical calculations for their interpretation, which are also a challenge to perform [5]. To be less dependent on theoretical modelling and to apply attosecond pump-probe spectroscopy to polyatomic molecules, where complexity is even increased compared to diatomics, it is therefore

desirable to collect as much information about the products of the interaction – photoelectrons with either a parent ion or charged and neutral fragments from a dissociation process – as possible.

Using reaction microscopes in attosecond pump-probe experiments

The detection of charged particles in attosecond pump-probe beamlines is typically facilitated by time-of-flight or velocity-map-imaging spectrometers [228, 229]. Compared to these, a reaction microscope allows the coincident detection of the three-dimensional momentum vectors for all charged particles created in a single event (see chapter 4). This promises a range of conceivable advantages that can help in the interpretation of attosecond spectroscopy experiments:

- When the axial-recoil approximation holds in a fast dissociation (see page 58), detection of the ejection direction of a recoil ion allows the transformation of a coincidently detected electron into the molecular frame, which may be advantageous compared to measurements averaged over all orientations. Knowing the molecular orientation with respect to the XUV polarization direction in addition allows one to select specific transitions which are more likely for a particular orientation [136].
- Ionization to different final electronic states of the ion involves different potential-energy surfaces with different dissociation dynamics and possibly different resulting ion fragments. Electrons from such different channels may be distinguished by the coincident detection of the ion species (as in the strong-field experiments presented in part II) or, in the case of multiple ionization, by selecting events lying in specific regions of ion-ion correlation maps [18].
- For the single-photon ionization of a single electron in atomic targets, the relation $E_\gamma = E_\mathrm{e} + \mathrm{IP}$ holds between the photon energy E_γ and the kinetic energy of the released electron E_e, where IP is the ionization potential for the final electronic state of the cation. In general, multiple final electronic states are accessible for a given photon energy, each associated with a cross section. Using a broadband XUV source, this may lead to overlapping combs in the electron energy spectrum originating from different final cationic states already for atomic targets [133]. For molecules, the relation between E_γ and E_e is more complicated, in particular when the final cationic state dissociates. In this case, $E_\gamma = E_\mathrm{e} + \mathrm{KER} + I_\mathrm{DL}$, where KER is the kinetic-energy release from the dissociation and I_DL is the dissociation limit of the dissociating state, i.e. the value of the potential-energy surface corresponding to the dissociating cation state at infinite nuclear separation [230]. The kinetic-energy release further smears out the features in the electron energy spectrum. Using a reaction microscope, one can measure the kinetic-energy release coincidently with the photoelectron energy and

thus reverse this smearing.

- Electron-electron correlation maps provide insight into entangled multi-electron dynamics present in molecular systems [134].

These advantages have become evident in a range of recent experiments combining attosecond pulses and a reaction microscope: Already in single-beam experiments using attosecond pulse trains, the great wealth of information afforded by reaction-microscope detectors has proven to be useful, e.g. for the observation of a molecular-frame asymmetry in the ejection direction of the photoelectron with respect to the proton in the dissociative ionization of H_2 [230] or the determination of the lifetime of doubly excited, autoionizing states in the same molecule [231]. Pump-probe experiments relying on attosecond pulses and reaction microscopes have been primarily performed in the context of RABITT (see section 3.3). In particular, in ref. [134], RABITT has made it possible to determine the attosecond delay in the double ionization of xenon, revealing signatures of electron-electron correlations. Similar RABITT measurements have recently been performed in linear molecules: In ref. [136], the ionization delay in the dissociative ionization of H_2 was determined as a function of the photoelectron energy and the kinetic-energy release, demonstrating that coupled nuclear-electron dynamics influence the ionization delay. In ref. [137], a different ionization delay was measured in the dissociative photoionization of CO depending on whether the electron was emitted towards the C or towards the O side of the molecule. All of the above measurements rely crucially on the virtues afforded by reaction microscopes.

The inherent disadvantage of coincidence-detection schemes is the high repetition rate often required for reasonable acquisition times of data with good enough signal-to-noise ratio, since the fraction of ionization events per laser pulse must be significantly less than one in order to avoid false coincidences (see chapter 4). High laser repetition rates, on the other hand, imply that the energy per pulse is lower and/or the average power is higher compared to laser systems operating at lower repetition rates. Both consequences require special consideration in the design of an attosecond XUV-IR beamline which is to be combined with a reaction microscope.

Design goals for the beamline presented in this thesis

Such an attosecond XUV-IR beamline has been planned and installed in the context of this thesis. The goal of the project was to provide isolated attosecond XUV pulses and few-cycle IR pulses to a reaction microscope in a pump-probe scheme, where the delay between the pulses can be varied with attosecond precision. The flux of the XUV radiation must be high enough to interact with a target particle approximately every tenth laser pulse when focused into the molecular beam of the reaction microscope, in accordance with the requirements for coincidence detection and in order not to waste any laser pulses. The operating repetition rate is 100 kHz, which constitutes

an improvement by a factor of 10 compared to existing setups combining attosecond pump-probe spectroscopy with coincidence detection [229, 232]. Attosecond pump-probe beamlines operating at $\geq 100\,\mathrm{kHz}$ are also currently under development elsewhere [233–235].

At the time of writing, the beamline has been fully installed and tested with a velocity-map-imaging spectrometer instead of the reaction microscope. The results of these first tests will be presented in this part of the thesis (chapter 13), along with a detailed explanation of the design of the setup (chapter 12).

CHAPTER 12

Description of the Beamline

12.1 The laser system

Requirements for the laser system

A crucial prerequisite for (isolated- or close-to-isolated-) attosecond pulse generation via HHG is the availability of CEP-stable, few-cycle driving laser pulses, most commonly in the near-IR spectral regime. The focused intensity at the generation point must be high enough to efficiently initiate the HHG process via SFI. Typical laser peak intensities for phase-matched HHG in argon are in the range of 1 to 2×10^{14} W/cm^2. Usually, few-cycle laser systems operating at a few kHz deliver pulses with energies of at least a few hundred μJ, and such peak intensities can be easily reached with relatively loose focusing (FWHM beam sizes $> 100\,\mu$m in the focus).

Increasing the repetition rate implies that either the energy per pulse decreases or the average power of the laser system needs to be increased. A lower energy per pulse requires tighter focusing conditions to reach the intensities necessary for HHG. While the conversion efficiency can, in principle, be maintained for small focal spot sizes if the phase-matching pressure is adjusted accordingly [128, 129], the goal for the laser system used in the presented setup was to provide pulse energies not too much lower than what is used in other attosecond beamlines operating at lower repetition rates, since the available high-harmonic photon number still scales quadratically with the focus size [128] and due to practical problems with extremely tight focusing conditions because of the high divergence of the high-harmonic radiation. This requires

an increase in the average power of the laser system, which can be achieved by relying on the *optical parametric chirped-pulse amplification (OPCPA)* principle. Optical parametric amplification is a non-linear interaction of a *signal* beam and a *pump* beam in a crystal, whereby the signal beam is amplified and a third beam, the *idler*, with a frequency equal to the difference of the pump and signal beams, is created [95]. In the present case, a non-colinear geometry is applied, which means that the beams interact in the crystal at an angle. This allows the amplification of the signal over a broad bandwidth [236]. Compared to laser amplifiers based on titanium:sapphire crystals, which are most commonly employed in attosecond beamlines, the limitations imposed by thermal effects in the crystal are less severe for OPCPA laser systems, due to the instantaneous nature of optical parametric amplification [237]. An alternative approach to high-average-power laser systems delivering few-cycle pulses that is currently in development is the coherent combination of multiple, individually amplified beams [238] with subsequent non-linear post-compression [239].

Description of the OPCPA system

The attosecond setup presented in this thesis relies on an OPCPA laser system, which was designed and installed by Federico Furch and is capable of delivering CEP-stable 7 fs-pulses (central wavelength: 790 nm) with an energy per pulse of $\sim$200 μJ at a repetition rate of 100 kHz, resulting in $\sim$20 W of average power [240]. CEP stability has been confirmed on a pulse-to-pulse basis and is better than 300 mrad [241]. Furthermore, post-compression using a neon-filled hollow-core fibre has been implemented, resulting in sub-4 fs pulses with an energy of 70 μJ. The details of the system can be found in refs. [240, 242]. Here, a brief overview is presented.

The CEP-stable signal pulses are supplied by a titanium:sapphire oscillator (Venteon Pulse:One). A small fraction of the radiation from the oscillator is seeded into the pump laser in order to synchronize both lasers. The thin-disk Yb:YAG pump laser from Trumpf Scientific is able to deliver 900 fs-pulses at a central wavelength of 515 nm, a repetition rate of 100 kHz, and with an average power of 120 W. After going through a pulse shaper, which can be used to temporally manipulate the pulses, and a stretcher, which increases the pulse duration to 300 fs, the signal pulses are amplified from 250 pJ to 240 μJ in two non-colinear optical parametric amplification stages, where 10 % of the pump power goes to the first stage and 90 % to the second. The overall conversion efficiency is 0.22. Output power fluctuations are on the order of 1 %. Since the amplified spectrum depends on the delay between the pump and signal beams, this delay is kept constant by an active delay-stabilization system. In addition, several systems for beam-pointing stabilization ensure stable spatial overlap of the beams in the crystals and stable pointing of the amplified beam going to the HHG setup. Note that the stability of the laser output is also crucial

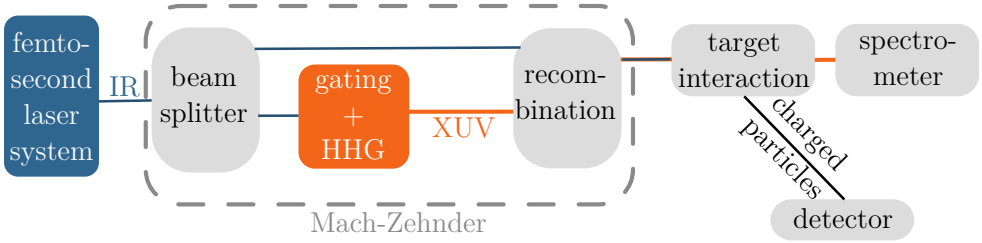

Figure 12.1: Schematic overview of attosecond pump-probe beamlines.

for the overall stability of the attosecond pump-probe setup. To recompress the stretched amplified pulses (i.e. adjust the spectral phase of the broadband pulses to get close to the Fourier limit), a set of chirped mirrors [243] is utilized. Higher-order dispersion is adjusted using the pulse shaper.

As already mentioned, after compression the duration of the 7 fs-pulses can be further decreased by broadening the spectrum using a gas-filled hollow-core fibre. Broadening in such a fibre is achieved by relying on the non-linear effect of self-phase modulation [95]. The fibre has a length of 1 m and a diameter of 340 μm and is usually filled with ∼2.5 bar of neon. It is additionally pumped from the entrance side to create a pressure gradient from entrance to exit. This improves spectral broadening and the transmission of the fibre [244]. After broadening, the pulses are compressed again using another set of chirped mirrors. This way, pulses with a duration of less than 4 fs, a spectrum ranging from less than 500 nm to more than 1050 nm, and an energy per pulse of 70 μJ are available for experiments. The hollow-core fibre was used for some but not all of the results presented in chapter 13.

12.2 DESIGN CONSIDERATIONS

General structure of attosecond pump-probe beamlines

Before proceeding to the presentation of the beamline designed in the framework of this thesis, common features of existing attosecond pump-probe setups [12, 229, 245–250] will be presented. Generally, the setups consist of an interferometer, with the generation of the short XUV pulses via HHG in one arm and propagation of unconverted IR pulses in the other. The IR pulses typically have a duration of less than 10 fs. HHG needs to take place in vacuum, because the generated radiation with photon energies in the XUV regime would otherwise be immediately reabsorbed by the air. Furthermore, from the high-harmonic generation point to the point of interaction with the target (hereinafter referred to as the *interaction point*), the vacuum conditions are usually improved by one or several stages of differential pumping (see footnote on page 50). This is necessary because the HHG gas target puts

significant gas loads on its environment, whereas the detectors in the interaction region require a lower pressure to be operated.

The target at the generation point usually consists of a gas-filled cell, with a hole for the laser to propagate through. The laser is focused into the cell with a typical focal length of 0.5 m to 1 m. After generation, since only a negligible fraction of the driving laser power is transformed into XUV radiation, one needs to filter out the co-propagating driving laser beam. This is achieved using a thin (∼200 nm) metal filter, which absorbs the IR and transmits a significant fraction of the XUV.

There are two different basic designs of the interferometer: The split-mirror design employed in the setups in refs. [245–247] is very compact and inherently stable, but it is difficult to manipulate the IR and XUV arms independently and to implement gating schemes to isolate a single attosecond pulse. The second type of design used in the setups in refs. [12, 229, 248–250] and schematically shown in fig. 12.1 relies on a spatially more separated Mach-Zehnder interferometer, where the two beams are steered by independent optical elements: The IR beam is initially split up using either an optical beam splitter or a mirror with a hole. The larger portion of the power is sent to the HHG chamber. Before HHG, a gating scheme may be implemented. After HHG and filtering of the driving IR radiation, the generation point is imaged to the interaction point using a grazing-incidence toroidal mirror. The smaller portion of the IR power travels from the beam splitter via a delay stage to the recombination mirror, which is a conventional IR-reflecting mirror with a hole in the centre for the XUV to propagate through, due to the lack of suitable dichroic mirrors for XUV and IR. Recombination can either occur before or after the toroidal mirror, where, in the latter case, an additional curved mirror focuses the IR beam into the interaction region. Note that, due to the relatively long interferometer arm length, an active stabilization system is needed, which consists of a stable, narrow-bandwidth cw-laser, following the beam paths in the two arms of the interferometer, such that, after recombination, from the fringe pattern from the interference of the beams in the two arms, unwanted drifts in the interferometer can be detected and compensated. Putting the complete interferometer in vacuum is also beneficial for the stability [248].

While the attosecond XUV-IR pump-probe beamline developed in the framework of this thesis is similar to the existing setups, the high repetition rate and the use of a reaction microscope as the detector pose a number of additional challenges, which need to be considered in the design:

High average power due to the high repetition rate

As explained above, the high repetition rate implies a higher-than-usual average power propagating through the beamline. This adds a complication when filtering the driving IR radiation after HHG: The standard approach of using a metal filter is no longer viable for average powers exceeding a few watts,

because the heat from the absorbed IR radiation would destroy the filter [97, 251, 252]. A range of alternative approaches exists for the separation of the IR from the XUV radiation [252, 253]. Using a simple silicon plate at Brewster's angle offers relatively high (~ 0.5) reflectivity in the XUV and high suppression in the IR ($\sim 10^{-4}$) [254]. However, the disadvantage is that the IR radiation is absorbed, which is expected to lead to significant heating of the silicon substrate. This could induce deformations, which would be detrimental for stability. In addition, the IR suppression only works well for p-polarization, whereas both components are significant when using polarization gating (see page 34). This is why a different solution was chosen, namely the application of an anti-reflective coating for the IR on a fused-silica substrate. The final layer of the anti-reflective coating consists of SiO_2, which, at the employed high angle of incidence and in the relevant spectral region, provides decent reflectivity (~ 0.4) for the XUV radiation, which does not penetrate beyond the top layer. The anti-reflective coating leads to an IR transmission of 0.8 (p-polarization) and 0.85 (s-polarization) over a significant portion of the spectrum of the IR pulse.[1] The design and fabrication of the coating was done in the group of Carmen Menoni at Colorado State University. After reflection from this *filter mirror*, the remaining IR power is low enough to be removed using a metal filter.

A further consequence of the high average power could be that thermal issues arise close to the HHG target. As mentioned, the target is typically a gas-filled cell with small entrance and exit orifices for the laser beams. With a well-focused beam with stable pointing, this solution is expected to also work with higher average power. However, under non-ideal conditions, it may occur that stray light due to imperfect focusing is absorbed by the cell, which could either increase the size of the orifices over time (increasing the gas load into the HHG chamber and changing the steady-state pressure conditions within the cell) or even lead to the complete destruction of the target. A solution to this possible issue is to allow for the use of a free-standing jet target in the design.

Lower-than-usual energy per pulse and sufficient high-harmonic flux for experiments

The beamline was designed to work with pulse energies as low as 60 μJ available for HHG and as long as 8 fs, since the actually available laser parameters were not yet known in the design phase of the setup. As mentioned in section 12.1, to achieve the required intensity needed for HHG in argon with these parameters, the driving laser beam must be focused to a significantly smaller spot size than what is commonly used in attosecond pump-probe setups, and this, in

[1] Note that the design for the anti-reflective coating was optimized for the 7 fs-pulses prior to broadening with the hollow-core fibre. A new design having a high transmissivity for the whole broadened spectrum should be feasible.

turn, requires high target densities for phase-matched HHG. Increasing the pressure, however, puts increasing demands on the vacuum pumps, which need to keep the pressure in the generation chamber low enough to prevent the reabsorption of the high-harmonic radiation while propagating through the chamber. In the tight-focusing regime, high target pressures can be reached more efficiently (i.e. requiring less pumping speed) with a jet instead of a cell target, because there is a regime, where increasing the nozzle size (which determines the interaction length) actually decreases the required pumping speed. This is because the gas density at the same distance to the nozzle is larger for a larger nozzle, and thus a lower backing pressure can be used [129]. Therefore, using a nozzle diameter larger than the optimum interaction length L_{med} (see section 3.2) helps to reduce the gas load in the tight-focusing regime. In the loose-focusing regime, on the other hand, the long optimum interaction length implies prohibitively large nozzle diameters, making a cell, where the gas flow is independent of L_{med}, the preferred solution. Since the expected pulse energies were in a transition regime between tight and loose focusing conditions, the beamline was designed to allow easy switching between cell and jet targets.

Vacuum requirements

In additions to the requirement of having good enough vacuum for the high-harmonic radiation not to be reabsorbed on its way to the reaction microscope (10^{-3} mbar from the HHG generation chamber onwards [25]) and to be able to operate the multi-channel plate detectors ($<10^{-5}$ mbar), the reaction microscope poses even more severe constraints on the required vacuum conditions. This is because the distance from the molecular-beam source to the interaction region in the centre of the reaction microscope is relatively large compared to a velocity-map-imaging spectrometer, where the source nozzle can be brought very close to the point of interaction [255]. This means that, in the reaction microscope, the density of the molecular beam will be much lower, and, therefore, the density of the background gas needs to be lower, too. Otherwise, contributions from the background gas, for which the interaction volume is much higher, would dominate the signal from the molecular beam. The pressure in the reaction microscope should thus be better than $\sim 10^{-8}$ mbar [232].

In order to achieve this, several measures have been taken: A catcher system can be used in combination with a jet target – where the gas loads are expected to be especially high for not very tight focusing conditions –, and the HHG chamber has been designed to accommodate turbomolecular pumps with high pumping speeds (which have large flanges), such that the pressure is kept as low as possible right from the point of generation. In addition, two differential-pumping stages and the relatively large spatial extent of the setup from the HHG chamber to the reaction microscope[2] help to establish a large

[2]This is the result of the fact that, due to spatial constraints, the reaction microscope

pressure differential.

Attosecond stability

Whether pump-probe experiments are performed using isolated attosecond pulses or attosecond pulse trains, to achieve attosecond temporal resolution it is crucial that the timing between the XUV and IR fields is very stable, such that fluctuations are less than a few tens of attoseconds, which can already be caused by mechanical movement with an amplitude on the order of 10 nm. Since the interferometer in the presented setup is relatively large, high stability is even more difficult to achieve. The following measures were taken to increase stability:

- All optical elements were placed in stable mounts with as short posts as possible.
- Within the chambers, the optical elements are placed on breadboards, which are mounted directly on the laser table but decoupled from the chamber walls via flexible bellows. This reduces vibrations from the pumps mounted on the chambers (and minimizes distortions when the chamber is evacuated or vented). The design of the breadboard feet in order to achieve this is shown in fig. 12.3b). The chambers, in turn, are decoupled from the table by placing them on special vibration-isolation feet.
- The turbomolecular pumps are magnetically levitated, which means that they induce less vibrations than pumps with conventional bearings.
- An active-stabilization system is installed.
- The whole interferometer may be evacuated and operated under vacuum. This removes disturbing influences from air flow.
- The spatial separation of the detection system from the interferometer and laser system helps to reduce disturbances due to operating personnel.

12.3 DETAILED DESCRIPTION OF THE BEAMLINE

Overview

An overview of the setup is shown in fig. 12.2. The beam coming from the laser system with a polarization perpendicular to the table surface enters the L-shaped *interferometer chamber* through a 500 μm-thick fused-silica window. A beam splitter (BS, typical transmission-to-reflection ratio: $^{90}/_{10}$ or $^{80}/_{20}$) is used to split the beam into the two parts of the interferometer. The larger fraction is sent to a focusing mirror (FM1) with a focal length of 50 cm, which focuses the beam through a 500 μm-thick fused-silica window into the *HHG*

needed to be placed in a separate room from the laser system, since a toroidal mirror with 1 : 1-imaging is employed to minimize aberrations [256].

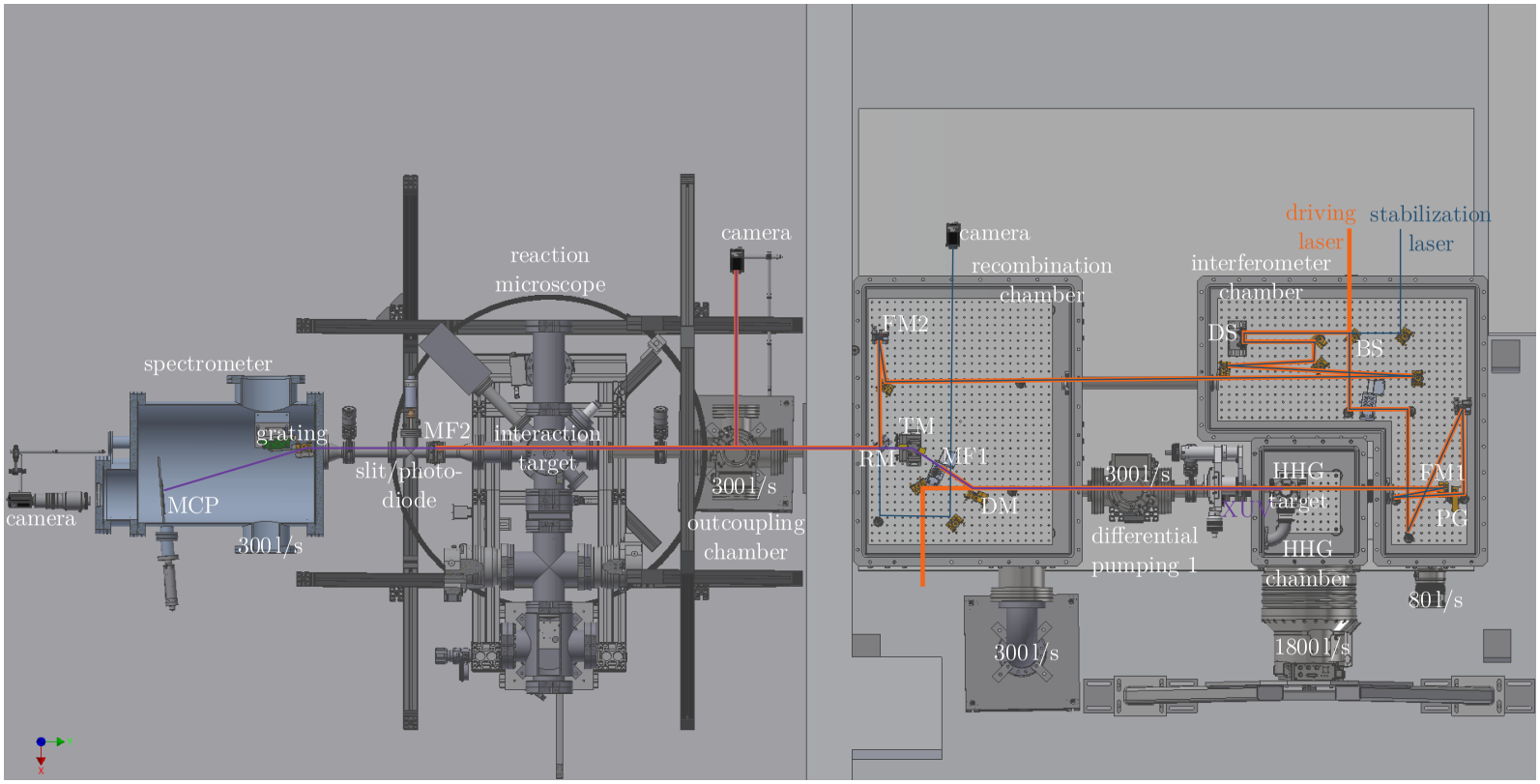

Figure 12.2: Overview of the designed attosecond pump-probe beamline. The following abbreviations are used: BS - beam splitter; DS - delay stage; FM1 - focusing mirror 1; PG - polarization-gating setup; FM2 - focusing mirror 2; TM - toroidal mirror; RM - recombination mirror; MF1 - metal filter 1; MF2 - metal filter 2; DM - dichroic filter mirror. Also indicated are the pumping speeds utilized in the various parts of the beamline.

chamber, where it interacts either with a jet or cell target. The target is usually placed slightly behind the focus to enforce phase matching for the short trajectory. Close to the focusing mirror, a polarization-gating setup (PG) can be accommodated. Between the polarization-gating setup and the high-harmonic generation point, only reflections close to normal incidence take place in order not to disturb the polarization of the beam containing both s- and p-contributions.

After HHG, the XUV and driving IR beams co-propagate through the *first differential-pumping stage* into the *recombination chamber*, where the XUV is reflected off the dichroic filter mirror (DM), placed at an angle of incidence of 75°. The transmitted IR light is sent out of the chamber, where it is deposited, to avoid heating of parts within the chamber, which could lead to unwanted thermal effects. The remaining IR radiation is filtered out using a metal filter (MF1, usually aluminium with a thickness of 200 nm) mounted on a motorized stage (Zaber T-NA08A25-SV2), allowing the filter to be moved into and out of the beam path.

A significant portion of the XUV beam is transmitted by the filters and continues to propagate to the gold-coated *toroidal mirror* (TM). A toroidal mirror has two different radii of curvature, R_T and R_S, in the horizontal (*tangential*) plane and in the vertical (*sagittal*) plane, respectively. The radii of curvature required for 1 : 1-imaging of the high-harmonic generation point to the interaction point in the reaction microscope are determined according to [257]

$$R_\mathrm{T} = s \cdot \frac{1}{\cos\theta}$$
$$R_\mathrm{S} = s \cdot \cos\theta,$$

where $\theta = 75°$ is the angle of incidence on the toroidal and $s = 1250\,\mathrm{mm}$ is the distance from the high-harmonic generation point to the toroidal and from the toroidal to the interaction point in the reaction microscope, leading to $R_\mathrm{T} = 4830\,\mathrm{mm}$ and $R_\mathrm{S} = 324\,\mathrm{mm}$. A toroidal mirror is needed because the large angle of incidence would cause inacceptable aberrations when using a spherical mirror. The large angle of incidence increases reflectivity for the XUV radiation. The two 75°-reflections from the filter mirror and the toroidal mirror lead to a geometry where the beams coming from the HHG chamber and going to the reaction microscope are parallel but displaced with respect to each is other. The toroidal mirror is mounted on a motorized five-axis stage (Newport 8081-UHV), which allows the precise alignment of the toroidal mirror in order to minimize aberrations.

Closely behind the toroidal mirror, the XUV beam is recombined with the IR beam from the other arm of the interferometer, the XUV beam going through a 5 mm-hole in the *recombination mirror* (RM), whereas the outer portion of the IR beam is reflected off the mirror.

The beam in the other arm of the interferometer first encounters a pair of mirrors mounted on a linear stage (DS, Smaract SLC-1750-S-HV), which is used to adjust the delay between the two arms. The stage combines nanometre resolution with a long travel range of 30 mm and thus circumvents the use of two separate delay units for precise scanning with a small step size and longer-range adjustments, respectively. The IR beam is subsequently sent to the recombination chamber through a 500 μm-thick fused-silica window, to completely vacuum-separate the two chambers. A concave mirror (FM2) with a focal length of 1.5 m then starts focusing the beam, which is recombined with the XUV beam as explained. Both the focusing and the recombination mirrors are motorized and can be used to make the XUV and IR beams precisely parallel: Even a small angle between the IR and the XUV beams leads to a position-dependent delay over the extent of the focus in the interaction region of the reaction microscope, which degrades the temporal resolution.

The dispersion of the beams in the two arms can be independently adjusted using a pair of glass wedges in each arm. One of the wedges from each pair can be moved using motorized linear translation stages (Zaber T-NA08A25-SV2), thus changing the amount of glass through which the beam propagates. In addition, the two beams can be independently blocked using motorized Thorlabs ELL6 stages, where a mirror sends the beams to a beam dump in the blocked state.

After recombination, the IR beam, having an annular shape, co-propagates with the XUV beam towards the reaction microscope. In the *outcoupling chamber*, a mirror on a linear-motion vacuum feedthrough can be used to send the beams through a window out of the vacuum towards a beam profiler placed in the focus of the beams. This assists in finding both the spatial and the temporal overlaps of the beams. Note that in order to do this the metal filter is removed from the XUV beam path, such that the driving IR beam can be used as a substitute for the actual XUV beam in this procedure. The temporal overlap can be detected from the appearance of fringes where the two beams spatially overlap. At time zero, the maximum modulation depth is attained. In addition, for precisely parallel beams, the fringes form concentric rings, whose overall intensity is modulated by the delay.

The focus of the IR beam is larger than the one of the XUV beam, because of the larger focal length of the focusing mirror FM2 compared to FM1 and the generally smaller divergence of the XUV radiation. This minimizes variations of the IR intensity and phase over the interaction volume of the XUV with the molecular beam.

After the interaction with the target in the reaction microscope, the beams continue to propagate towards the XUV spectrometer, which monitors the spectral composition of the XUV radiation. Before entering the spectrometer, the IR beam is removed using an aluminium filter (MF2, thickness: 200 nm), which is mounted on a gate valve. This also serves as a vacuum separator between the reaction microscope and the spectrometer. In addition, either a

slit or a calibrated XUV photodiode (Optodiode AXUV100G) can be moved into the beam path using a linear-motion vacuum feedthrough. The slit, whose size is adjustable, only transmits a thin slice of the XUV beam, which is then imaged by the grating in the spectrometer to the MCP (see below), to improve the spectral resolution of the spectrometer at the cost of losing intensity. The calibrated photodiode can be used to obtain an absolute measurement of the XUV photon flux impinging on it. The small current induced in the diode is measured directly using a picoammeter and can be converted to a photon flux using the known spectral responsivity of the photodiode.

The grating in the spectrometer is mounted on a motorized stage, such that it can be moved out of the beam path, which allows the beams to leave the spectrometer at the back through a window. This is useful for purposes of alignment.

The various chambers in the setup can be separated by several gate valves with integrated windows, such that parts of the beamline can be under atmospheric pressure while doing the alignment without affecting the vacuum in other parts.

Active delay stabilization

As mentioned previously, active delay stabilization is used in the interferometer to ensure its long-term stability. The approach used here is similar to those introduced in refs. [229, 249]. A Cobolt Blues cw-laser operating at a wavelength of 473 nm with a FWHM bandwidth <1 MHz and an output power of 50 mW is used as the reference laser. The short wavelength improves the accuracy of the stabilization system.

The output from the stabilization laser enters – upon increasing its beam size with a telescope – the interferometer chamber through a window. In the chamber, it is coupled into the interferometer using the beam splitter BS. There, it is split up and subsequently co-propagates with the IR/XUV beams all the way to the recombination mirror. Note that the coating of the filter mirror in the HHG arm also reflects a significant portion of the stabilization beam. In order for the stabilization beam to also be able to propagate past the metal filter MF1, the filter's size was chosen to match the beam diameter of the XUV beam (5 mm) and the filter is mounted on a fused-silica substrate, such that the stabilization beam, which has a larger diameter, is transmitted in a ring around the centre.[3]

The recombination mirror has been drilled twice, at angles ±45° with respect to the surface normal, to have a clear path for both the propagation of the XUV beam and the central portion of the stabilization beam in the other arm of the interferometer. In addition, the mirror has a transparent

[3]Note that this is also true for the outer part of the driving IR beam, which is, however, subsequently blocked by the recombination mirror, such that no driving IR radiation reaches the interaction region in the reaction microscope.

substrate, such that the stabilization beam in the XUV arm can reach the back surface of the silver coating, where it is reflected. The parts of the stabilization laser beam going through the hole in the mirror and reflected off its back surface are subsequently picked off by two mirrors and spatially overlapped on a beam profiler outside of the recombination chamber. The stabilization beams from the two arms form a spatial interference pattern where they overlap, which is recorded with the beam profiler and from which changes in the length difference between the two arms (for example due to mechanical movement or thermal drifts) can be inferred and compensated by moving the delay stage DS. In addition, the interference pattern is also used to purposefully change the delay between the two arms by a well-defined amount. These functions are facilitated using a software developed by Tobias Witting. The stabilization operates at a rate of 500 Hz, thus being able to correct slower drifts of the system, but not very fast disturbances such as noise from the pumps.

Interferometer chamber

The L-shaped interferometer chamber is completely vacuum-separated from the other chambers, allowing the full operation of the beamline with the interferometer chamber either under vacuum or atmospheric conditions. The design is thus a hybrid between beamlines placing the whole interferometer or only the XUV part, respectively, in vacuum. Optical elements in the interferometer chamber can be quickly adjusted manually in the preparation phase of an experiment, and the interferometer chamber can be evacuated when performing a measurement to increase stability. Under vacuum, further adjustments can be made by several motorized components in the chamber. In order to allow the visual inspection of all optical elements even when the chamber is evacuated, transparent top lids made from acrylic glass are used.

The shape of the chamber makes it possible to place the HHG chamber close to the focusing optics in the interferometer chamber (and thus to use relatively short focal lengths) and, at the same time, to have enough space in the chamber for all parts needed for the Mach-Zehnder interferometer and manipulation of its two arms. The two chambers are connected via a flexible bellow.

The interferometer chamber is pumped by a small 80 l/s turbomolecular pump, since the vacuum inside only needs to be good enough to prevent disturbances of the interferometer due to air flow, as it is well separated from the neighbouring chambers, where stricter vacuum requirements are demanded. The vacuum separation is facilitated by sealing surfaces on both sides of the wall around the output flanges towards the HHG and recombination chambers, such that vacuum-separating windows can be mounted on the inside of the chamber. The mild vacuum requirements also imply that (well-cleaned) normal optomechanical components can be used in the interferometer chamber instead

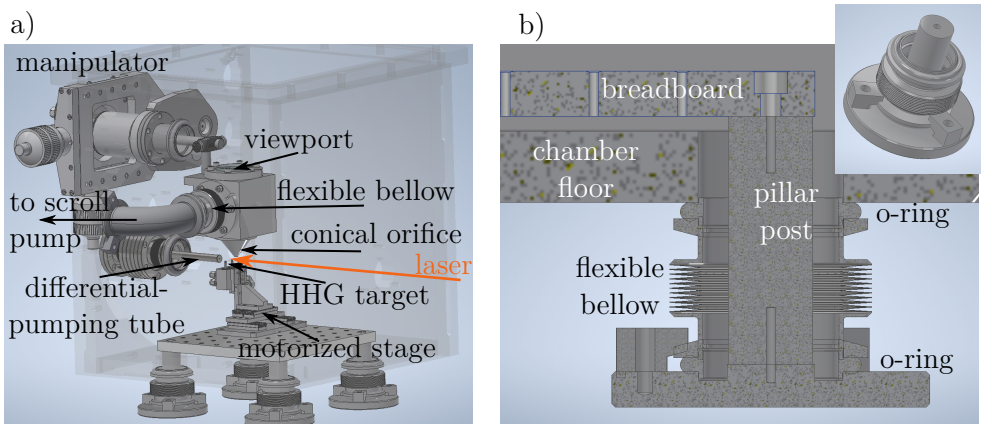

Figure 12.3: a) Design details of the gas-catching system in the HHG chamber used in combination with a jet target. b) Design of the feet decoupling the optical breadboards from the chambers.

of components rated for high vacuum. Nonetheless, in practice, pressures in the 10^{-4} mbar-range are reached in the chamber.

The flanges on the sidewalls of the chamber accommodate electrical feedthroughs for the various motorized elements in the chamber and windows for the IR and stabilization beams to enter. Additional output flanges allow some flexibility in how the chamber is connected to the neighbouring chambers. All optical elements are placed on a single L-shaped breadboard, decoupled from the chamber as shown in fig. 12.3b), while the chamber itself is placed on compact elastomeric vibration-isolating feet (Newport M-ND01-A).

HHG chamber

The HHG chamber provides a separated space for the HHG target, which is mounted on a motorized compact stage with three translational degrees of freedom (custom product by Smaract). The chamber is placed on the optical table using the pneumatic isolation feet Newport CM-225, because none of the available (more compact) elastomeric isolators were suited for the weight of the chamber. The size of the chamber is determined by the requirement that a pump with a pumping speed of up to 3000 l/s could be installed, for which a flange diameter of 250 mm is needed. Such high pumping speeds might have been necessary when using a jet target and relatively loose focusing conditions. In addition, the relatively large size of the chamber would also make it possible to move the focusing optics from the interferometer into the HHG chamber, in case very tight focusing conditions (focal length ∼20 cm) were necessary.

To reduce the pressure load from the jet further, it is additionally possible to mount a gas-catching system in the chamber, whose design is presented in

fig. 12.3a) and is adapted from a similar design developed in the group of Ralph Ernstorfer at the Fritz Haber Institute in Berlin [258]. The position of the catcher with respect to the jet can be controlled from outside the chamber using a manual vacuum manipulator with three translational degrees of freedom. The catcher itself consists of a hollow aluminium block, on the bottom surface of which a cone is attached. The gas from the jet enters the catcher through a 3 mm-hole in the tip of the cone. Due to the conical shape, the catcher can be brought close to the laser (and thus to the nozzle, which is expected to improve the catching efficiency), while at the same time pumping it efficiently, using a $40\,\mathrm{m}^3/\mathrm{h}$ scroll pump (which is well suited for the 10^{-2} mbar regime present in the catcher under a typical load). On the top surface of the block, a viewport (in combination with the transparent top lid of the chamber) makes it possible to look at and align the nozzle below the catcher. In practice, the catcher improves the pressure in the HHG chamber by one order of magnitude, when loaded by a jet target.

The nozzle for the jet target was made from a glass capillary glued into a drilled Swagelok blanking plug. The design for the cell target consists of a block accommodating three cells in a row, which can be independently filled with gas from outside. This makes it possible to easily switch from one cell to another without breaking the vacuum, by moving the stage horizontally in the direction perpendicular to the laser beam. A tape is wrapped around the holes in the cells, in which subsequently a smaller hole is drilled directly with the laser, which helps to reduce the gas flow from the cell to the vacuum chamber. However, slight changes in the pointing of the laser, for example due to small adjustments, increase the hole size, which is why there is the possibility to quickly switch to a different cell. Only after consuming three cells in this way, the chamber needs to be opened to replace the tape around the cells. The gas to the targets is supplied via flexible plastic tubes.

Shortly behind the high-harmonic generation point, the beams enter a tube with a diameter of 10 mm protruding into the chamber, as shown in fig. 12.3a). The tube can be positioned from the outside, because the flange it attaches to is connected to the neighbouring elements via flexible bellows. The tube end can additionally be sealed with aluminium tape through which a hole is drilled with the driving laser, making the orifice just big enough for beam propagation. Since the tube end is very close to the generation point, where the beam diameter is small, the tube with the drilled tape has a low vacuum conductance, resulting in effective differential pumping. In addition, the generated high harmonics quickly leave the region of high pressure, minimizing reabsorption of the radiation.[4]

[4]Note that, while the overall pressure in the HHG chamber is low enough for reabsorption of the high-harmonic radiation to be negligible, the local pressure around the target is expected to be higher.

Recombination chamber

The recombination chamber is the place where the IR-only and XUV beams are recombined and focused and where the co-propagating generating IR light is removed from the XUV beam. It is sealed on the top with two lids, where aluminium is used instead of acrylic glass due to the higher demands on the vacuum in this chamber because of its proximity to the reaction microscope. To nonetheless allow the visual inspection of the beamline under operation (using cameras), several larger viewports are installed on the sidewalls of the chamber. The remaining flanges are used for the connection to the neighbouring chambers, electrical feedthroughs for the motorized components, and windows for the stabilization laser and IR radiation transmitted by the filter mirror. The chamber is pumped by a 300 l/s turbomolecular pump. Decoupling from the table is again facilitated by Newport M-ND01-A vibration-isolation feet.

Spectrometer

The spectrometer[5] contains a flat-field imaging grating (Hitachi 001-0640), which angularly separates the spectral components of the incoming XUV beam according to eq. (3.2) and maps them to a flat plane, in which the screen is placed. The mount of the grating makes it possible to adjust all six rotational and translational degrees of freedom in order to facilitate precise positioning and alignment of the grating. The screen consists of a stack of an MCP and a phosphor screen and is mounted on a linear-motion vacuum feedthrough, which allows translation within the focal plane. The MCP amplifies electrons created by the impact of XUV photons, and the phosphor screen emits visible light at the position of the electron cloud at the back of the MCP. The higher the photon flux impinging on the MCP front surface is, the brighter the emitted visible light from the phosphor screen is. The image seen on the phosphor screen thus corresponds to the intensity of the spectral components of the incoming XUV beam dispersed in the horizontal direction, whereas the intensity distribution in the vertical direction is representative of the vertical spatial intensity profile of the beam. The image on the phosphor screen is recorded using a camera with a zoom objective from outside the chamber through a viewport. The spectrometer is pumped by a 300 l/s turbomolecular pump.

[5] A significant portion of the design of the spectrometer has been done by Peter Šušnjar, based on a design by Sascha Birkner.

CHAPTER 13

First Characterization of the Beamline

In this chapter, first results obtained with the beamline described in the previous chapter are presented. Since the beamline had not yet been fully installed at the time of writing of this thesis, the scope of the results is limited to high-harmonic spectra recorded under various conditions (section 13.1) and a first pump-probe FROG-CRAB measurement for pulse characterization using a velocity-map-imaging spectrometer as the detector (section 13.2).

13.1 High-harmonic generation

High-harmonic spectrum

An example of a high-harmonic spectrum, recorded using a cell target (inner diameter: 1 mm) filled with 110 mbar of argon, is shown in fig. 13.1a). To obtain a discrete spectrum, the few-cycle pulses from the hollow-core fibre were slightly stretched using a pair of wedges. Figure 13.1b) displays an image similar to what is recorded on the phosphor screen in the spectrometer: The spectral composition is shown along the (energy-calibrated) horizontal and the spatial profile of the XUV beam along the vertical axis. Because the difference in energy between any two adjacent harmonics needs to be twice as large as the fundamental laser photon energy, the initially non-linear spacing of the harmonics on the screen according to eq. (3.2) allows an absolute calibration of the energy axis, using the distance of the screen from the grating, and the fundamental laser wavelength. The harmonics extend up to an energy

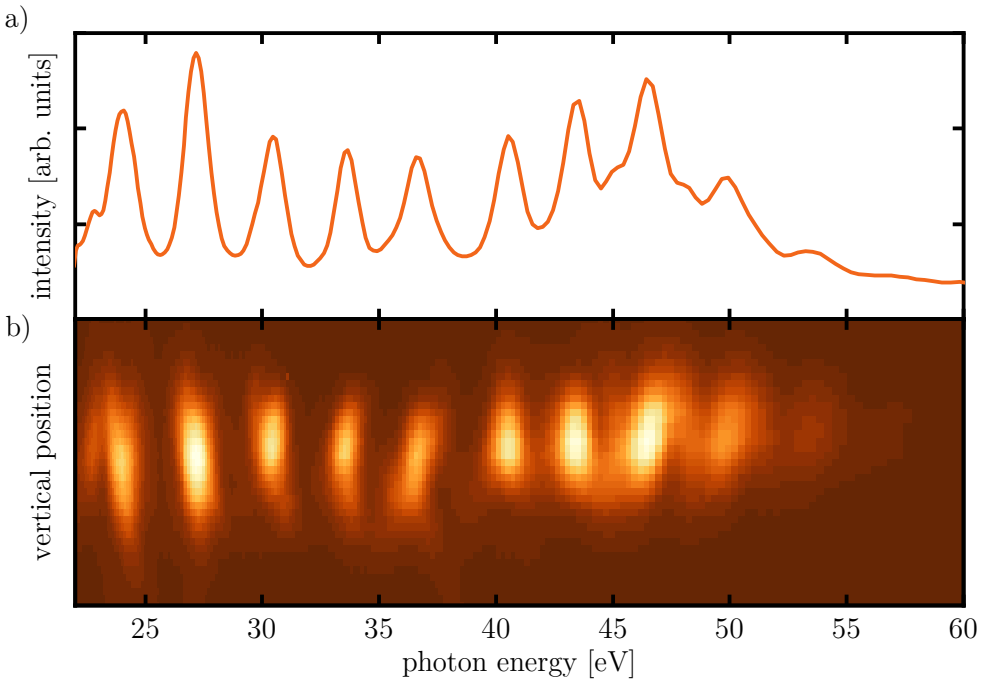

Figure 13.1: a) Calibrated high-harmonic spectrum generated with stretched few-cycle pulses using a cell target filled with 110 mbar of argon. Adjacent harmonics are spaced by the photon energy, in accordance with the calibration. The target was placed slightly behind the focus to select the short trajectory. b) additionally displays the spatial XUV beam profile along the vertical axis.

of ∼55 eV, from which a peak intensity of $I \approx 2 \times 10^{14}\,\mathrm{W/cm^2}$ can be deduced according to eqs. (1.18) and (3.1), using the known IP of argon of 15.8 eV.

The slight tilt of the harmonics in fig. 13.1b) indicates a *spatial chirp* in the XUV beam, i.e. different parts of the spatial beam profile feature a different spectral composition. This spatial chirp of the XUV beam likely derives from a spatial chirp in the driving laser. The different directions of the tilt for different energies could be the result of spatiotemporal couplings [259] in the driving laser, leading to a locally different transient ionization fraction and thus plasma dispersion.

Influence of the target position along the propagation direction

The phase-matching conditions are influenced by the position of the HHG target along the driving-laser focus (see section 3.2). In fig. 13.2, the dependence of the generated harmonics on this position is investigated. According to fig. 13.2e), there is a single position of maximum high-harmonic intensity,

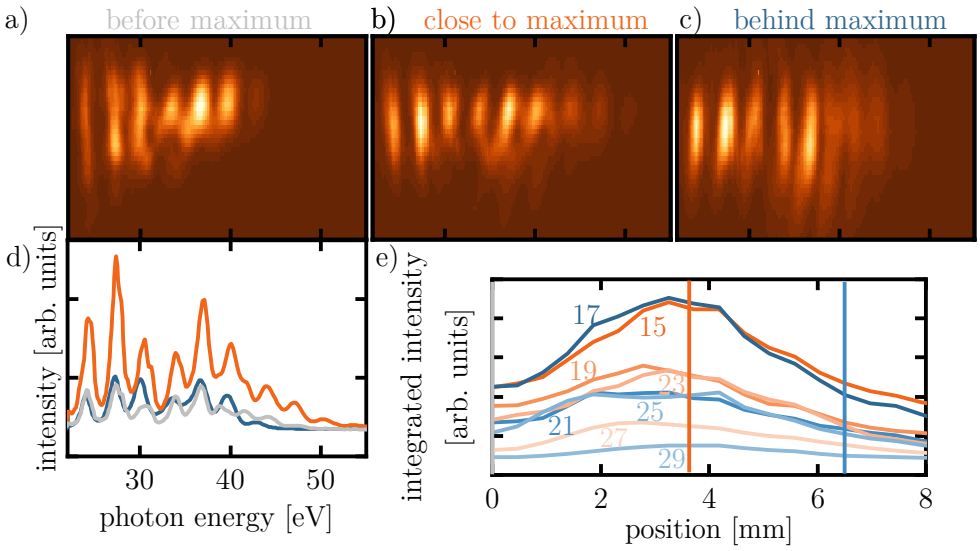

Figure 13.2: a), b), c): Spatially resolved high-harmonic spectra, generated under similar conditions as the one shown in fig. 13.1, for different target positions along the beam propagation direction (indicated in e)). Note that the colour scale is different for the three spectra. d) The corresponding projections onto the energy axis (orange: close to maximum, grey: before maximum, blue: behind maximum). e) Scan of the intensity of various high-harmonic orders (indicated in the figure) as a function of the position.

which is almost independent of the harmonic order. Figures a), b), and c) display spatially resolved spectra where the target was placed before, close to, and behind this maximum position, respectively. The spectrum in fig. 13.2a) looks distorted, which is likely due to (partly overlapping) contributions from both the short and the long trajectories. Note that long-trajectory harmonics are generated with a larger divergence [125, 126] and thus are expected to arrive at the detector further away from the centre of the beam. In fig. 13.2c), on the other hand, the spectrum looks much cleaner, and the high harmonics show up as approximately parallel stripes on the screen of the spectrometer. In fig. 13.2b), a small contribution from the long trajectory is still evident. Therefore, to completely suppress these contributions – and thus obtain a temporally clean attosecond pulse – the target should be placed a little behind the position of maximum high-harmonic intensity.

Pressure dependence, comparison of different targets, and absolute photon flux

As explained in section 3.2, for efficient HHG it is important that phase matching is achieved over the interaction length of the laser with the target.

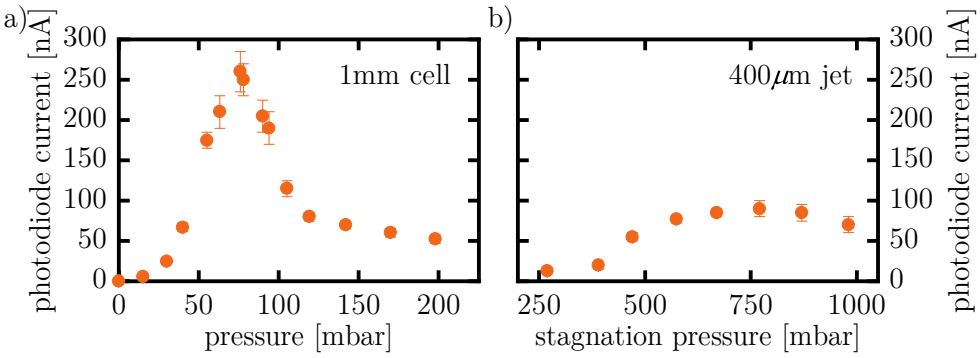

Figure 13.3: The photon flux from high-harmonic radiation, generated by sub-4 fs-pulses, on a calibrated photodiode as a function of the pressure for a) a cell target (inner diameter: 1 mm) and b) a jet target (nozzle diameter: 400 μm). The indicated pressure is the pressure in the cell in a) and the stagnation pressure before the expansion through the nozzle in b). Note that the actual pressure of the target after the expansion is lower than this value. The indicated error bars are estimated from the fluctuations of the diode current.

The simplest parameter to adjust the phase-matching conditions is the density of the target. The required density is determined by how tightly the driving laser beam is focused into the target. Under tight-focusing conditions, the necessary densities may be more easily achieved using a jet instead of a cell target (see page 148).

Thus, in fig. 13.3, a comparison of pressure scans for a jet target (nozzle diameter: 400 μm)[1] and a cell target (inner diameter: 1 mm), using compressed sub-4 fs-pulses from the hollow-core fibre for HHG, is shown. Note that the target density is proportional to the applied pressure in both cases. The absolute photon flux, integrated over the portion of the spectrum transmitted by the aluminium filter (i.e. photon energies $\gtrsim 20$ eV), was measured using the calibrated XUV photodiode. With the cell target, an overall larger current from the photodiode is obtained compared to the jet target for the respective optimum pressure. Note that for a cell target higher reabsorption of the generated high-harmonic radiation is to be expected, due to a potentially locally higher gas density along the propagation path of the XUV radiation. Since, however, the attainable flux is higher for the cell than for the jet target and since the cell is able to withstand the high average power of the laser beam, a cell target appears to be the preferred solution for the focusing conditions present in the beamline. Cells with a larger inner diameter may further increase the high-harmonic flux.

[1] Note that a smaller nozzle diameter of 150 μm was also tested and resulted in significantly lower photon fluxes even when using several bars of stagnation pressure.

From the measured current on the calibrated XUV photodiode, using the average quantum efficiency of the photodiode of 0.26 A/W over the spectral region occupied by the XUV pulses and taking the transmission from the source to the photodiode into account, an absolute photon flux at the source of 5×10^6 photons/laser pulse is obtained. This corresponds to a conversion efficiency of 10^{-6} averaged over the XUV spectrum of the pulse, which is similar to other attosecond setups [132].

Dependence on the CEP

High-harmonic spectra generated by short pulses are expected to display a pronounced CEP dependence. Figure 13.4 shows spectra, where the CEP ϕ_{CEP} was scanned over a range from 0 to 4π, using the fully compressed pulses from the hollow-core fibre, whose duration was below 4 fs, as characterized with a SEA-F-SPIDER device [260]. The high-energy domain of the spectra changes from discrete ($\phi_{\mathrm{CEP}} = 2.6\pi$) to continuous ($\phi_{\mathrm{CEP}} = 3.1\pi$), whereas the lower-energy domain remains discrete for any CEP value. As explained on page 33, this change in the spectrum as a function of the CEP is due to the fact that, depending on ϕ_{CEP}, either one or two maxima in the electric field strength of the driving pulse are present close to the maximum of the pulse envelope (also see fig. 3.2). For two maxima with approximately equal magnitude, there are two consecutive attosecond bursts, whose interference modulates the spectrum of the XUV pulse. On the contrary, if there is only a single dominating maximum in the pulse, there is also only a single attosecond burst with spectral components reaching the highest energies. Therefore, when the continuous, high-energy portion is filtered using a suitable metal filter, keeping the CEP fixed at an appropriate value is expected to result in the generation of isolated attosecond pulses. To prove that this is actually the case, it is necessary to fully characterize the XUV pulses generated under these conditions, using e.g. the FROG-CRAB technique.

Another observation is the shift of the high-harmonic peak position with the CEP for high energies (forming the tilted stripes in fig. 13.4a) ranging from ∼30 eV to ∼45 eV). This is due to the consecutive half cycles in the pulse having different maximum intensities, whose relative magnitudes depend on the CEP. For a given return energy (determining the energy of the high-harmonic radiation according to eq. (1.30)), recombination (and thus high-harmonic emission) takes place at different instants in the two half cycles, altering the time interval between the consecutive XUV bursts as a function of the CEP [261]. In the frequency domain, this altered temporal spacing leads to a shift of the peaks in the spectrum away from odd multiples of the fundamental frequency (also see refs. [261–263]).

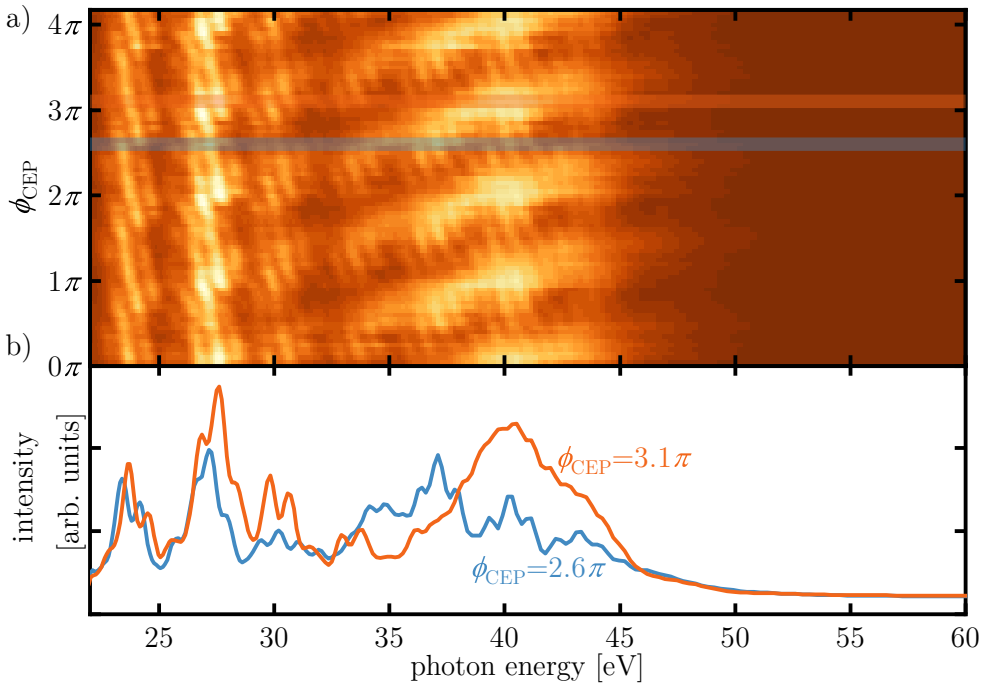

Figure 13.4: a) High-harmonic yield as a function of the photon energy and the CEP ϕ_{CEP}. Sub-4 fs-pulses and a cell target filled with 70 mbar of argon were used for HHG. b) Sections for two different CEP-values as indicated in a). The fact that the high-energy portion of the spectrum becomes continuous for specific CEP-values indicates the possibility to isolate a single burst when employing suitable spectral filtering.

13.2 OUTLOOK: COMPLETE RECONSTRUCTION OF THE ATTOSECOND PULSES.

In this section, first measurements where the radiation from the attosecond beamline was used to ionize another target and the charged particles were detected are presented. For simplicity, the output from the OPCPA system was used directly as input for the beamline, i.e. without further compression in the hollow-core fibre (resulting in IR pulses with a duration of ∼7 fs), and a velocity-map-imaging spectrometer was used as the detector instead of the reaction microscope. The measurements presented in this section were performed and analysed by Mikhail Osolodkov, and they serve as a demonstration of the proper functioning of the designed beamline.

Velocity-map-imaging spectrometers

A velocity-map-imaging spectrometer allows the detection of two-dimensional projections of either electron or ion momentum distributions. A non-homogeneous electric field created by two electrodes, the *repeller* and the *extractor*, guides the charged particles to an MCP detector combined with a phosphor screen, whose image is recorded with a camera [228]. For suitably chosen extraction fields, the image on the detector corresponds to the projection of the velocity distribution of the charged particles along the acceleration direction. If the actual three-dimensional distribution has cylindrical symmetry around that axis, a so-called *Abel transform* [264] can be used to reconstruct it from the detector image.

In the velocity-map-imaging spectrometer used here, the nozzle providing the gas for the interaction is integrated into the repeller electrode [255], which allows the laser to come as close as possible to the nozzle and thus provides much higher target densities compared to what is possible in the reaction microscope.[2] This should make it easier to find the ionization signal in a velocity-map-imaging spectrometer. Once the proper and reliable functioning of the beamline has been established, replacing the velocity-map-imaging spectrometer with the reaction microscope is expected to be easier than testing the beamline directly with the reaction microscope.

Photoelectron momentum distributions

Figure 13.5a) shows an electron distribution as recorded in the velocity-map-imaging spectrometer using only the XUV pulses for ionization. The target in the velocity-map-imaging spectrometer was a beam of argon atoms using a stagnation pressure of ∼1 bar. As mentioned, the driving laser had a duration of ∼7 fs, thus discrete harmonics were obtained. Correspondingly, in fig. 13.5, a pattern of discrete concentric rings can be observed. This pattern is created by the single-photon ionization of argon atoms from the various harmonic orders, where the resulting electron kinetic energy is given by the difference between the photon energy of the respective harmonic order and the IP of argon (see eq. (3.4)). The spacing between the rings is expected to correspond to twice the fundamental photon energy, as in the high-harmonic spectrum itself. The intensity of the distribution along the polar axis is peaked along the XUV polarization direction.

As shown in fig. 13.5b), when the XUV pulse ionizes the target in the presence of the IR pulse, additional rings appear between the rings observed in

[2] Note that, on the other hand, also much lower count rates are required in a reaction microscope, because coincidence detection demands that the count rate is limited to ∼0.1 events/laser pulse, whereas in a velocity-map-imaging spectrometer typically hundreds of events occur per laser pulse.

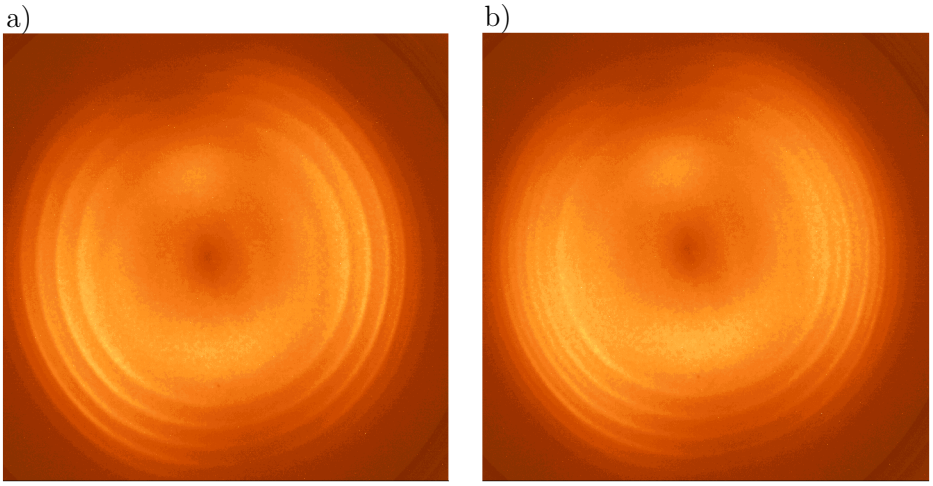

Figure 13.5: Two-dimensional projections of the photoelectron momentum distributions (recorded using a velocity-map-imaging spectrometer), generated a) by the XUV beam alone and b) by the temporally overlapping XUV and IR beams. The driving IR pulses had a duration of ∼7 fs. The target in the velocity-map-imaging spectrometer was argon, using a stagnation pressure of ∼1 bar. The target for HHG was also argon in a cell filled with 90 mbar of gas.

the XUV-only spectrum. These are the sidebands, whose origin is explained on page 37.

Time-dependent photoelectron spectra

Figure 13.6 shows a delay scan of the kinetic-energy distribution of the photoelectrons, using the active delay-stabilization system.[3] For each delay, this distribution was obtained by applying the Abel transformation to the corresponding velocity-map-imaging spectrometer image [265], resulting in the three-dimensional momentum distribution, from which the kinetic-energy distribution can be calculated. The delay step size was 200 as. Figure 13.6c) displays the time-dependent signal integrated over various sidebands. As expected from eq. (3.5), the sideband intensity oscillates with the delay between the XUV and IR pulses, with a frequency twice as large as the fundamental laser frequency. Due to the relatively short driving-pulse duration, the assumption of infinitely narrow harmonics is not fulfilled in the presented measurement,

[3] Note that the data shown in fig. 13.6 has been acquired with a slightly modified beamline compared to the design shown in fig. 12.2. In particular, recombination of the IR and XUV beams took place before the toroidal mirror, which helped to increase the IR intensity, since this results in a larger IR beam on the recombination mirror, where accordingly less intensity is lost to the hole.

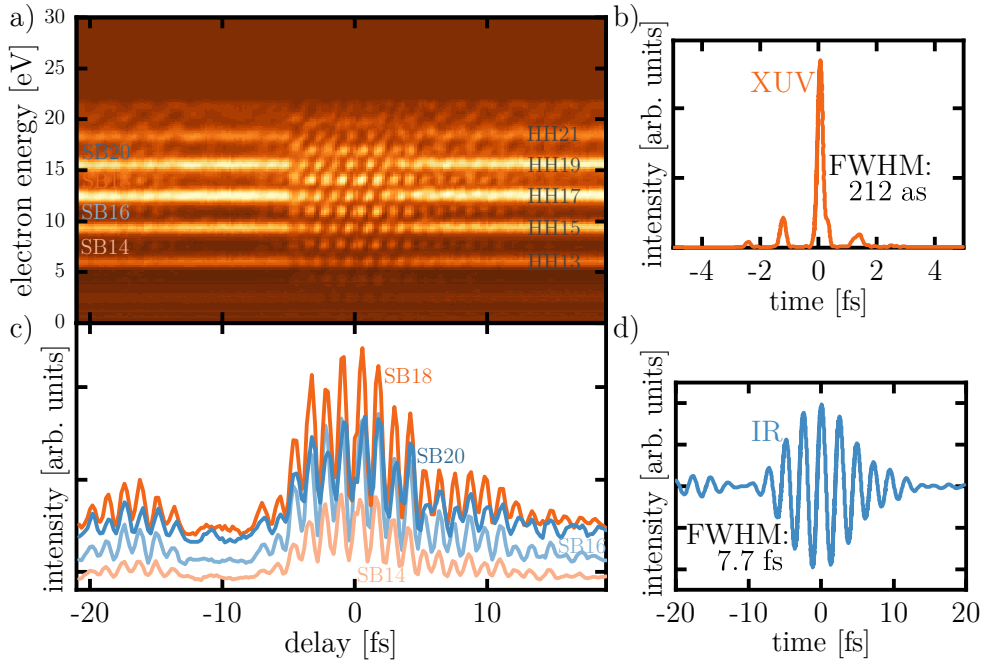

Figure 13.6: a) Photoelectron yield as a function of the delay between the XUV and IR pulses and the photoelectron energy. c) Line-outs thereof at the indicated sideband energy positions. From a), the attosecond pulse train and the driving-laser IR field, shown in b) and d) respectively, can be reconstructed.

thus eqs. (3.3) and (3.5) cannot be used to retrieve the attosecond pulse train. Instead, FROG-CRAB (see page 38), simultaneously making use of all the data in fig. 13.6a) [266, 267], is employed to reconstruct the short attosecond pulse train and the driving IR pulse. The result is shown in fig. 13.6b) and d), respectively. The successful complete reconstruction of the attosecond pulse train from the presented time-dependent photoelectron spectra demonstrates the attosecond stability of the designed beamline over the timespan in which the time-dependent spectra were acquired.

Note, however, that the reconstructed attosecond pulse train in fig. 13.6b) is unrealistically short considering that a 7 fs multi-cycle driving pulse was employed. A possible reason for this lies in the fact that the CEP of the driving pulse has not been actively stabilized during the acquisition of the data in fig. 13.6a): Simulations have shown that the pulse train reconstructed from calculated sideband spectra averaged over all CEP values shows a strong main pulse accompanied by satellite pulses with drastically underestimated intensities compared to the pulse trains reconstructed for each individual CEP value. An improved reconstruction procedure taking the averaging over CEP

values into account is currently being developed by my colleagues.

Next steps and current status

The next step in the test of the setup is to record time-dependent photoelectron spectra (still with a velocity-map-imaging spectrometer), including post-compression of the driving laser pulses in the hollow-core fibre, with the aim of demonstrating the generation of isolated attosecond pulses. This goal has meanwhile been reached by my colleagues. Furthermore, the reaction microscope has been integrated into the setup by now and is currently being tested. First static photoelectron spectra have already been acquired using the reaction microscope. This shows that the final goal of XUV-IR pump-probe experiments operating at a repetition rate of 100 kHz and combining isolated attosecond pulses and coincidence detection is well within reach.

Summary and Outlook

The overarching theme of the present thesis has been the implementation of kinematically complete coincidence experiments using a reaction microscope to study the interaction of beams of coherent electromagnetic radiation with molecules. Whereas in part II actual measurements on a polyatomic molecular target have been performed relying on SFI with an intense IR beam, in part III a beamline carrying over coincidence detection to attosecond pump-probe experiments has been presented.

In the experiments in part II, the coincidence capabilities of the reaction microscope were used to study not only properties of the 1,3-butadiene target but also of the three-step model underlying SFI – which is of fundamental importance for attosecond science – itself, by testing some of its common assumptions. The experiments relied on the multiple ionization channels participating in the strong-field response of butadiene (as in many other polyatomic molecules) and the possibility to correlate different ionization continua with the detected ion species. Focusing on the detected channel-resolved kinetic-energy distributions of the rescattered electrons affords novel insights into the continuum propagation and rescattering steps: From the different dependencies of the yield of rescattered electrons on the SFI laser's ellipticity for two different ionization channels, the participation of multiple channels in rescattering could be experimentally demonstrated. By aligning the molecules prior to SFI, the molecular-frame angular dependence of the rescattering probability could be measured for electrons originating from different molecular orbitals. The observed channel dependence is clear experimental evidence for the proposition that information on the initial orbital is preserved during the propagation in the continuum. In particular, the probability for a released electron to return to the core depends on the orientation of the molecule with respect to the laser polarization axis. This most likely derives from the shape of the continuum wave packet, which is determined by the shape of the orbital from which the electron was born. The angular dependence of the return probability has so far been ignored in most LIED and high-harmonic–spectroscopy studies. The rather strong dependence observed for 1,3-butadiene here could imply that the neglect of this factor in the interpretation of such experiments might introduce,

in some cases, errors in the analysis, especially when investigating polyatomic molecular targets. While the presented experiment can only make a definite statement about the electron density of the central portion of the returning wave packet and not about the curvature of its wavefront, an extension of the measurements was suggested, to answer the question if the curvature of the returning wave packet can be regarded as planar over the extent of the target and if this could be a relevant factor in the interpretation of LIED and high-harmonic–spectroscopy experiments.

Part III of the thesis dealt with the application of the reaction microscope to experiments beyond SFI and towards attosecond pump-probe coincidence studies. To this end, a novel beamline has been designed and built from scratch, with the aim of generating isolated attosecond pulses that are intense enough to perform experiments on molecular targets in a reaction microscope. In comparison with existing setups combining coincidence detection with attosecond pump-probe spectroscopy, the presented beamline features a ten times larger repetition rate, facilitating unprecedented acquisition rates for such experiments and, thus, making it possible to perform measurements which would lead to prohibitively long acquisition times in setups running at lower repetition rates. However, this also imposes unique design challenges due to the high average power and lower energy per pulse. Although the beamline has not yet been fully put into operation with the reaction microscope, the presented results provide a promising perspective that the beamline will fulfil its set goals. HHG at 100 kHz was demonstrated using driving pulses with a duration <4 fs. The CEP dependence of the high-harmonic spectrum, changing from discrete to continuous in a broad spectral region, indicates that isolated attosecond pulses can be obtained by simple spectral filtering. Furthermore, first successful pump-probe measurements requiring attosecond stability were presented, using a short pulse train and a velocity-map-imaging spectrometer as the detector.

Two important points remain to be demonstrated: the long-term attosecond stability of the setup (on the order of several tens of hours) and a high enough photon flux to achieve on average 0.1 events/laser pulse in the less dense molecular beam of the reaction microscope. Then, the presented beamline has the potential to enable novel experiments with attosecond temporal resolution on complex molecular targets, exploiting the wealth of information afforded by a reaction microscope in order to be in a better position regarding the interpretation of the processes occurring in such targets. An experiment with the simplest neutral molecule, H_2, could serve as a first benchmark project for the beamline, building on existing work where a less powerful velocity-map-imaging detector was employed in a pump-probe configuration [222] or static data was acquired in a reaction microscope [230]. Of particular interest in this target is the fact that a laser-induced transition of an electron ionized by the XUV influences the localization of the remaining bound electron, i.e. the continuum electron and the ion are entangled [2]. A time-resolved

experiment where the electron and H^+-fragment are detected in coincidence could help to further study this entanglement. It will be useful to gain experience in the operation of the beamline from the measurements performed on this well-studied target, before moving on to experiments in larger diatomic and polyatomic molecules, harnessing the potential promised by attosecond coincidence spectroscopy.

Bibliography

[1] A. H. Zewail. "Femtochemistry: Atomic-Scale Dynamics of the Chemical Bond". *The Journal of Physical Chemistry A* **104** (2000), p. 5660.

[2] F. Lépine, G. Sansone, and M. J. J. Vrakking. "Molecular applications of attosecond laser pulses". *Chemical Physics Letters* **578** (2013), p. 1.

[3] G. A. Worth and L. S. Cederbaum. "Beyond Born-Oppenheimer: Molecular Dynamics Through a Conical Intersection". *Annual Review of Physical Chemistry* **55** (2004), p. 127.

[4] J. Breidbach and L. S. Cederbaum. "Universal Attosecond Response to the Removal of an Electron". *Physical Review Letters* **94** (2005), p. 033901.

[5] M. Nisoli et al. "Attosecond Electron Dynamics in Molecules". *Chemical Reviews* **117** (2017), p. 10760.

[6] L. S. Cederbaum and J. Zobeley. "Ultrafast charge migration by electron correlation". *Chemical Physics Letters* **307** (1999), p. 205.

[7] F. Remacle and R. D. Levine. "An electronic time scale in chemistry". *Proceedings of the National Academy of Sciences* **103** (2006), p. 6793.

[8] P. B. Corkum. "Plasma perspective on strong field multiphoton ionization". *Physical Review Letters* **71** (1993), p. 1994.

[9] T. Gaumnitz et al. "Streaking of 43-attosecond soft-X-ray pulses generated by a passively CEP-stable mid-infrared driver". *Optics Express* **25** (2017), p. 27506.

[10] P. M. Paul et al. "Observation of a Train of Attosecond Pulses from High Harmonic Generation". *Science* **292** (2001), p. 1689.

[11] M. Hentschel et al. "Attosecond metrology". *Nature* **414** (2001), p. 509.

[12] G. Sansone et al. "Isolated Single-Cycle Attosecond Pulses". *Science* **314** (2006), p. 443.

[13] E. Goulielmakis et al. "Real-time observation of valence electron motion". *Nature* **466** (2010), p. 739.

[14] C. Ott et al. "Reconstruction and control of a time-dependent two-electron wave packet". *Nature* **516** (2014), p. 374.

[15] A. Kaldun et al. "Observing the ultrafast buildup of a Fano resonance in the time domain". *Science* **354** (2016), p. 738.

[16] O. Smirnova et al. “Strong-field control and spectroscopy of attosecond electron-hole dynamics in molecules”. *Proceedings of the National Academy of Sciences* **106** (2009), p. 16556.

[17] P. M. Kraus et al. “Measurement and laser control of attosecond charge migration in ionized iodoacetylene”. *Science* **350** (2015), p. 790.

[18] B. Wolter et al. “Ultrafast electron diffraction imaging of bond breaking in di-ionized acetylene”. *Science* **354** (2016), p. 308.

[19] C. I. Blaga et al. “Imaging ultrafast molecular dynamics with laser-induced electron diffraction”. *Nature* **483** (2012), p. 194.

[20] S. Haessler, J. Caillat, and P. Salières. “Self-probing of molecules with high harmonic generation”. *Journal of Physics B: Atomic, Molecular and Optical Physics* **44** (2011), p. 203001.

[21] J. Ullrich et al. “Recoil-ion and electron momentum spectroscopy: reaction-microscopes”. *Reports on Progress in Physics* **66** (2003), p. 1463.

[22] A. E. Boguslavskiy et al. “The Multielectron Ionization Dynamics Underlying Attosecond Strong-Field Spectroscopies”. *Science* **335** (2012), p. 1336.

[23] I. V. Hertel and C.-P. Schulz. *Atoms, Molecules and Optical Physics 1: Atoms and Spectroscopy*. Springer Berlin Heidelberg, 2015.

[24] F. Krausz and M. Ivanov. “Attosecond physics”. *Reviews of Modern Physics* **81** (2009), p. 163.

[25] Z. Chang. *Fundamentals of Attosecond Optics*. CRC Press, 2011.

[26] H. R. Reiss. “Limits on Tunneling Theories of Strong-Field Ionization”. *Physical Review Letters* **101** (2008), p. 043002.

[27] M. Y. Ivanov, M. Spanner, and O. Smirnova. “Anatomy of strong field ionization”. *Journal of Modern Optics* **52** (2005), p. 165.

[28] M. V. Ammosov, N. B. Delone, and V. P. Krainov. “Tunnel ionization of complex atoms and of atomic ions in an alternating electromagnetic field”. *Soviet Physics – Journal of Experimental and Theoretical Physics* **64** (1986), p. 1191.

[29] A. Perelomov, V. Popov, and M. Terent’ev. “Ionization of Atoms in an Alternating Electric Field”. *Soviet Physics – Journal of Experimental and Theoretical Physics* **23** (1966), p. 924.

[30] A. N. Pfeiffer et al. “Probing the Longitudinal Momentum Spread of the Electron Wave Packet at the Tunnel Exit”. *Physical Review Letters* **109** (2012), p. 083002.

[31] M. Li et al. “Subcycle Dynamics of Coulomb Asymmetry in Strong Elliptical Laser Fields”. *Physical Review Letters* **111** (2013), p. 023006.

[32] X. Sun et al. “Calibration of the initial longitudinal momentum spread of tunneling ionization”. *Physical Review A* **89** (2014), p. 045402.

[33] N. B. Delone and V. Krainov. *Multiphoton Processes in Atoms*. Springer Berlin Heidelberg, 1994.

[34] I. Dreissigacker and M. Lein. “Quantitative theory for the lateral momentum distribution after strong-field ionization”. *Chemical Physics* **414** (2013), p. 69.

[35] M. Meckel et al. “Laser-Induced Electron Tunneling and Diffraction”. *Science* **320** (2008), p. 1478.

[36] L. Arissian et al. “Direct Test of Laser Tunneling with Electron Momentum Imaging”. *Physical Review Letters* **105** (2010), p. 133002.

[37] D. Comtois et al. “Laser-induced orbital projection and diffraction of O_2 with velocity map imaging”. *Journal of Modern Optics* **60** (2013), p. 1395.

[38] S. G. Walt et al. “Dynamics of valence-shell electrons and nuclei probed by strong-field holography and rescattering”. *Nature Communications* **8** (2017), p. 15651.

[39] M. Spanner et al. “Reading diffraction images in strong field ionization of diatomic molecules”. *Journal of Physics B: Atomic, Molecular and Optical Physics* **37** (2004), p. L243.

[40] I. V. Litvinyuk et al. “Alignment-Dependent Strong Field Ionization of Molecules”. *Physical Review Letters* **90** (2003), p. 233003.

[41] D. Pinkham and R. R. Jones. “Intense laser ionization of transiently aligned CO”. *Physical Review A* **72** (2005), p. 023418.

[42] D. Pavičić et al. “Direct Measurement of the Angular Dependence of Ionization for N_2, O_2, and CO_2 in Intense Laser Fields”. *Physical Review Letters* **98** (2007), p. 243001.

[43] J. L. Hansen et al. “Orientation-dependent ionization yields from strong-field ionization of fixed-in-space linear and asymmetric top molecules”. *Journal of Physics B: Atomic, Molecular and Optical Physics* **45** (2011), p. 015101.

[44] R. Murray et al. “Tunnel Ionization of Molecules and Orbital Imaging”. *Physical Review Letters* **106** (2011), p. 173001.

[45] Y. Mairesse et al. “Electron wavepacket control with elliptically polarized laser light in high harmonic generation from aligned molecules”. *New Journal of Physics* **10** (2008), p. 025015.

[46] M. Spanner and S. Patchkovskii. “One-electron ionization of multielectron systems in strong nonresonant laser fields”. *Physical Review A* **80** (2009), p. 063411.

[47] X. M. Tong, Z. X. Zhao, and C. D. Lin. “Theory of molecular tunneling ionization”. *Physical Review A* **66** (2002), p. 033402.

[48] S.-F. Zhao et al. “Effect of orbital symmetry on the orientation dependence of strong field tunnelling ionization of nonlinear polyatomic molecules”. *Journal of Physics B: Atomic, Molecular and Optical Physics* **44** (2011), p. 035601.

[49] J. Mikosch et al. “Channel- and Angle-Resolved Above Threshold Ionization in the Molecular Frame”. *Physical Review Letters* **110** (2013), p. 023004.

[50] J. Yao et al. “Alignment-Dependent Fluorescence Emission Induced by Tunnel Ionization of Carbon Dioxide from Lower-Lying Orbitals”. *Physical Review Letters* **111** (2013), p. 133001.

[51] M. Lein. "Antibonding molecular orbitals under the influence of elliptically polarized intense light". *Journal of Physics B: Atomic, Molecular and Optical Physics* **36** (2003), p. L155.

[52] J. Muth-Böhm, A. Becker, and F. H. M. Faisal. "Suppressed Molecular Ionization for a Class of Diatomics in Intense Femtosecond Laser Fields". *Physical Review Letters* **85** (2000), p. 2280.

[53] F. Schell et al. "Molecular orbital imprint in laser-driven electron recollision". *Science Advances* **4** (2018), eaap8148.

[54] S. Patchkovskii et al. "High harmonic generation and molecular orbital tomography in multielectron systems". *The Journal of Chemical Physics* **126** (2007), p. 114306.

[55] H. Akagi et al. "Laser Tunnel Ionization from Multiple Orbitals in HCl". *Science* **325** (2009), p. 1364.

[56] B. K. McFarland et al. "High Harmonic Generation from Multiple Orbitals in N_2". *Science* **322** (2008), p. 1232.

[57] O. Smirnova et al. "High harmonic interferometry of multi-electron dynamics in molecules". *Nature* **460** (2009), p. 972.

[58] M. Möller et al. "Dependence of high-order-harmonic-generation yield on driving-laser ellipticity". *Physical Review A* **86** (2012), p. 011401.

[59] Z. Chen et al. "Quantitative rescattering theory for laser-induced high-energy plateau photoelectron spectra". *Physical Review A* **79** (2009), p. 033409.

[60] G. G. Paulus et al. "Above-Threshold Ionization by an Elliptically Polarized Field: Quantum Tunneling Interferences and Classical Dodging". *Physical Review Letters* **80** (1998), p. 484.

[61] S. V. Popruzhenko. "Keldysh theory of strong field ionization: history, applications, difficulties and perspectives". *Journal of Physics B: Atomic, Molecular and Optical Physics* **47** (2014), p. 204001.

[62] P. Agostini et al. "Free-Free Transitions Following Six-Photon Ionization of Xenon Atoms". *Physical Review Letters* **42** (1979), p. 1127.

[63] L. B. Madsen. "Strong Field Dynamics: Scattering and Multiphoton Ionization". PhD thesis. University of Aarhus, 1998.

[64] H. Niikura et al. "Sub-laser-cycle electron pulses for probing molecular dynamics". *Nature* **417** (2002), p. 917.

[65] H. Sakai et al. "Nonsequential double ionization of D_2 molecules with intense 20-fs pulses". *Physical Review A* **67** (2003), p. 063404.

[66] P. Dietrich et al. "High-harmonic generation and correlated two-electron multiphoton ionization with elliptically polarized light". *Physical Review A* **50** (1994), R3585.

[67] V. R. Bhardwaj et al. "Quantum Interference in Double Ionization and Fragmentation of C_6H_6 in Intense Laser Fields". *Physical Review Letters* **87** (2001), p. 253003.

[68] M. Oppermann et al. "Multichannel contributions in the nonsequential double ionization of CO_2". *Physical Review A* **88** (2013), p. 043432.

[69] W. Zuo et al. "Experimental and theoretical study on nonsequential double ionization of carbon disulfide in strong near-IR laser fields". *Physical Review A* **93** (2016), p. 053402.

[70] M. G. Pullen et al. "Transition from nonsequential to sequential double ionization in many-electron systems". *Physical Review A* **96** (2017), p. 033401.

[71] M. G. Pullen et al. "Imaging an aligned polyatomic molecule with laser-induced electron diffraction". *Nature Communications* **6** (2015), p. 7262.

[72] Y. Ito et al. "Extracting conformational structure information of benzene molecules via laser-induced electron diffraction". *Structural Dynamics* **3** (2016), p. 034303.

[73] Y. Ito et al. "Extraction of geometrical structure of ethylene molecules by laser-induced electron diffraction combined with ab initio scattering calculations". *Physical Review A* **96** (2017), p. 053414.

[74] E. T. Karamatskos et al. "Atomic-resolution imaging of carbonyl sulfide by laser-induced electron diffraction". *The Journal of Chemical Physics* **150** (2019), p. 244301.

[75] K. Amini et al. "Imaging the Renner–Teller effect using laser-induced electron diffraction". *Proceedings of the National Academy of Sciences* **116** (2019), p. 8173.

[76] H. Fuest et al. "Diffractive Imaging of C_{60} Structural Deformations Induced by Intense Femtosecond Midinfrared Laser Fields". *Physical Review Letters* **122** (2019), p. 053002.

[77] A. Becker and F. H. M. Faisal. "Intense-field many-body S-matrix theory". *Journal of Physics B: Atomic, Molecular and Optical Physics* **38** (2005), R1.

[78] C. D. Lin et al. "Elements of the quantitative rescattering theory". *Journal of Physics B: Atomic, Molecular and Optical Physics* **51** (2018), p. 104001.

[79] A.-T. Le et al. "Quantitative rescattering theory for high-order harmonic generation from molecules". *Physical Review A* **80** (2009), p. 013401.

[80] C. D. Lin et al. "Strong-field rescattering physics—self-imaging of a molecule by its own electrons". *Journal of Physics B: Atomic, Molecular and Optical Physics* **43** (2010), p. 122001.

[81] S. Sukiasyan et al. "Exchange and polarization effect in high-order harmonic imaging of molecular structures". *Physical Review A* **82** (2010), p. 043414.

[82] J. Xu et al. "Self-imaging of molecules from diffraction spectra by laser-induced rescattering electrons". *Physical Review A* **82** (2010), p. 033403.

[83] J. Xu et al. "Laser-Induced Electron Diffraction for Probing Rare Gas Atoms". *Physical Review Letters* **109** (2012), p. 233002.

[84] T. Bredtmann and S. Patchkovskii. "Robust transverse structures in rescattered photoelectron wave packets and their observable consequences". *Physical Review A* **99** (2019), p. 063424.

[85] T. Morishita and O. I. Tolstikhin. "Adiabatic theory of strong-field photoelectron momentum distributions near a backward rescattering caustic". *Physical Review A* **96** (2017), p. 053416.

[86] D. J. Griffiths and D. F. Schroeter. *Introduction to Quantum Mechanics*. 3rd ed. Cambridge University Press, 2018.

[87] J. F. Williams and B. A. Willis. "The scattering of electrons from inert gases. I. Absolute differential elastic cross sections for argon atoms". *Journal of Physics B: Atomic and Molecular Physics* **8** (1975), p. 1670.

[88] D. Ray et al. "Large-Angle Electron Diffraction Structure in Laser-Induced Rescattering from Rare Gases". *Physical Review Letters* **100** (2008), p. 143002.

[89] M. Okunishi et al. "Experimental Retrieval of Target Structure Information from Laser-Induced Rescattered Photoelectron Momentum Distributions". *Physical Review Letters* **100** (2008), p. 143001.

[90] Z. Chen et al. "Origin of species dependence of high-energy plateau photoelectron spectra". *Journal of Physics B: Atomic, Molecular and Optical Physics* **42** (2009), p. 061001.

[91] T. Morishita et al. "Potential for ultrafast dynamic chemical imaging with few-cycle infrared lasers". *New Journal of Physics* **10** (2008), p. 025011.

[92] P. Colosimo et al. "Scaling strong-field interactions towards the classical limit". *Nature Physics* **4** (2008), p. 386.

[93] M. Lewenstein et al. "Theory of high-harmonic generation by low-frequency laser fields". *Physical Review A* **49** (1994), p. 2117.

[94] T. Popmintchev et al. "Bright Coherent Ultrahigh Harmonics in the keV X-ray Regime from Mid-Infrared Femtosecond Lasers". *Science* **336** (2012), p. 1287.

[95] J.-C. Diels and W. Rudolph. *Ultrashort Laser Pulse Phenomena (Second Edition)*. Academic Press, 2006.

[96] E. Goulielmakis et al. "Single-Cycle Nonlinear Optics". *Science* **320** (2008), p. 1614.

[97] F. Calegari et al. "Temporal gating methods for the generation of isolated attosecond pulses". *Journal of Physics B: Atomic, Molecular and Optical Physics* **45** (2012), p. 074002.

[98] I. J. Sola et al. "Controlling attosecond electron dynamics by phase-stabilized polarization gating". *Nature Physics* **2** (2006), p. 319.

[99] B. Shan, S. Ghimire, and Z. Chang. "Generation of the attosecond extreme ultraviolet supercontinuum by a polarization gating". *Journal of Modern Optics* **52** (2005), p. 277.

[100] X. Feng et al. "Generation of Isolated Attosecond Pulses with 20 to 28 Femtosecond Lasers". *Physical Review Letters* **103** (2009), p. 183901.

[101] K. Zhao et al. "Tailoring a 67 attosecond pulse through advantageous phase-mismatch". *Optics Letters* **37** (2012), p. 3891.

[102] M. J. Abel et al. "Isolated attosecond pulses from ionization gating of high-harmonic emission". *Chemical Physics* **366** (2009), p. 9.

[103] F. Ferrari et al. "High-energy isolated attosecond pulses generated by above-saturation few-cycle fields". *Nature Photonics* **4** (2010), p. 875.

[104] H. Vincenti and F. Quéré. "Attosecond Lighthouses: How To Use Spatiotemporally Coupled Light Fields To Generate Isolated Attosecond Pulses". *Physical Review Letters* **108** (2012), p. 113904.

[105] K. T. Kim et al. "Photonic streaking of attosecond pulse trains". *Nature Photonics* **7** (2013), p. 651.

[106] P. Ranitovic et al. "Attosecond vacuum UV coherent control of molecular dynamics". *Proceedings of the National Academy of Sciences* **111** (2014), p. 912.

[107] J. Itatani et al. "Controlling High Harmonic Generation with Molecular Wave Packets". *Physical Review Letters* **94** (2005), p. 123902.

[108] K. Yoshii, G. Miyaji, and K. Miyazaki. "Dynamic Properties of Angle-Dependent High-Order Harmonic Generation from Coherently Rotating Molecules". *Physical Review Letters* **101** (2008), p. 183902.

[109] N. L. Wagner et al. "Monitoring molecular dynamics using coherent electrons from high harmonic generation". *Proceedings of the National Academy of Sciences* **103** (2006), p. 13279.

[110] S. Baker et al. "Probing Proton Dynamics in Molecules on an Attosecond Time Scale". *Science* **312** (2006), p. 424.

[111] W. Li et al. "Time-Resolved Dynamics in N_2O_4 Probed Using High Harmonic Generation". *Science* **322** (2008), p. 1207.

[112] H. Niikura, D. M. Villeneuve, and P. B. Corkum. "Mapping Attosecond Electron Wave Packet Motion". *Physical Review Letters* **94** (2005), p. 083003.

[113] S. Haessler et al. "Attosecond imaging of molecular electronic wavepackets". *Nature Physics* **6** (2010), p. 200.

[114] Y. Mairesse et al. "High Harmonic Spectroscopy of Multichannel Dynamics in Strong-Field Ionization". *Physical Review Letters* **104** (2010), p. 213601.

[115] R. Cireasa et al. "Probing molecular chirality on a sub-femtosecond timescale". *Nature Physics* **11** (2015), p. 654.

[116] H. J. Wörner et al. "Following a chemical reaction using high-harmonic interferometry". *Nature* **466** (2010), p. 604.

[117] H. J. Wörner et al. "High-Harmonic Homodyne Detection of the Ultrafast Dissociation of Br_2 Molecules". *Physical Review Letters* **105** (2010), p. 103002.

[118] H. J. Wörner et al. "Conical Intersection Dynamics in NO_2 Probed by Homodyne High-Harmonic Spectroscopy". *Science* **334** (2011), p. 208.

[119] P. M. Kraus et al. "Observation of laser-induced electronic structure in oriented polyatomic molecules". *Nature Communications* **6** (2015), p. 7039.

[120] J. Itatani et al. "Tomographic imaging of molecular orbitals". *Nature* **432** (2004), p. 867.

[121] D. Shafir et al. "Atomic wavefunctions probed through strong-field light–matter interaction". *Nature Physics* **5** (2009), p. 412.

[122] C. Vozzi et al. "Generalized molecular orbital tomography". *Nature Physics* **7** (2011), p. 822.

[123] D. Shafir et al. "Resolving the time when an electron exits a tunnelling barrier". *Nature* **485** (2012), p. 343.

[124] B. D. Bruner et al. "Multidimensional high harmonic spectroscopy". *Journal of Physics B: Atomic, Molecular and Optical Physics* **48** (2015), p. 174006.

[125] M. B. Gaarde et al. "Spatiotemporal separation of high harmonic radiation into two quantum path components". *Physical Review A* **59** (1999), p. 1367.

[126] X. He et al. "Spatial and spectral properties of the high-order harmonic emission in argon for seeding applications". *Physical Review A* **79** (2009), p. 063829.

[127] C. Lyngå et al. "Temporal coherence of high-order harmonics". *Physical Review A* **60** (1999), p. 4823.

[128] C. M. Heyl et al. "High-order harmonic generation with μJ laser pulses at high repetition rates". *Journal of Physics B: Atomic, Molecular and Optical Physics* **45** (2012), p. 74020.

[129] J. Rothhardt et al. "Absorption-limited and phase-matched high harmonic generation in the tight focusing regime". *New Journal of Physics* **16** (2014), p. 033022.

[130] A. Paul et al. "Phase-matching techniques for coherent soft X-ray generation". *IEEE Journal of Quantum Electronics* **42** (2006), p. 14.

[131] E. Constant et al. "Optimizing High Harmonic Generation in Absorbing Gases: Model and Experiment". *Physical Review Letters* **82** (1999), p. 1668.

[132] G. Sansone, L. Poletto, and M. Nisoli. "High-energy attosecond light sources". *Nature Photonics* **5** (2011), p. 655.

[133] S. Haessler et al. "Phase-resolved attosecond near-threshold photoionization of molecular nitrogen". *Physical Review A* **80** (2009), p. 011404.

[134] E. P. Månsson et al. "Double ionization probed on the attosecond timescale". *Nature Physics* **10** (2014), p. 207.

[135] M. Sabbar et al. "Resonance Effects in Photoemission Time Delays". *Physical Review Letters* **115** (2015), p. 133001.

[136] L. Cattaneo et al. "Attosecond coupled electron and nuclear dynamics in dissociative ionization of H_2". *Nature Physics* **14** (2018), p. 733.

[137] J. Vos et al. "Orientation-dependent stereo Wigner time delay and electron localization in a small molecule". *Science* **360** (2018), p. 1326.

[138] J. Itatani et al. "Attosecond Streak Camera". *Physical Review Letters* **88** (2002), p. 173903.

[139] R. Kienberger et al. "Atomic transient recorder". *Nature* **427** (2004), p. 817.

[140] Y. Mairesse and F. Quéré. "Frequency-resolved optical gating for complete reconstruction of attosecond bursts". *Physical Review A* **71** (2005), p. 011401.

[141] C. Liu et al. "Carrier-Envelope Phase Effects of a Single Attosecond Pulse in Two-Color Photoionization". *Physical Review Letters* **111** (2013), p. 123901.

[142] D. J. Kane. "Recent progress toward real-time measurement of ultrashort laser pulses". *IEEE Journal of Quantum Electronics* **35** (1999), p. 421.

[143] J. Gagnon, E. Goulielmakis, and V. S. Yakovlev. "The accurate FROG characterization of attosecond pulses from streaking measurements". *Applied Physics B* **92** (2008), p. 25.

[144] M. Chini et al. "Characterizing ultrabroadband attosecond lasers". *Optics Express* **18** (2010), p. 13006.

[145] D. Spangenberg et al. "Ptychographic ultrafast pulse reconstruction". *Optics Letters* **40** (2015), p. 1002.

[146] R. Moshammer et al. "A 4π recoil-ion electron momentum analyzer: a high-resolution "microscope" for the investigation of the dynamics of atomic, molecular and nuclear reactions". *Nuclear Instruments and Methods in Physics Research Section B: Beam Interactions with Materials and Atoms* **108** (1996), p. 425.

[147] S. Birkner. "Strong Field Ionization of Atoms and Molecules: Electron-Ion Coincidence Measurements at High Repetition Rate". PhD thesis. Freie Universität Berlin, 2015.

[148] O. Jagutzki et al. "A broad-application microchannel-plate detector system for advanced particle or photon detection tasks: large area imaging, precise multi-hit timing information and high detection rate". *Nuclear Instruments and Methods in Physics Research Section A: Accelerators, Spectrometers, Detectors and Associated Equipment* **477** (2002), p. 244.

[149] J. Ladislas Wiza. "Microchannel plate detectors". *Nuclear Instruments and Methods* **162** (1979), p. 587.

[150] B. Wolter. "Electron re-collision dynamics in strong mid-IR fields for diffraction imaging of molecular structure and its fragmentation". PhD thesis. Universitat Politècnica de Catalunya, 2017.

[151] H. Pauly. *Atom, Molecule, and Cluster Beams I: Basic Theory, Production and Detection of Thermal Energy Beams*. Springer Berlin Heidelberg, 2000.

[152] M. Hillenkamp, S. Keinan, and U. Even. "Condensation limited cooling in supersonic expansions". *The Journal of Chemical Physics* **118** (2003), p. 8699.

[153] W. Christen, K. Rademann, and U. Even. "Efficient cooling in supersonic jet expansions of supercritical fluids: CO and CO_2". *The Journal of Chemical Physics* **125** (2006), p. 174307.

[154] J. F. O'Hanlon. *A User's Guide to Vacuum Technology*. John Wiley & Sons, Ltd, 2004.

[155] S. S. Andrews. "Using Rotational Averaging To Calculate the Bulk Response of Isotropic and Anisotropic Samples from Molecular Parameters". *Journal of Chemical Education* **81** (2004), p. 877.

[156] C. Z. Bisgaard. "Laser-induced alignment: towards fixed-in-space molecules". PhD thesis. University of Aarhus, 2006.

[157] H. Stapelfeldt and T. Seideman. "Colloquium: Aligning molecules with strong laser pulses". *Reviews of Modern Physics* **75** (2003), p. 543.

[158] D. Williams. *Molecular Physics*. Academic Press, 1962.

[159] I. V. Hertel and C.-P. Schulz. *Atoms, Molecules and Optical Physics 2: Molecules and Photons - Spectroscopy and Collisions*. Springer Berlin Heidelberg, 2015.

[160] J. Mikosch et al. "The quantitative determination of laser-induced molecular axis alignment". *The Journal of Chemical Physics* **139** (2013), p. 024304.

[161] R. d. L. Kronig and I. I. Rabi. "The Symmetrical Top in the Undulatory Mechanics". *Physical Review* **29** (1927), p. 262.

[162] T. Seideman. "Revival Structure of Aligned Rotational Wave Packets". *Physical Review Letters* **83** (1999), p. 4971.

[163] F. Rosca-Pruna and M. J. J. Vrakking. "Experimental Observation of Revival Structures in Picosecond Laser-Induced Alignment of I_2". *Physical Review Letters* **87** (2001), p. 153902.

[164] P. R. Bunker and P. Jensen. *Fundamentals of Molecular Symmetry*. CRC Press, 2004.

[165] M. Leibscher et al. "Semiclassical catastrophes and cumulative angular squeezing of a kicked quantum rotor". *Physical Review A* **69** (2004), p. 032102.

[166] M. Leibscher, I. S. Averbukh, and H. Rabitz. "Enhanced molecular alignment by short laser pulses". *Physical Review A* **69** (2004), p. 013402.

[167] A. Rouzée et al. "Field-free one-dimensional alignment of ethylene molecule". *Physical Review A* **73** (2006), p. 033418.

[168] C. N. Banwell and E. M. McCash. *Fundamentals of Molecular Spectroscopy*. McGraw-Hill Publishing Company, 1994.

[169] E. Hamilton et al. "Alignment of symmetric top molecules by short laser pulses". *Physical Review A* **72** (2005), p. 043402.

[170] M. D. Poulsen et al. "Nonadiabatic alignment of asymmetric top molecules: Rotational revivals". *The Journal of Chemical Physics* **121** (2004), p. 783.

[171] V. Kumarappan et al. "Role of rotational temperature in adiabatic molecular alignment". *The Journal of Chemical Physics* **125** (2006), p. 194309.

[172] P. Hockett. "General phenomenology of ionization from aligned molecular ensembles". *New Journal of Physics* **17** (2015), p. 023069.

[173] P. W. Dooley et al. "Direct imaging of rotational wave-packet dynamics of diatomic molecules". *Physical Review A* **68** (2003), p. 023406.

[174] L. Christensen et al. "Deconvoluting nonaxial recoil in Coulomb explosion measurements of molecular axis alignment". *Physical Review A* **94** (2016), p. 023410.

[175] P. Bajorski. *Statistics for Imaging, Optics, and Photonics*. John Wiley & Sons, Ltd, 2011.

[176] M. Meckel et al. "Signatures of the continuum electron phase in molecular strong-field photoelectron holography". *Nature Physics* **10** (2014), p. 594.

[177] D. Comtois et al. "Observation of Coulomb focusing in tunnelling ionization of noble gases". *Journal of Physics B: Atomic, Molecular and Optical Physics* **38** (2005), p. 1923.

[178] M. Lezius et al. "Nonadiabatic Multielectron Dynamics in Strong Field Molecular Ionization". *Physical Review Letters* **86** (2001), p. 51.

[179] M. Lezius et al. "Polyatomic molecules in strong laser fields: Nonadiabatic multielectron dynamics". *The Journal of Chemical Physics* **117** (2002), p. 1575.

[180] M. R. Miller et al. "Laser-driven nonadiabatic electron dynamics in molecules". *Optica* **3** (2016), p. 259.

[181] A. E. Boguslavskiy et al. "Excited state non-adiabatic dynamics of the smallest polyene, trans 1,3-butadiene. I. Time-resolved photoelectron-photoion coincidence spectroscopy". *The Journal of Chemical Physics* **148** (2018), p. 164302.

[182] J. Dannacher et al. "Unimolecular fragmentations of internal energy selected 1,3-butadiene cations". *Chemical Physics* **51** (1980), p. 189.

[183] D. M. P. Holland et al. "An experimental and theoretical study of the valence shell photoelectron spectrum of butadiene". *Journal of Physics B: Atomic, Molecular and Optical Physics* **29** (1996), p. 3091.

[184] J. W. Keister et al. "Methyl Loss Kinetics of Energy-Selected 1,3-Butadiene and Methylcyclopropene Cations". *The Journal of Physical Chemistry A* **101** (1997), p. 1866.

[185] W. Fang et al. "Dissociative photoionization of 1,3-butadiene: Experimental and theoretical insights". *The Journal of Chemical Physics* **134** (2011), p. 174306.

[186] Y. Li et al. "Molecular-orbital tomography beyond the plane-wave approximation". *Physical Review A* **89** (2014), p. 045401.

[187] C. Zhai et al. "Coulomb-corrected molecular orbital tomography of nitrogen". *Scientific Reports* **6** (2016), p. 23236.

[188] Y. He et al. "Direct imaging of molecular rotation with high-order-harmonic generation". *Physical Review A* **99** (2019), p. 053419.

[189] M. Bashkansky, P. H. Bucksbaum, and D. W. Schumacher. "Asymmetries in Above-Threshold Ionization". *Physical Review Letters* **60** (1988), p. 2458.

[190] G. Gingras, A. Tripathi, and B. Witzel. "Wavelength and Intensity Dependence of Short Pulse Laser Xenon Double Ionization between 500 and 2300 nm". *Physical Review Letters* **103** (2009), p. 173001.

[191] M. Berglund and M. E. Wieser. "Isotopic compositions of the elements 2009 (IUPAC Technical Report)". *Pure and Applied Chemistry* **83** (2009), p. 397.

[192] J. P. Simons et al. "Observing molecular dynamics with timed Coulomb explosion imaging". *Philosophical Transactions of the Royal Society of London. Series A: Mathematical, Physical and Engineering Sciences* **356** (1998), p. 329.

[193] J. Xu et al. "Diffraction using laser-driven broadband electron wave packets". *Nature Communications* **5** (2014), p. 4635.

[194] M. G. Pullen et al. "Influence of orbital symmetry on diffraction imaging with rescattering electron wave packets". *Nature Communications* **7** (2016), p. 11922.

[195] K. S. Budil et al. “Influence of ellipticity on harmonic generation”. *Physical Review A* **48** (1993), R3437.

[196] A. Flettner et al. “Ellipticity dependence of atomic and molecular high harmonic generation”. *The European Physical Journal D* **21** (2002), p. 115.

[197] B. Shan, S. Ghimire, and Z. Chang. “Effect of orbital symmetry on high-order harmonic generation from molecules”. *Physical Review A* **69** (2004), p. 021404.

[198] T. Kanai, S. Minemoto, and H. Sakai. “Ellipticity dependence of high-order harmonic generation from aligned molecules.” *Physical Review Letters* **98** (2007), p. 053002.

[199] T. Kanai, S. Minemoto, and H. Sakai. “Quantum interference during high-order harmonic generation from aligned molecules”. *Nature* **435** (2005), p. 470.

[200] A. F. Alharbi et al. “Effects of nodal planes on strong-field ionization and high-order-harmonic generation in ring-type molecules”. *Physical Review A* **96** (2017), p. 043402.

[201] A. Ferré et al. “Multi-channel electronic and vibrational dynamics in polyatomic resonant high-order harmonic generation”. *Nature Communications* **6** (2015), p. 5952.

[202] W. Komatsubara, S. Minemoto, and H. Sakai. “Electron-wave-packet dynamics extracted from the ellipticity dependence of high-order harmonic generation in benzene molecules”. *Physical Review A* **98** (2018), p. 023416.

[203] K. I. Ramachandran, G. Deepa, and K. Namboori. *Computational Chemistry and Molecular Modeling*. Springer Berlin Heidelberg, 2008.

[204] V. I. Lebedev and D. N. Laikov. “A quadrature formula for the sphere of the 131st algebraic order of accuracy”. *Doklady Mathematics* **59** (1999), p. 477.

[205] E. W. Larsen et al. “Sub-cycle ionization dynamics revealed by trajectory resolved, elliptically-driven high-order harmonic generation”. *Scientific Reports* **6** (2016), p. 39006.

[206] X. Ren, V. Makhija, and V. Kumarappan. “Multipulse Three-Dimensional Alignment of Asymmetric Top Molecules”. *Physical Review Letters* **112** (2014), p. 173602.

[207] L. Holmegaard et al. “Photoelectron angular distributions from strong-field ionization of oriented molecules”. *Nature Physics* **6** (2010), p. 428.

[208] Q. Ji et al. “Orbital-resolved strong-field single ionization of acetylene”. *Physical Review A* **92** (2015), p. 043401.

[209] X. Zhou et al. “Elliptically Polarized High-Order Harmonic Emission from Molecules in Linearly Polarized Laser Fields”. *Physical Review Letters* **102** (2009), p. 073902.

[210] D. Zeidler et al. “Alignment independence of the instantaneous ionization rate for nitrogen molecules”. *Journal of Physics B: Atomic, Molecular and Optical Physics* **39** (2006), p. L159.

[211] Z. B. Walters, S. Tonzani, and C. H. Greene. "Limits of the Plane Wave Approximation in the Measurement of Molecular Properties". *The Journal of Physical Chemistry A* **112** (2008), p. 9439.

[212] P. Salières et al. "Imaging orbitals with attosecond and Angström resolutions: toward attochemistry?" *Reports on Progress in Physics* **75** (2012), p. 062401.

[213] C. Zhai et al. "Diffractive molecular-orbital tomography". *Physical Review A* **95** (2017), p. 033420.

[214] D.-D. T. Vu et al. "Dynamic molecular structure retrieval from low-energy laser-induced electron diffraction spectra". *Journal of Physics B: Atomic, Molecular and Optical Physics* **50** (2017), p. 245101.

[215] P. Tzallas et al. "Extreme-ultraviolet pump-probe studies of one-femtosecond-scale electron dynamics". *Nature Physics* **7** (2011), p. 781.

[216] P. A. Carpeggiani et al. "Disclosing intrinsic molecular dynamics on the 1-fs scale through extreme-ultraviolet pump-probe measurements". *Physical Review A* **89** (2014), p. 023420.

[217] T. Okino et al. "Direct observation of an attosecond electron wave packet in a nitrogen molecule". *Science Advances* **1** (2015), e1500356.

[218] M. Uiberacker et al. "Attosecond real-time observation of electron tunnelling in atoms". *Nature* **446** (2007), p. 627.

[219] M. Schultze et al. "Delay in Photoemission". *Science* **328** (2010), p. 1658.

[220] J. Mauritsson et al. "Attosecond Electron Spectroscopy Using a Novel Interferometric Pump-Probe Technique". *Physical Review Letters* **105** (2010), p. 053001.

[221] V. Gruson et al. "Attosecond dynamics through a Fano resonance: Monitoring the birth of a photoelectron". *Science* **354** (2016), p. 734.

[222] G. Sansone et al. "Electron localization following attosecond molecular photoionization". *Nature* **465** (2010), p. 763.

[223] W. Siu et al. "Attosecond control of dissociative ionization of O_2 molecules". *Physical Review A* **84** (2011), p. 063412.

[224] F. Kelkensberg et al. "Attosecond Control in Photoionization of Hydrogen Molecules". *Physical Review Letters* **107** (2011), p. 043002.

[225] C. Neidel et al. "Probing Time-Dependent Molecular Dipoles on the Attosecond Time Scale". *Physical Review Letters* **111** (2013), p. 033001.

[226] F. Calegari et al. "Ultrafast electron dynamics in phenylalanine initiated by attosecond pulses". *Science* **346** (2014), p. 336.

[227] A. Trabattoni et al. "Mapping the Dissociative Ionization Dynamics of Molecular Nitrogen with Attosecond Time Resolution". *Physical Review X* **5** (2015), p. 041053.

[228] A. T. J. B. Eppink and D. H. Parker. "Velocity map imaging of ions and electrons using electrostatic lenses: Application in photoelectron and photofragment ion imaging of molecular oxygen". *Review of Scientific Instruments* **68** (1997), p. 3477.

[229] M. Sabbar et al. "Combining attosecond XUV pulses with coincidence spectroscopy". *Review of Scientific Instruments* **85** (2014), p. 103113.

[230] A. Fischer et al. "Electron Localization Involving Doubly Excited States in Broadband Extreme Ultraviolet Ionization of H_2". *Physical Review Letters* **110** (2013), p. 213002.

[231] A. Fischer et al. "Measurement of the autoionization lifetime of the energetically lowest doubly excited $Q_1\,{}^1\Sigma_u^+$ state in H_2 using electron ejection asymmetry". *Journal of Physics B: Atomic, Molecular and Optical Physics* **47** (2013), p. 021001.

[232] M. Reduzzi. "Time-resolved investigation of electron dynamics in few-particle systems using a versatile attosecond beamline". PhD thesis. Politecnico di Milano, 2015.

[233] A. Harth et al. "Compact 200 kHz HHG source driven by a few-cycle OPCPA". *Journal of Optics* **20** (2017), p. 014007.

[234] S. Kühn et al. "The ELI-ALPS facility: the next generation of attosecond sources". *Journal of Physics B: Atomic, Molecular and Optical Physics* **50** (2017), p. 132002.

[235] J. Rothhardt et al. "High-repetition-rate and high-photon-flux 70 eV high-harmonic source for coincidence ion imaging of gas-phase molecules". *Optics Express* **24** (2016), p. 18133.

[236] S. Witte and K. S. E. Eikema. "Ultrafast Optical Parametric Chirped-Pulse Amplification". *IEEE Journal of Selected Topics in Quantum Electronics* **18** (2012), p. 296.

[237] A. Vaupel et al. "Concepts, performance review, and prospects of table-top, few-cycle optical parametric chirped-pulse amplification". *Optical Engineering* **53** (2013), p. 1.

[238] M. Müller et al. "1 kW 1 mJ eight-channel ultrafast fiber laser". *Optics Letters* **41** (2016), p. 3439.

[239] S. Hädrich et al. "Energetic sub-2-cycle laser with 216 W average power". *Optics Letters* **41** (2016), p. 4332.

[240] F. J. Furch et al. "CEP-stable few-cycle pulses with more than 190 μJ of energy at 100 kHz from a noncollinear optical parametric amplifier". *Optics Letters* **42** (2017), p. 2495.

[241] D. Hoff et al. "Continuous every-single-shot carrier-envelope phase measurement and control at 100 kHz". *Optics Letters* **43** (2018), p. 3850.

[242] T. Witting, F. J. Furch, and M. J. J. Vrakking. "Spatio-temporal characterisation of a 100 kHz 24 W sub-3-cycle NOPCPA laser system". *Journal of Optics* **20** (2018), p. 044003.

[243] R. Szipöcs et al. "Chirped multilayer coatings for broadband dispersion control in femtosecond lasers". *Optics Letters* **19** (1994), p. 201.

[244] J. S. Robinson et al. "The generation of intense, transform-limited laser pulses with tunable duration from 6 to 30 fs in a differentially pumped hollow fibre". *Applied Physics B* **85** (2006), p. 525.

[245] M. Schultze et al. “State-of-the-art attosecond metrology”. *Journal of Electron Spectroscopy and Related Phenomena* **184** (2011), p. 68.

[246] E. Magerl et al. “A flexible apparatus for attosecond photoelectron spectroscopy of solids and surfaces”. *Review of Scientific Instruments* **82** (2011), p. 063104.

[247] F. Frank et al. “Invited Review Article: Technology for Attosecond Science”. *Review of Scientific Instruments* **83** (2012), p. 071101.

[248] M. Fieß et al. “Versatile apparatus for attosecond metrology and spectroscopy”. *Review of Scientific Instruments* **81** (2010), p. 093103.

[249] M. Chini et al. “Delay control in attosecond pump-probe experiments”. *Optics Express* **17** (2009), p. 21459.

[250] M. C. E. Galbraith. “Time-resolved spectroscopy with attosecond pulses and pulse trains: ultrafast relaxation in benzene cations”. PhD thesis. Freie Universität Berlin, 2016.

[251] O. Pronin et al. “Ultrabroadband efficient intracavity XUV output coupler”. *Optics Express* **19** (2011), p. 10232.

[252] S. Hädrich et al. “Single-pass high harmonic generation at high repetition rate and photon flux”. *Journal of Physics B: Atomic, Molecular and Optical Physics* **49** (2016), p. 172002.

[253] Q. Zhang et al. “Suppression of driving laser in high harmonic generation with a microchannel plate”. *Optics Letters* **39** (2014), p. 3670.

[254] E. J. Takahashi et al. “High-throughput, high-damage-threshold broadband beam splitter for high-order harmonics in the extreme-ultraviolet region”. *Optics Letters* **29** (2004), p. 507.

[255] O. Ghafur et al. “A velocity map imaging detector with an integrated gas injection system”. *Review of Scientific Instruments* **80** (2009), p. 033110.

[256] C. Bourassin-Bouchet et al. “How to focus an attosecond pulse”. *Optics Express* **21** (2013), p. 2506.

[257] H. Coudert-Alteirac et al. “Micro-Focusing of Broadband High-Order Harmonic Radiation by a Double Toroidal Mirror”. *Applied Sciences* **7** (2017), p. 1159.

[258] M. Puppin et al. “Time- and angle-resolved photoemission spectroscopy of solids in the extreme ultraviolet at 500 kHz repetition rate”. *Review of Scientific Instruments* **90** (2019), p. 023104.

[259] A. Giree et al. “Numerical study of spatiotemporal distortions in noncollinear optical parametric chirped-pulse amplifiers”. *Optics Express* **25** (2017), p. 3104.

[260] T. Witting et al. “Characterization of high-intensity sub-4-fs laser pulses using spatially encoded spectral shearing interferometry”. *Optics Letters* **36** (2011), p. 1680.

[261] C. Ott et al. “Strong-field spectral interferometry using the carrier–envelope phase”. *New Journal of Physics* **15** (2013), p. 073031.

[262] M. Nisoli et al. “Effects of Carrier-Envelope Phase Differences of Few-Optical-Cycle Light Pulses in Single-Shot High-Order-Harmonic Spectra”. *Physical Review Letters* **91** (2003), p. 213905.

[263] P. Rudawski et al. “Carrier-envelope phase dependent high-order harmonic generation with a high-repetition rate OPCPA-system”. *The European Physical Journal D* **69** (2015), p. 70.

[264] M. J. J. Vrakking. “An iterative procedure for the inversion of two-dimensional ion/photoelectron imaging experiments”. *Review of Scientific Instruments* **72** (2001), p. 4084.

[265] G. A. Garcia, L. Nahon, and I. Powis. “Two-dimensional charged particle image inversion using a polar basis function expansion”. *Review of Scientific Instruments* **75** (2004), p. 4989.

[266] M. Lucchini et al. “Ptychographic reconstruction of attosecond pulses”. *Optics Express* **23** (2015), p. 29502.

[267] T. Witting et al. “Time-domain ptychography of over-octave-spanning laser pulses in the single-cycle regime”. *Optics Letters* **41** (2016), p. 4218.

Abbreviations

ATI	above-threshold ionization
CEP	carrier-envelope phase
CRATI	channel-resolved ATI
DCS	differential elastic scattering cross section
HHG	high-harmonic generation
HOMO	highest occupied molecular orbital
IP	ionization potential
IR	infrared
LIED	laser-induced electron diffraction
MCP	multi-channel plate
OPCPA	optical parametric chirped-pulse amplification
QRS	quantitative rescattering theory
SFI	strong-field ionization
TDRIS	time-dependent resolution-in-ionic-states
TDSE	time-dependent Schrödinger equation
XUV	extreme ultraviolet

List of Publications

- F. J. Furch, T. Witting, A. Giree, C. Luan, F. Schell, G. Arisholm, C.-P. Schulz, and M. J. J. Vrakking. "CEP-stable few-cycle pulses with more than 190 μJ of energy at 100 kHz from a noncollinear optical parametric amplifier". *Optics Letters* **42** (2017), p. 2495.
- F. Schell, T. Bredtmann, C.-P. Schulz, S. Patchkovskii, M. J. J. Vrakking, and J. Mikosch. "Molecular orbital imprint in laser-driven electron recollision". *Science Advances* **4** (2018), eaap8148.
- F. Schell, A. E. Boguslavskiy, C.-P. Schulz, S. Patchkovskii, M. J. J. Vrakking, A. Stolow, and J. Mikosch. "Sequential and direct ionic excitation in the strong-field ionization of 1-butene molecules". *Physical Chemistry Chemical Physics* **20** (2018), p. 14708.
- M. Osolodkov, F. J. Furch, F. Schell, P. Šušnjar, F. Cavalcante, C. S. Menoni, C.-P. Schulz, T. Witting, and M. J. J. Vrakking. "Generation and characterization of few-pulse attosecond pulse trains at 100 kHz repetition rate". *Journal of Physics B: Atomic, Molecular and Optical Physics*, **53** (2020), p. 194003.

Acknowledgements

Finally, I would like to acknowledge those who supported me during the last years:
First, I would like to thank Marc Vrakking for giving me the opportunity to carry out this doctoral research including work on both interesting physical problems and technical challenges. I am also indebted to Robert Moshammer, who generously accepted to co-referee the thesis. Funding by the DFG is gratefully acknowledged.
I am especially grateful to Claus-Peter Schulz for the excellent direct supervision and for always having an open door for issues and discussions of any kind. Furthermore, I would like to thank Jochen Mikosch for help in the lab, useful discussions, and for pushing the butadiene campaign to a successful conclusion. I would also like to express my gratitude to Federico Furch, who built the OPCPA system and helped me a lot, in particular in the planning of the attosecond beamline, and to Tobias Witting for his expertise and support in building the beamline. To Timm Bredtmann and Serguei Patchkovskii I am grateful for the theoretical support and successful collaboration in the butadiene project.
Support by the technical staff is also appreciated, in particular by Roman Peslin, who manufactured many customized mechanical parts for the attosecond beamline. I would also like to acknowledge Oleg Kornilov and Ahmet Ünal for their help with the kHz laser system.
In addition, I would like to thank Mikhail Osolodkov for performing the RABITT measurement, Sascha Birkner for building an operational reaction microscope ready to do experiments with, Peter Šušnjar for helping in the design of the XUV spectrometer, and Johannes Feldl for useful hints regarding the construction of the catcher setup. I would also like to thank all other PhD students and colleagues with whom I had the pleasure of working during my time at MBI, in particular Federico Branchi, Lorenz Drescher, Judith Dura, Friedrich Freyse, Martin Galbraith, Achut Giree, Johan Hummert, Sebastian Raabe, Katrin Reininger, and Geert Reitsma for sharing their experimental experience with me and for friendly conversations.
Naturally, a special thanks goes to my family, Gerrit, my four-pawed friends, and my wife Helene for all their support.

Selbstständigkeits-erklärung

Hiermit versichere ich, dass ich die vorliegende Dissertation selbstständig und nur unter Verwendung der angegebenen Literatur und Hilfsmittel verfasst habe. Die Arbeit ist weder in einem früheren Promotionsverfahren angenommen noch als ungenügend beurteilt worden.

Berlin, den 04. Mai 2020